

ISSN 1913-1844

MODERN APPLIED SCIENCE

**Vol. 2, No. 6
November 2008**

Editor-in-chief

Daniel Kingst

Managing Editor

Steven Clayer



Canadian Center of Science and Education



Contents

Investigating Issues in Mobile Network (In)Security <i>Johnnes Arreymbi</i>	3
Three Dimensional Finite Element Analysis of Radial-flow Impeller Temperature Field <i>Liangwei Zhong, Kangmin Chen, Jing Ni & Anyang He</i>	11
Modeling and Simulation of Three-phase ac-dc Converter-Fed dc Drive Systems with Uniform Pulse-Width Modulation Control <i>Chams-Eddine Feraga, Ali Yousfi & Abdallah Bouldjedri</i>	16
Characterizations and Applications of Semistrictly Prequasi-invex Functions <i>Zaiyun Peng, Dacheng Wang, Yawei Liu, Zhi Lin</i>	26
Reactions of <i>trans</i> -[Pt(¹⁵ NH ₃) ₂ (H ₂ O) ₂] ²⁺ with Glutathione <i>Sutopo Hadi & Trevor G. Appleton</i>	30
The Analysis of Vibro-Acoustic Coupled Characteristics of Ball Mill Cylinder Under Impact Excitation <i>Zhihong Liu & Chuijie Yi</i>	37
Effective Resources Management in Construction Industries for Success <i>Jayakumar Muthuramalingam</i>	41
Fabrication and Characterization of Nanometer-sized AgCl/PMMA Hybrid Materials <i>Xiangting Dong, Jinxian Wang, Xiuli Feng, L. Y. Wang, Nancy Kariuki, J. Luo, C. J. Zhong</i>	49
Self-Tuning of PI Speed Controller Gains Using Fuzzy Logic Controller <i>Mutasim Nour, Omrane Bouketir & Ch'ng Eng Yong</i>	55
The Way to Control the Flux in Sulfuric Acid Producing <i>Rui Cai & Ping Wang</i>	66
Operation and Combustion Characteristics of a Direct Injection Diesel Engine Fuelled with Esterified Cotton Seed Oil <i>Murugu Mohan Kumar Kandasamy, Sarangan Jeganathan & Rajamohan Ganesan</i>	71
Study on the Duality between MFP and ACP <i>Xiaojun Lei & Zhian Liang</i>	81
UPM-APSB AISA Airborne Hyperspectral Technology for Managing Mangrove Forest in Malaysia <i>Kamaruzaman Jusoff</i>	90
The Quality Test to Tarim River Sluice Concrete by the Rebound Method <i>Xindong Zhang & Yue Han</i>	97
Simulation of a Four-Car Elevator Operation Using MATLAB <i>Saw Soon King & Omrane Bouketir</i>	100
Analysis of Factors to Influence Single Yarn Strength CV Value <i>Dan Shen & Yi Zhang</i>	110
Sorption Kinetic Studies of Medical Grade Activated Carbon Prepared from Papaya Seeds <i>J.G. Collin & Mei P. Lee</i>	115
Study on the GMRES (m) Method of Krylov Subspace and Its Application <i>Silin Bai & Jianping Liu</i>	124



Contents

Experimental Studies on Disposal of Various Industrial Solid Wastes <i>K.Senthilkumar, V. Sivakumar & P. Akilamudhan</i>	128
A System Matrix Equations over an Arbitrary Skew Field <i>Youcai Xue</i>	133
Error Estimates to A Kind of Boundary Value Problem about An Elliptic Differential Equation with Variable Coefficient <i>Rao Li, Yiming Chen, Yong Li & Wei Guan</i>	138
The Choice of AC Electricity Bridge Adjustment Parameters <i>Zaiqi Fu, Changji Shan, Yuhui Luo & Xungang Yang</i>	143
Artificial Neural Network Based Rotor Position Estimation for Switched Reluctance Motor <i>L.Jessi Sahaya Shanathi, R.Arumugam, Y.K.Taly & S.B.Nandha Kumar</i>	148
Synthesis Study of Nucleus-cell Style High-property Water-absorbent Polymer <i>Cuirong Zhang, Shucai Mao & Zhenyu Jia</i>	156
An N-Component Series Repairable System with Repairman Doing Other Work and Priority in Repair <i>Jianyong Yang, Xianyun Meng, Weiyan Guo, Yanqin Guan & Taotao Wang</i>	163
Periodic Solutions of Higher Order with Restoring Terms Delay Functional Differential Equation with Neutral Type <i>Haiqing Wang</i>	169
Existence of Nonoscillatory Solution of High Order Linear Neutral Delay Difference Equation <i>Shasha Zhang, Xiaozhu Zhong, Ping Yu, Wenxia Zhang & Ning Li</i>	173
Bandwidth Enhancement for Microstrip Antenna in Wireless Applications <i>RSA Raja Abdullah, D Yoharaaj & A Ismail</i>	179
Application of Nanometer Aluminum Magnesium Hydroxide in PVDF Membrane Modification <i>Hanhui Wei, Dong Liu</i>	188

Investigating Issues in Mobile Network (In)Security

Johannes Arreymbi

School of Computing and Technology

University of East London

London- UK

E-mail: j.arreymbi@uel.ac.uk

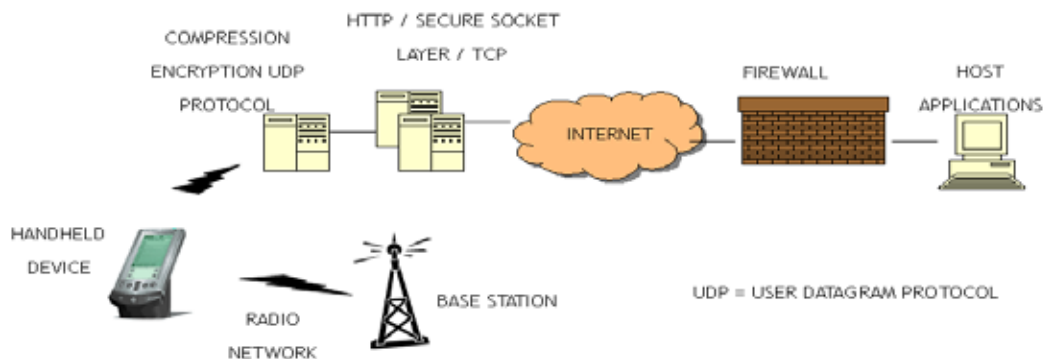
Abstract

The provision of adaptive content to mobile wireless devices has increasingly become very pertinent. Mobile smart phones and other wireless device usage is increasing daily with ground breaking technological developments – in design, style, content and micro-chips performance. Transmission of data in such environments requires absolute security to protect the individual and content. Any interference and interceptions in the communication process would bring about reduce system usage and development benefits. And with the rapid development in global communication networks, the threat of security and in particular that of cellular telecommunication systems is real and highly dangerous. This paper presents Investigating Issues to evaluate the data security protection accorded by the global telecommunication systems against interception, using encryption, authentication, and ciphering. It will also attempt to discuss several issues of mobile wireless (in)security. In so doing, some security flaws in these approaches will be examined and some suggestions made.

Keywords: Cellular communication, Data protection, Mobile Wireless networks, Multimedia content, Security, Encryption, Authentication, Ciphering, Interception, Identity Management (IDM)

1. Introduction

Mobile computing is pervading our society and lifestyles. In most cases, connecting to other devices in a mobile environment requires wireless networks. Connectivity could be done via Bluetooth, Infrared, RF Signals, GSM and satellite etc and depending on the nature, purpose and distance of the systems used. The delivery of contents of the multimedia packages – conversation (audio), text, graphics, colour, and video messages - delivered may be very important and confidential. In fact, mobile computing has contributed in increasing productivity and operational efficiency on individuals and businesses, some with highly sensitive and confidential information that needs to be protected for competitive advantage. However, the flexibility and ubiquity of the mobile - wireless system comes at a price – that of (in)security. Network (in)security is of paramount concern to any wireless or mobile network provider and practitioner. The fact that radio signals travel through air space, they can easily be intercepted with the right equipments. The mobility of such equipments makes them difficult to trace. Increasingly, hackers and scammers are scanning airwaves and siphoning off cellular ID numbers for improper use, manipulative scams, and sometimes even jamming the airwaves with denial-of-service (DOS) attacks, reducing through-puts and making it difficult for services to function. Nowadays, even pager messages are no longer safe. The security of a mobile network such as GSM includes multiple technologies that attempt to resolve ID authentication, integrity and other identification problems. Some come in the form of firewalls, authentication servers, biometrics, cryptography, intrusion detection, virus protection and Virtual Private Networks.



A Model of Security Architecture in a Mobile Environment [19]

Nowadays, millions of people use mobile phones over radio links for communication any time, any where, for business and /or convenience. The Global System for Mobile communication or Group Special Mobile (GSM) platform which was formed in 1982 [1] is a hugely successful wireless technology and an unprecedented invention of global achievement. Some research showed that at the end of Jan 2004 [2] there were over 1 billion GSM subscribers across more than 200 countries. In Japan alone, there were more than 87million phone subscribers, with internet-enabled phones accounting for 80% of the subscriptions in 2005. Today the world-wide figures are increasing even more, especially in Africa, Asia and other advancing economies where mobile communication uptake has increased by approximately 65% [17, 18].

The passage of time has moved wireless telecommunication some steps further. In the older analogue-based cellular telephone systems such as the Advanced Mobile Phone System (AMPS) and the Total Access Communication System (TACS) [3], cellular drop rate, interference and interception rate and general fraud on such systems were extensive and very rampant. It was very simple and easy for a radio hobbyist to tune in and hear mobile telephone conversations. Mostly, without any encryption [4], the voice and user data of the subscriber was in pure raw form and sent over the networks. SIM card cloning too was very easy and they together posed dangerous threat to the users. Such fatal flaws in the mobile phone and wireless technologies were all prevalent [5]. To prevent such flaws in mobile communication and to make mobile phone traffic more secure, GSM (Global System for Mobile communication or Group Special Mobile) became an apparent and relevant solution. GSM operates in the 900MHz, 1800MHz, or 1900 MHz frequency bands, which in essence provide a secure and confidential channel of communication.

The prevalence of GSM technologies, together with the introduction of multimedia content delivery, provided means for users to begin to enjoy some of the benefits of having stable, continuous, private and secure environments for communication – audio, SMS, MMS services - through GSM network systems [18]. But how safe and secure is the GSM technology? Can it really protect vitally important information? In this paper we would provide a brief overview of GSM, its security and encryption technologies. Furthermore, we will attempt to provide a model for GSM security optimization. The third section will look at some GSM flaws and provide possible measures to overcome them. The final section gives an evaluative critique and conclusion to this paper.

2. Security Techniques used in Mobile Systems

2.1 Encryption:

All cellular communication operates using air waves which can easily be intercepted with easily available suitable eavesdropping receivers. Considering this issue, the GSM technology integrated some security controls [6] in order to make the cellular system as secure as a fixed line phone. The system offers some level of physical security such that physical access is needed to the phone line for listening-in to be possible. This kind of control measures provides better security for conversation between two mobile phone users. According to GSM specification 02.09 [6], the security functions put in place are: authentication of a user, data and signaling confidentiality and Confidentiality of a user. Authentication of a user means that a mobile phone needs to prove that it has access to a particular network account with the operator. In other words, a person is not allowed to personate certain subscriber to use that person's account. This function proves very important in protecting all subscribers' cellular air-time fee and other benefits. Data and signaling confidentiality can be more appropriately understood. This function is to make sure that all signaling and user data, such as text messaging and speech are protected against interception by means of ciphering. Meanwhile confidentiality of a user function keeps the unique International Mobile Subscriber Identity (IMSI) and prevents it from being disclosed and displayed in plaintext to avoid leaving tracks of the user. It also means that intruders cannot easily track down certain subscriber of the GSM system.

Besides some of the above security functions, there are other functions that prove to make the mobile phone more secured. The most commonly known protective system is that of the PIN which GSM system provides. In this kind of security control, if a user fails to provide a valid PIN number, the system would not allow the user to continue to perform any other authentication functions. And, in order to distribute the authentication and ciphering information throughout the network, the root key of all ciphering key generation and authentication, Ki [4] have to be distributed by another form known as vectors. This too adds another security level in the proposed security model as would be highlighted below and aims to improve the security of GSM technology

In managing mobile access to network system resources, it is very essential to enforce security measures. The system should be able to know who is accessing resources at what point and know the purpose of each access. Controlling access to systems is best illustrated in the AAA framework: *Authentication, Authorisation and Accounting* [20, 21]. Authentication is the ability to identify network or system users through the validation of a set of assigned credentials such as user identification number and passwords. Authorisation defines the ability of a specific user to perform certain tasks, such as creating, modifying and deleting, after authentication has taken place. And, Accounting allows it to measure and record the consumption of network or system resources. This framework adapts well in a mobile or wireless environment. In this paper we will concern more on Authentication issues.

The most challenging amongst the three issues in the AAA framework is authentication. The complexity of attacks nowadays has pushed the network society to build up strong authentication techniques. Rather than only relying on the inadequate use of usernames and passwords, different and efficient technologies have been developed for improve security, such as RADIUS (Remote Authentication Dial up User Service), Token-based Strong authentication, 802.11i Security, Secure Socket Layer (SSL), Virtual Private Networks (VPN) and Media Access Control (MAC) Filtering. In most instances, GSM networks utilises encryption for three purposes: authentication, encryption and key generation [7], which would be discussed later.

2.2 Authentication:

Authentication service within a system is concerned with assuring that a communication is authentic. It can prohibit an unauthorized user claiming to be a bonafide mobile subscriber logging into the network [6]. In order to ascertain the position, some kind of challenge needs to be issued by the network, for which the mobile station (MS) such as mobile phone, must respond to correctly. And if all fails, the unauthorized user therefore fails to personate the bonafide subscriber because of the challenge provided in connecting to the network. Others techniques, such as the SIM card, A3 Algorithm IMSI and Ki provide certain levels of security as would be discussed.

The Subscriber Identity Module (SIM) card is a small smartcard with embedded micro-chip which is inserted into the GSM phone and provides the appropriate details of an account. The SIM card contains information which is necessary to gain access to a particular account. Some of which are: International Mobile Subscriber Identity (IMSI), and Individual Subscriber Authentication Key (Ki) etc. The IMSI is a sequence of 15-digit code, used to identify an individual GSM mobile station (MS) to a GSM network. It is like an ID card of a person. The format of IMEI is AABBBB--CC-DDDDDD-E and it denotes basic coded identifier information as shown in the table 1 below.

Ki is utilised as a highly protected secret key shared between the MS and the Home Location Register (HLR) of the subscriber's home network [10]. It is a randomly generated 128-bit number and all keys and challenges used in the GSM system are generated according to Ki.

Also used in authentication is the A3 algorithm. The figure 2 below identifies the A3 algorithm procedure.

In this procedure, two 128-bit input codes are calculated by A3 algorithm and then a 32-bit output code is generated. However, A3 algorithm does not refer to a particular algorithm; it is rather the algorithm the operator has chosen to be implemented for authentication. The most common implementations for A3 are COMP128. The authentication procedure can simply be described as: mobile phone provides the Ki to network and the latter could verify the Ki to prove the mobile phone is not the impersonated one. But, this is highly insecure because the Ki could be intercepted by an eavesdropper. If Ki is lost, the authentication will disappear because the eavesdropper will personate that subscriber by providing the same Ki.

In such situations, the GSM technology provides a better method to resolve such a problem. The network generates a 128-bit random number, RAND [10] which is 128-bit random challenge generated by the Home Location Register (HLR). It then uses the A3 algorithm (see figure 2) to generate an authentication sign, SRES [10] which is the 32-bit Signed Response (SRES) generated by the MS and the Mobile Services Switching Center. After the generation of SRES, the network then sends the RAND to the phone. The phone respond by doing the same, generating a 32-bit SRES and then transmitting the SRES back to the network for comparison. Authentication is complete and becomes successful only when the two values of SRES are the same. This enables the subscriber to then join the network. If authentication fails the first time, the network may choose to repeat the authentication procedure with the IMSI. If that too fails, the network releases the radio connection. The mobile then considers that SIM to be invalid. Therefore, the protection of Ki is provided. And just in case an eavesdropper manages to intercept the RAND, no relevant information can be retrieved by listening to the channel because, each time, a new RAND number is generated.

2.3 Ciphering:

It is vitally important that providers keep user data and signaling data secure from interception by ciphering. The GSM system uses symmetric cryptography. And, in symmetric cryptography, the data is encrypted using an algorithm and the ciphering key. In GSM systems, the ciphering key is named Kc. Kc is the 64-bit ciphering key [10] and used as a Session Key for encryption of the air channel. Kc is generated by the MS from the RAND presented by the GSM network and the Ki from the SIM utilising the A8 algorithm. Like symmetric cryptography, this same Kc is needed by the decryption algorithm to decrypt the data. The idea is that the Kc should only be known by the phone and the network. If this is the case, the data is meaningless to anyone intercepting it. As earlier mentioned, the A8 algorithm uses the RAND and Ki as input to generate a 64-bit ciphering key (see figure 3) Kc which is then stored in the SIM and readable by the phone [11]. Like the SRES, the network also generates the Kc and distributes it to the base station (BTS) handling the connection.

The A5 algorithm uses the 64-bit cipher key [12] derived from the 128-bit authentication key by the A8 algorithm in the SIM card to perform the encryption. The A5 algorithm is also 'seeded' by the value COUNT [6], which is sequentially

applied to each 4.615ms GSM frame (see figure 4). Currently there are 3 algorithms defined for ciphering algorithms – A5/1, A5/2 and A5/3 [6]. A5/1 and A5/2 were the original algorithms defined by the GSM standard. A5/2 was a deliberate weakening of the algorithm for certain export regions, where A5/1 is used. In countries such as the US, UK and Australia, A5/3 was added in 2002 and is based on the open Kasumi algorithm defined by 3GPP. The output of A5 algorithm is the cipher text which is very secure and cannot be easily decrypted by eavesdroppers.

2.4 Anonymity:

According to Srinivas [13], when a new GSM subscriber switches on his/her phone for the first time, its International Mobile Subscriber Identity (IMSI), for example real identity, is used and a Temporary Mobile Subscriber Identity (TMSI) is issued to the subscriber, which from then on is always used to identify the user. Anonymity is a process set to make it difficult to track and trace a mobile phone user of the system. In this process, once ciphering has commenced an initial TMSI is allocated. The VLR controlling the LA in which the TMSI is valid maintains a mapping between the TMSI and IMSI such that, the new VLR (if the MS moves into a new VLR area) can ask the old VLR who the TMSI (which is not valid in the new VLR) belongs to (See figure 5, 6) [6]. The use of TMSI prevents the recognition of a GSM user by the potential eavesdropper. To track a GSM user via the TMSI, an eavesdropper must intercept the GSM network communication where the TMSI was initially negotiated. In addition, because the TMSI is frequently changed, the eavesdropper must intercept each additional TMSI changing session.

The TMSI is updated at least during every location update procedure such as when the phone changes location area (LA) or after a set period of time. The TMSI can also be changed at any time by the network. The new TMSI is sent in ciphered mode whenever possible so an attacker cannot maintain a mapping between an old TMSI and a new one [6]. The TMSI is valid in the location area in which it was issued. For communications outside the location area, the Location Area Identification (LAI) [14] is necessary in addition to the TMSI

2.5 Using authentication vectors:

In the GSM communications, the AuC (Authentication Centre), which is a part of HLR (Home Location Register), as it is well known, stores the SRES, Kc and RAND for every particular subscriber. And if the subscriber is roaming, the foreign GSM database known as VLR (Visitor Location Register) would learn and source the Ki from HLR [13]. This process is very insecure because the Ki transfers directly from HLR to VLR and can be intercepted. However, the HLR distributes authentication vectors [6], including a valid SRES, Kc and RAND for the particular IMSI, which the VLR has specified. So therefore, the transmitted data are not Kis but other authentication and ciphering information, and given protection to the Ki.

2.6 SIM security:

Most SIM card systems are often protected by an optional PIN code which resembles that of an ATM PIN card system. A set of numbers is keyed on the phone's keypad by the user, and the PIN is passed to the SIM for verification. If the PIN code is incorrect, and does not match that stored by the SIM, the result will be invalid code and the system will fail to perform authentication functions [8] unless the correct PIN is entered. Furthermore, when given the chance, if a user inputs the wrong PIN code three (3) times, the system will automatically lock out and block the user from using the system again. In such instance, a PIN Unlock called PUK is required to unlock the system before any use, if the PUK is correct. And incorrectly entering the PUK code 10 times, the SIM card would be permanently blocked and refusing local access to privileged information making the SIM useless.

3. GSM loopholes and possible solutions:

The security algorithms discussed above tends to provide the global communication network with adequate security, which may seem absolute protection. However, when reality checks in, and with the increasing commonly available technologies around today, the networks have become increasingly vulnerable and more complicated to protect. As a result many are finding bigger loopholes in the GSM security system.

Recently, some of the system loopholes have gradually been resolved by specialists, in line with the improved GSM specifications. Other new technologies such as GSM 1800, HSCSD, GPRS and EDGE have been added to enhance GSM system [3]. And, the 3rd generation (3G) technologies such as UMTS [6] have also been used to improve the security in GSM. The next section will explore some of the network security issues.

3.1 The UMTS technology:

The authentication procedure in the GSM network systems does not require the network to prove its knowledge of the Ki or any other authentication context to the mobile phone. Therefore, it is possible for an attacker to setup an impersonated mobile base station with the same Mobile Network Code as the user's network. And with this, all calls or text messages sent by the subscriber could easily be intercepted. The Universal Mobile Telecommunications System (UMTS) is the world's choice for 3rd Generation wireless service delivery [15], as defined by the International Telecommunications Union (ITU). The UMTS technology makes it near impossible for an attacker to mimic or imitate

the network in terms of a 2-way authentication procedure. The procedure for which the mobile authenticates itself to the network is almost the same as GSM. But in UMTS, the network also sends an Authentication Token known as AUTN along with the RAND. The AUTN contains the MAC code, which works much like the GSM SRES but in the opposite direction. Therefore, if the MAC sent by the network does not match the MAC calculated by the SIM, the phone respond by sending an authentication reject message to the network and the connection is then terminated.

3.2 Using the A3/A8 Algorithms:

As earlier discussed, the common implementation of the A3 and A8 algorithms is concerned with a single algorithm - COMP128; which generates the 64-bit Kc and the 32-bit SRES from the 128-bit RAND and the 128-bit Ki input. This algorithm has been found to be insecure, because, as it is, the RANDs can provide enough information for an attacker to determine the Ki in significantly less than the ideal number of attempts. Earlier attacks based on repeated 2R attacks [6] could typically crack a SIM in approximately 217 RANDs. Increasingly, and even more so, some users have found it useful to 'clone' several of their SIMs [16] onto a single programmable smartcard with easily available technology.

The common implementation of A3/A8, COMP128 has another flaw, in that, when generating the 64-bit Kc, it always sets the least significant 10 bits of the Kc to 0 [3] this is almost certainly a deliberate weakening. This effectively reduces the strength of the data ciphering algorithm to 54 bits, regardless of which ciphering algorithm is used. Therefore, faced with the above insecurity, the newer implementations of A3/A8 have been introduced such as COMP128-2 and COMP128-3 [6] to help alleviate the problems. So far, these algorithms have held up reasonably well, however, they are still a mystery as they are developed in secret. COMP128-2 still has the deliberate 10-bit weakening of the ciphering Kc however. COMP128-3 is the same basic algorithm without this weakening, such as a truly 64-bit Kc. In fact, the new algorithms of COMP128-2 and COMP128-3 have managed to stop SIM cloning somehow and have also made the serious over-the-air Ki extraction difficult and unfeasible, even if they do not approach the ideal strength of 2128.

3.3 Exploring A5/3, A5/1 and A5/2 algorithms:

The A5/1 output is based on the modulo-2 which is performed using an exclusive OR known as xor operation summed output of 3 LFSRs whose clock inputs are controlled by a majority function of certain bits in each LFSR. However, the attack exploits flaws [15] in the algorithm and A5/1 could be cracked in less than 1 second on a typical PC. A5/2 is a deliberately weakened version of A5/1, which has been demonstrated to be also flawed. A5/2 can be cracked on the order of about 216, and thus is even weaker than A5/1. GSM supports up to 7 different algorithms for A5 ciphering. Until recently, only the A5/1 and A5/2 algorithms were used. In 2002, GSM added a much stronger algorithm A5/3 which is based on the Kasumi core which is the core encryption algorithm for UMTS [6]. However, only few networks and handsets support this algorithm currently.

4. Conclusion:

The security measures used in the global telecommunication systems such as encryption, authentication, ciphering and anonymity, attempt to provide the mobile phone users some privacy and anonymity, in addition to protecting the system from the fraudulent use. However, we have also seen some weaknesses in the security of the system. There can be no perfect security for any system and this paper does not attempt to provide the silver bullet answer. Although some new measures by which the security of GSM have been suggested, it is just a matter of time before hackers find ways around these measures. In fact, it could be argued that the GSM technology is the most secure, globally accepted wireless system, with public standard to date. The system could be made more secured by implementing appropriate security measures in certain areas of system management – compliance and governance. Adequate and proper management of user identities in open systems networks is crucial in providing better security and improve efficiency. Identity management (IDM) requires an integrated and often complex infrastructure where all parties involved, must be trusted for specific purposes and satisfaction gained depending on their role and function. The future may be, is in the direction of User-Centric ID management. However, in this paper, many algorithms have been implored to demonstrate the mechanisms of security in the GSM specification in order that some level of security is maintained in the cellular telecommunications system process. Also, other flaws such as exist in COMP128 and A5/1 have been examined, these vulnerabilities give access to attackers to mimic, scan and intercept contents - conversations and/or text messages for dubious purposes. Some measures have also been explored to an extent, in plugging the loopholes. Imploring new technologies such as UMTS and other improved algorithm will in future take care of the security weakness in GSM technology. Furthermore, with new developments in the GSM technologies, easily detected and recorded IME and SIM technologies, together with well managed International Standards and agreements it is very likely that, more secure methods will be developed and used in 3G and 4G mobile network environments to give it added improved security, that would also bring added benefits of improved user confidence and reduce device theft and fraud.

5. References

Arreymbi, J. (2002), Issues in Delivering Multimedia Content to Mobile devices, In Proceedings of the 6th International

Conference on Information Visualization. IEEE, Computer Society, London 2002.

Biryukov, Shamir, Wagner, Real Time Cryptanalysis of A5/1 on a PC, <http://www.cs.berkeley.edu/~daw/papers/a51-fse00.ps>

Charles Brookson, Can you clone a GSM Smart Card (SIM)? July 2002, <http://www.brookson.com/gsm/clone.pdf>

Chengyuan Peng, GSM and GPRS security, (24th Oct. 2004) <http://www.tml.hut.fi/Opinnot/Tik-110.501/2000/papers/peng.pdf>

Comparison of Airlink Encryptions, 2003,

Dimitris N. Chorafas, (1997), *High Performance Networks, Personal Communications and Mobile Computing*, 109-137, Macmillan Press Ltd.

GSM Tutorial, International Engineering Consortium, 2004, <http://www.iec.org/online/tutorials/gsm/topic02.html>

Have the A3 and A8 algorithms been broken? <http://www.gsm-security.net/faq/gsm-a3-a8-comp128-broken-security.shtml>

How is encryption utilized in GSM? 2004, <http://www.gsm-security.net/faq/gsm-encryption.shtml>

http://www.dcs.warwick.ac.uk/~esvvv/docs/specification_10-10-03.pdf

<http://www.gsm-security.net/faq/gsm-ki-kc-rand-sres.shtml>

http://www.qualcomm.com/technology/1xev-do/webpapers/wp_Airlink_Encryption.pdf

International Telecommunication Union (ITU) (2004), African Telecommunication Indicators 2004. <http://www.itu.int/ITU-D/ict/publications/africa/2004>.

James Arlin Cooper, 281-401, (1989), *Computer and Communications Security, Strategies for the 1990s*, McGraw-Hill Book Company.

Jeremy Quirke, Security in the GSM system, May 2004

Paul Montague and Rai Safavi-Naini, Eds, (2005), Security workshop 2005, Conferences in Research and Practice in Information Technology, Vol. 44, Australian Computer Society, Inc.

Priyanka Agarwal, Security of GSM System, Jan. 2005, Distribution Source: Article Warehouse.

Secure Mobile Communication, Oct. 2003,

SIM card, GSM system, Chapter 7, <http://www.mc21st.com/techfield/systech/gsm/g7-4.htm>

Srinivas, The GSM Standard (An overview of its security), Oct. 2004, <http://www.sans.org/rr/papers/index.php?id=317>

Today's GSM, 2005, <http://www.gsmworld.com/technology/gsm.shtml>

What are Ki, Kc, RAND, and SRES?

What is an IMEI? 2004, <http://www.gsm-security.net/faq/imei-international-mobile-equipment-identity-gsm.shtml>

Yong LI, Yin CHEN, Tie-Jun MA, Security in GSM, 2003, <http://www.gsm-security.net/papers/securityingsm.pdf>

Table 1. The format of IMEI [9]

AA	Country Code
BBBB	Final Assembly Code
CC	Manufacturer Code
DDDDDD	Serial Number
E	Unused

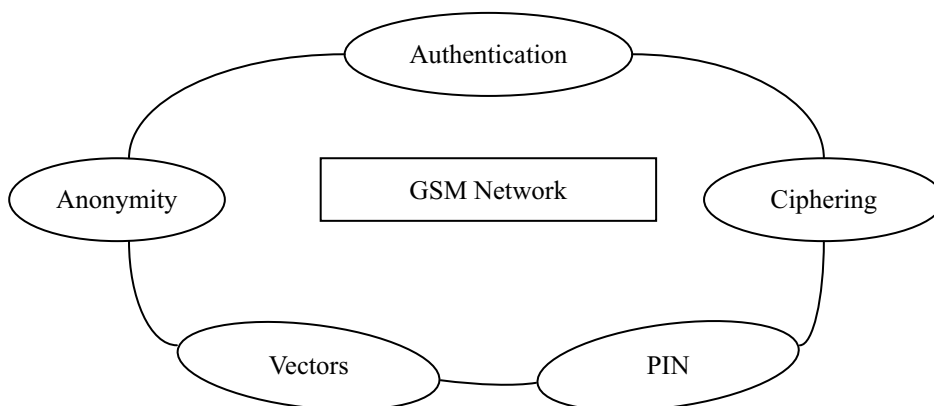


Figure 1. Proposed Model for improve GSM Security

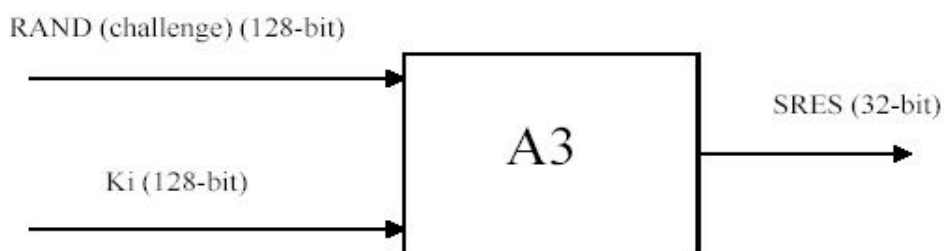


Figure 2. A3 algorithm [6]

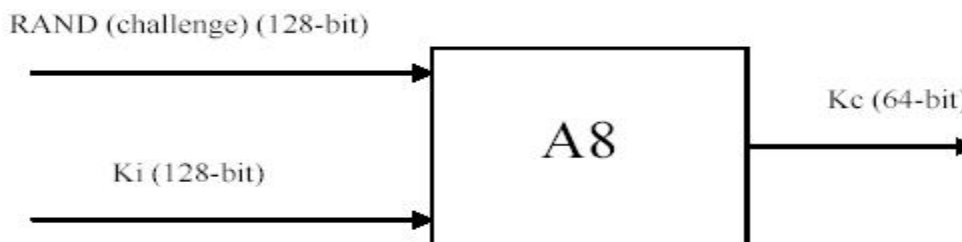


Figure 3. A8 algorithm [6]

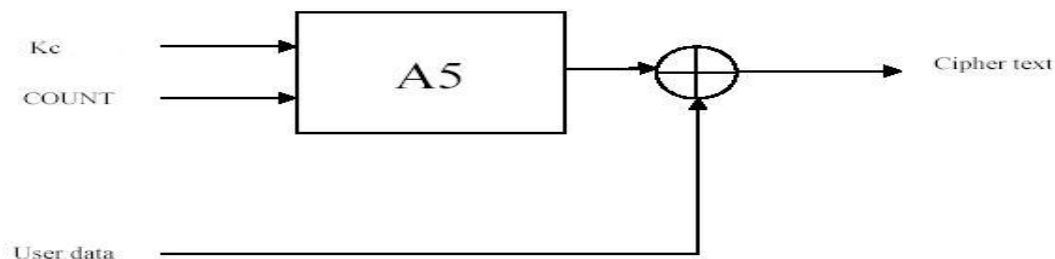


Figure 4. A5 algorithm [6]

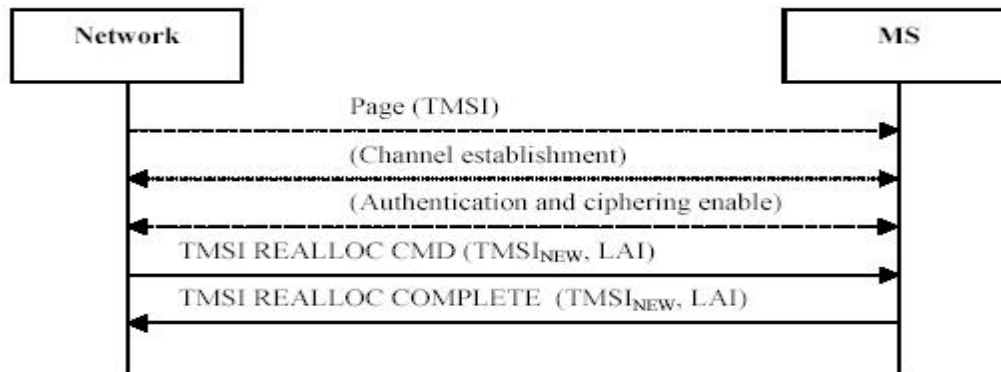


Figure 5. Allocating a new TMSI [6]

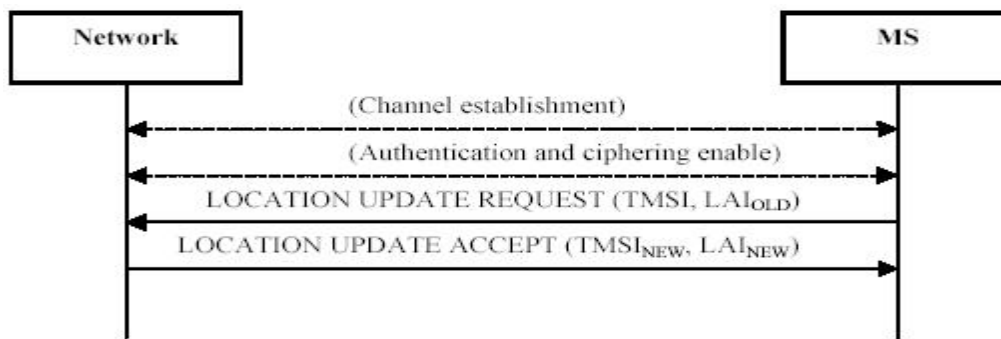


Figure 6. Allocating a new TMSI [6]



Three Dimensional Finite Element Analysis of Radial-flow Impeller Temperature Field

Liangwei Zhong

CAD center, University of Shanghai for Science and Technology

Shanghai 200093, China

Tel: 86-21-55276487 E-mail: zlvcad@126.com

Kangmin Chen

College of Power Engineering

University of Shanghai for Science and Technology

Shanghai 200093, China

Tel: 86-21-55274627 E-mail: chenkm@usst.edu.cn

Jing Ni

Business School

University of Shanghai for Science and Technology

Shanghai 200093, China

Tel: 86-21-55276487 E-mail: nijing501@126.com

Anyang He

CAD center, University of Shanghai for Science and Technology

Shanghai 200093, China

Tel: 86-21-55276487 E-mail: heay@yahoo.com

Supported by Shanghai Leading Academic Discipline Project (T0502) and Shanghai Education Committee (05EZ30)

Abstract

The technique of three dimensional solid element model and assembly was used to determine the temperature field of radial-flow impeller. The FEM software Cosmos was applied to analyze model system, and the precise analytic results were obtained. The results show that the analytic model can reflect the stead-state and transient temperature field characteristics of impeller directly, and thus can be worthy reference to analyze and calculate the temperature field of impeller in engineering design.

Keywords: Runoff blade wheel rotor, Three dimension, Assembly, Finite element, Temperature field

Turbine wheel and compressor wheel are the most important elements of a gas turbine. The analysis of a gas turbine's temperature field characteristics under the circumstances of coldness, heat, start, stop and steady working condition is vital to the study of fatigue and service life loss of a rotor. Because the geometry shape of an impeller is complicated, the two-stage analysis method and the direct computing method of an impeller are often used in engineering practice. The two-stage analysis method is relatively effective for computing an impeller with complicated geometry shape, but the computing process is complex and the work capacity is large, thus the deviation of the computing result is easily made. The advantage of the direct computing method is the effectiveness and accuracy of it is higher. However, both of these two computing methods take no consideration of the local variation of a body wheel's structure and they can not exactly reflect the distribution of the temperature field of every part, either. The structural finite element computing method takes the complexity and every kind of boundary and constraint condition of the blade wheel rotor's structure into full account, so the computing of the complicated structure's temperature field is effectively achieved and the temperature characteristics of the blade wheel rotor's every part is clearly reflected. Moreover, the assembly finite element computing method makes enough allowance for the practical situation of loading and thermal transmission and

the analytic result of the whole rotor system is obtained. In this paper, Solidworks was used in modeling and the FEM software Cosmos was applied to wholly analyze the turbo rotor of the micro gas turbine system. Because of the complicated structure and the difficulty of dividing the net element by using the rotation symmetry method, in this paper, the finite element analysis towards the whole blade wheel is made.

1. The analytic model and the computing method of the steady and transient temperature field of an blade wheel rotor

The rotor heat analytic system is used for computing the temperature distribution characteristics of a system and the other thermo physical parameters, such as heat, heat gradient, heat-flow density (heat flux) and so on.

As long as a sealed system is concerned, according to the first law of thermodynamics, that is the law of conservation of energy, we can have the following equation:

$$Q - W = \Delta U + \Delta KE + \Delta PE \quad (1)$$

In this equation,

Q —— heat

W —— work

ΔU —— internal energy of a system

ΔKE —— kinetic energy of a system

ΔPE —— potential energy of a system

As long as most of the engineering thermal transmission problems are concerned:

$$\Delta KE = \Delta PE = 0$$

Usually, the work is taken as: $W = 0$, so we can get:

$$Q = \Delta U$$

As for the steady situation, $Q = \Delta U = 0$, and this means that the heat flowing into the system and the heat flowing out of the system are the same. As for the transient thermal analysis, $q = \frac{dU}{dt}$, and this means that the heat transmission rate q is equal to the change of the internal energy of a system.

1.1 Steady thermal analysis

In engineering field, equipment is said to be in the condition of steady thermal transmission when it is operating steadily. Besides this, when the problem of thermal transmission grading from steady to transient is dealt with, the steady thermal analysis should be taken as the last step of the transient thermal analysis and the condition of the system in the steady can be determined.

When the equipment is in the steady, the total of the heat quantity generated by the system itself and the heat quantity flowing into the system is equal to the heat quantity flowing out of the system. Thus, we can get $q_{in} + q_{gen} - q_{out} = 0$. In the process of the steady, the temperature at any pitch point is invariable with time.

The equation of energy balance of the steady thermal analysis can be expressed in the form of matrix like this:

$$[K]\{T\} = \{Q\} \quad (2)$$

In this equation, [K] refers to a conduct matrix including coefficient of heat conductivity, coefficient of convective heat transfer, radiation factor, shape factor and so on. {T} refers to pitch point temperature vector. And {Q} refers to pitch point heat flow rate vector including thermogene.

[K], {T} and {Q} can be obtained through using model geometric parameter, material thermal characteristic parameter and boundary conditions.

$[K]_e\{T\}_e = \{Q\}_e$, the equation of every unit, superposed according to its sequence number can form the entity matrix as

$$[K]_{m \times n}\{T\} = \{P\}_n \quad (3)$$

1.2 Transient thermal analysis

During the process of unsteady, the temperature field is changing with time. As long as the problem of un-periodic thermal transmission is concerned, the temperature inside the objects going up or down constantly with time will go to the temperature of the environment and achieve the balance ultimately after a long time.

The basic steps of the transient thermal analysis are similar to those of the steady thermal analysis, and the main

difference between them is that the load of the transient thermal analysis is changing with time. In order to express the load changing with time, the load-time curve should be divided into load steps firstly. Every inflection point of the load-time curve is regarded as a load step, the load value and the time value of every load step should be defined to every load step, and at the same time, the load step should be clearly differentiate from gradual changing to step-changing.

In the process of the transient heat transfer, the temperature, heat flow rate, heat flow boundary conditions and the inner energy of the system is changing with time. According to the principle of conservation of energy, we can get

$$[C]\{T^{\&}\} + [K]\{T\} = \{Q\} \quad (4)$$

In this equation, [K] refers to a conduct matrix including coefficient of heat conductivity, coefficient of convective heat transfer, radiation factor, shape factor and so on. [C] refers to specific heat capacity matrix. {T} refers to pitch point temperature vector. $\{T^{\&}\}$ refers to temperature vs. time derivate. And {Q} refers to pitch point heat flow rate vector including thermogene.

During the concrete heat-transfer process, the material thermal characteristic parameter and boundary conditions might be changing with time, then the above equation can be changed as:

$$[C(T)]\{T^{\&}\} + [K(T)]\{T\} = [Q(T)] \quad (5)$$

This kind of problems can also be taken as non-linear thermal analysis which mainly includes the following instances:

- a. material characteristics is the function of temperature, such as K(T), C(T) and so on.
- b. boundary conditions are changing with time, eg. h(T).
- c. radiative heat transfer is involved.

2. Finite element load simplification and result analysis

2.1 Temperature field analysis of flat blower blade wheel composite structure

As Diagram 1 shows, rotor mainly includes turbo-expander wheel, compressor blade, axis of rotation and other parts.

Mainly because of the contact between turbo-expander wheel and compressor blade, the heat conduction exists among the parts inside the rotor. As the contact surfaces incline to each other or unhitch slightly for the air pressure, there are air gap units between the contact surfaces, by which the turbo-expander wheel and compressor blade form a holistic heat transfer system.

According to the literature, the rotor heating power boundaries can be divided into three types: the first kind of boundary condition, the third kind of boundary condition and adiabatic boundary condition.

- a. the first kind of boundary condition

The first kind of boundary condition refers that the boundary temperature value of the appointed object is already known. The pitch point temperature of the axis surface is obtained according to the gas temperature of the air bearing.

- b. the third kind of boundary condition

The third kind of boundary condition refers to the boundary condition under which the gas temperature of the rotor surfaces and the hear transfer coefficient are already known. The heat convection between high-speed gas flow or air flow and the water passage surface is the central mode of heat transfer of the rotor.

- c. adiabatic boundary condition

Other than the above tow types of boundary conditions, all the other boundary conditions are presupposed as transferring no heat with the environment.

2.2 Finite element result and analysis

The temperature field in steady is illustrated by Diagram 2. The heat quantity is transferred through turbo-expander wheel to compressor blade. The temperature of the part of the turbo-expander wheel close to the interval channel is the highest, and the temperature of compressor blade close to the interval channel is similar to the compressed air. The temperature is changing as the shape of a stairway from the turbo-expander wheel to compressor blade.

Transient temperature field in different hour of the day is illustrated as Diagram 3 and Diagram 4. The total time is calculated as 140 seconds, and the delta time is 2 seconds. Diagram 3 and 4 show the temperature field at time of 80s and 140s separately. The temperature distribution tendency is the same as that of the temperature field in steady. The highest temperature at the time of 80s is only 222.5°C, while the highest temperature after 140s is 544.3°C which is close to the temperature of fuel gas, then the temperature grades into the values of the temperature field in steady.

3. Conclusion

- 1) Because the geometry and operating condition of blade wheel rotor are complex, through the analysis by using three dimensional finite element model, the temperature distribution of it can be obtained effectively and exactly. The analyzing result is visualizable and engineering precise.
- 2) The blade graticule is divided more densely in calculation, and a blade consists at least three units. The precision of calculation can be improved.
- 3) The analytic technique of the finite element in assembly makes the model closer to the practical working condition and simplifies the loading difficulty of single element model.

References

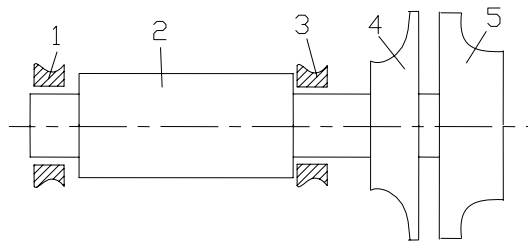
ANSYS guide of thermal analysis.

Шубенко-шубин,Л.А. *Intension of Steam Turbine*. China Machine Press,1980.

Ding Youyu, Zhou Hongli and Xu Zhu. *Intensity determination of Steam Turbine*. China Water Publish, 1985.

Tang Xinrun, Fang Qunbo,etc. *ANSYS engineering apply tutorial (heat and electromagnetism section)*. China Railway Publishing House, 2003.

Xian Jiaotong University, Zhejiang University. *Start-stop and test adjust of the large steam turbine*. Publishing house of electronics industry, 1982.



1.3 bearing 2. motor rotor
4. compressor blade 5. turbo-expander wheel
Diagram 1. Structural diagram of gas turbine

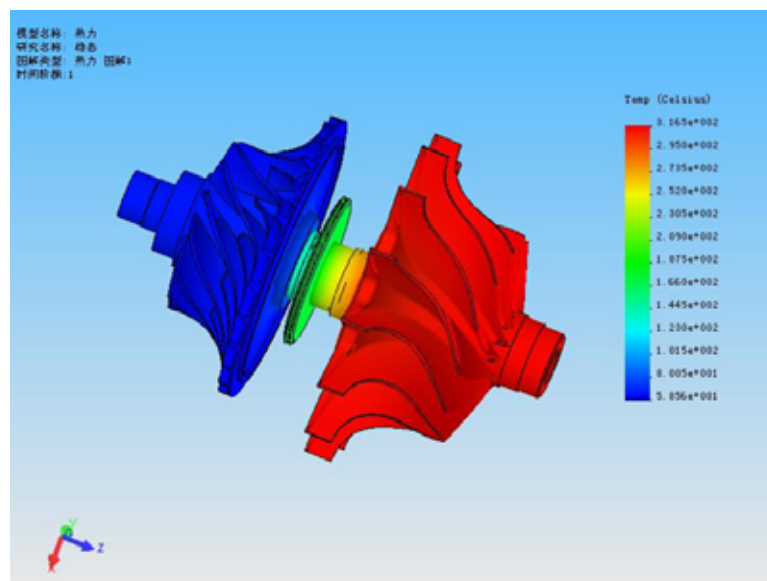


Diagram 2. the temperature field of rotor in steady

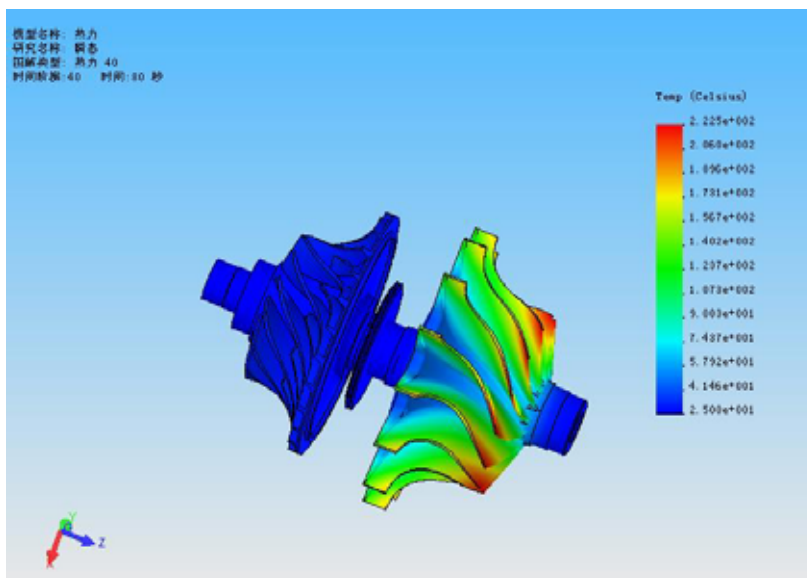


Diagram 3. the temperature field of rotor in transient (80s)

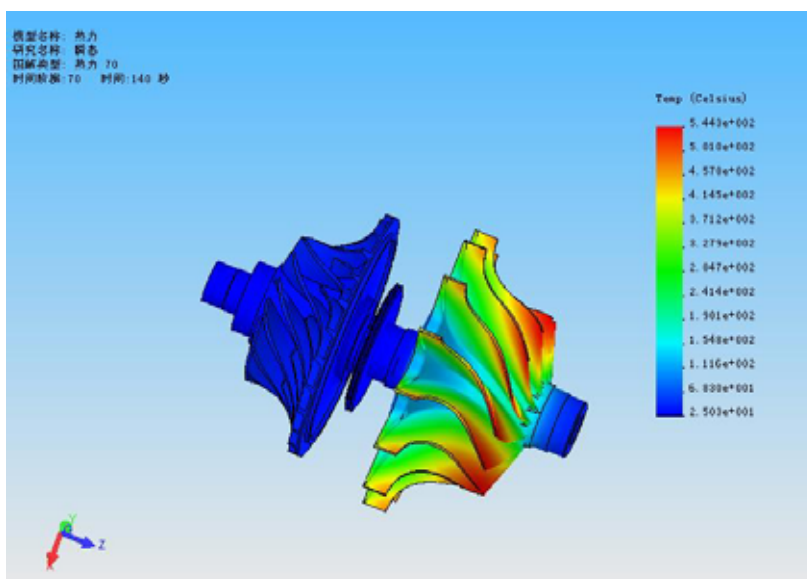


Diagram 4. the temperature field of rotor in transient (140s)



Modeling and Simulation of Three-phase ac-dc Converter-Fed dc Drive Systems with Uniform Pulse-Width Modulation Control

Chams-Eddine Feraga

Department of electrical Engineering

Guelma University

PO box 401, Guelma 24000, Algeria

E-mail: chferaga@yahoo.fr

Ali Yousfi

Department of electromechanical Engineering

Annaba University

PO box 12, Annaba 23000, Algeria

E-mail: yousfiali51@yahoo.fr

Abdallah Bouldjedri

Department of electrical Engineering

Annaba University

PO box 12, Annaba 23000, Algeria

E-mail: b_abj67@yahoo.fr

Abstract

A three-phase ac-dc GTO (gate turn off) thyristor converter-fed dc motor is studied employing uniform pulse-width modulation (UPWM) scheme, and verified by computer simulation. It is found to offer good performance. It offers only two-quadrant operation because of the unidirectional current conduction nature of GTO's. A four-quadrant converter that employs a single six-GTO bridge converter and four thyristors serving as a reversing switch is described. The four-quadrant dc drive employing the proposed converter and the control structure including speed and current control loop is also presented. Simulation results with a separately excited dc motor are given for steady-state and transient responses of the drive.

Keywords: Pulse Width Modulation, Ac-dc Converter, Dc drive, GTO

1. Introduction

Three-Phase ac-to-dc converters are severally applied to speed control of dc motors. They are ideal electronic actuators for DC drives because of their virtually unlimited output power and excellent controllability (Leonhard, 1997; Kazmierkowski and Tunia, 1994). The thyristor converters employing phase control have disadvantages of having harmonics in the source current and poor power factor, particularly at low-output voltages. When they are used for dc motor control, the armature current ripple increases losses, derates the motor, and causes discontinuous conduction, which increases speed regulation and slows down the transient response at light loads (Mohan and al; 2003). Forced-commutated converters with pulse width modulation (PWM) control have been developed and offer considerable performance improvement over phase-controlled converters. It makes the fundamental power factor unity the ripple of the load current and the zone of discontinuous conduction operation are reduced when compared to conventional converters (Sato and al; 1998;Wernekinck, 1991).

The increasing availability and power capability of controlled-on and controlled-off power switching devices, such as gate turn-off thyristors (GTO's), insulated gate bipolar transistors (IGBT's), and MOS-controlled thyristors (MCT's), are expected to reinforce self-commutated ac-dc converters with PWM control strategy to replace the conventional

phase-controlled converters within the available power ratings (Zhou and Rouaud, 1999).

The flexibility to operate with variable chopping frequency is an additional merit of self-commutated PWM converters (Hamad, 1997; Trzynadlowski, 1998).

A three-phase PWM GTO converter-fed dc motor drive offers only two-quadrant operation because of the unidirectional current conduction nature of GTO's. A dual-converter is realized by employing two converters connected in antiparallel across the load, Allows operation in all four quadrants (Leonhard, 1997).

The present paper describes a four-quadrant converter that employs a single six-GTO bridge converter and four thyristors serving as a reversing switch. This allows substantial reduction in cost because GTO's are quite expensive compared to thyristors. The reduction in cost, however, is obtained at the expense of increase in losses and lower efficiency due to two extra devices in armature circuit at all times (Mohan and al; 2003; Kenjo, 1990).

We analyse the performance characteristics of an ac-dc GTO thyristor converter, employing uniform pulse width modulated (UPWM). This control strategy is employed in the normal operation of the converter either as a rectifier or an inverter. A four-quadrant dc drive employing the proposed converter and closed-loop speed control with inner current control loop is also presented. Simulation results with a separately excited dc motor are given for steady-state and transient responses of the drive. The simulation results are shown to be in good agreement with the theory.

2. Operation principle

The power circuit configuration of a three phase ac-dc converter supplying an active load such as a dc motor is showed in Figure1. The source impedance is neglected. The power semiconductor switches, operating in chopping mode, are used to vary amplitude of the average output voltage. If thyristors were employed, they must be force commutated. On the other hand, if power transistors, MOSFET's, IGBT's, IGCT'or GTO's were employed; they are self-commutated without any need for forced commutation (Mohan and al; 2003; Khan and al; 1991). Although a GTO thyristor is employed, as seen in Figure1, UPWM control strategy is used in order to control the output voltage. The Principe of this control strategy is explained in Figure 2. The carrier wave V_{cr} is compared with a variable time independent dc control voltage V_m to generate the drive signal V_g of the switching devices. The supply source is connected to the load during the interval when V_m is greater than V_{cr} . The frequency f_p of the carrier signal depends on the number of desired output voltage pulses P in one cycle of the ac supply voltage. The switching-on and switching-off times of the switching devices for the K^{th} pulse are given by the following expressions:

$$t_{kon} = \frac{t_p}{2}(2.k - 1 - m) \quad (1)$$

$$t_{koff} = \frac{t_p}{2}(2.k - 1 + m) \quad (2)$$

The output period of the carrier wave is given by:

$$t_p = \frac{2\pi}{P} = \frac{1}{f_p} \quad (3)$$

Where:

$$P = 6, 12, 18, 24, 30, \dots$$

$$k = 1, 2, 3, \dots, P.$$

The mean output voltage of the converter is determined by the modulation index m , which for the UPWM control strategy, is varied by the control scheme in the range ($0 \leq m \leq 1$), with the index m given by:

$$m = \frac{V_{mm}}{V_{cm}} \quad (4)$$

Where V_{mm} = peak of modulated signal, V ; V_{cm} = peak of carrier signal, V .

The expressions for the corresponding modulating signal, switching-on angles α 's and switching-off angles β 's for the K^{th} pulse in a supply cycle are given by:

$$\alpha_k = \frac{\pi}{P}(2k - 1 - m) \quad (5)$$

$$\beta_k = \frac{\pi}{P}(2k - 1 + m) \quad (6)$$

2.1 Output voltage

According to Figure 2, the expression for the average output voltage V_{av} for a number P of pulses is given by (Khan and al; 1991):

$$V_{av} = \frac{3\sqrt{6}V_s}{2\pi} \sum_{i=1}^{P/3} \int_{\pi/6+\alpha_i}^{\pi/6+\beta_i} \sin(\omega t + \theta r) d(\omega t) \quad (7)$$

$$V_{av} = \frac{3\sqrt{6}V_s}{\pi} \sum_{i=1}^{P/3} \left[\cos(\alpha_i + \frac{\pi}{3}) - \cos(\beta_i + \frac{\pi}{3}) \right] \quad (8)$$

Where V_{av} = mean dc voltage, V ; V_s = RMS amplitude of the line voltage, V ; θ_r = phase angle corresponding to i th pulse, rad; ω = supply frequency, rad/s.

2.2 Output current

The expression for the armature current during the i^{th} voltage pulse is given by:

$$i_a = I_p \sin(\omega t - \phi + \frac{\pi}{3}) - I_E + \left[I_{\alpha i} + \frac{E_a}{R_a} - I_p \sin(\alpha_i - \phi + \frac{\pi}{3}) \right] e^{\frac{R_a}{L_a \omega}(\alpha_i - \omega t)} \quad (9)$$

$$\alpha_i \leq \omega t \leq \beta_i$$

$$i_a = -\frac{E_a}{R_a} + [I_p \sin(\beta_i - \phi + \frac{\pi}{3}) + (I_{\alpha i} + \frac{E_a}{R_a} - I_p \sin(\alpha_i - \phi + \frac{\pi}{3})) e^{\frac{R_a}{L_a \omega}(\alpha_i - \beta_i)}] e^{\frac{R_a}{L_a \omega}(\beta_i - \omega t)} \quad (10)$$

$$\beta_i \leq \omega t \leq \alpha_{i+1}$$

Where E_a = motor back emf, V ; i_a = instantaneous armature current, A ; L_a = armature circuit inductance, H ; R_a = armature circuit resistance, Ω ; Z = armature impedance at supply frequency = $[R^2 + (L\omega)^2]^{1/2}$, Ω ; ϕ = load phase angle, rad; $I_{\alpha i}$ = armature current at α_i , A ; $I_{\beta i}$ = armature current at β_i , A ; I_p = peak current = $\sqrt{2}V_s/Z$, A ; I_E = current component = E_a/R_a , A .

3. Four-quadrant converter

The converter power circuit with a dc motor load is shown in Figure 3. The GTO converter employs a six-GTO bridge converter. This two-quadrant GTO converter is operated with uniform PWM to produce 12 output voltage pulses during a cycle of the ac source voltage. The principle of armature reversal is shown in Figure 3 with the help of static reversing switch that consists of four reversing thyristors.

Thyristor pair (T_1, T'_1) continuously conduct for positive direction of motor current while the others are blocked. When zero current is reached, the opposite pair of thyristors (T_2, T'_2) can be fired in order to reverse the polarity of the armature current.

4. Control structure of the drive

The schematic block diagram of speed control scheme is given in Figure 4. The schematic diagram of the closed loop speed control scheme is shown in Figure 5. It employs an inner-current control loop within the speed loop. The speed controller output, which forms the current reference for the current controller, is clamped to provide a current-limiting feature.

4.1 Dc motor

The equivalent circuit of the separately excited dc motor coupled to a separately excited dc generator for the purpose of loading can be represented in a schematic form as shown in Figure 6. Assuming constant field excitation, the equations are expressed as:

$$V_a = R_a i_a + L_a \frac{di_a}{dt} + E_a \quad (11)$$

$$m_M = J \frac{d\omega_m}{dt} + m_L \quad (12)$$

$$E_a = K_m \cdot \omega_m \quad (13)$$

$$m_M = K_m \cdot i_a \tag{14}$$

With m_M = Motor torque, Nm; m_L = load torque, Nm; N_m = mechanical speed, RPM; ω_m = mechanical angular velocity = $2\pi N_m/60$, rad/s; K_m = back emf constant, V/rad/s; J = moment of inertia.

Taking Laplace transform of (11) – (14) and rearranging the terms of the equations, we obtain

$$I_a = \frac{V_a(s) - K_m \cdot \omega_m(s)}{R_a(1 + T_a \cdot S)} \tag{15}$$

$$\omega_m = \frac{K_m I_a(s) - m_L(s)}{J \cdot S} \tag{16}$$

$$\omega_m = \frac{m_M(s) - m_L(s)}{J \cdot S} \tag{17}$$

where S is the Laplace operator.

The dynamic system, described by equations (15), (16), (17), is represented by a block diagram in Figure 7. As a constant field dc generator connected to a fixed resistance forms the load on the motor shaft, the load torque varies linearly with the speed. The equation is:

$$m_L = B \cdot \omega_m \tag{18}$$

4.2 Converter

The secondary voltage of the power transformer is chosen in such a way that for the control voltage $V_c = 0.9 V_{cmax}$, the converter voltage is equal to the rated voltage of the dc motor.

The control voltage varies from - 5 to + 5V. Gain K_t of the converter (including the firing circuit) is given as the ratio of the maximum value of desired output voltage to the change in control voltage V_c required to vary the output voltage from 0 to V_{cmax} . The time delay of the converter is approximated by first-order time constant T_t which is equal to half the interval between two consecutive voltage pulses (Leonhard, 1997, Khan and al; 1991).

Thus,

$$T_t = \frac{1}{2} \cdot \frac{20}{6} ms \quad \text{for } P = 6$$

And

$$T_t = \frac{1}{2} \cdot \frac{20}{12} ms \quad \text{for } P = 12$$

The transfer function of the converter can be written as:

$$\frac{V_a(s)}{V_c(s)} = \frac{K_t}{1 + T_t \cdot S} \tag{19}$$

4.3 Current transducer

A signal proportional to the armature current is obtained by using a small resistance in series with the armature circuit. The feedback signal derived from the current transducer is applied to an RC filter with a time constant T_2 in order to reduce the ripple in the current signal. Thus, the transfer function of the current transducer with the filter is written as:

$$\frac{I_m(s)}{I_a(s)} = \frac{K_2}{1 + T_2 \cdot S} \tag{20}$$

4.4 Speed transducer

A tacho-generator is used to get the speed signal. Since a 5V dc signal corresponds to the rated speed (1500 r/min). An RC filter with a time constant T_1 is used to smooth out the spikes in the speed signal. The transfer function of the speed transducer with the filter is given as:

$$\frac{V_m(s)}{\omega_m(s)} = \frac{K_1}{1 + T_1 \cdot S} \tag{21}$$

5. Simulated Results and Discussions

The parameters of the used machine model are given in Table 1. The source voltage; the motor armature voltage and current waveforms for motoring and regenerating (for rectification and inversion) operation, are shown in Figure 8 and Figure 9 respectively. The waveforms of the developed torque and the motor speed for a different number of pulses P ($P=6$ and $P=12$) are shown in Figure 10, where the load is applied at $t=1s$. The ripples in the developed torque were

observed.

There is an improvement in performance with an increase in the pulse number. Four-quadrant drive ability is demonstrated in Figure 11 and Figure 12. The former shows the speed response for a speed reversal command from $+1500$ to -1500 rpm. As the speed reversal is initiated, the armature current quickly reverses through the static reversing switch. The motor decelerates to standstill as the converter operates as an inverter feeding power back the ac supply. The motor is then accelerating fast in the reverse direction and the speed settles down to the desired value.

Figure 12 shows the speed response for control voltage varying from -5 to $+5$ v, with a load torque $m_L = \text{constant}$. The armature current reverses through the reversing switch the motor is decelerated quickly. When desired speed is reached, the current is again set back in previous direction (corresponding to the operation in a four quadrant drive).

6. Conclusion

The study of pulse width modulation scheme for an ac-dc PWM converter shows that the uniform pulse width modulation scheme offers good performance. Simulation results show that the control strategy can be applied to both rectifying and regenerating modes of operation. A four-quadrant dc drive employing the proposed converter and closed-loop speed control with inner current control loop has been described and verified by computer simulation. The simulation results are shown to be in good agreement with the theoretical calculations.

References

- Hamed, S.A., (1997). Performance Evaluation of Three-Phase Variable –Speed DC Drive Systems with Uniform PWM Control. *IEEE, Trans. on Power Electronics*,12: 228-242.
- Kazmierkowski M. P., & H. Tunia, (1994). *Automatic Control of Converter-Fed Drives*. Elsevier Amsterdam.
- Kenjo, T., (1990). *Electric Motors and Their Controls: An Introduction*. Oxford Science Oxford UK.
- Khan, B.H., Doradla, & G. K. Dubey, (1991). A Three Phase AC-DC GTO Converter Employing Equal Pulse Width Modulation (EPWM). *IEEE Trans. on Industry Applications*, 27: 370–379.
- Khan, B.H., S. R. Doradla, & G. K. Dubey, (1991). A New Simultaneous Gating GTO Dual Converter- fed DC Motor Drive without Circulating Current. *IEEE Trans. on Industry Applications*, 27: 560-566.
- Leonhard, W., (1997). *Control of Electrical Drives*. Springer Verlag Berlin Heidelberg.
- Mohan, N., T.M. Undeland, & W.P. Robbins, (2003). *Power Electronics: Converters Applications and Design*. Wiley & sons NewYork.
- Sato, Y., T.Ishizuka, K. Nezu & T. Kataoka, (1998). A New Control Strategy for Voltage- Type PWM Rectifiers to Realize Zero Steady-State Control Error in Input Current. *IEEE Trans. on Power Electronics*, 34: 480 -486.
- Trzynadlowski, A. M.,(1998). *Introduction to Modern Power Electronics*. John Wiley New York.
- Wernekinck, E., A.Kawamura, & R.Hoft, (1991). A High Frequency AC/DC Converter with Unity Power Factor and Minimum Harmonic Distortion. *IEEE Trans. on Power Electronics*, 6: 364-371.
- Zhou, D., & D. Rouaud, (1999). Regulation and design issues of a PWM three-phase rectifier. *The 25th Annual Conference of the IEEE IECON '99*, San Jose, California, USA, November 29 – December 03, 1: 485-489.

Table 1. Separately excited DC machine data

Components	Rating values
Power	$P = 3hp$
Voltage	$V = 220V$
Current	$I = 11.6A$
Speed	$N_m = 1500r/min$
Armature resistance	$R_a = 3.1\Omega$
Electrical time constant of the armature circuit	$T_a = 7.74 ms$
Moment of inertia	$J = 0.025kg.m^2$
Coefficient of viscous friction	$B = 0.089Nm/rad/s$
Mechanical time constant	$T_m = 4.1 ms$

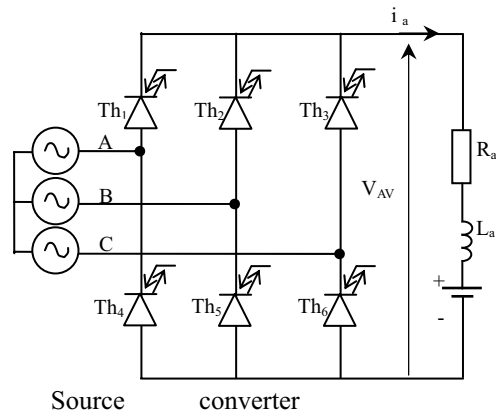


Figure 1. Three-phase ac-dc converter

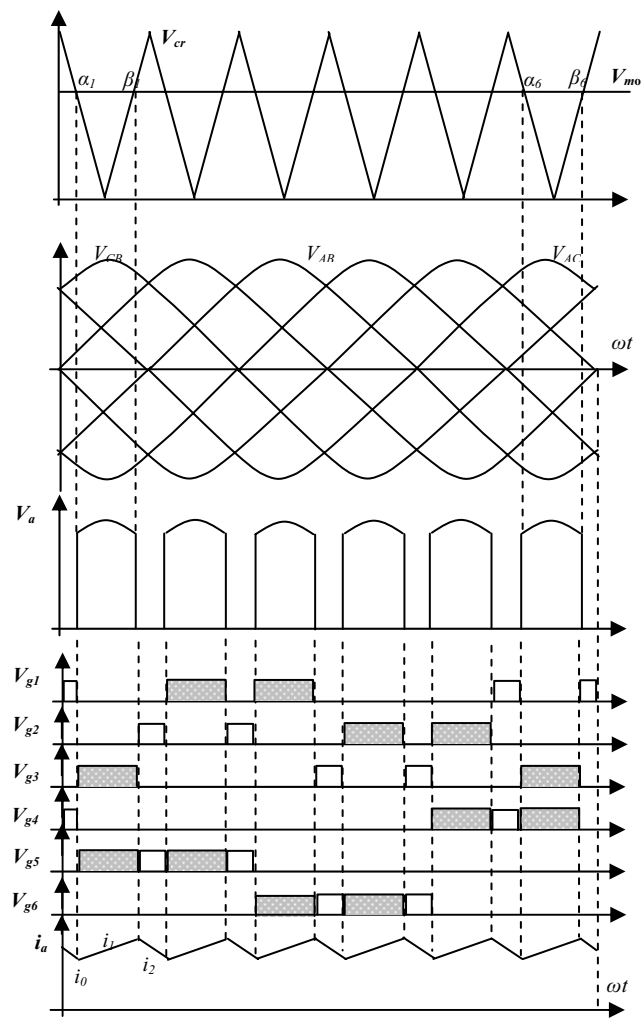


Figure 2. Principle of UPWM control strategy

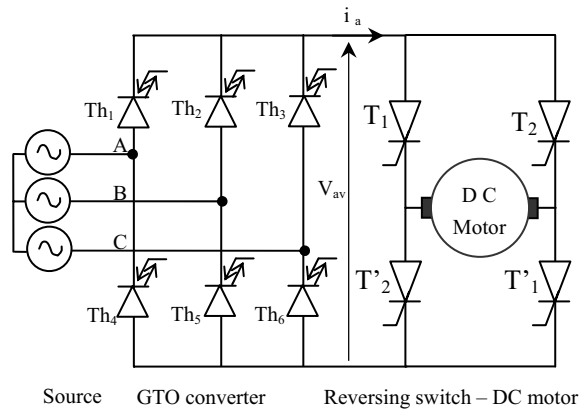


Figure 3. Four-quadrant operation of a DC drive

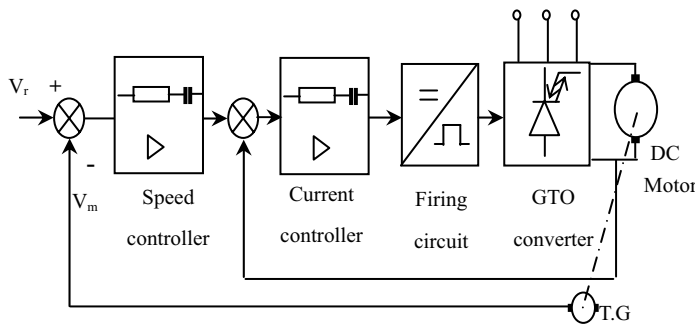


Figure 4. General schematic of closed-loop speed control

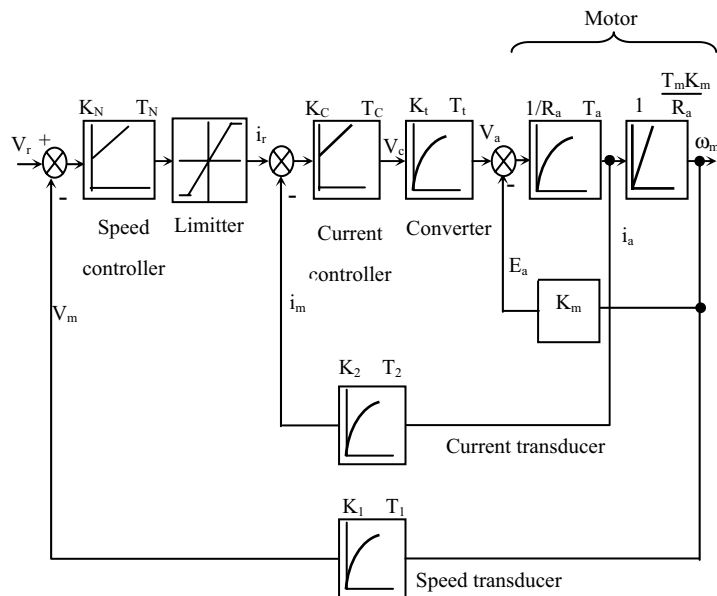


Figure 5. Control structure of a drive including speed and current control loop

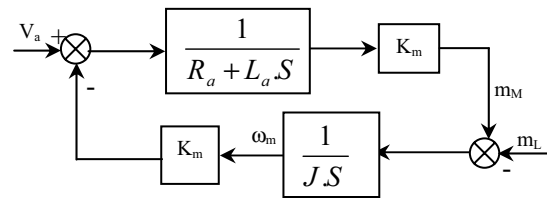
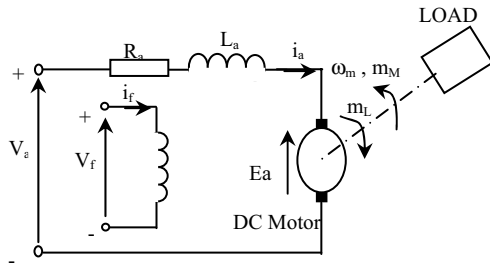


Figure 6. Equivalent circuit of dc motor+load system. Figure 7. Block diagram of motor+load system

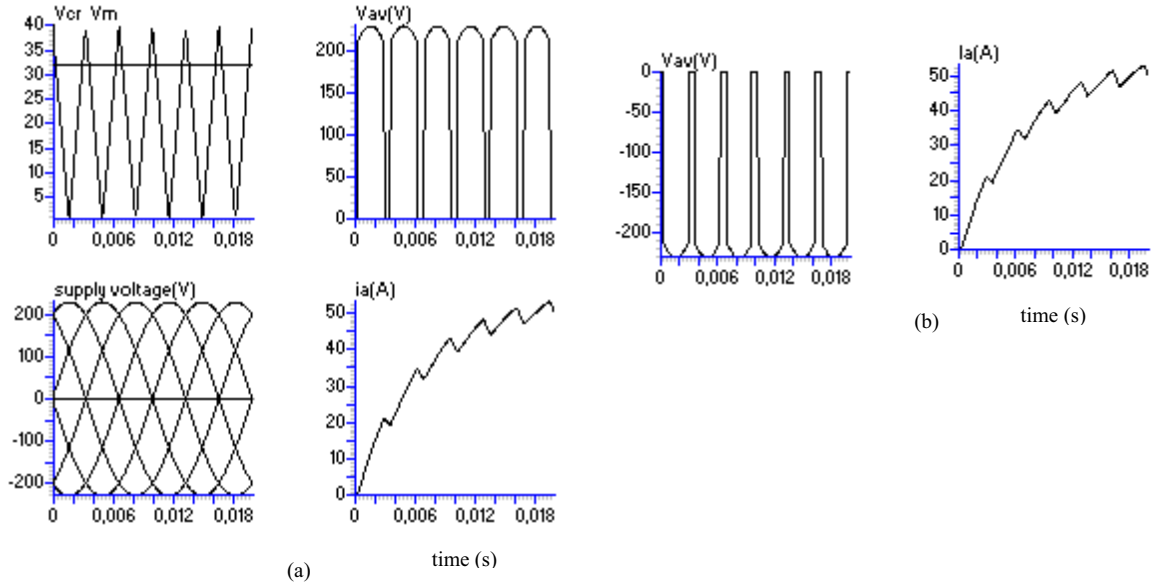


Figure 8. Simulated waveforms of output voltage and load current through UPWM GTO converter

- (a) for motoring operation ($P=6, m=0.8$)
- (b) for regenerating operation ($P=6, m=0.8$)

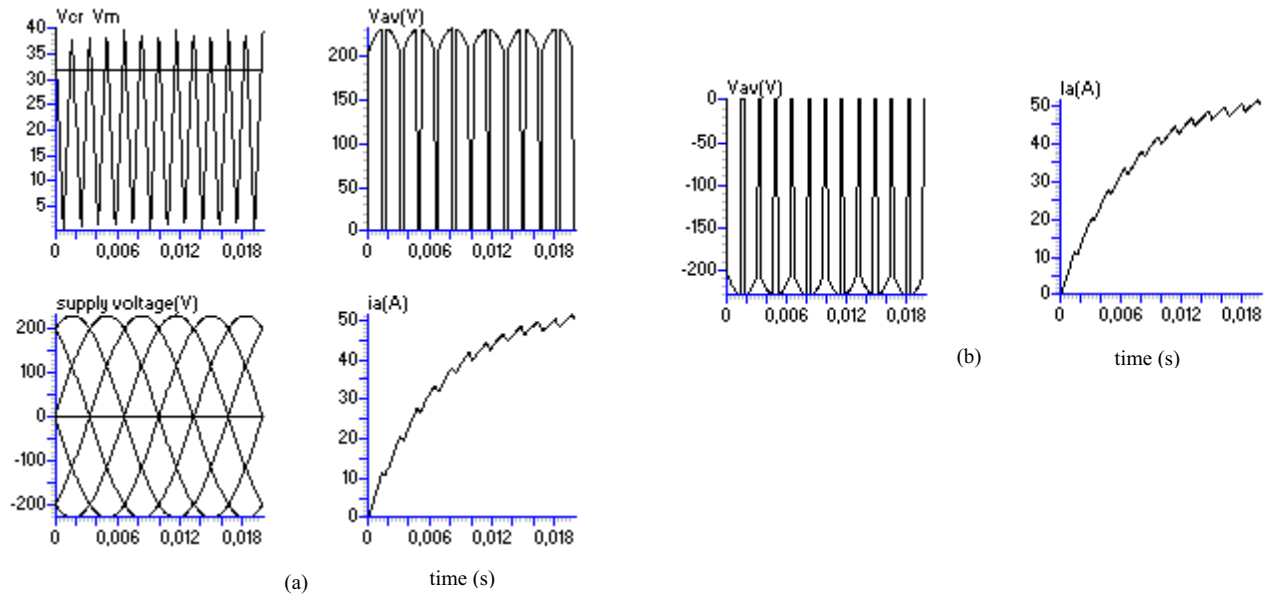


Figure 9. Simulated waveforms of output voltage and load current through UPWM GTO converter

- (a) for motoring operation ($P=12, m=0.8$)
- (b) for regenerating operation ($P=12, m=0.8$)

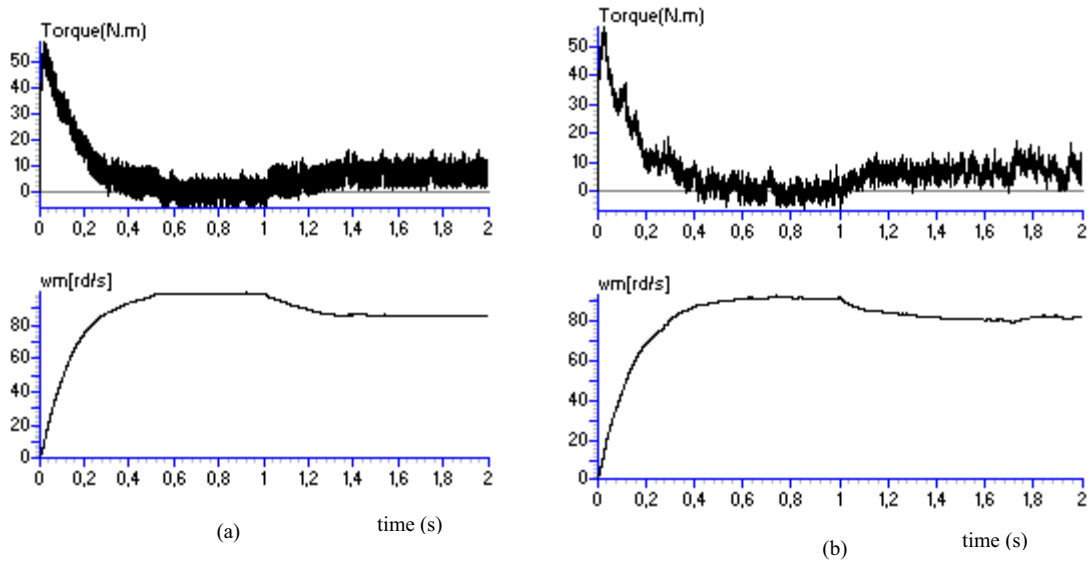


Figure 10. Response of torque and speed of UPWM ac-dc converter-fed dc motor

- (a) when $(P=6, m=0.6)$
- (b) when $(P=12, m=0.6)$

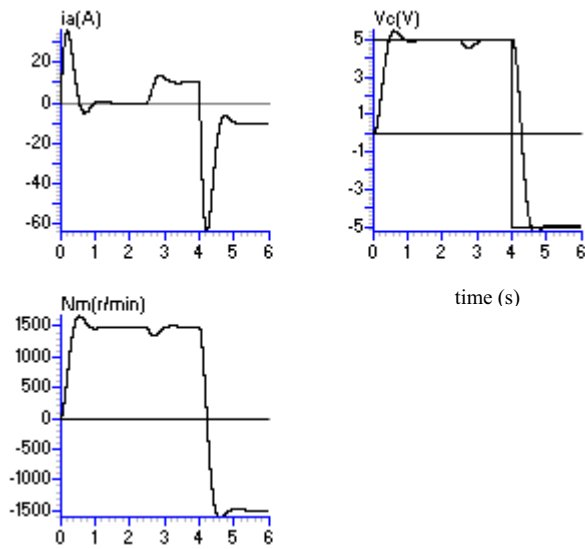


Figure 11. Speed and torque responses for reversal of speed command
From 1500 to -1500 r/min of closed loop scheme When $m_L = B \cdot \omega$

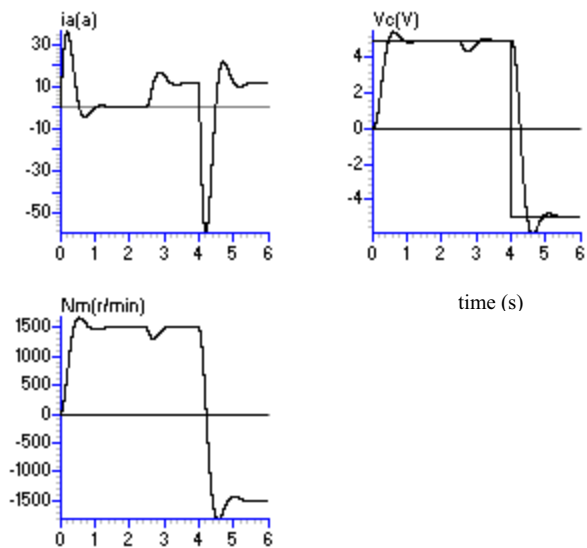


Figure 12. Speed and torque responses for reversal of speed command From 1500 to -1500 r/min of closed loop scheme When $m_L = \text{constant}$



Characterizations and Applications of Semistrictly Prequasi-invex Functions

Zaiyun Peng

Institute of Mathematics, College of Science

Chongqing JiaoTong University

66 Xue Fu Da Dao Street, Nan Ping, Chongqing 400074, China

E-mail: pengzaiyun@126.com.

Dacheng Wang, Yawei Liu, Zhi Lin

Institute of Mathematics, College of Science, Chongqing JiaoTong University

66 Xue Fu Da Dao Street, Nan Ping, Chongqing 400074, China

Abstract

A new type of generalized convex functions, termed semistrictly prequasi-invex functions, is further discussed in this paper. A sufficient condition and an important application of semistrictly prequasi-invex functions are obtained.

Keywords: Prequasi-invex functions, Semistrictly prequasi-invex functions, Applications

MSC(2000): 90C26,26B25 **CLC number:** O174.13

1. Introduction

Convexity and generalized convexity play a central role in mathematical economics and optimization theories. Therefore, the research on convexity or generalized convexity becomes one of the most important aspects in mathematical programming. A significant generalization of convex functions termed preinvex functions was introduced by (Weir,1998, p.29). Yang and Li obtained some properties of preinvex function in (Yang,2001, p.256). Yang also discussed the relationships among convexity, semistrictly convexity and strictly convexity in (Yang,1994, p.15). Recently, in (Yang,2001, p.645). Yang established characterizations of prequasi-invex functions and semistrictly prequasi-invex functions. In this paper, the relationship of prequasi-invex and semistrictly prequasi-invex function are further discussed, we obtain a new result that if a prequasi-invex function satisfies intermediate-point weakly semistrict prequasi-invexity then it is also a semistrictly prequasi-invex function. Then an important application of semistrictly prequasi-invex functions is obtained.

We give first the following definitions .

Definition 1.1 (Weir,1998, p.29) A set $K \subseteq R^n$ is said to be invex if there exist a vector function $\eta : R^n \times R^n \rightarrow R^n$, such that

$$\forall x, y \in K, \forall \lambda \in [0,1] \Rightarrow y + \lambda\eta(x, y) \in K .$$

Definition 1.2 (Yang,2001, p.645). Let $K \subseteq R^n$ be an invex set with respect to $\eta : R^n \times R^n \rightarrow R^n$. Let $f : K \rightarrow R$. We say that f is prequasi-invex on K , if $\forall x, y \in K, \lambda \in [0,1]$,

$$f(y + \lambda\eta(x, y)) \leq \max \{f(x), f(y)\} .$$

Definition 1.3 (Yang,2001, p.645). Let $K \subseteq R^n$ be an invex set with respect to $\eta : R^n \times R^n \rightarrow R^n$. Let $f : K \rightarrow R$. We say that f is semistrictly prequasi-invex on K , if $\forall \lambda \in (0,1) \forall x, y \in K, f(x) \neq f(y)$,

$$f(y + \lambda\eta(x, y)) < \max \{f(x), f(y)\} .$$

Condition C. Let $\eta : R^n \times R^n \rightarrow R^n$. We say that the function η satisfies Condition C if, for any $x, y \in K$, for any $\lambda \in [0,1]$,

$$\eta(y, y + \lambda\eta(x, y)) = -\lambda\eta(x, y),$$

$$\eta(x, y + \lambda\eta(x, y)) = (1 - \lambda)\eta(x, y).$$

Example 1.1: Let

$$\eta(x, y) = \begin{cases} x - y, (x \geq 0, y \geq 0) \\ x - y, (x < 0, y < 0) \\ -2 - y, (x > 0, y \leq 0) \\ 2 - y, (x \leq 0, y > 0) \end{cases}$$

By Example 2.2 in (Yang,2003, p.607),we know that η satisfies the Condition C. Another example that η satisfies the Condition C may refer Example 2.4 in (Yang,1995, p.901).

2. Main Results

In (Yang,2001, p.256), the authors have discussed the preinvex functions and semistrictly preinvex functions. In this section, we will discuss the properties of semistrictly prequasi-invex functions. At first, we will get a new result as follows.

Theorem 2.1 Let $K \subseteq R^n$ be an invex set with respect to $\eta: R^n \times R^n \rightarrow R^n$ which satisfies Condition C. Let $f: K \rightarrow R$, be a prequasi-invex function for the same η , and if for each pair of $x, y \in K, f(x) \neq f(y)$ there exists an $\alpha \in (0,1)$, such that

$$f(y + \alpha\eta(x, y)) < \max \{f(x), f(y)\} \tag{1}$$

Then f is semistrictly prequasi-invex on K with respect to η .

Proof. By contradiction, we assume that f is not semistrictly prequasi-invex on K . Then there exist $x, y \in K, f(x) \neq f(y), \lambda \in (0,1)$ such that

$$f(y + \lambda\eta(x, y)) \geq \max \{f(x), f(y)\}. \tag{2}$$

Let $z = y + \lambda\eta(x, y)$. Since f is prequasi-invex, we have

$$f(z) = f(y + \lambda\eta(x, y)) \leq \max \{f(x), f(y)\} \tag{3}$$

The above two inequalities imply that

$$f(z) = \max \{f(x), f(y)\} \tag{4}$$

We note that the pair $x, z \in K$ and $y, z \in K$, such that $f(x) \neq f(z), f(z) \neq f(y)$. From inequality (1), there exists an $\beta_1, \beta_2 \in (0,1)$, such that

$$f(z + \beta_1\eta(x, z)) < \max \{f(x), f(z)\} \tag{5}$$

$$f(y + \beta_2\eta(z, y)) < \max \{f(z), f(y)\} \tag{6}$$

Denote

$$\bar{x} = z + \beta_1\eta(x, z), \quad \bar{y} = y + \beta_2\eta(z, y)$$

Then, from(4)-(6), we have

$$f(z) > f(\bar{x}), \quad f(z) > f(\bar{y}) \tag{7}$$

And from condition C,

$$\begin{aligned} \bar{x} &= z + \beta_1\eta(x, z) = y + \lambda\eta(x, y) + \beta_1\eta(x, y + \lambda\eta(x, y)) \\ &= y + [\lambda + \beta_1(1 - \lambda)]\eta(x, y) \end{aligned}$$

$$\begin{aligned} \bar{y} &= y + \beta_2\eta(z, y) = y + \beta_2\eta(y + \lambda\eta(x, y), y) \\ &= y + \beta_2\eta(y + \lambda\eta(x, y), y + \lambda\eta(x, y) - \lambda\eta(x, y)) \\ &= y + \beta_2\eta(y + \lambda\eta(x, y), y + \lambda\eta(x, y) + \eta(y, y + \lambda\eta(x, y))) \\ &= y + \beta_2\lambda\eta(x, y) \end{aligned}$$

Let $u_1 = \lambda + \beta_1(1 - \lambda)$, $u_2 = \beta_2\lambda$, $u = (\lambda - u_2)/(u_1 - u_2)$.

It is easy to verify that $u_1, u_2, u \in (0, 1)$. Again from Condition C,

$$\begin{aligned} \bar{y} + u\eta(\bar{x}, \bar{y}) &= y + u_2\eta(x, y) + u\eta(y + u_1\eta(x, y), y + u_2\eta(x, y)) \\ &= y + u_2\eta(x, y) + u\eta(y + u_1\eta(x, y), y + u_1\eta(x, y) + (u_2 - u_1)\eta(x, y)) \\ &= y + u_2\eta(x, y) - u[(u_2 - u_1)/(1 - u_1)]\eta(x, y + u_1\eta(x, y)) \\ &= y + [u_2 - u(u_2 - u_1)]\eta(x, y) = y + \lambda\eta(x, y) = z \end{aligned}$$

Since f is prequasi-convex function on K , this implies

$$f(z) \leq \max\{f(\bar{x}), f(\bar{y})\}$$

Which contradicts (7). This completes the proof.

Remark1. From the Theorem 2.1, we obtain a sufficient condition of semistrictly prequasi-convex functions, and we also see that a uniform $\alpha \in (0, 1)$ is not necessary for inequality (1) in Theorem 2.1.

Let the problem of minimum $f(x)$ subject to $x \in K$ be denoted by (P). Now, we can discuss an application of semistrictly prequasi-convex functions to the problem (P).

Theorem 2.2 Let $K \subseteq R^n$ be a nonempty invex set with respect to $\eta: R^n \times R^n \rightarrow R^n$ and $f: K \rightarrow R$ be a semistrictly prequasi-convex function with respect to η . If \bar{x} is a local minimum to the problem (P), then \bar{x} is a global one.

Proof. If \bar{x} is a local minimum to the problem (P), then there exists a neighborhood $U \in R^n$ with $\bar{x} \in U$ and

$$f(\bar{x}) \leq f(x), \forall x \in K \cap U \quad (8)$$

Assume that \bar{x} is not a global one of (P), then there exists $\hat{x} \in K$ with

$$f(\hat{x}) < f(\bar{x}) \quad (9)$$

Since $K \subseteq R^n$ be a nonempty invex set with respect to $\eta: R^n \times R^n \rightarrow R^n$ and $f: K \rightarrow R$ be a semistrictly prequasi-convex function, then $\forall \lambda \in (0, 1)$

$$f(\bar{x} + \lambda\eta(\hat{x}, \bar{x})) < \max\{f(\hat{x}), f(\bar{x})\} = f(\bar{x}) \quad (10)$$

i.e., for any $\forall \lambda \in (0, 1)$, we have

$$f(\bar{x} + \lambda\eta(\hat{x}, \bar{x})) < f(\bar{x})$$

$\lim_{\lambda \rightarrow 0} (\bar{x} + \lambda\eta(\hat{x}, \bar{x})) = \bar{x}$, so there exists a δ and $0 < \delta < 1$ and for all $\lambda \in (0, \delta)$ with $\bar{x} + \lambda\eta(\hat{x}, \bar{x}) \in K \cap U$. Then (10) is contrary to (8). This completes the proof.

Remark 2. From Theorem 2.2, we can conclude that the class of semistrictly prequasi-convex functions constitutes an important class of generalized convex functions in mathematical programming.

3. Acknowledgment

This study is supported by Supported by Natural Science Foundation Project of CQ CSTC(2008BB0346) and Youth Science Project Research Foundation of Chongqing Jiao Tong University.

The authors also would like to thank two anonymous referees for their valuable comments and suggestions, which helped to improve the paper.

References

- Weir, T and Mond, B. Preinvex Functions in Multiple Objective Optimization. *J Math Anal Appl.* 1988, 136:29-38.
 Yang, X, M and Li, D. On Properties of Preinvex Functions. *J Math Anal Appl* 2001, 256:229-241.
 Yang, X, M. Semistrictly convex Functions. *Opsearch*, 1994, 31(1):15-27.
 Yang, X, M and Li, D. Semistrictly Preinvex Functions. *J Math Anal Appl* 2001, 258:287-308.

- Mohan, S, R and Neogy, S, K. On Invex sets and Preinvex Functions. *J Math Anal Appl*,1995,189:901-908.
- Yang, X, M, Yang, X, Q and Teo, K, L. Characterization and Applications of prequasi-invex functions, *Journal of optimization theory and Applications* 2001,110(3): 645-668.
- Yang, X, M, Yang, X, Q and Teo, K, L. Generalized invexity and invariant monotonicity. *J Optim Theory Appl.* 2003,117:607-625.
- Luo, H. L. and Peng, Z. Y. General Convergence analysis for generalized n-step projection methods and applications to a kind of Variational Inequality problems, *J. of Southwest University(Natural Science)*,2007 (32)1-4.
- Peng, Z. Y. and Luo, H. L. The Three-step Projection Method in Generalized Analysis and Its Application to Variational Inequality Problems. *Journal of Sichuan Normal University(Natural Science edition)*,2007.p681-683.
- Peng, Z. Y. and Chen, Guo. Remarks on Prequasi-invex Functions. *Journal of China Three Gorges University (Natural Science edition)*,2007.p70-72.
- Peng, Z. Y. and Long, X.J. A Class of Random F-complementarity Problems in Hilbert Spaces, *Advanced in Nonlinear Variational Inequalities*,11(2008)51--59.
- Peng, Z. Y. and Luo, H. L. Technical Note on Characterizations of Strongly Preinvex Functions. *Journal of Chongqing Normal University(Natural Science edition)*,23(2006)36--39.(in chinese).



Reactions of $trans$ -[Pt($^{15}\text{NH}_3$) $_2$ (H $_2$ O) $_2$] $^{2+}$ with Glutathione

Sutopo Hadi (Corresponding author)

Department of Chemistry

University of Lampung

Bandar Lampung 35145 Indonesia

Tel: 62-813-6905-9733 E-mail address: sutopohadi@unila.ac.id

Trevor G. Appleton

Centre for Metals in Biology

Department of Chemistry

University of Queensland

Brisbane QLD 4072, Australia

Abstract

A study of the reaction between $trans$ -[Pt($^{15}\text{NH}_3$) $_2$ (H $_2$ O) $_2$](NO $_3$) $_2$ and glutathione (GSH) was undertaken to confirm the identity of the products formed. In alkaline solution, the platinum products observed were mononuclear species, while in acidic solution, the oligomeric products were products obtained. The mass spectrometry of the reaction in alkaline solution showed a sulfur-bridged dinuclear platinum(II) species, $trans$ -[Pt(SG) $_2$ ($^{15}\text{NH}_3$) $_2$] $^{2+}$ giving m/z 1380 and the loss of two amines was observed.

Keywords: Thiolate, Oligomers, 2D NMR, Glutathione

1. Introduction

The chemistry of cisplatin interacting with thiol groups has been extensively studied (Appleton et al., 1989; Dedon and Borch, 1987; Odenheimer and Wolf, 1982; El-Khateeb et al., 1999; Appleton et al., 2003; Hadi and Appleton, 2006) the corresponding reactions of the trans analogue on the other hand are relatively unexplored due to the lack of antitumour activity of $trans$ -diammineplatinum(II) complexes (Berners-Price and Kuchel, 1990; Van Beusichem and Farrell, 1990; Hadi and Appleton, 2005, Oehlsen et al., 2003). The reaction of platinum(II) complexes with sulfur-containing ligands is of interest as it is believed that before the platinum(II) complexes reaching the DNA, they will bind first to the constituents of cells containing sulfur donor (Borch, and Pleasants, 1979; Borch et al., 1980; Bodener et al., 1986a,b; El-Khateeb et al., 1999; Gale et al., 1982; Hadi and Appleton, 2006; Johnson et al., 1985).

Lempers *et al.* (1988) and Lempers and Reedijk (1990) have shown that in the reaction of [PtCl(dien)] $^{+}$ with glutathione, a sulfur donor, the products obtained depended on the pH. At pH < 7, the favoured coordinating mode of the thiol group was to bridge two platinum centers, whereas at pH > 7 mononuclear species were preferred. At pH < 7, the thiol group is still protonated, so it is not readily available for coordination. A thiol already coordinated to the metal is still a good nucleophile, and therefore at lower pH a second metal will preferentially bind with this coordinated thiol, forming a bridged species. At high pH a greater percentage of the free thiol is deprotonated and the preferred binding mode is non-bridging.

It has been shown that when cis -[Pt($^{15}\text{NH}_3$) $_2$ (H $_2$ O) $_2$] $^{2+}$ reacts with thiols at low pH, the preferred products involved sulfur bridges at the concentration of platinum complex ~0.1 M, and the thiolate tends to bridge more in acidic condition than in basic condition (Appleton et al., 1990). This observation is also useful in characterizing the products obtained from the reactions carried out in this study. In this paper, we reported the study of the reaction between $trans$ -[Pt($^{15}\text{NH}_3$) $_2$ (H $_2$ O) $_2$](NO $_3$) $_2$ and glutathione (GSH).

2. Experiment

2.1 Starting Materials

$trans$ -[Pt($^{15}\text{NH}_3$) $_2$ (NO $_3$) $_2$] was prepared based on the procedure as previously described (Appleton et al., 1992). Glutathione (GSH) was used as supplied by Sigma – Aldrich Chemical Company without further purification.

$^{15}\text{NH}_4)_2\text{SO}_4$ (99% ^{15}N , Cambridge Isotopes) was supplied by Novachem, Melbourne, Australia.

2.2 Preparation of *trans*-[Pt($^{15}\text{NH}_3)_2(\text{H}_2\text{O})_2](\text{NO}_3)_2$ (**1**)

trans-[Pt($^{15}\text{NH}_3)_2(\text{NO}_3)_2]$ was converted to *trans*-[Pt($^{15}\text{NH}_3)_2(\text{H}_2\text{O})_2](\text{NO}_3)_2$ in aqueous solution with the following procedure: A certain amount of *trans*-[Pt($^{15}\text{NH}_3)_2(\text{NO}_3)_2]$ (based on the concentration desired, normally either 1 mM or 5 mM) was weighed out, then it is dissolved by warming in 2 mL of water for about 30 minutes. 0.1 M nitric acid was added to adjust the pH. Any solid remaining was removed by gravity filtration to give a solution containing *trans*-[Pt($^{15}\text{NH}_3)_2(\text{H}_2\text{O})_2](\text{NO}_3)_2$ (**1**) which was then checked with ^{15}N NMR.

2.3 Reaction of *trans*-[Pt($^{15}\text{NH}_3)_2(\text{H}_2\text{O})_2](\text{NO}_3)_2$ (**1**) with GSH

The reaction was followed and monitored routinely with 2D [^1H , ^{15}N] HSQC NMR. The procedure used in this reaction is as follows: To a small bottle containing solid GSH (0.307 mg, 1 mmol) was added 0.5 mL 1 mM *trans*-[Pt($^{15}\text{NH}_3)_2(\text{H}_2\text{O})_2](\text{NO}_3)_2$ (**1**) (0.5 mmol). The pH was adjusted to ~ 2.0 under argon gas. The solution was immediately transferred to a 5-mm NMR tube, then placed in the AV400 NMR spectrometer which has been tuned for ^{15}N NMR and accumulation 2D [^1H , ^{15}N] HSQC NMR spectrum was commenced. The spectrum was monitored periodically. 30 hours after the initial mixing, the pH was adjusted to > 7 and the spectrum was again monitored. The reaction was also carried out at the same way with the initial pH of the solution was > 7 .

2.4 NMR Spectra

The 1D 40.54 MHz ^{15}N NMR spectra were recorded using DEPT pulse sequence (Berners-Price and Kuchel, 1990) to increase the sensitivity in a Bruker Avance 400 MHz spectrometer with a 5 mm broadband multinuclear probe. The number of scans used to obtain spectra was normally 250 - 500. A recycle time of 3.54 s was used with pulse width of 12.55 μs (tilt angle of 45 degrees). The number of data points used was 32 K. Chemical shifts are reported relative to 2.5 M ($^{15}\text{NH}_4)_2\text{SO}_4$ in 1 M H_2SO_4 ($\delta_{\text{N}} = 0.00$) in coaxial capillary.

The 2D [^1H , ^{15}N] heteronuclear single-quantum coherence (HSQC) NMR spectra were recorded on a Bruker Avance 400 MHz spectrometer (^1H , 400.1 MHz; ^{15}N , 40.54 MHz) using the sequence of Stonehouse *et al.* (1994).

2.5 Electrospray Mass spectrometry

The following method was used to prepare sample for ES-MS: To a small bottle containing solid GSH (1.535 mg, 5 mmol) was added 0.5 mL 5 mM solution (**1**) (2.5 mmol) and pH was adjusted to ~ 2.0 under argon gas. The bottle was then sealed with parafilm to minimise the oxidation of GSH. The mole ratio of GSH and Platinum complex was 2 : 1. The reaction mixture was left for 45 minutes to 1 hour then electrospray ionization mass spectrometry (ES-MS) was undertaken.

3. Results and Discussion

The reaction of (**1**) with GSH was followed by 2D [^1H , ^{15}N] NMR with the initial concentration of (**1**) was 1 mM. The mole ratio used in this reaction any condition was 1 : 2 platinum complex to GSH. As indicated by the 2D NMR spectra, the reaction between *trans*-[Pt($^{15}\text{NH}_3)_2(\text{H}_2\text{O})_2]^{2+}$ and glutathione tends to mimic those of *trans*-[Pt($^{15}\text{NH}_3)_2(\text{H}_2\text{O})_2]^{2+}$ with H_3accys (Hadi and Appleton, 2005). Based on the series of these NMR spectra (Figure 1 - 3), the reactions occurred both in acidic and alkaline solution are shown in Scheme 1

The reaction was carried out initially at higher pH (pH > 7). In this reaction, apart from a peak due to *trans*-[Pt(OH) $_2$ ($^{15}\text{NH}_3)_2$] (**2**) ($\delta_{\text{N}}/\delta_{\text{H}} -62.59/3.67$ ppm), two new peaks were present in the 2D NMR spectrum (Figure 1), labelled as **A** ($\delta_{\text{N}}/\delta_{\text{H}} -59.26/3.77$ ppm) and **B** ($\delta_{\text{N}}/\delta_{\text{H}} -63.44/3.47$ ppm). Peak **B** was slightly more intense than **A**. No change occurred with time.

As thiolate bridging is not enhanced at higher pH (Appleton *et al.*, 1989; Lempers *et al.*, 1988; Lempers and Reedijk, (1990; Hadi and Appleton, 2006) these two peaks were assigned to *trans*-[Pt(OH)(SG)($^{15}\text{NH}_3)_2$] (**3**) and *trans*-[Pt(SG) $_2$ ($^{15}\text{NH}_3)_2$] (**4**) respectively. This can be seen from the two NMR spectra in Figure 1 and 3. In Figure 1, the reaction was undertaken at higher pH, as a result (**3**) was dominant in the mixture reaction while in Figure 3, the NMR spectrum was run from a sample at a moderate pH, so (**3**) is expected to be less in the mixture reaction. From the spectrum, it can also be seen that the ^{15}N chemical shift for (**3**) and (**4**) is similar, but in the ^1H NMR, there is a greater separation on their chemical shifts. These results are consistent with those reported by Oehlsen *et al.* (2003) who detected *trans*-[Pt(SG) $_2$ ($\text{NH}_3)_2$] and [$\{\text{trans}(\text{GS})\text{Pt}(\text{NH}_3)_2\}_2(\text{SG})$] in reactions between *trans*-[PtCl $_2$ ($^{15}\text{NH}_3)_2$] with glutathione. When the pH of the solution was lowered to ~ 2 , the two peaks above disappeared, and new peaks (the strongest of which are labelled **C**, **D**, **E** and **F**) were present in the 2D NMR spectrum, a similar observation as in acidic condition as discussed in the next discussion.

Then the reaction between *trans*-[Pt($^{15}\text{NH}_3)_2(\text{H}_2\text{O})_2]^{2+}$ (**1**) and GSH was carried out in acidic solution (pH ~ 2). 1 hour after mixing, apart from the peak from starting material (**1**) ($\delta_{\text{N}}/\delta_{\text{H}} -62.39/4.08$ ppm) four major peaks were present in the 2D NMR spectrum. They are labelled as **C** ($\delta_{\text{N}}/\delta_{\text{H}} -55.55/4.18$ ppm), **D** ($\delta_{\text{N}}/\delta_{\text{H}} -55.93/4.13$ ppm), **E** ($\delta_{\text{N}}/\delta_{\text{H}}$

–60.23/3.79 ppm) and **F** (δ_N/δ_H –59.54/3.74 ppm). This spectrum did not change significantly for a further 30 hours (Figure 2) and was similar to the spectrum described above, from the solution which was initially alkaline, then acidified. When the pH of this solution mixture was increased to about 7, all these peaks disappeared and two peaks appeared in the 2D NMR spectrum corresponding to those labeled **A** and **B** from reaction at higher pH (Figure 3).

The peaks observed from the reaction of (**1**) at lower pH are assigned to sulfur-bridged complexes. The formation of dinuclear, trinuclear, tetranuclear and pentanuclear platinum complexes would be possible in this reaction.

If the dinuclear platinum complex (**5**) is formed, in the 2D NMR, it would give rise to a single peak at the region near δ_N/δ_H –60/3.7 ppm, the region for terminal $\text{Pt}(\text{NH}_3)_2$. When the trinuclear complex (**6**) is formed, it would give rise to two peaks in the NMR spectrum, one for terminal $\text{Pt}(\text{NH}_3)_2$ and one for “internal” $\text{Pt}(\text{NH}_3)_2$ at the region δ_N/δ_H –55/4.1 ppm, with the intensity ratio of 2 : 1. If the tetranuclear species (**7**) is present in the mixture reaction, it would also give rise to two peaks, but in this complex the intensity of terminal $\text{Pt}(\text{NH}_3)_2$: “internal” $\text{Pt}(\text{NH}_3)_2$ would be in 1 : 1 ratio. For a pentanuclear (**8**) species, there would be one peak from terminal $\text{Pt}(\text{NH}_3)_2$, and two different peaks for internal $\text{Pt}(\text{NH}_3)_2$ with intensity ratios 2 : 2 : 1. The spectrum shown in Figure 2 showed poorly resolved peaks in the “terminal” region (labelled **E** and **F**) and four clearly resolved peaks in the “internal” region (most intense labelled **C** and **D**). The presence of four distinct “internal” peaks indicates that oligomers up to pentanuclear must be formed in the solution.

From the mass spectrometry data obtained at low pH, the strongest peaks were from complex (**5**) with the m/z 1380 (Figure 4). The separation between isotope lines is showed that charge was +1. The isotope pattern obtained corresponded to the pattern expected for 2 platinum atoms.

There were also two other peaks present in the spectrum with the difference of 36 amu between one peak to another. From this difference, these peaks are due to the sequential loss of two ammine ligands at a time ($^{15}\text{NH}_3 = 18$ amu).

However, when the reaction was carried out at higher pH ($\text{pH} > 7$), the mass spectrometry data did not show any peaks. This is probably due to the formation of platinum complexes with neutral or negative charge.

4. Conclusion

From this study, the results obtained clearly support the previous studies that in the reaction of both *cis*- and *trans*-diaquaplatinum(II) complexes with thiols, the tendency to bridge is more in acidic condition than in basic condition. The preferred products in such reaction always involve sulfur bridges when the reaction is carried out at low pH.

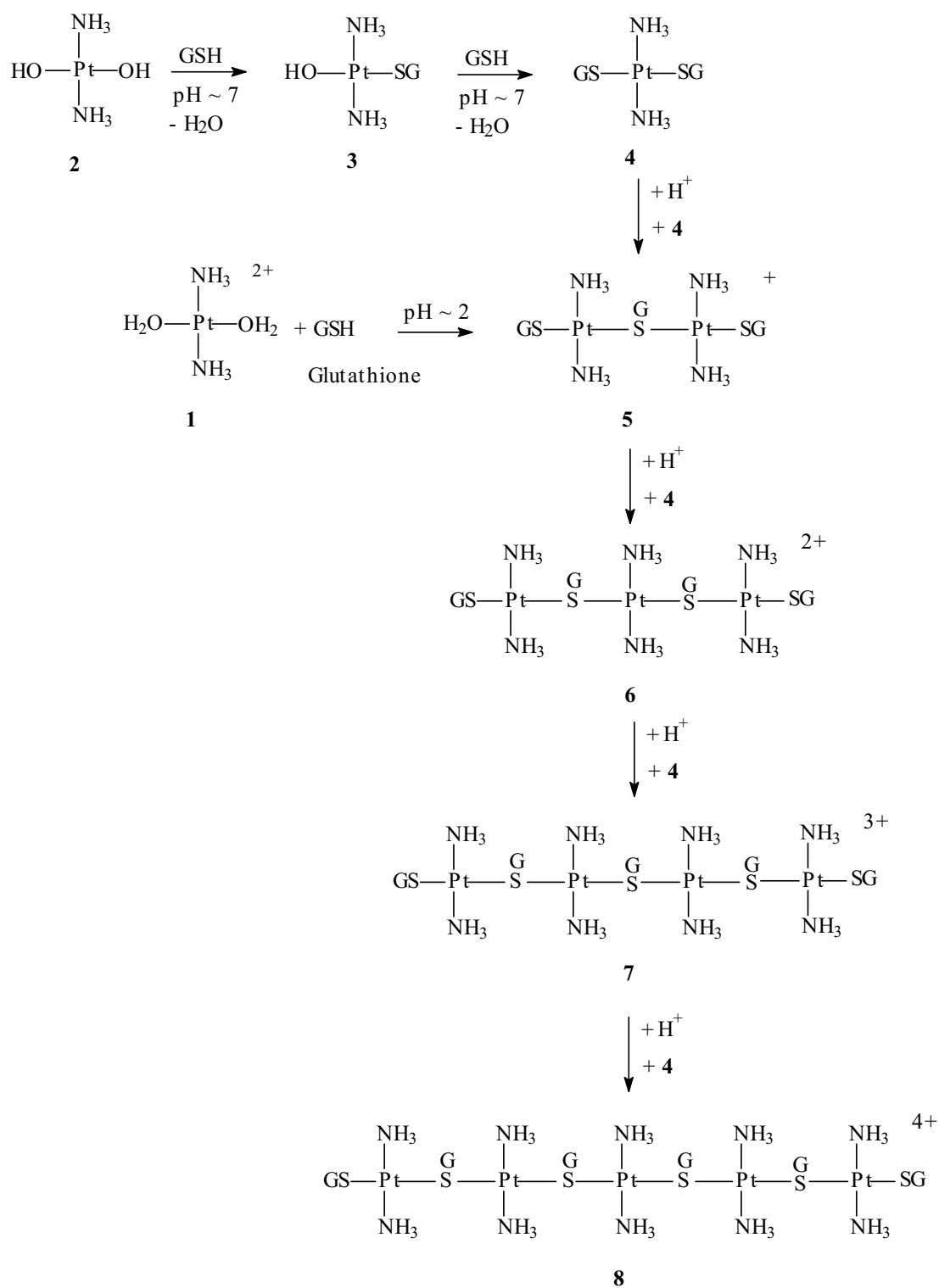
Acknowledgments

We thank DUE Project University of Lampung and Australian Research Council for the financial supports. Thank also goes to Ms. L. Lambert for her help in NMR experimentation and Mr. G. McFarlane for his help in running electrospray mass spectrometry.

References

- Appleton, T.G., Connor, J.W., Hall, J.R. and Prenzler, P.D. (1989). NMR Study of the Reactions of the *cis*-Diamminediaqua-platinum(II) Cation with Glutathione and Amino Acids Containing a Thiol Group. *Inorganic Chemistry*, 28, 2030-2037.
- Appleton, T.G., Bailey, A.J., Barnham, K.J. and Hall, J.R. (1992). Aspects of the solution chemistry of *trans*-diammineplatinum(II) complexes. *Inorganic Chemistry*, 31, 3077-3082.
- Appleton, T.G., Begum, S. and Hadi, S. (2003). Reactivity of Platinum(II) Ammine Bonds *Trans* to Sulfur in Methionine and Thiolate Complexes. *Journal of Inorganic Biochemistry*, 96, 92.
- Berners-Price, S.J. and Kuchel, P.W. (1990). Reactions of *Cis*- and *Trans*- $[\text{PtCl}_2(\text{NH}_3)_2]$ with Reduced Glutathione Inside Human Red Blood Cells, Studied by ^1H and $^{15}\text{N}\{-^1\text{H}\}$ DEPT NMR. *Journal of Inorganic Biochemistry*, 3, 327-345.
- Bodenner, D.L., Dedon, P.C., Keng, P.C., Katz, J.C. and Borch, R.F. (1986a). Effect of diethyldithiocarbamate on *cis*-Diamminedichloroplatinum(II)-induced Cytotoxicity, DNA Cross-Linking, and γ -Glutamyl *Trans*-peptidase Inhibition. *Cancer Research*, 46, 2745-2750.
- Bodenner, D.L., Dedon, P.C., Keng, P.C., Katz, J.C. and Borch, R.F. (1986b). Selective Protection against *cis*-Diamminedichloroplatinum(II)-induced Toxicity in Kidney, Gut and Bone Marrow by Diethyldithiocarbamate. *Cancer Research*, 46, 2571-2755.
- Borch, R.F. and Pleasants, J.M. (1979). Inhibition of *cis*-platinum nephrotoxicity by diethyldithiocarbamate rescue in a rat model. *The Proceeding of the National Academic Sciences U.S.A.*, 26, 6611-6614.
- Borch, R.F., Katz, J.C., Leider, P.H., Pleasants, M.E. (1980). Effect of Diethyldithiocarbamate rescue on tumor response to *cis*-platinum in a rat model. *The Proceeding of the National Academic Sciences U.S.A.*, 77, 5441 - 5444.

- Dedon, P.C. and Borch, R.F. (1987). Characterization of the Reactions of Platinum Antitumour Agents with Biologic and Nonbiologic Sulfur-containing Nucleophiles. *Biochemical Pharmacology*, 36, 1955-1964.
- El-Khateeb, M., Appleton, T.G., Gahan, L.R., Charles, B.G., Berners-Price, S.J. and Bolton, A.-M. (1999). Reactions of cisplatin hydrolytes with methionine, cysteine, and plasma ultrafiltrate studied by a combination of HPLC and NMR techniques. *Journal of Inorganic Biochemistry*, 77, 13-21.
- Gale, G.R., Atkins, L.M. and Walker Jr., E.M. (1982). Further Evaluation of iethylthiocarbamate as an Antagonist of Cisplatin Toxicity. *Annals of Clinical Laboratory Science*, 12, 345 – 355.
- Hadi, S. and Appleton, T.G. (2006). Reactions of Cisplatin Hydrolytes with Thiols 2: Reactions of $cis\text{-[Pt}^{(15}\text{NH}_3)_2(\text{H}_2\text{O})_2]^{2+}$ with L-cysteine. *Science International (Lahore)*, 18 (2), 137 – 142.
- Hadi, S. and Appleton, T.G. (2005). Reactions of $trans\text{-[Pt}^{(15}\text{NH}_3)_2(\text{H}_2\text{O})_2]^{2+}$ with N-Acetyl-L-Cysteine. *Indonesian Journal of Chemistry*, 5, 54 - 57.
- Johnson, N.P., Mazard, J., Escalier, J. and Macquet, J.P. (1985). Mechanism of The reaction between $cis\text{-[Pt}(\text{NH}_3)_2\text{Cl}_2]$ and DNA in vitro. *Journal of the American Chemical Society*, 107, 6376 - 6380.
- Lempers, E.L.M., Inagaki, K. and Reedijk, J. (1988). Reactions of $[\text{PtCl}(\text{dien})]\text{Cl}$ with glutathione, oxidized glutathione and S-methyl glutathione. Formation of an S-bridged dinuclear unit. *Inorganica Chimica Acta*, 152, 201-207.
- Lempers, E.L.M., and Reedijk, J. (1990), Reversibility of binding of cisplatin-methionine in proteins by diethylthiocarbamate or thiourea: a study with model adducts. *Inorganic Chemistry*, 29, 217-222.
- Odenheimer, B. and Wolf, W. (1982). Reactions of Cisplatin with Sulfur-containing Amino Acids and Peptide I. Cysteine and Glutathione *Inorganica Chimica Acta*, 66, L41-L42.
- Oehlsen, M.E., Qu, Y., Farrell, N. (2003). Reaction of Polynuclear Platinum Antitumor Compounds with reduced Glutathione Studied by Multinuclear (^1H , $^1\text{H}\text{-}^{15}\text{N}$ Gradient Heteronuclear Single-Quantum Coherence, and ^{195}Pt) NMR Spectroscopy. *Inorganic Chemistry*, 42, 5498-5506.
- Stonehouse, J., Shaw, G.L., Keeler, J. and Laue, E.D. (1994). Minimizing Sensitivity Losses in Gradient-Selected $^{15}\text{N}\text{-}^1\text{H}$ HSQC Spectra of Proteins. *Journal of Magnetic Resonance*, 107 A, 178-184.
- Van Beusichem, M. and Farrell, N. (1992) Activation of the trans geometry in platinum antitumor complexes. Synthesis, characterization, and biological activity of complexes with the planar ligands pyridine, N-methylimidazole, thiazole, and quinoline. Crystal and molecular structure of trans-dichlorobis(thiazole)platinum(II). *Inorganic Chemistry*, 31, 634 - 639.



Scheme 1. Reaction of (1) with GSH in alkaline and acidic conditions

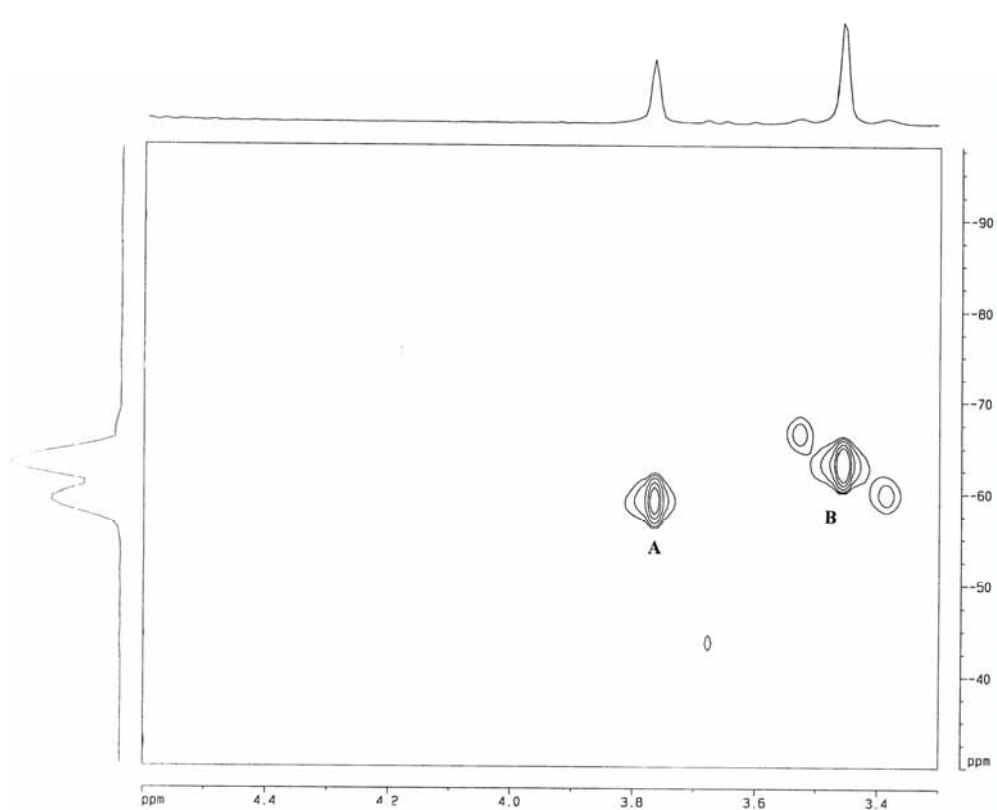


Figure 1. 2D [^1H , ^{15}N] HSQC NMR spectrum of obtained from the reaction of 1 mM (**1**) and GSH in 1:2 mole ratio at the pH ~9, 1 hour after the reaction commenced

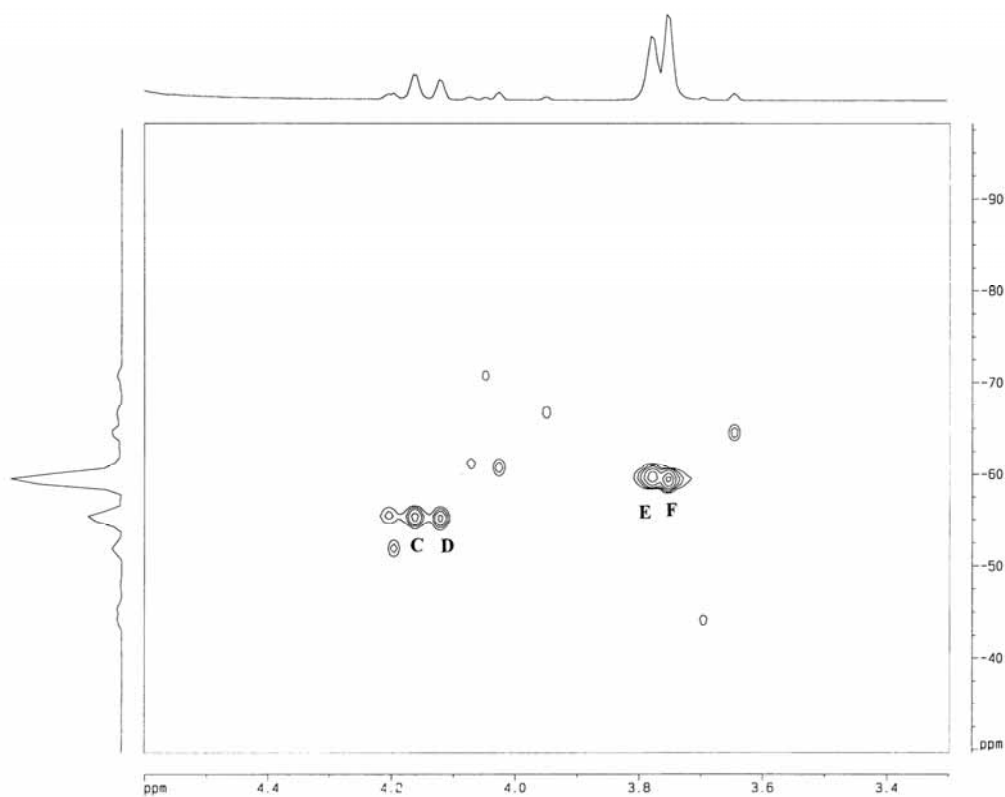


Figure 2. 2D [^1H , ^{15}N] HSQC NMR spectrum of obtained from the reaction of 1 mM (**1**) and GSH in 1:2 mole ratio at pH ~2, 30 hours after the reaction commenced

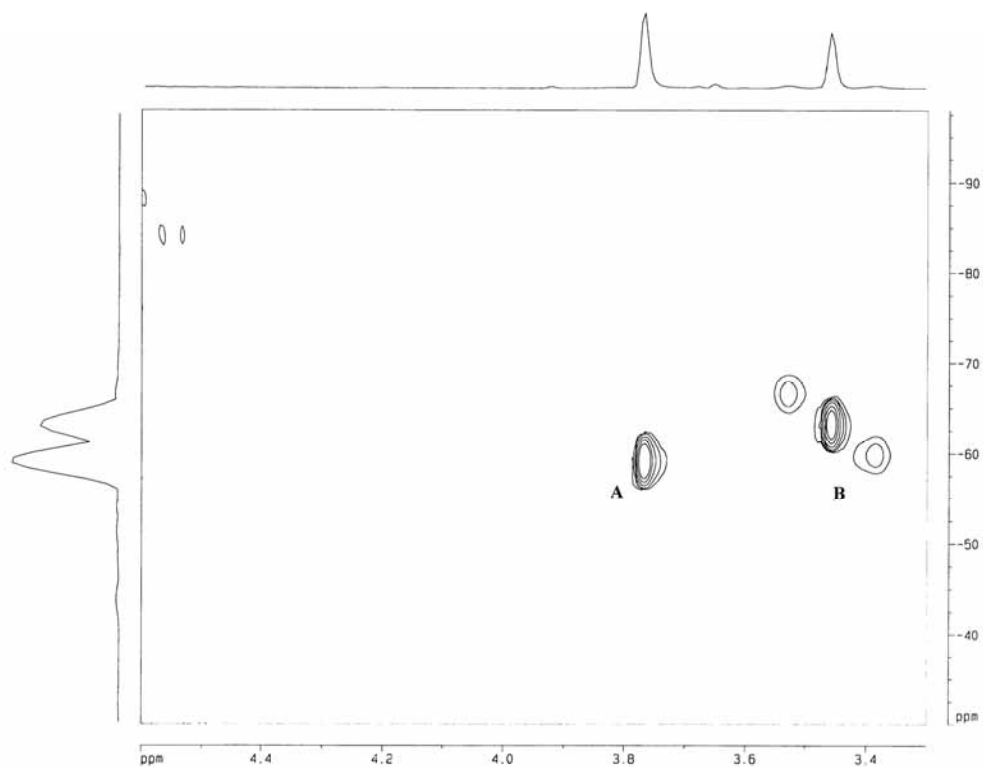


Figure 3. 2D $[^1\text{H}, ^{15}\text{N}]$ HSQC NMR spectrum of obtained from the reaction of 1 mM (**1**) and GSH in 1:2 mole ratio at initially pH \sim 2, then the pH was adjusted to \sim 7, 32 hours after the reaction commenced

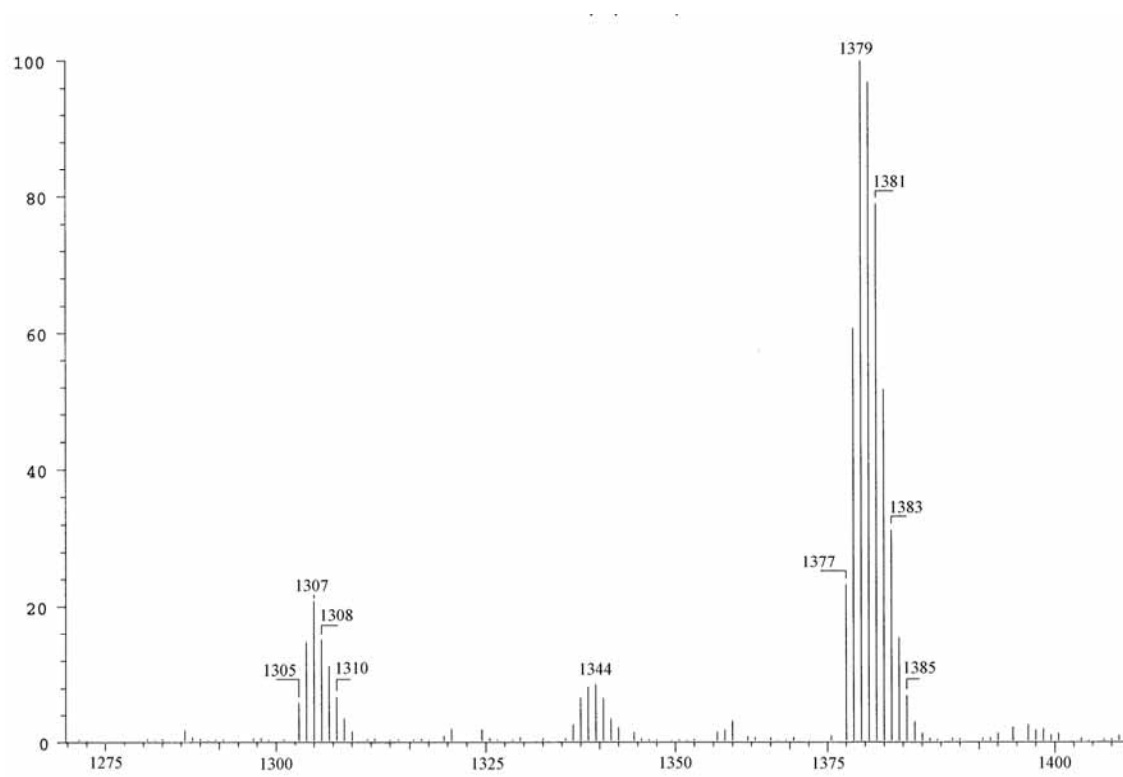


Figure 4. Electrospray mass spectrometry obtained from the reaction of 5 mM (**1**) and GSH in 1 : 2 mole ratio, taken 1 hour after mixing.



The Analysis of Vibro-Acoustic Coupled Characteristics of Ball Mill Cylinder Under Impact Excitation

Zhihong Liu

Center of Energy and Environment
The QingDao Technology University
11 FuShun Road, QingDao 266033, China
E-mail: lzhqingdao@163.com

Chuijie Yi

Center of Energy and Environment
The QingDao Technology University
11 FuShun Road, QingDao 266033, China
E-mail: Chuijieyi@vip.163.com

Abstract

In this paper, a fully coupled vibro-acoustic finite element model (FEM) is developed to characterize the structural and acoustic coupling of a flexible thin shell by a cylinder-like cavity. The combined integral-modal approach is used to handle the acoustic pressure inside the cavity. Based on the modal proposed, the impact excitation effect on the vibro-acoustic behavior of the coupled system is investigated using the modal radiation efficiency at particular frequencies. Simulations are conducted to examine the effect on acoustic natural frequencies, acoustic pressure and structural responses using ANSYS and SYSNOISE software.

Keywords: Structural modal, Acoustic modal, Vibro-acoustic coupling, Ball Mill

1. Introduction

The noise radiation by a vibrating structure is of particular interest for many industrial applications. Typical examples include cabin noise inside vehicles and aircraft, which are usually modeled by a cavity enclosed by a flexible vibrating structure. In the past, a large amount of efforts has been devoted to investigating the vibro-acoustic behavior of such systems, such as analysis of structural-acoustic modal interaction^[1] and sound radiation prediction^[2-3]. In general, structural vibration radiates sound into the enclosure through its coupling with acoustic modes. Therefore, an accurate characterization of the sound-structure interaction is essential for the prediction of acoustic field. Some techniques and methods such as the Green theorem, acousto-elastic theory and acoustic modal theory have been developed so far to address the increasing interest on sound-structure interactions of varied geometrical cavity. Base on those theories, the vibro-acoustic characteristics of Ball Mill cylinder are searched using a fully coupled vibro-acoustic finite element model and combined integral-modal approach^[4-5].

Ball Mills are larger-scale crush equipment, which are used to crush material in chemical process, steam electric power generation, metallurgy, cement production, etc. In the working state, the noise of Ball Mill affected the health of people, decreased the production efficiency. With the development of acoustic theories and techniques, more attentions are paid to the vibratory noise control of Ball Mill. Understanding the mechanism of vibratory noise of Ball Mill is essential for controlling it. From the past researches^[6-8] of Ball Mill noise, Ball Mill noise mainly includes cylinder structural vibratory noise, motor electromagnetic noise and gear mesh noise, in which the cylinder structural vibratory noise is the most important contributor of structural vibration radiation sound.

This paper is a new research about Ball Mill vibratory noise and attempts to provide some useful information of the relationship between structural vibration modal properties and acoustic radiation mode of cylinder and searches main acoustic radiation modes affected significantly by structural vibration using under impact excitation from cycle rolling steel balls inside the cylindrical cavity. A fully coupled vibro-acoustic finite element model and the combined integral-modal approach are used to research the vibro-acoustic characteristics of Ball Mill cylinder. Simulations are introduced to examine the effect on acoustic natural frequencies, acoustic pressure and structural responses by impact excitation.

2. vibro-acoustic FEM modeling

The structure under investigation is a cylinder-like enclosure with homogeneous and isotropic vibrating thin shell, as shown in Fig.1. In the linear-elastic system, the homogeneous Structure can be discrete by differential mass particles. Following this, the motion differential equation of cylinder under impact force $\{f_s\}$ is defined as

$$[M_s]\{\ddot{u}\} + [C_s]\{\dot{u}\} + [K_s]\{u\} = [A]^T \{p\} + \{f_s\} \quad (1)$$

where $[M_s]$, $[C_s]$, $[K_s]$ and $[A]$ are the structural mass matrix, the damping matrix, the stiffness matrix and the vibro-acoustic coupling coefficients matrix, respectively. $\{p\}$, $\{\dot{u}\}$, $\{u\}$ and $\{u\}$ are the acoustic pressure vectors inside the cavity, the acceleration vector, the velocity and the displacement at discrete nodes. T denotes transpose.

For the litter damping acoustic field, the acoustic pressure P inside the enclosure satisfies the ideal fluid hypothesis, the discrete FEM equation can be written as

$$[M_a]\{\ddot{p}\} + [C_a]\{\dot{p}\} + [K_a]\{p\} = -\rho_a [A]\{\ddot{u}\} \quad (2)$$

Where $[M_a]$, $[C_a]$, $[K_a]$ and ρ_a are the acoustic cavity mass matrix, the damping matrix, the stiffness matrix and acoustic fluid density, respectively.

Combined Eqs.(1) and Eqs.(2), structural-acoustic FEM equation is

$$[M]\{\ddot{x}\} + [C]\{\dot{x}\} + [K]\{x\} = \{f\} \quad (3)$$

Where

$$[M] = \begin{bmatrix} [M_a] & \rho_a [A] \\ 0 & [M_s] \end{bmatrix} \quad [C] = \begin{bmatrix} [C_a] & 0 \\ 0 & [C_s] \end{bmatrix} \quad [K] = \begin{bmatrix} [K_a] & 0 \\ -[A]^T & [K_s] \end{bmatrix} \quad x = \begin{Bmatrix} p \\ u \end{Bmatrix} \quad f = \begin{Bmatrix} 0 \\ f_s \end{Bmatrix}$$

Assumed $\ddot{u} = -\omega^2 u$, $\ddot{p} = -\omega^2 p$, Eigenequation of vibro-acoustic system can be described as

$$(\lambda^2 [M] + \lambda [C] + [K])\{\psi\} = 0 \quad (4)$$

Where ω , λ and $\{\psi\}$ denote natural frequency of the coupling system, eigenvalues and eigenvectors of the Eigenequation(4).

3. Results and discussions

3.1 structural modal analysis

Under free state, the right of Eqs.(1) is equal to zero. The eigenvalues and eigenvectors computed from Eqs.(4) denote the natural frequencies and modal shapes of structure. Numerical analysis are conducted using the configuration shown in Fig.1 with a dimension of $\phi D \times L = 3.8m \times 6.5m$, the thickness of the cylindrical thin shell is set as $h = 0.08m$, the flexible rigidity and the density are $2e11$ and $7800kg/m^3$, respectively. Cylinder structural natural properties including modal frequencies and modal shapes can be solved using Block Lanczos arithmetic by ANSYS software with the 0.02 thickness Solid92 mesh cell. The results are shown in Table.1 and Fig.2(1-4). Table.1 presents the natural frequencies of cylinder. Under the 200Hz frequencies are main structural vibration frequencies. 30Hz and 81Hz are shaft and circle direction vibration, which are not the vital influential frequencies for cylinder shell sound radiation. We therefore neglect them during the following discussion. Fig.2(2) shows the maximal magnitude of structural vibration occurs on the mid of Cylinder shell with the 0.01m distorting displacement.

3.2 acoustic modal analysis

Acoustic modal and radiation efficiency of the acoustic cavity are like the structural nature frequencies and shapes. Acoustic modal is described a group independence orthogonal vectors and each vector represents a kind of sound radiation mode. The degree of sound radiation is shown by radiation efficiency. In research, we found that acoustic radiation efficiency only relates with geometrical figure and structural vibration characteristics and is independent of material properties and boundary conditions. Numerical analyses are conducted with the eigenequation(4), eigenvalues and eigenvectors represent acoustic radiation modal and radiation efficiency, respectively. The results from the simulation of SYSNOISE FEM are presented in Table.1 and Fig.3(1-4) and the frequency range from 20 to 200Hz.

3.3 vibro-acoustic coupling analysis

Following the above analysis, we research the vibro-acoustic characteristics of cylinder under the impact excitation from the cycle rolling steel balls inside the cylinder cavity. In working state, steel balls impact the cylindrical thin shell seasonally. The magnitude of impact force is up to 10GPa. The time of interaction is very short and is only several

milliseconds. Under this state, we combine the structural vibration and acoustic radiation using combined integral-modal approach by system FEM. The calculated results are shown in Table.1 and Fig.4(a-d) at particular frequencies.

For the effect on the acoustic cavity from the structural surface impact force, the acoustic radiation mode has been changed at constant frequency. The Figures clearly indicate this.

4. Conclusions

This paper presents a vibro-acoustic modeling of Ball Mill Cylinder and analyzes the characteristics of cylinder's structure vibration-acoustic radiation coupling. Different from previous studies, emphasis is put on analyzing the effect on the vibro-acoustic behavior and the coupling mechanism of the system under impact excitation, leading to the following conclusions.

(1) Under impact excitation, Ball Mill Cylinder vibration frequencies concentrate on low frequency field and the range from 20 to 200Hz. The maximal magnitude of structural vibration is appeared on the mid of Cylinder shell.

(2) The acoustic radiation modal has close relationship with the structural vibration, The head four structural vibratory frequencies significantly affect the acoustic radiation of Cylinder shell and acoustic radiation efficiency can be amplified at resonated frequencies.

References

- Cunefare KA.(1992) Effect of modal interaction on sound radiation from vibrating structures. *AIAA* .PP.2819–28.
- Jian Chen. (2002). The Noise Control Techniques of Ball Mill. PeKing:Power Press of China.
- Kronast M, Hildebrandt M.(2000). Vibro-acoustic modal analysis of automobile body cavity noise. *Sound Vib*. PP.20–3.
- Li YY, Cheng L. (2007). vibro-acoustic analysis of a rectangular-like cavity with a titled wall. *Applied Acoustic*. PP.739–751.
- Li YY, Cheng L.(2004). Modifications of acoustic modes and coupling due to a leaning wall in a rectangular cavity. *Acoust Soc Am*. PP.3312–8.
- PP.1-38.
- Sum KS, Pan J. (2000).On acoustic and structural modal cross-couplings in plate-cavity systems. *Acoust Soc Am*. PP.2021–38.
- Yanli Fu. (2004). Noise Analysis and complex control of Ball Mill. *Energy Environmental Protection*.PP.30-33.
- Zhiqing Zhu. (2007). Noise Control of MB1870 Ball Mill. *Environmental Science And Management*.PP.157-179.

Table 1. Natural frequencies (Hz) of the fluid cavity, the structure and the coupled system

Mode number	Structural frequency	Mode number	Acoustic frequency	Mode number	Coupled frequency
1	20.6	-	-	1	20.1
-	-	1	37.6	2	35.2
-	-	2	47.8	3	42.3
2	61.7	3	62.9	4	62.0
3	72.1	4	71.1	5	72.0
-	-	5	81.3	-	-
-	-	6	90.6	6	94.3
4	101.5	7	100.8	7	101.2
5	115.5	8	112.4	8	116.0
6	123.1	9	122.1	9	124.3
-	-	10	135.5	10	136.4
7	142.3	11	142.2	11	141.2
8	162.2	-	-	12	168.0
9	175.9	12	171.8	13	170.3
10	180.1	13	182.6	14	183.4

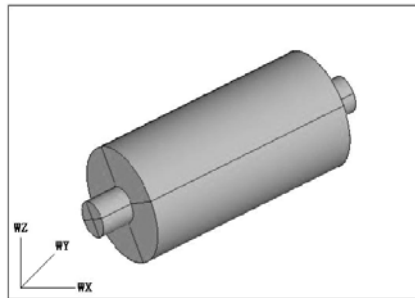


Figure 1. The structural sketch of Ball mill cylinder

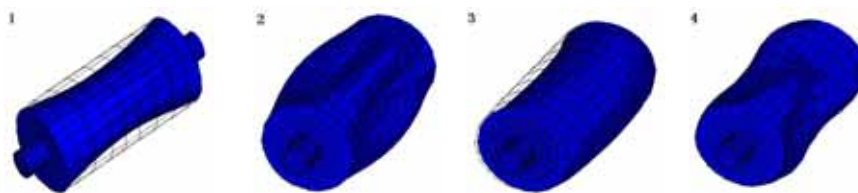


Figure 2. structural natural vibration modal shape of cylinder:
 (1) $f = 61.7\text{Hz}$, (2) $f = 72.1\text{Hz}$ (3) $f = 101.5\text{Hz}$ and (4) $f = 123.1\text{Hz}$.

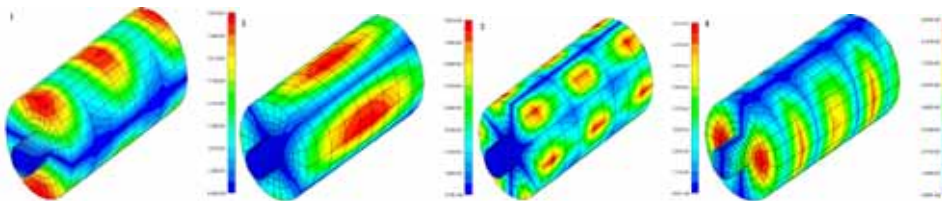


Figure 3. acoustic radiation modal shape of cylindrical cavity :
 (1) $f = 62.9\text{Hz}$, (2) $f = 71.1\text{Hz}$ (3) $f = 100.8\text{Hz}$ and (4) $f = 122.1\text{Hz}$.

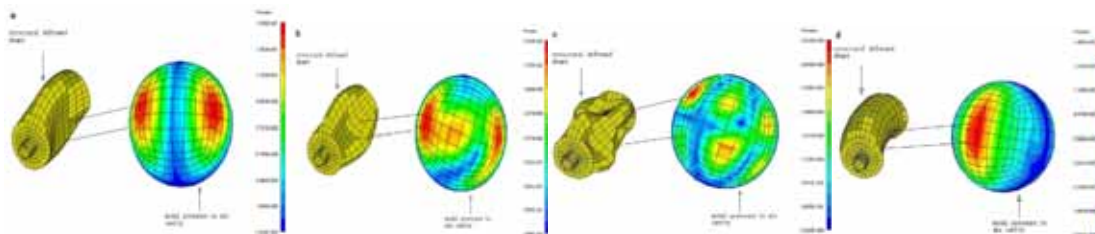


Figure 4. Deformed modal shape of coupled system:
 (a) $f = 62.0\text{Hz}$, (b) $f = 72.0\text{Hz}$, (c) $f = 124.3\text{ Hz}$ and (d) $f = 101.2\text{Hz}$.



Effective Resources Management in Construction Industries for Success

Jayakumar Muthuramalingam

School of Engineering and Science, Curtin University Technology

Sarawak Campus, CDT 250, 98009, Miri, Sarawak, Malaysia

Tel: 6-085-443-827 E-mail: m.jayakumar@curtin.edu.my

Abstract

In most of the cases, the only poor planning and control of resources makes the projects plunge into crises. The ultimate aim of success or profit of the projects is achieved the objectives of specified performance of scope with in the stipulated time by utilizing minimum resources. Today's open market demands not only cheaper products and services but also better product and services. Increased pressures to reduce the cost have not only led to the migrations of U.S. manufacturing operations to Mexico and Far East but also Singapore and Malaysian manufactures into China and other Asian Countries. The process-based project management system controlled by the quality standards may be viable solutions for the success. In construction sector, rather than adopting the optimum design procedures, the effective construction methodology and planning will result in significant savings in resources. This paper describes the line of balancing techniques to minimize the quantity and maximize the productivity of human resources. The effective utilization of resources by establishing average demand over the maximum project periods by resources smoothening techniques are outlined in this paper.

Keywords: Resources controlling, Process management, Line of balance, Resources smoothening

1. Introduction

Definition of project is "A unique temporary process of definite start and end, comprising controlled activities achieving objectives which conform to constraints of time, cost, resources, quality, safety and environmental protection". Process means "A set of interrelated or interacting activities which adds value to inputs and converts them to acceptable outputs". Procedure (Design and Construction) means "A specified way of carrying out a series of processes to achieve a defined objective" (Les west, 2001). The general scope of any project of same categories may almost be the same but uniquely different only by the constraints which may directly or indirectly have impact on the design and construction process.

2. Process Management

7C's of Process Management Principles (Mike, 2007):

1. Consistency of Purpose between process and external stakeholders. The process exists to meet their needs and expectations.
2. Clarity of Purpose between process objectives and consequent actions and decisions.
3. Connectivity of Objectives so actions and decisions deliver outputs that achieve process objectives.
4. Competency of people and capability of equipment.
5. Certainty of Meeting Results through sound measurement and review against targets.
6. Conformity to Best Practices of work performance
7. Clear Line of Sight that process meets customer needs and expectations. Where it doesn't is cause for continuous improvement.

It is a systematic method connecting organisational activities and resources in order to achieve valued objectives and results shown in Fig.1.

3. Parties involved in construction projects

In general most of the construction contracts are executed by mainly two types of contracting systems such as “construct only” contracts and “design and construct” contracts commonly known as “turn key” projects. The major parties involving in construct only contracts are client, consultant and main contractor may be with some specialised sub contractors. In design and construct contracts, main parties involved are only client and main contractor. Normally in this type of contracts there will be a competent person or a firm nominated as work superintendent by the client. Design engineers or a firm may be engaged by the main contractor as their sub contractors. In execution of the same project, each parties involved will have a different critical objectives to be controlled for their success.

Client's objectives:

- *Complete and achieve all the indented scope of projects*
- *Achieve the project completion within the proposed time line*
- *Mobilize the required cash flow for the entire project as budgeted*

The critical objective for the client is only the finance requirements and to meet cash flow needs for the completion of project. The nominated consultant or superintendent will assist to achieve the other two objectives.

Consultant's objectives:

- *Achieve all the scope of works as specified and designed*
- *Control and maintain the progress as planed*
- *Control and minimize the variations in the projects except due to the additional scope of works*

All are critical and only service oriented activities which are not involved with any requirements of resources mobilisations.

Contractor's objectives:

- *Achieve all the scope of works as specified and detailed*
- *Control and maintain the progress as proposed and approved*
- *Mobilise all the required resources to achieve the completion of project within the given time line*
- *Control and minimise the resources required to execute all the scope of works by suitable construction methodology and planning*

The main contractor is the only party responsible and directly involved to execute all the scope of works. They are the only real productive parties. This paper describes the role of resources managements and its importance for the success of the contractor in the construction sector.

4. Process based project management system

1. *Management Responsibility*
2. *resource management*
3. *Product realisation*
4. *Measurement, analysis and improvement*

The above are the main elements of the process based quality management system for the continual improvements (ISO 9001, 2000). The proposed effective process based management system to construction industries is shown in Fig.2. In this project management and resource management may be attached with corporate level or organization depending on the size of the projects but construction management should be effectively site based.

5. Project Management Framework

Design and Construction of civil engineering projects within schedule of time and budget by considering all the constraints (time, scope and cost) encountered during the execution is a great challenge. In the project management, project planning is the first key towards the success in construction, as it determines the time and sequence of the activities in the project, combines them to give an overall completion time. One of the objectives of Project Management Institute Malaysia Chapter (PMIMY) is providing framework for standardised project management requirements (Wong and Jayakumar, 2007). The following section describes the proposed framework for road construction in Malaysia. The steps in the framework include the scope of works, construction activities, consequences and resources controlling, shown in Fig.3.

6. Line of Balance

The overall quantities of the components are determined from the drawing and estimated calculation. If the quantity of

the components is very large or little, the alternative construction methodology may be considered, as the alternative methodology may give better solution than the general methods that usually employed. The activities are subdivided into few sections based on the site constraints. It is used to arrange the activities to be executed in different location in an order, rather than waiting for the entire precedence activities to be completed first. Once the activity is completed in one section, the activity can be repeated in the next section.

The resource usage is kept as minimum as possible, since the activity is arranged to be executed with longer time but still can be completed within the completion date. Indirectly, it can help in the resource management by increase the efficiency of the resources because the labour is kept repeat doing the same work through out the project. Furthermore, the subdivision can help in reducing the cost, as the resource mobilisation cost can be reduced. The skill and human sources are considerably increased by achieving the on job experiences from repeatedly doing the same tasks (Chang and Ive, 2007).

The Fig.4 shows the principle of line of balancing technique. In Ladder A, two groups are required with Group 1 working on units 1, 3, 5, etc and Group 2 on units 2, 4, etc. It is noted that no loss of time as each group moves to its next unit. In Ladder B, the two groups work on the same units as in Ladder B. However it is noted that apart from units 1 and 2, each group has to wait before starting work on its next unit.

Although the line of balancing technique was developed prior to the introduction of Critical Path and Precedence diagram methods, the Line of Balance method can utilize these two methods to great advantage. The basic method assumes that the delivery for several respective completed activities is expressed as a uniform **Rate of Delivery** or as uniform **Handover Rate** for the whole project or section of a project, as an example, four sections of a road per month or three foundations per week. The typical illustrative example of line of balancing technique recommended for housing projects is shown in Fig.5.

7. Team Productivity

The resource teams for each activity task are formed so that the efficiency of resources is increased while repeatedly doing the same task (Chang and Ive, 2007). The productivity of each team is called team productivity. The team productivity can be getting from the methodology databases, research observations, case studies, experiments, and etc. Team productivity is depending on the combination of machinery and manpower. Hence, the productivity for both machinery and manpower are determined respectively. After that, an optimum team capacity may be obtained by merging a reasonable, logic amount of manpower and machine. It is also called optimum labour/machine ratio (Wong and Jayakumar, 2007).

The general machinery productivity is estimated using the formula stated as below:

$$\text{Machinery productivity} = \frac{\text{output of machinery}}{\text{time used}} \quad (1)$$

The manpower productivity is determined by using the formula stated as below:

$$\text{Manpower productivity} = \frac{\text{output of manpower}}{\text{time used}} \quad (2)$$

8. Resource and minimum Productivity

The resource productivity is the productivity chosen in order to execute the job. In planning management, the resource productivity is always greater than minimum productivity required to complete the task. The minimum productivity is the lowest productivity in order to complete the work on time. Based on the detail discussion with project team, the duration for each activity is determined by the project manager or planner. The duration is subjected to the project methodology and the techniques for estimating activity duration, varied from one situation to another, depending on the type of work, the scheduler, and other factors. The project manager needs to consider the condition of contracts, risks, confidences, complexity of works, unexpected risks, latent condition, resource constraints and etc.

$$\text{Minimum productivity} = \frac{\text{total quality or amount}}{\text{duration used}} \quad (3)$$

Next, the number of team needed for each activity is determined by the following equation.

$$\text{Number of team} = \frac{\text{Minimum productivity}}{\text{Team productivity}} \quad (4)$$

$$\text{Resource productivity} = \text{number of resource} \times \text{team productivity} \quad (5)$$

9. Time Arrangement

The total estimated duration to complete activities in each section is calculated based on the following equation.

$$\text{Estimated Duration} = \frac{\text{Quantity}}{\text{Resource productivity}} \quad (6)$$

The duration needed to complete each activity in every section is added to become the total duration of completing that component. Next, the activities are put together in the logical relationship analysed from consequences analysis. The line of balance concept is used here by putting lead and lag duration in between two activities. By this way, the activities are overlapped together without affecting the progress, since both activities are done in different location. The total duration needed to complete scope of works involved in the project is determined. If the total duration exceeds the duration specified in the contract, the productivity of the critical activities has to be increased. It can be done either increasing the number of team or modifying the team resource. It is repeated until the project could be finished within the period specified. The computer software can help in calculating the total duration of the project. After the activities have been arranged, the resources are allocated to the activities. In the computer software such as Primavera, the resources can be assigned to the activities and the resources usage graphs are obtained for the reference.

10. Resource Leveling and smoothening

Resource leveling is done by delaying the activities when the resource usage at any time exceeds the resource availability. If the required resources exceed the resources available, the progresses of activities on that period are delayed proportionally. Resource smoothening is done by shifting the activities to the free float when the resource demand is high on that day. First, the resource usages are analysed and determine the peak resource usages. Later, the activities on that day are shifted by considering their free float. It is also done by shifting the daily uses of certain resources as uniform as possible to minimise the changeability. The illustrative example for resources smoothening is shown in Fig.6 and 7.

11. Costs of poor quality of work

The poor qualities of works cost more for rectification of defects and make good during construction and after construction than the cost for providing and maintaining the required quality management system to avoid poor quality of works. Crosby has said that "Quality is Free" in that the money we spend on preventive measures should be more than returned in the elimination of waste effort and materials (Les West, 2001).

- The costs of poor quality during construction: Poor quality management while engaged in the work causes additional costs and resources for rework, failure analysis, re-test and re-inspection and for storing and disposing the Scrap.
- The costs of poor quality after construction: There are costs which may not been seen during the work but still have to be borne by the organization. These will include the cost for warranty, legal liabilities and loss of customers and potential customers.

12. Case Study: Lumut Bypass

The proposed Lumut-Seria bypass stretches for about 14.5km, within 3km from the seashore (South China Sea). This region forms part of the wide alluvial flood plain of Belait and adjoining Baram river basins. On the Lumut end the site is characterized by the Pleistocene Liang formations, consisting of sand, sandy clay, clay and thin lignite seams overlain by delaic clay, coarse sand, lignite and tuffaceous clay and by Pleistocene Miri formation, consisting of sandstone, sandy shale and shale (Jayakumar, 2005). While only a small reach of this road, less than 1km lies in this kind of formation, the major length of this road lies on the Quaternary clay and sand overlain by PEAT, spreading over the river basin. The contract title of the project was "Lumut Bypass Phase1", new alignment of 14.5 km. This project consisted of two sections, 0 to 7500M and 7500 to 14500M. The total contract period together for both the sections was 28 months. The contract sum was about 43.0 million Brunei dollars. Based on the geological conditions, the general scope of the work for phase 1 of the project was as below.

- Setting out and clear the vegetations.
- Removal of top peaty clay and unsuitable soil up to the depth instructed by the Engineer.
- Back fill with suitable granular fill up to design formation level.
- Construction of 19 Culverts on piled base.
- Construction of 3 Bridges including piled embankment for the Bridge over the BLNG pipe lines.
- Laying turf on both shoulders and side slopes along the entire length of the road.

The awarded main contractors, Dara Construction and Tong & Tong divided the entire scope of the work into two portions as CH 0 to 7500 and CH 7500 to 14500. Each contractor subdivided their portion into 10 smaller section of length approximately 750 meters and formed the team with required machineries and plants to carry out each task of the planned activities from section to section by using line of balance technique. Both contractors completed the assigned scope of the works very successfully within the time line with their estimated budget without much variation. A few

project progress photos are shown in Fig.8 to 10.

13. Conclusion

Control the resources to have the optimum utilization and have a minimum wastage al ways leads to the success of construction projects. This could be effectively achieved proper planning and resource management by using line of balance and resources smoothening techniques as well as by avoiding the poor quality of work resulting the heavy cost for rectifications and repairs.

Acknowledgements

Sincere acknowledgements to Mr. Abey Rathna, Project Manager, Dara Constructions, Brunei and Mr. Jai Mukund, Executive Director, J-Associates, India.

References

AS/NZS ISO 9001: 2000 “Quality management systems-Requirements”, pp. 24.

Chang, C. Y. and Ive.G, (2007), “The hold-up problem in the management of construction projects: A case study of the Channel Tunnel”, International Journal of Project Management, vol. 27, pp. 394-404.

David Redfern (2005) “Civil Project Control” Presentation for Civil Engineering, Curtin University, Perth, Australia, pp. 1-16.

Jayakumar.M and Gajendra (2005), “Construction of highway in soft soil regions of Borneo” The international Conference ICCREM 2005, Penang, Malaysia, pp. 215-218.

Les West (2001), “Quality Management for Engineers” Presentation for Civil Engineering, Curtin University, Perth, Australia, pp. 126.

Mike Sodalini (2007), “Quality Control” Presentation-1 for Civil Engineering, Curtin University, Perth, Australia, pp. 1-24.

Wong Chung Meng and Jayakumar. M. (2007), Project Management of Road Construction in Malaysia” Research report on Civil Engineering Project, Curtin University, Miri, Malaysia, pp. 115.

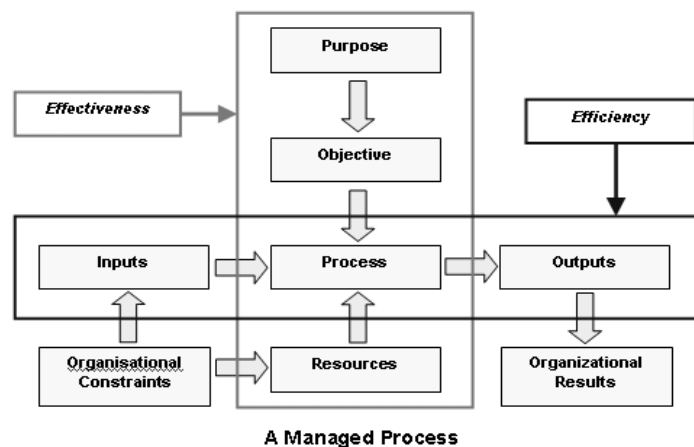


Figure 1. Process management

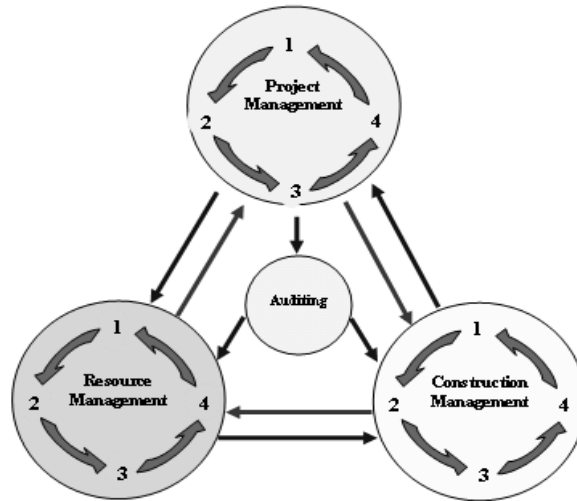


Figure 2. Process based project management system for construction sector

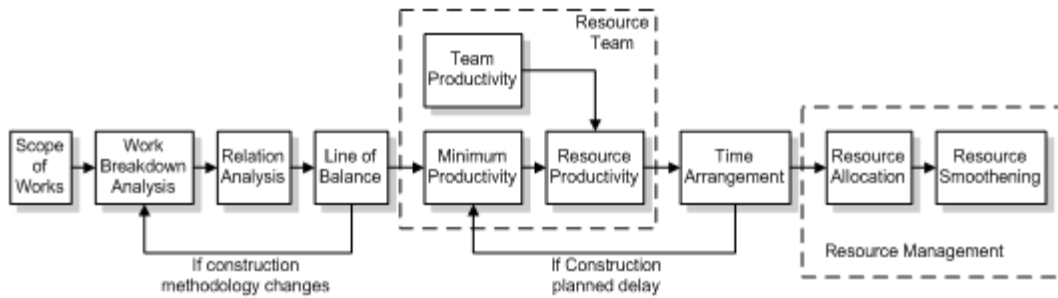


Figure 3. Illustration of Project Management Framework

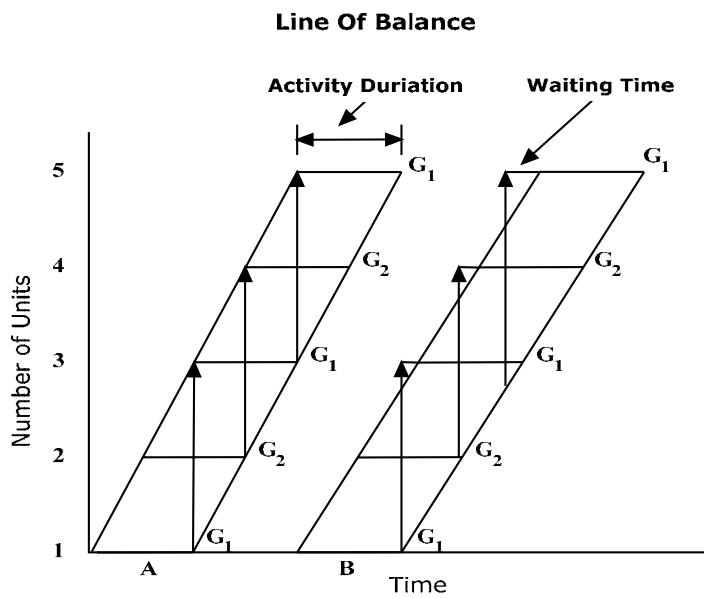


Figure 4. Line of balancing (David Redfern, 2005)

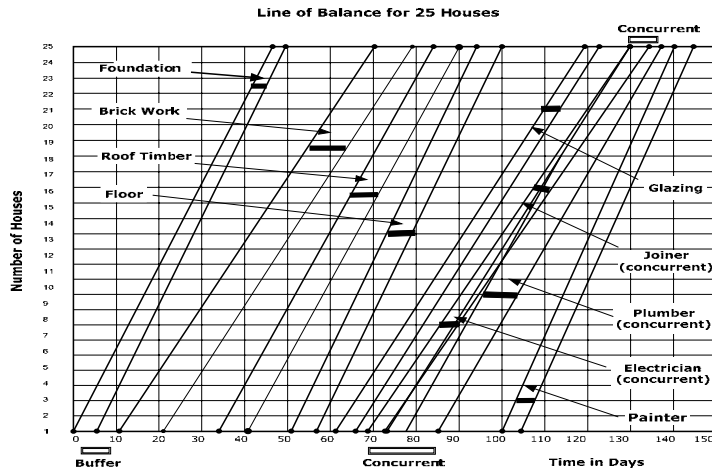


Figure 5. Line of balancing for housing projects

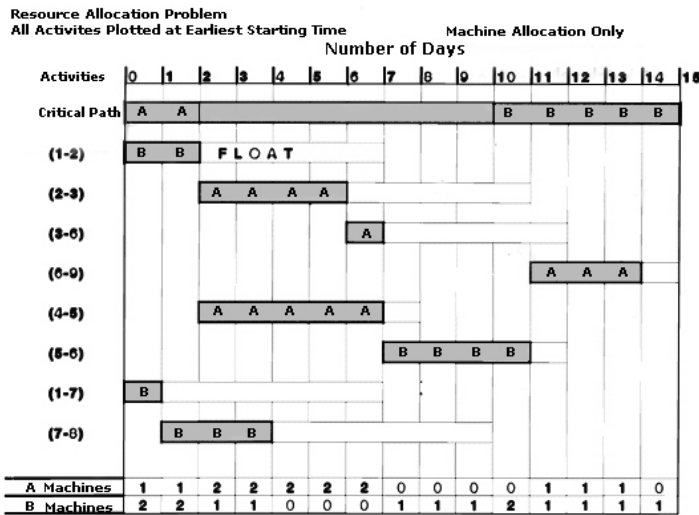


Figure 6. Machinery requirement before balance (David Redfern, 2005)

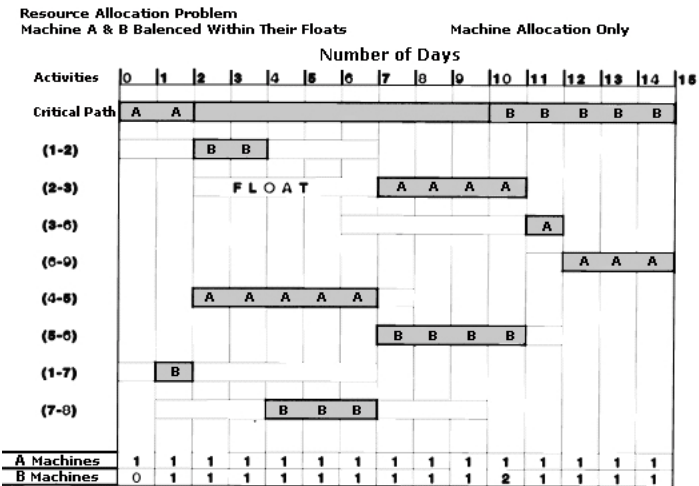


Figure 7. Machinery requirement after balance (David Redfern, 2005)



Figure 8. Installation of Slurry Pump



Figure 9. Jet Pumps melting the sand in Borrow Pits



Figure 10. Completed stage of fill along with sand slurry pipe line



Fabrication and Characterization of Nanometer-sized AgCl/PMMA Hybrid Materials

Xiangting Dong (Corresponding author), Jinxian Wang, Xiuli Feng
School of Chemistry and Environmental Engineering
Changchun University of Science and Technology
Changchun 130022, Jilin Province, China
Tel: 86-431-8558-2574 E-mail: dongxiangting888@yahoo.com.cn

L. Y. Wang, Nancy Kariuki, J. Luo, C. J Zhong
Department of Chemistry
State University of New York at Binghamton
Binghamton, New York 13902, USA

This work was financially supported by the Science and Technology Development Planning Project of Jilin Province (Grant Nos. 20040125, 20060504, 20070402), the Scientific Research Planning Project of the Education Department of Jilin Province (Under grant Nos. 200224, 2005109, 2007-45)

Abstract

Nanometer-sized AgCl/PMMA hybrid materials were synthesized by in situ polymerization. XRD analyses indicated that the prepared samples were amorphous in structure. SEM and EDS analyses indicated that the elements of Ag, Cl in the materials were homogeneous distribution. HSEM images showed that the AgCl nanoparticles in the hybrid materials were spherical in shape, the size was ca. 50nm, particle size distribution was in narrow range, and no agglomerates were clearly observed. The transmissivity and the solubility of the hybrid materials decreased with the increase of AgCl contents in hybrid materials. The TG-DTA analyses indicated that the weight of the hybrid material kept constant above 400°C, the weight loss was 96.98%, and organic compounds were completely decomposed at 385.60°C. The nanometer-sized AgCl/PMMA hybrid materials had some photochromic effect.

Keywords: AgCl, Nanoparticles, Hybrid materials, Nanomaterials, Photochromism

1. Introduction

Inorganic/organic nanometer hybrid materials are the nanomaterials which organic materials hybridize with inorganic materials in nanoscale, including inorganic nanoparticles dispersed in organic matrix and nanoscaled organic compounds in inorganic materials. Inorganic/organic nanometer hybrid materials have attracted increasing interests due to their unique optical, electronic properties and many other specialities[1-7]. AgCl has good photochromism, and it has been well documented. There are also some papers on the preparation and properties of AgX nanoparticles[8-12], but the hybridization of nanometer-sized AgCl with polymer was rarely reported. In the paper, inorganic/organic nanometer hybrid photochromic plexiglass was prepared by hybridization of AgCl nanoparticles with polymethyl methacrylate (PMMA), and some preliminary results were obtained.

2. Experimental Section

2.1 Preparation of nanometer-sized AgCl(coated with oleic acid)/PMMA hybrid material

AgCl nanoparticles, AgCl and Cu²⁺ coexistence nanoparticles in hydrosol were modified with oleic acid which has unsaturated double bond, and AgCl nanoparticles, AgCl and Cu²⁺ coexistence nanoparticles organosols were obtained, as indicated in references[10-11]. These nanoparticles were mixed with methyl methacrylate (MMA) at a certain ratio. Prepolymerization was performed after an amount of initiator was added into the above mixture. When the viscosity of the mixture increased to a certain value, the mixture was poured into a mould. Then the mould was placed into an oven, polymerization was carried out at 110°C for 2h. After the mould was naturally cooled down to room temperature,

nanometer-sized AgCl/PMMA hybrid materials were obtained.

2.2 Characterization methods

XRD analysis was performed with a Japanese Rigaku D/MAX-IIB X-ray diffractometer using Cu $K\alpha_1$ radiation and a curved graphite crystal filter, the working current and voltage were 20mA and 40kV, respectively. The scanning speed was 4°/min, and step was 0.02°. The transmissivity was measured by 754 UV-Visible spectrophotometer made by Shanghai electric optical instruments limited company. The morphology of the hybrid materials was observed with a JXA-840 scanning electron microscope made by Japanese JEOL company. EDS analysis was performed using OXFORD ISIS-300 energy dispersion x-ray spectrometer. High resolution SEM observation of the fracture plane of the hybrid materials was conducted by a S-4200 scanning electron microscope made by Japanese Hitachi company. TG-DTA analysis was carried out with a SDT-2960 thermal analyzer made by American PERKIN-ELMER company in atmosphere, measuring temperature range was 100°C-600°C, and the temperature-rising rate was 10 °C /min.

3. Results and Discussion

3.1 XRD analysis of nanometer-sized AgCl/PMMA hybrid materials

Sample 1 (Volume content of AgCl was 1%), sample 2 (AgCl and Cu²⁺ volume content 1.5%), sample 3 (Volume content of AgCl 2%) were characterized by XRD, as shown in Figure 1. It is seen from Figure 1 that a wide peak appeared at diffraction angle $2\theta=14^\circ$, the peak is the characteristic peak of the typical amorphous organic compound. Therefore, the hybrid material was amorphous in structure. There are no obvious diffraction peaks of AgCl. This is probably due to little AgCl content, or AgCl nanoparticles without crystallization.

3.2 SEM and EDS analysis

In order to investigate the influence of AgCl content on the structure of the hybrid materials, the samples 1, 2 and 3 were fractured at room temperature, and the fracture planes were studied by SEM, as shown in Figure 2. It can be seen that the fracture planes were tenacity fractures. The convex-concave extent decreased with the increase of AgCl content. The samples were further observed by high resolution SEM in order to understand the existence and distribution of AgCl nanoparticle in the matrix, as shown in Figure 3. It is seen from Figure 3 that AgCl nanoparticles were spherical in shape, size distribution was in narrow range, and no obvious aggregates were observed. AgCl nanoparticles size was ca. 50nm. Samples were also investigated with EDX in order to understand the elements distribution in the matrix, as indicated in Figure 4. It is seen that elements of C, O, Ag, Cl uniformly dispersed in the matrix, and Ag and Cl distribution density increased with the increasing in AgCl content.

3.3 Optical property of nanometer-sized AgCl/PMMA hybrid materials

The transmissivity of samples 1, 2 and 3 was measured using pure PMMA as a reference, as indicated in Figure 5. It is seen that transmissivity of the hybrid materials decreased with the decrease of wavelength at high wavelength range (800-600nm) and with the increase of AgCl content. This is owing to the absorbance and reflection of AgCl. The transmissivity of sample 2 was lower than that of sample 3 at middle wavelength range (550-360nm), and this is due to the absorbance of Cu. The transmissivity of samples increased gradually with the decrease of wavelength at low wavelength range (450-360nm), and this is attributed to the decrease in absorbance of the materials.

3.4 Solubility of hybrid materials analysis

100mg of samples 1, 2 and 3 were added into 6ml of chloroform, toluene and ethanol, respectively, for 2h. The results were summarized in Table 1. It is seen that sample 1 and 2 dissolved in chloroform, not in toluene and ethanol, sample 3 dissolved partly in chloroform, also not in toluene and ethanol. This is due to AgCl served as cross-linking dots in the matrix. For one thing, the polymer chains twisted to form physical cross-linking on the surfaces of AgCl nanoparticles; for another, polymerization of surface modifier on the surface of AgCl nanoparticles with matrix formed chemical cross-linking. With the increase of AgCl content, the cross-linking networks centered at AgCl nanoparticles increased, the structure of the samples was transformed from soluble linear structure to insoluble cross-linking structure. The dissolution behavior also indicated the hybrid materials were surely formed [1,6]. Figure 6 is the relationship between transmissivity and wavelength for samples dissolved in chloroform. It is seen that transmissivity decreased with the increase of AgCl content.

3.5 TG-DTA analysis

TG-DTA curves of sample 3 were shown in Figure 7. From TG curve, it can be seen that the weight loss of hybrid material was 96.98%, and the weight kept constant when temperature was above 400°C. It is seen from DTA curve that an obvious exothermic peak appeared at 385.60°C, this is owing to decomposition of the organic compounds.

3.6 Photochromism analysis

Samples 1, 2 and 3 were placed under sunlight, change of color of hybrid material was observed, as shown in Table 2. It is indicated that color of samples became darker with the increase of AgCl content and prolongation of lighting-time.

Consequently, AgCl content should be high in order to obtain an ideal photochromic materials.

4. Conclusions

4.1 Nanometer-sized AgCl/PMMA hybrid materials were synthesized by in situ polymerization. The transmissivity and dissolution of the hybrid materials decreased with the increase of AgCl content.

4.2 XRD analyses indicated that the prepared samples were amorphous in structure.

4.3 The TG-DTA analyses indicated that the weight of the hybrid material kept constant above 400 °C, the weight loss was 96.98%, organic compounds were entirely decomposed at 385.60 °C.

4.4 SEM analysis revealed that the fracture plane of the hybrid material was tenacity fracture at room temperature. EDS analyses indicated that the elements of Ag, Cl in the materials were homogeneous distribution. HRSEM images showed that the AgCl nanoparticles in the hybrid materials were spherical in shape, the size was ca. 50nm, particle size distribution was in narrow range, and no agglomerates were observed.

4.5 The nanometer-sized AgCl/PMMA hybrid materials had some photochromic effect.

References

- Golden J.H., Deng H.B., Disalvo F.J., et al. (1995). Monodisperse 10 Å diameter metal clusters in a polymeric host: the monomer as solvent approach. *Science*, 268, 1463-1466
- Wang J., Tang M., Zhang F., et al. (2007). Modification of optical waveguide material PMMA with nano-silicon by sol-gel approach. *Key Eng. Mater.*, 336-338, 549-551
- Zhuang W., Zhang J. H., Liu J., et al. (2008). Preparation and characterization of nano-TiO₂/polylactide composites. *Acta Materiae Compositae Sinica*, 25(3), 8-11
- Liao J. G., Li Y. B., Wang X. J., et al. (2008). Nano-hydroxyapatite/polycarbonate composite I: Preparation and characterization. *Acta Materiae Compositae Sinica*, 25(3), 63-67
- Dong X.T., Zhang L., Zhang W., et al. (2001). Preparation and characterization of nanometer-sized CeO₂ polystyrene hybrid material. *Acta Phys.-Chim. Sin.*, 17(8), 739-742
- Zhang Y., Zhou G. E., Li L. et al. (1998). Preparation and structure of monodispersed nano-TiO₂/PMMA materials. *Chin. J. Mater. Res.*, 12(3), 291-294
- Dong X.T., Sun J., Liu G. X., et al. (2003). Preparation and characterization of nanometer-sized CeO₂/PMMA hybrid material. *Acta Chim. Sin.*, 61(1), 122-125
- Fu S.L., Yue J., Liu S.W. (1997). Study of preparation and properties of AgBr/I nanoparticles latex. *Light Sensitive Materials*, 15(3), 14-20
- Dong X. T., He Y., Yan J.H., et al. (2003). Preparation and characterization of nanosized AgBr/PMMA photochromic hybrid material. *Acta Phys.-Chim. Sin.*, 19(12), 1159-1162
- Feng X. L., Dong X. T., Li X. Q., et al. (2004). Preparation and characterization of AgCl and Cu²⁺ coexistent nanoparticles sol. *Rare Metal Mater. Eng.*, 33(9), 1003-1005
- Dong X. T., Feng X. L., Wang J. X., et al. (2005). Preparation and characterization of nanosized AgCl hydrosol. *Mater. Sci. Technol.*, 13(1), 45-48
- Dong X. T., Feng X. L., Wang J. X., et al. (2005). Preparation and characterization of AgI nanoparticles hydrosol. *Rare Metal Mater. Eng.*, 34(5), 761-763

Table 1. Solubility of different AgCl contents in hybrid materials

Solvents	Sample 1	Sample 2	Sample 3
Chloroform	Soluble	Soluble	Partly soluble
Toluene	Insoluble	Insoluble	Insoluble
Ethanol	Insoluble	Insoluble	Insoluble

Table 2. Photosensitivity of nanometer-sized AgCl/PMMA hybrid materials

Lighting-time	Sample 1	Sample 2	Sample 3
2h	No obvious change	No obvious change	Slightly dark
4h	No obvious change	Slightly dark	Darker

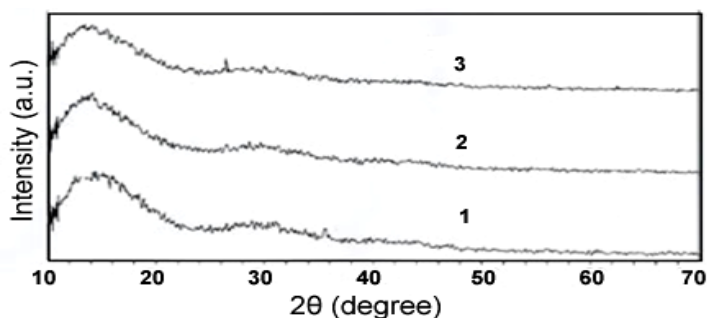
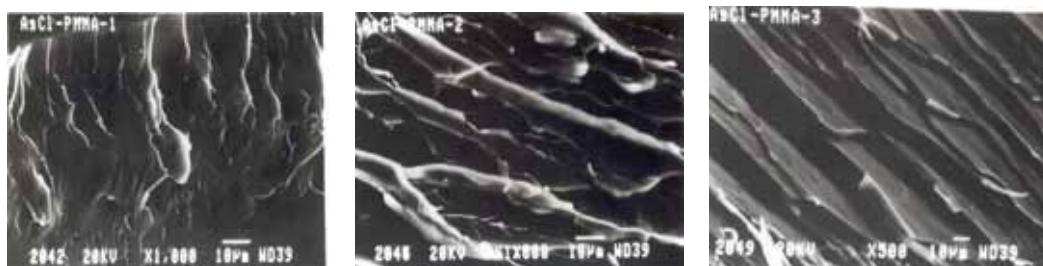


Figure 1. XRD patterns of nanometer-sized AgCl/PMMA hybrid materials

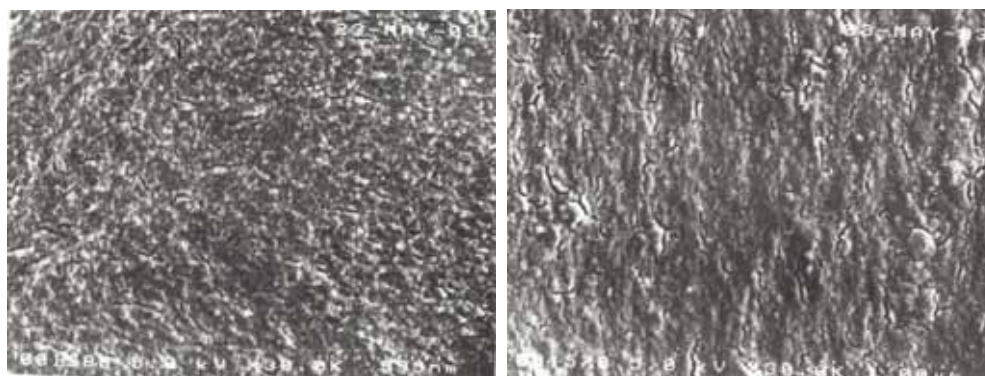


Sample 1 (×1K)

Sample 2(×1K)

Sample 3(×500)

Figure 2. SEM images of the fracture planes of nanometer-sized AgCl/PMMA hybrid materials



Sample 2(×30K)

Sample 3(×30K)

Figure 3. HRSEM images of the fracture planes of nanometer-sized AgCl/PMMA hybrid materials

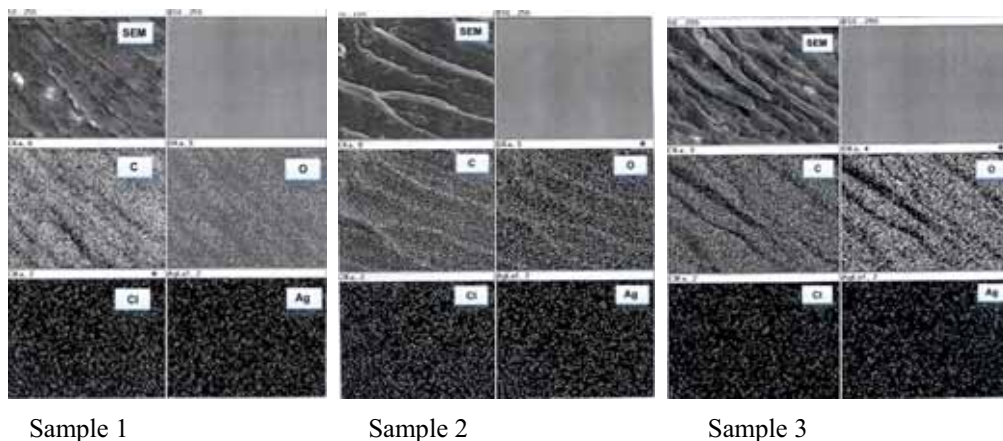


Figure 4. SEM and EDS surface analysis of fracture planes of nanometer-sized AgCl/PMMA hybrid materials

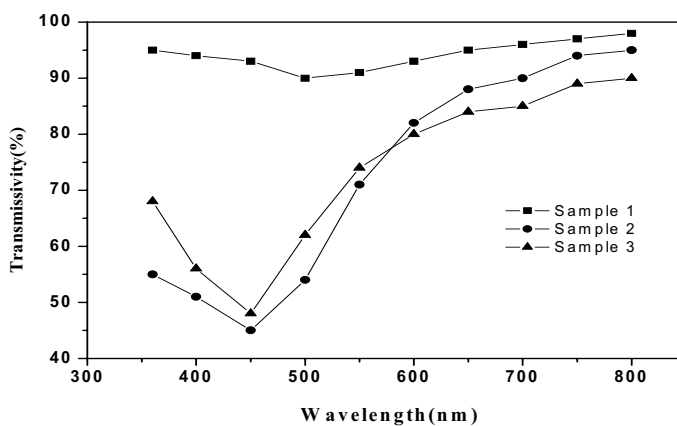


Figure 5. Relationship between transmissivity of different AgCl contents in hybrid materials and wavelength

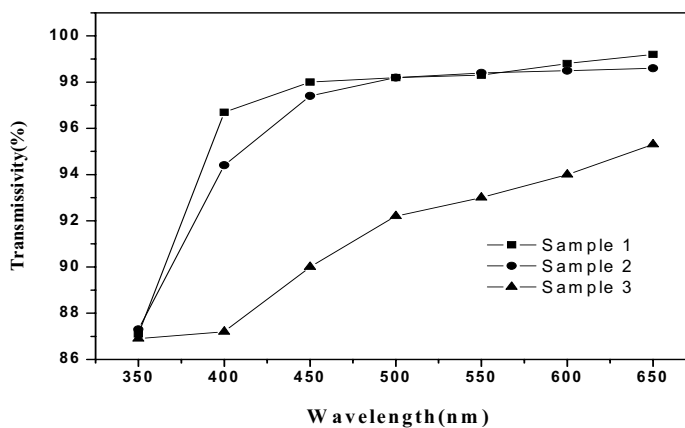


Figure 6. Relationship between transmissivity of the mixtures of hybrid materials dissolved in chloroform and wavelength

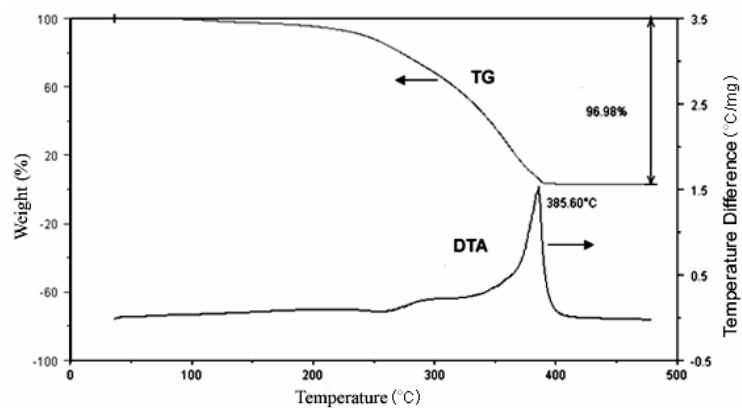


Figure 7. TG-DTA curves of nanometer-sized AgCl/PMMA hybrid material



Self-Tuning of PI Speed Controller Gains Using Fuzzy Logic Controller

Mutasim Nour (Corresponding author)

School Electrical and Electronic Engineering, University of Nottingham Malaysia campus

Jalan Broga, 43500 Semenyih, Salangor, Malaysia

Tel: 60-3-8924-8122 E-mail: mutasim.nour@nottingham.edu.my

Omrane Bouketir & Ch'ng Eng Yong

School Electrical and Electronic Engineering, University of Nottingham Malaysia campus

Jalan Broga, 43500 Semenyih, Salangor, Malaysia

Tel: 60-3-8924-8159 E-mail: omrane@nottingham.edu.my

Abstract

The role of proportional-integral (PI) controller and proportional-integral-derivative (PID) controller as a speed controller for a Permanent Magnet Synchronous Motor (PMSM) in high performance drive system is still vital although new control techniques such as vector control theory that is more effective -but complex- is available. However, PI controller is slow in adapting to speed changes, load disturbances and parameters variations without continuous tuning of its gains. Conventional approach to these issues is to tune the gains manually by observing the output of the system. The tuning must be made on-line and automatic in order to avoid tedious task in manual control. Hence, an on-line self-tuning scheme using fuzzy logic controller (FLC) is proposed in this paper. The performance of the developed proposed controller is tested through a wide range of speeds as well as with load and parameters variations through simulation using MATLAB/SIMULINK. It is found that the proposed 25 rules FLC with adaptive input and output scaling factors enhances the performance of the system especially at high load inertia. The simulation results show that the developed controller can well adapt to speed changes as well as sudden speed reduction besides fast recovery from load torque and parameters variation and these show remarkable improvement compared to conventional PI controller performance.

Keywords: Adaptive Control, Fuzzy Logic, PI Controller, Speed Controller

1. Introduction

In process control today, more than 95% of the control loops are of PID type, most loops are actually PI control (Karl, 2002), (Gupta,2002). For example, it is used to regulate the speed of a motor, pressure of a chamber and heat of an oven. The popularity of PI control can be attributed to its simplicity (in terms of design and from the point of view of parameter tuning) and to its good performance in a wide range of operating conditions (Leandro et al., 2000). The design of PI or PID controller is simple as the computations of the proportional gain, integral gain and derivative gain by means of second-order method or Ziegler-Nichols method are well-defined. However, the normal PI controllers present as a disadvantage the need of retuning whenever the processes are subjected to some kind of disturbance or when processes present complexities (non-linearities) (Karasakal, 2005).

To overcome these problems various new control techniques such as fuzzy logic control and neural network principles are being investigated. These new techniques are not meant to replace the conventional methods which still widely used in industry. In some particular systems such as first-order and second-order linear systems, fuzzy logic or other new techniques do not improve much in terms of the output performance. As a result, the available conventional controllers that can do their job are never replaced by fuzzy controller to avoid adding unnecessarily cost to the system. It is the job of a control engineer to opt for new control techniques or conventional methods in designing a controller based on the necessity and complexity of the system. In some cases, fuzzy logic controller (FLC) can be used to aid conventional method to enhance the output performance. This is very important issue as in some existing conventional PI controllers

fixed gains calculated is good when the system is running with rated speed and rated conditions. Often, when running a system there will be a lot of speed changes, load disturbances and parameter variations (Mutasim & Shirren, 2006). Hence, the fixed gains of the PI controller will not be able to perform the compensation role for such conditions without re-tuning its parameters. This collaboration is practical as most of the industrial system that are using conventional controller can insert a FLC to their control system for optimization purposes without changing much of the system topology and scrapping the conventional controller.

In recent years, there has been an increasing interest in developing alternative methodologies for designing industrial PI controllers such as auto-tuning, self-tuning, pattern recognition, fuzzy logic, neural network and genetic algorithm. For fuzzy logic alone, many investigations and research on different types of adaptive fuzzy PI and PID controllers have been reported in (Hoang, 1995), (Onur et al., 2003), (Kouzi, et al., 2003) and (Mutasim et al., 2005). In general, fuzzy logic PI controller design can be classified into two major categories according to the way of their construction: Either the gains of the conventional PI controller are tuned on-line in according to the knowledge base and fuzzy inference, and then the conventional PI controller generates the control signal or a typical FLC is constructed as a set of heuristic control rules, or the control signal is directly deduced from the knowledge base and the fuzzy inference (Mudi & Pal., 1999).

In this paper, a two-input and two-output FLC is used to tune the PI gains of permanent magnet synchronous motor (PMSM) controller. The tuning is made on-line to compensate for any load disturbances, speed changes and system parameter variations. The inputs for the FLC are error (E) and change of error (CE) while the outputs are change in proportional gain (CKp) and change in the integral gain (CKi). The outputs of the FLC are used to tune the respective gains of the PI controller to optimum values. Since the FLC tunes the existing PI controller gains on-line, it is described as the self-tuning of PI gains using fuzzy logic controller. Throughout the paper, this controller is described as fuzzy-PI controller for simplicity.

2. Controller Design Methodology

A typical control structure of a PMSM is shown in Figure 1 (Krishnan, 2001). As the current time constant is much smaller than the mechanical time constant, a change in current loop is very much faster compared to a change in speed loop. Hence, current loop can be represented by simply a gain or constant. This can ease the design of speed controller as the control structure is reduced to second-order system and Figure 1 is simplified to Figure 2.

Based on A 380W PMSM parameters given in Table 1, satisfactory values for proportional gain (K_p) and integral gain (K_i) were determined using Ziegler-Nichols method ($K_p = 0.2$ and $K_i = 2.1$). These values were used as a starting point for the fuzzy-PI controller to update the gains accordingly based on the error and change of error. The starting points of gains are chosen to be at half rated speed to make the tuning of gains to be equivalent for lowest speed and highest speed.

2.1 Extraction of the FLC Rules

An experiment to study the effect of rise time (T_r), maximum overshoot (M_p) and steady-state error (SSE) when varying K_p and K_i was conducted. The results of the experiment were used to develop 25-rules for the FLC of K_p and K_i . The followed procedure is outlined below.

The effects on the rise time (T_r), maximum overshoot (M_p) and steady state error (SSE) of the response were observed when varying K_i while fixing K_p at 0.2 and varying K_p while fixing K_i at 2.1. Table 2 records these effects. The values of K_p and K_i are obtained through the design of PI Controller as stated above. The reference speed is set to be from 300 to -300 rad/s that is about 50 % of the rated speed with full-load (FL). The results in Table 2 are used to create Table 3 that shows the effect of varying K_p and K_i . This table is created in such a way that the magnitude of the effects on T_r , M_p and SSE are determined when the gains of K_p and K_i are varied.

2.2 Membership Functions Selection

The design of FLC is based on Table 3 in deciding when to manipulate K_p and K_i based on the response of the system. For example, when steady-state error is big, gains of K_p and K_i should be increased and vice versa. Error E_k can be represented by steady-state error (SSE) while change in error CE_k can be approximated by rise time (T_r) since:

$$CE = \frac{E_2 - E_1}{T} \quad (1)$$

where T is sampling time, E_2 is current error and E_1 is previous error. The normalised speed error E_k and the normalised change of error CE_k can be calculated from:

$$E_k = \frac{\omega_{ref\ k} - \omega_k}{\omega_{ref\ k}} \quad (2)$$

$$CE_k = \frac{E_k - E_{k-1}}{\omega_{ref_k}} \quad (3)$$

where ω_{ref_k} is reference speed (rad/s), ω_k is measured speed (rad/s) and E_{k-1} is previous normalised error. E_k and CE_k are the two inputs to the FLC to calculate the change of proportional gain CK_p and change of integral gain CK_i which will be summed together to form the new input current command i_q for the control of PMSM. Notice that, equation (2) and (3) are normalised by the reference speed at every instance. This is to scale the value of E_k and CE_k down to the range of -1 to 1 as the range of the universe of discourse for the membership functions of FLC is selected to be from -1 to 1 as will be seen later in the following sections.

The effective gain for proportional control (TK_p) and integral gain (TK_i) can be calculated as:

$$TK_p = K_p + TCK_p \quad (4)$$

$$TK_i = K_i + TCK_i \quad (5)$$

where TCK_p is sum of changes in proportional gain, TCK_i is sum of changes in integral gain, K_p is the initial proportional gain set and K_i is the initial integral gain set.

The behaviour of implementing the rules in Table 4 is identical to the often used rule base designed with a two-dimensional phase plane which has 49 rules (Yanan & Collin, 2003). Series of tests were performed to choose the most suitable membership function (MF). A comparison between the performance of four MFs types were conducted and revealed that the assymmetrical Bell-shaped performed better than symmetrical Bell-shaped, assymmetrical triangle-shaped and symmetrical triangle-shaped MFs. Therefore, assymmetrical Bell shaped MFs were employed in this work.

3. Tuning Mechanism

3.1 GCE Tuning

The FLC previously designed can be improved further by tuning one input of the FLC. This input gain (GCE) that needs to be tuned is the change of error (CE) input for the FLC. GCE is tuned with respect to speed changes. Different speed response has different optimum values of GCE as shown in Table 5. By using these values, the response of the system is tested to be significantly better in term of rise time. Hence, data from Table 5 is used to form an on-line tuning mechanism for different speed applied. The method chosen is called the look-up table method or gain scheduling. In this method, different GCE values from -628 to 628 rad/s are written into a programme and the other in between values are calculated based on interpolation method. Interpolation is a process for estimating values that lie between known data points. The high maximum overshoot output responses due to the change of moment of inertia can also be overcome by changing the values of GCE as shown in Table 6.

To minimize the maximum overshoot, the price for it is slower rise time. In other words, there is a need to compromise between rise time and maximum overshoot. In Table 6, the values of GCE are optimised so that the maximum overshoot is eliminated but the rise time for the system raised quite significant as can be seen in Table 7. The main reason for doing this is to avoid the system to be damaged by high overshoot. The simulation model in this stage is modified by including the gain scheduling process. The slow rise time due to the increased inertia cannot be tolerated in high performance drive system. Hence, further improvement for the rise time is done next.

3.2 GCE and GIQ (I/O Gains) Tuning

It is found that by tuning of GIQ as a function of inertia and speed and fixing GCE tuning results in smoother and faster response for certain speeds. In addition, high overshoot and slow response as a result of increased inertia can also be overcome. Hence the output control signal is scaled up or down accordingly by GIQ as a function of speed and moment of inertia. From Table 9, it is obvious that as inertia increases, GIQ decreases. This is to make sure the FLC updates the K_p and K_i with a smaller value to avoid overshoot because the overshoot increases when inertia increases as discovered previously.

When only the GIQ is changed, the recovery of speed from load changes become slower. To overcome this problem, GIQ needs to be tuned as a function of load as well. When load occurs, the output gain must be increased to ensure the response recovers from load changes faster. It is observed that for all speed, the recovery from load changes is fast by using a fix GIQ of 1. The final stage of the developed controllers can be seen clearly from the simple block diagram shown in Figure 3.

4. Results and Discussion

The performance of the tuned-gain FLC performance against the performance of the fixed gains PI controller, and the

performance of the fixed-gain FLC are presented in this section. The simulation block diagram model in Simulink is given in Figure 4.

4.1 Fixed Gains PI Controller

Graphs in Figure 5 shows a collection of results obtained from the simulation model that uses a fixed PI controller gains as a speed controller. The gains of the parameters are set based on half rated conditions at ± 300 rad/s. At these conditions, the PI controller plays its role well. However, when the speed changes to the rated speed which is 628 rad/s or any other speed, high overshoot and high steady-state error (SSE) occurs. This is because the fixed gains of the controller cannot adapt to speed changes well.

4.2 Fixed-Gain FLC

Figure 6 shows the performance of the FLC at first stage of development that is with fixed input and output gains. The performance of this control is good throughout a wide range of speed with zero SSE and fast rise time. The only drawback of this FLC is high overshoot at increased inertia. High overshoot occurs when the inertia is varied as can be seen from Figure 6 (a). This occurs because FLC tune the gains of PI controller to very high value due to the slow response of the system and by the time the response reaches the reference speed, FLC failed to decrease the high value of gains instantly and this causes the overshoot. However, the response tends to settle down to zero SSE after a short time but the overshoot for the response of 10 J is considered very high and is not acceptable in most of the applications. Although, it is very unlikely that 10 J is going to occur in real-time but effort in minimizing the overshoot is made as can be seen in next part of the results. As for the case of PI controller, the effect of varying the stator resistance and the stator inductance on the response of the system is not significant as shown in Figure 6 (b) and (c). Figure 6 (d) shows that the FLC can adapt to small speed reduction well at J and acceptable response with some overshoot is obtained at 2 J. These two responses follow the small speed reduction very fast with zero SSE.

Fast recovery from load changes to zero SSE can be seen in the magnified figures in Figure 7 whether at forward transient or reverse transient. The dip as a result of load is very small and is hardly visible if it is not magnified. These show that the developed FLC can adapt to load changes very well.

4.3 Tuned-Gains FLC

Results in this part shows the final developed FLC with I/O Gains tuning responses. The results seen below are proven to be very satisfactory especially for different moment of inertia as in Figure 8 (a). Smooth and considerably fast response with negligible overshoot is obtained for different values of J. As expected, response with different resistance and inductance does not have significant changes as it is the case for other controllers as previously discussed. Figure 8 (d) shows the controller can adapt to small speed reduction at nominal J as well as increased J well. The response time for the increased inertia is longer as expected.

Figure 9 shows that the proposed controller can improve the transient response and further smooth the speed response compared to results obtained with the FLC with fixed input and output gains as shown in Figure 7. Besides, very fast recovery from load changes can also be obtained at forward transient where the dip as a result of load disturbance is very small and not clearly visible even though when it is magnified. For the reverse transient case, the recovery from load changes is considerably fast. The variations in the gains depicted in Figure 10. Initially, it can be seen that both the gains increased to high value at starting point because the error at this point is very big. As the response reaching zero SSE, the gains are seen to decrease to avoid excessive gains that will cause overshoot and leads to deterioration of stability.

When FL is applied and removed at 0.02 s and 0.08 s respectively, the gains at this point are enough to compensate for the load disturbances as no increment of gains are seen. During reverse transient at 0.1 s, the gains are decreased abruptly for the motor to rotate in another direction and then settle down back when reaching zero SSE at the reverse transient. When FL is applied again at 0.12 s, it can be seen that the gains increased for load recovery. When FL is removed at 0.18 s, the gains are seen to decreased back to the original value before FL is applied.

The control signal i_q as a result from the self-tuning controller gains and the electromagnetic responses are shown in Figure 11. Initially, very high current is needed to start the motor to overcome friction and inertia. When the motor starts to rotate, lesser current is needed. However, the current increased to approximately 1.9 A (rms) when FL is applied at 0.02 s and 0.12 s. This current is the rated current of the motor.

5. Conclusion

A self-tuning fuzzy logic controller (FLC) that tunes the gains of PI controller was developed. This controller shows improvements in terms of zero steady-state error and fast recovery from load changes compared to the conventional PI controller with fixed gains which does not have fast speed tracking and fast recovery from load changes and parameters variations. The enhancement of the controller is made by tuning the input and output scaling factors of the FLC by gain scheduling. These enhancements efforts show noticeable improvement especially at increased inertia and response

smoothness. The developed controller is proven to be robust as it was applied to control the motor speed at different speeds and parameters variation. Since, PI controller is still widely used in industry; the developed FLC can be applied to the available PI controller for optimization purposes once the implementation is carried out successfully. The developed control algorithm has been proven successfully in simulation and the next step is to be implemented in hardware using "Intelligent Motor Drive Module Development (IMDMD15)".

References

- Gupta, S. (2002). *Elements of Control Systems*: Prentice Hall, Upper Saddle River, NJ.
- Hoang, L-H. (1995). An Adaptive Fuzzy Controller for Permanent Magnet AC Servo Drives, in *Conf. Rec. of IEEE IAS Annual Meeting*: 104-110.
- Karasakal, O., Yesil, E., Guzelkaya, M., Eksin, I. (2005). Implementation of a New Self-Tuning Fuzzy PID Controller on PLC. *Turk Journal of Electrical Engineering*, 13(2):277-286.
- Karl, J. A. (2002). Control System Design. Lecture Notes for ME155A. Department of Mechanical & Environmental Engineering University of California Santa Barbara. (Chapter 6). [Online] Available <http://www.cds.caltech.edu/~murray/courses/cds101/fa02/caltech/astrom.html> (June 9, 2007).
- Kouzi, K., Mokrani, L. & Naït-Saïd, M.S. (2003). A Fuzzy Logic Controller with Fuzzy Adapted Gains Based on Indirect Vector Control for Induction Motor Drive. *Journal of Electrical Engineering*. 3:49-54.
- Krishnan, R. (2001). *Electric Motor Drives, Modeling, Analysis and Control*: Prentice Hall (Chapter 9).
- Leandro dos Santos, C., Otacilio da Mota, A., & Antonio Augusto Rodrigues, C. (2000). Design and Tuning of Intelligent and Self-Tuning PID Controllers. In *The 5th Online World Conference on Soft Computing In Industrial Applications, Helsinki. IEEE Finland Section*: 213-220.
- MATLAB Manual, The MathWorks, Inc. 1984-1999.
- Mudi, R. K. & Pal N. R. (1999). A Robust Self-tuning Scheme for PI- and PD-type Fuzzy Controllers. *IEEE Trans. Fuzzy Systems*, 7 (1): 2-16.
- Mutasim, N. & Shirren, T. (2006). Adaptive Fuzzy Logic Speed Controller with Torque Adapted Gains for PMSM Drives. *Journal of Engineering Science and Technology*, 1(1): 59-75.
- Mutasim, N., Aris, I., Mariun, N., Mohibullah, S.M. (2005). Hybrid Model Reference Adaptive Speed Control for Vector Controlled PMSM Drive. *IEEE Sixth International Conference on Power Electronics and Drive Systems (PEDS05)*, Kuala Lumpur, Malaysia.
- Onur, K., Engin, Y., Mujded G., Ibrahim, E. (2003). An Implementation of Peak Observer Based Self-Tuning Fuzzy PID-Type Controller on PLC. *3rd International Conf. on Electrical and Electronics Engineering, 2003, Turkey*: 474-497.
- Yanan, Z. & Emmanuel G. C. (2003). Fuzzy PI Control Design for an Industrial Weigh Belt Feeder. *IEEE Trans. Fuzzy Systems*, 11(3), 311-319.

Table 1. PMSM parameters

Description	Value	Units
Nominal stall torque	0.6	[Nm]
Nominal stall current	1.9	[A rms]
Peak torque	2.4	[Nm]
Peak current	7.6	[A rms]
Back-EMF	20	[V/Krpm]
Torque constant (+/-5%)	0.27	[Nm/A]
Nominal speed	6000	[rpm]
Nominal power	377	[Watt]
Moment of inertia	0.251	[kg x cm ²]
Terminal inductance	5	[mH]
Weight	2.1	[kg]
Number of pole-pairs	2	[1]
Friction coefficient	5 x 10 ⁻⁵	[Nm/rad/s]
Magnetic flux constant	0.191	[volts/rad/s]

Table 2. Transient and steady-state response for speed from 300 to -300 rad/s at FL

K_p	K_i	T_r (ms)	M_p (%)	SSE (%)
0.2	0.2	1.80	0	2.67
	0.5	1.80	0	2.27
	1.0	1.80	0	2.00
	1.5	1.60	0	1.41
	2.0	1.50	0.06	1.18
	3	1.40	0.20	0.93
	4	1.35	0.46	0.80
	5	1.32	0.33	0.67
	10	1.22	2.1	0.17

K_p	K_i	T_r (ms)	M_p (%)	SSE (%)
0.10	2.1	1.90	0.282	2.73
0.15		1.62	1.98	2.07
0.20		1.50	2.05	1.60
0.25		1.36	2.46	1.54
0.30		1.2	2.61	1.17
0.40		1.12	4.91	1.10
0.50		1.10	7.67	1.00
1		1.09	10.91	0.67
2		1.08	11.73	0.37

Table 3. Effects of varying K_p and K_i

Gain		T_r	M_p	SSE
K_p	Increase	Decrease	Increase	Improved
	Decrease	Increase	Decrease	Deteriorated
K_i	Increase	Decrease	Increase	Improved
	Decrease	Increase	Decrease	Deteriorated

Table 4. The 25 rules for FLC

		CK_p					CK_i						
		CE	NB	NS	ZE	PS	PB	CE	NB	NS	ZE	PS	PB
E	CE	NB	NB	NS	NS	NS	ZE	NB	NB	NS	NS	NS	ZE
	NB	NS	NB	NS	NS	ZE	PS	NS	NB	NS	ZE	PS	PS
	NS	ZE	NB	NS	ZE	PS	PB	ZE	NB	NS	ZE	PS	PB
	ZE	PS	NS	ZE	PS	PS	PB	PS	NS	ZE	PS	PB	PB
	PS	PB	ZE	PS	PS	PS	PB	PB	ZE	PS	PB	PB	PB
	PB												

Where: NB: Negative Big; NS: Negative Small; ZE: Zero Error; PS: Positive Small; PB: Positive Big.

Table 5. GCE at different speed and load conditions

w(rad/s) (+-)	Input scaling factor for CE (GCE)
628	95
500	75
400	60
300	45
200	35
100	20
50	15
10	6
5	4
1	1.5

Table 6. GCE at different moments of inertia

Multiple of rated inertia, n	1	2	5	10
Input scaling factor, GCE	95	190	450	900

Table 7. Rise time of the system with different moments of inertia and GCE

Multiple of rated inertia, n	Input scaling factor, GCE	Rise time, Tr (ms)
1	95	6.71
2	190	12.36
5	450	25.62
10	900	49.51

Table 9. Output scaling factor for different speeds and inertias

w(rad/s) (+/-)	Moment of Inertia			
	J	2J	5J	10J
	Output Scaling Factor (GIQ)			
628	0.15	0.11	0.07	0.04
500	0.15	0.1	0.06	0.03
400	0.13	0.09	0.05	0.025
300	0.11	0.08	0.04	0.02
200	0.1	0.06	0.03	0.015
100	0.06	0.04	0.015	0.0075
50	0.05	0.04	0.0125	0.006
10	0.5	0.5	0.5	0.006
5	1	1	1	1
1	1	1	1	1

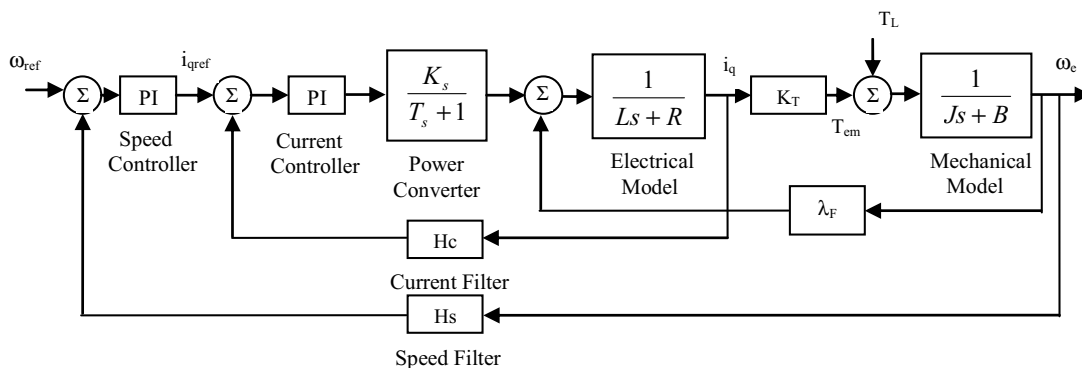


Figure 1. Typical Control Structure for PMSM

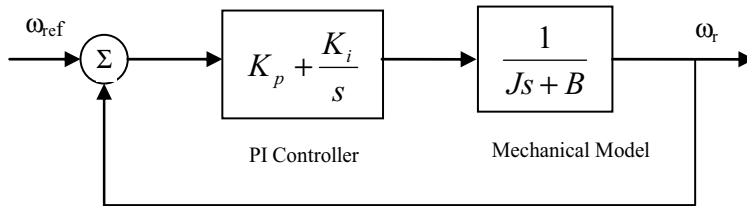


Figure 2. Simplified Control Structure of PMSM

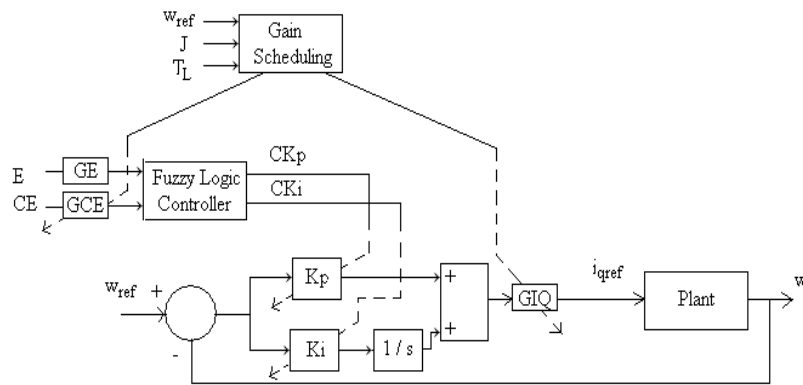


Figure 3. Simulation Block Diagram of the Proposed System

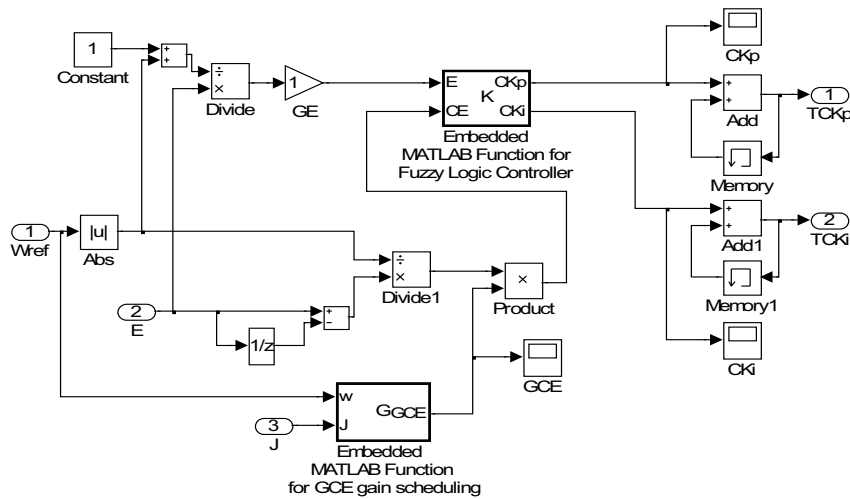


Figure 4. Internal Structure of FLC Model

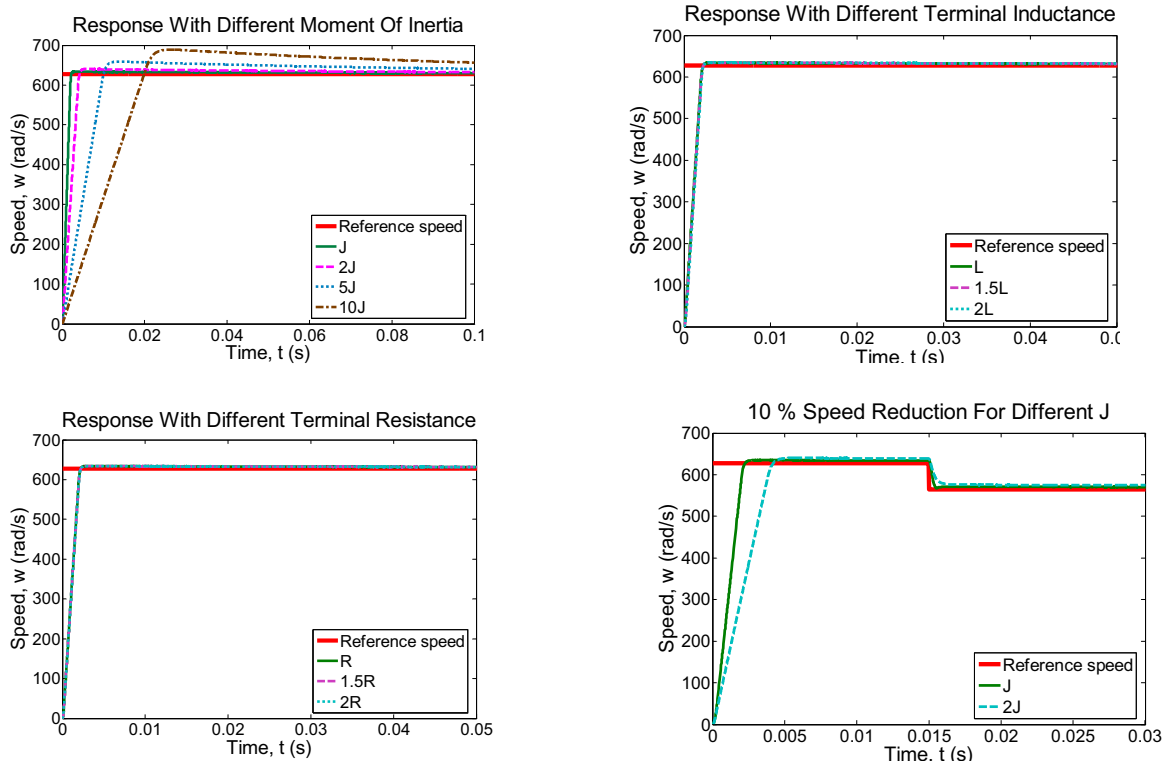


Figure 5. Response of the System Using Fixed Gains PI Controller

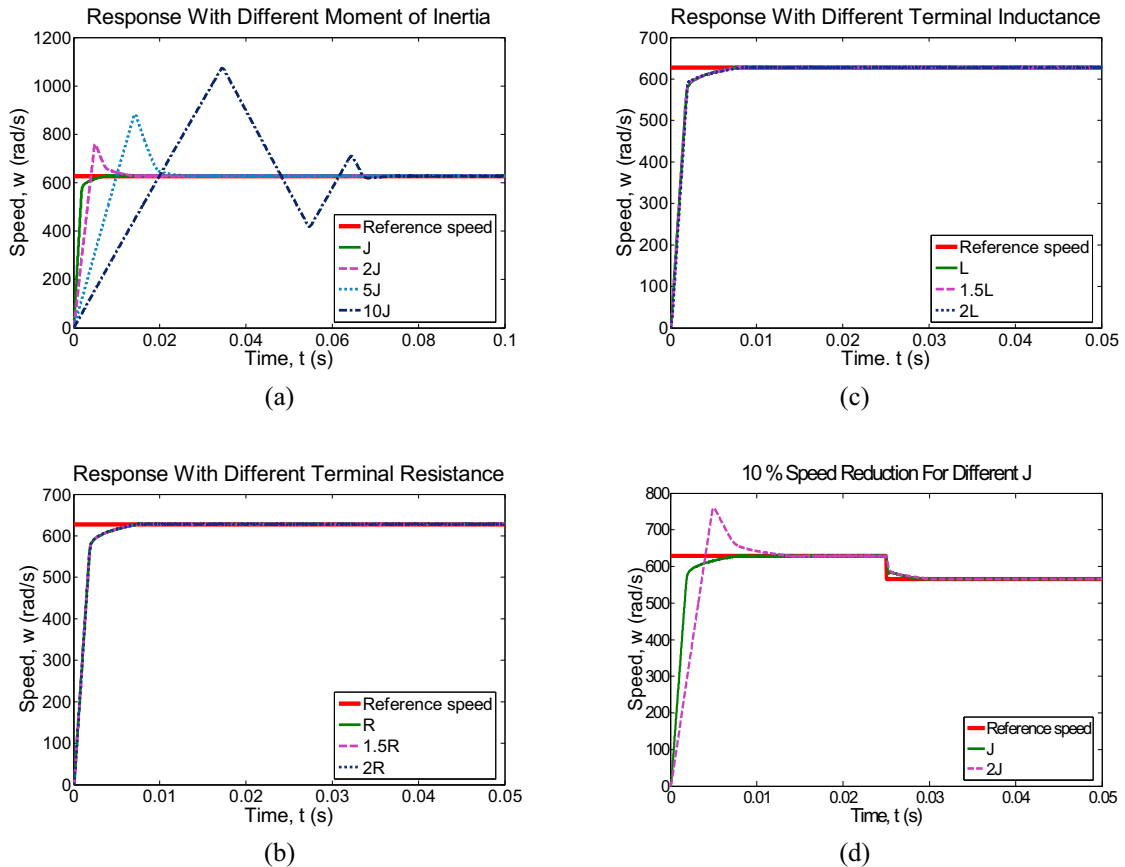


Figure 6. Response of the System Using Fixed I/O Gains FLC

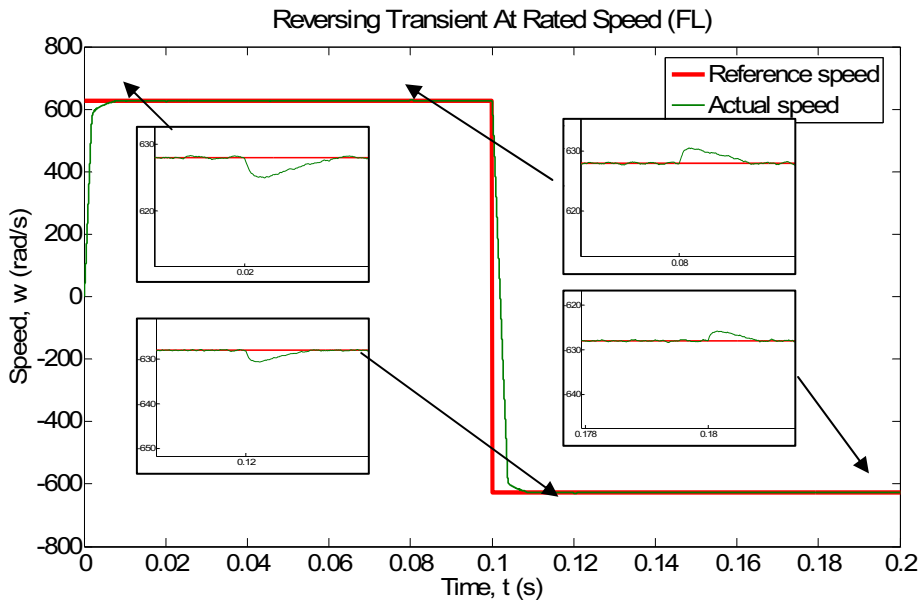


Figure 7. Reversing Transient at Full-load Using Fixed I/O Gains FLC

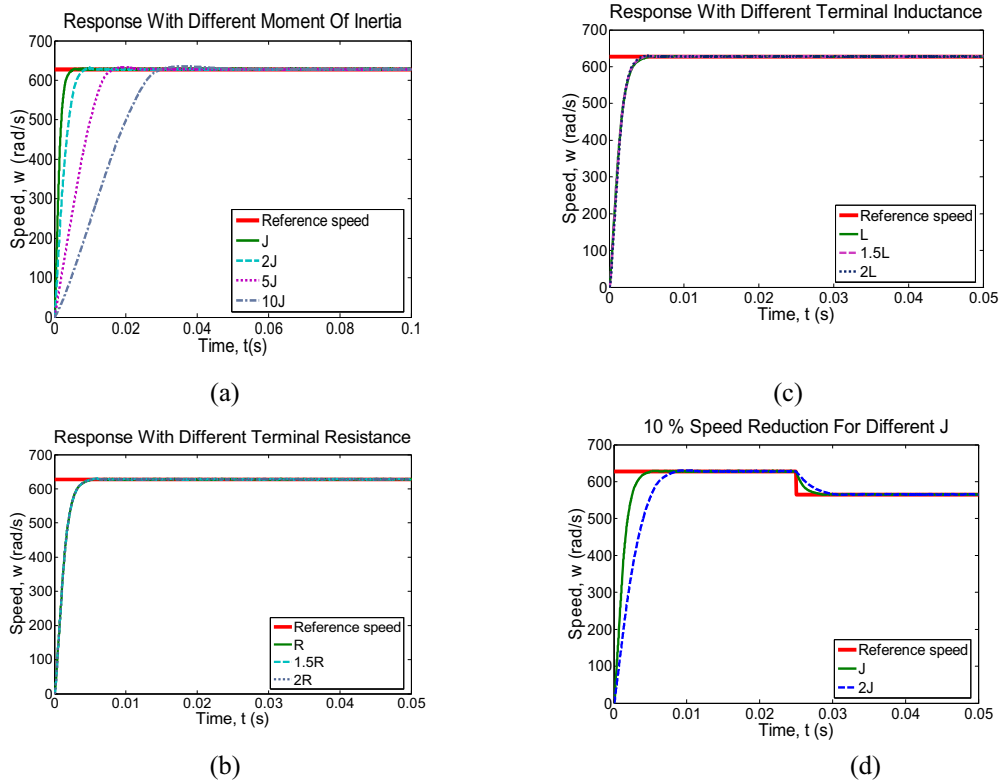


Figure 8. Response of the System Using I/O Gains-Tuning FLC

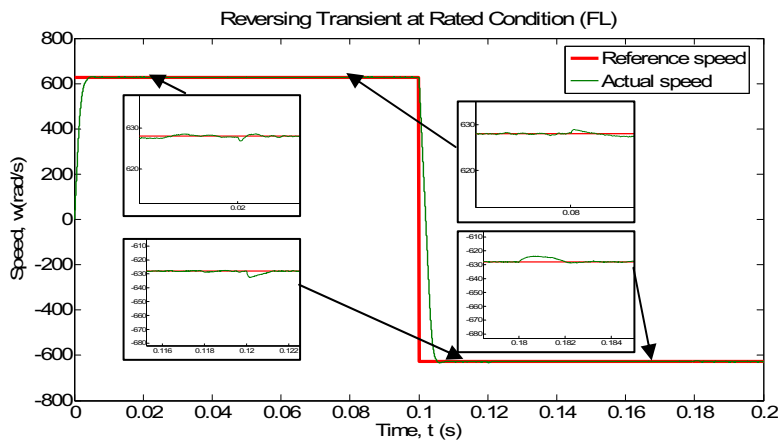


Figure 9. Reverse Transient at Full-load Using I/O Gains FLC

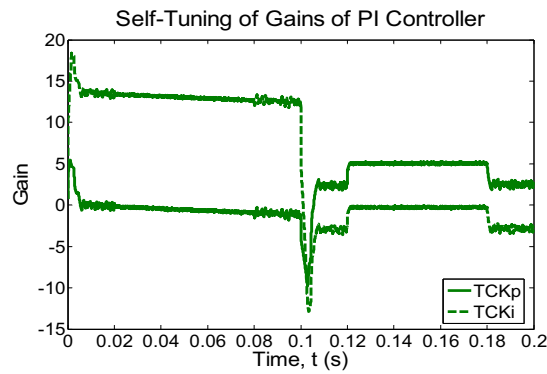


Figure 10. Self-tuning of TCKp and TCKi

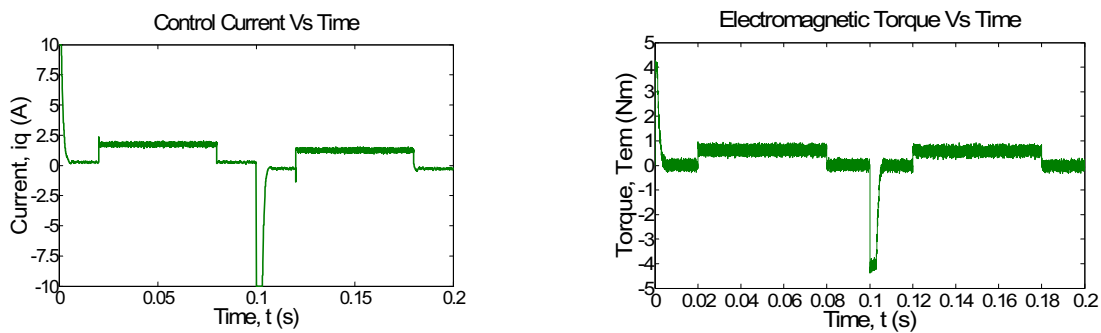


Figure 11. The Current and the Electromagnetic Torque Responses



The Way to Control the Flux in Sulfuric Acid Producing

Rui Cai

Computer And Automation Institute

Tianjin Polytechnic University

Tianjin 300160 China

E-mail:cairui715@126.com

Ping Wang

Computer And Automation Institute

Tianjin Polytechnic University

Tianjin 300160 China

E-mail:wangping@gmail.com

Abstract

A flow ratio control system using is introduced. It is composed of Sensor, Flow meter and Mitsubishi PLC, which is the core of the control system, and some other equipment as an example that Potassium Chloride and Sulfuric acid make Potassium Sulfate to introduce this control system using in the chemical industry. This control system controls the flowing of the Sulfuric acid based on the flowing of Potassium Chloride, satisfying the demanded of the technological requirement. The result of practiced application indicates that this system has high control precision and good Stability.

Keywords: Frequency-varying timing, Flow control, PLC

1. Introduction

In the process of producing, the system of mixing two or more materiel with a certain ratio is called as Proportional Control system. In the chemical industry, the controlling of flux is very important. This text introduced a system of flux Proportional Controlling. After the experiment and practice, the system is proved that it is provided with several merit such as more simple structure, less error of stability and higher precision of controlling.

2. Theory

The Proportional Control systems are composed by open loop Proportional Control systems, single Closed-loop Proportional Control system and double Closed-loop Proportional Control system. It is the most simple that open loop controlling system. The single Closed-loop Proportional Control system is used for conquering the flaw of open loop Proportional Control system. But it also owns its shortage that the main flux is not controlled as a Closed-loop. The system in the text is used the double Closed-loop Proportional Control system.

The first Closed-loop controlling system is the flux Closed-loop controlling system of the Potassium Chloride itself (fig 1). After setting, with the effect of Closed-loop modulation, the system can eliminate the effect of interfere, and make the flux of Potassium Chloride stabile at the number of setting. The main flux Closed-loop controlling system is a constant value one.

The second one is subsidiary flux Sulfuric acid Closed-loop controlling system, which input is the product which equal the flux signal Q_1 of Potassium Chloride multiplied ratio coefficient K_1 . The system is composed by subsidiary controller 1, Sulfuric acid pump inverter, Sulfuric acid pump, survey point 3 and inverter 2. It is a servo system.

3. System designing of flow Proportional Control

3.1 structure

The flux of Potassium Chloride and Sulfuric acid Proportional Control system is composed by Mitsubishi FX_{2NC} PLC, pump which is able to bear to be corrupt, inverter of Siemens MM440, screw of computing and electromagnetic flowmeter. This problem has been studied previously (liao, changchu, 2006) The system is showed as fig2. .

3.1.1 Mitsubishi FX_{2NC} PLC

Mitsubishi FX_{2NC} PLC is provided with higher ratio of performance and volume, and better communication function. It can be fixed in smaller place than normal PLC. Its linker as I/O type may reduce the cost of linking and saving hours. The number of I/O can reach 256. It can link 4 special function modules at most.

3.1.2 Uncorrupted pump

Sulfuric acid is a kind of medium which can corrupt others, so the pump for transportation must use uncorrupted pump. The system use fluoric plastic off-center pump typed IHF 65 50-160, whose inlet diameter is 65mm, whose exit diameter is 50mm, whose impeller normal diameter is 160mm, whose rotate speed is 2900r/min, whose flux is 25m³/h, whose lifting height is 32m and whose motor power is 5.5kw. It use timing of frequency conversion. It should use special frequency conversion for water pump towards the equipment of pump. The motor power of fluoric plastic off-center pump typed IHF 65 50-160 is 5.5kw, which choose special inverter of Siemens MM440 for water pump, which owns A level filter insides.

3.1.3 Inverter of Siemens MM440

The flow velocity of the substance is computed by the output impulse from the motor coder. It may effect the normal work of computing screw. As a result, it is vector controlling inverter of Siemens MM440 that is used in the system whose power supply is 380VAC, whose rating output power is 5.5KW, whose rating output current is 13.2A. In order to make the rotate speed of screw axial stabile and to compute the flow velocity of the substance, it takes the vector controlling with velocity coder. The inverter needs to add impulse coder impulse managing module (coder module for short) and coder.

3.1.4 computing screw

Potassium Chloride is a kind of materiel like powder. The screw of computing is used to transport the powder materiel, to measure at once and to control the flow. Computing screw of LSC type of wanxide company is used in the system.

After potassium Chloride powder comes into the powder storehouse, it goes into screw transportation, and then it moves to output door. The sensor under the output door will transport the weight signal to analog signal input module of PLC. At the same time, coder at the end of non-loading axis measures the number of round and the velocity. It makes the output impulse transported to the high-speed counters part of PLC. After the computing of CPU, the value of flow and accumulation weight of Potassium Chloride. The controlling signal from analog signal output module controls inverter and frequency conversion motor in order to control the flow of Potassium Chloride which is the initiative value of the system. The flow of powder is showed as:

$$Q = K \cdot q \cdot V \quad (1)$$

Where: Q—the flow of the computing screw, kg/s; K—the coefficient of weight; q—linear load of powder in the screw, kg/m; V—the flow velocity of powder in the screw, m/s.

The powder moves along the spiraled track in the screw, so the flow velocity is not easy to be measured. It is usually converted by coder which measures the velocity of motor. The computing screw is showed as fig3.

3.1.5 Electromagnetic flowmeter

Electromagnetic flowmeter is mostly used to measured the volume flow of electric liquid and liquid-solid. The result is independent of the temperature, mucosity, density, pressure and the component of liquid and solid, and also not affected when conductance changes in a larger range. So, after normal water demarcating, the electromagnetic flowmeter which is a real volume flowmeter is used to measure the flow of other electric liquid or liquid-solid. It takes WSDQ type electromagnetic flowmeter made in wanshan automatization instrument Ltd in Guangdong province.

3.2 the design of PLC controlling system

The output signal of weighting Potassium Chloride device and Sulfuric acid electromagnetism flowmeter are both 4~20mA signal which is sent to the current input1 and input2 of analog output module FX2N-4AD. It owns 4 12-bit analog input channels which may current signal (4~20mA) or voltage signal (-10~10V). The conversion velocity is 15ms/channel or 6ms/channel (high speed).

The computing screw and Sulfuric acid pump are with frequency conversion timing system. The controlling signals of the two inverter come from analog output module FX2N-4DA of PLC system. It owns 12 4-bit channels, whose output may current signal (4~20mA) or voltage signal (-10~10V). The conversion velocity equal to the value that four channels 2.1ms take 8 I/O pin. This problem has been studied previously (cai, erfu and chen, shuhui, 2004).

3.2.1 intercalating parameter data memorizer address

The value of intercalating computing screw input which equal to the flow of Potassium Chloride: D1D0, 8-bit BCD code.

The flow ratio coefficient of Potassium Chloride and Sulfuric acid: D3D2/D9D8.

The memorizer address of Potassium Chloride flow in fact: M500, 16-bit binary code.

The memorizer address of Sulfuric acid flow in fact: M501, 16-bit binary code.

The memorizer address of 16-step gain: from the first step to the tenth step: D110~D119,D140~D149.

3.2.2 accommodating inverter

when MM430 inverter is used to control the loadings such as pumps, the starting frequency must be given attention to in order to producing over modulation and shocking. After the sizes of pipelines and pump are confirmed, the flow starting frequency is also confirmed. When the frequency is more than 19Hz, the flow output is not null. So before measuring, the open loop experiment must be taken. The controlling arithmetic is restricted by measured first frequency. In the first frequency, taking open-loop module, the output signal is slope function (linearity gain voltage signal). After the first frequency produces flow, it changes to closed-loop controlling module, which is composed with proportion controlling module and proportion-integral controlling module. At first, the proportion controlling module runs. And then, it turns to the proportion-integral controlling module when the flow is nearly the enactment value in fact. In two modules controlling, the system dispels the large fluctuating of flow, improves the flow following capability, and also dispels the stability error.

3.2.3 PID controlling

The controlling instruction of FX_{2NC} type:

PID	D200	initial value SV, parameter initialization, binary data
	D201	the word of input, the data of flow feedback, binary data
	D500	the parameter of controlling
D500 sample period	T	1~32767ms
D501		action orientation
D502 the constant of input Filtering α		0~99%
D503		proportion gain Kp 1~32767%
D504 integral time Ti (0~32767ms)*100		D505 differential gain Kd 0~100%
D506 differential time Td (0~32767)*100ms		

3.2.4 the modulation of system

- (1) D503 (proportion gain Kp): about 8000(BCD code), the less value of P, the more overshoot, the more times of oscillatory.
- (2) D504 (integral time Ti) according to error data (D50), Ti is measured off by 10 steps, which is transferred automatically when the system runs in order to restrain overshoot and enhance the velocity of response. When the given value becomes bigger abruptly, the biggest overshoot is less 5%.

4. conclusion

The proportion controlling system or proportion-integral controlling system which is gain value and integral time constant are settled parameter, so it is hard to control the following performance and anti-interfere performance and to arrive the aim of restraining over modulation and enhancing the velocity of response. In the system, according to the value of flow closed-loop controlling system error, the proportion coefficient and integral time constant are divided by 10 steps which is automatically transfer appropriately when the system runs. The system owns the capability of restraining overshoot and enhancing the velocity of response. So the system may take better application effect.

References

- Cai, Erfu, & Chen, Shuhui (2004). *The System Designing in Chemical Factory*. Chemical Machine Press.
- Liao, Changchu (2006). *The Programming and Application of PLC of FX*. China Machine Press.

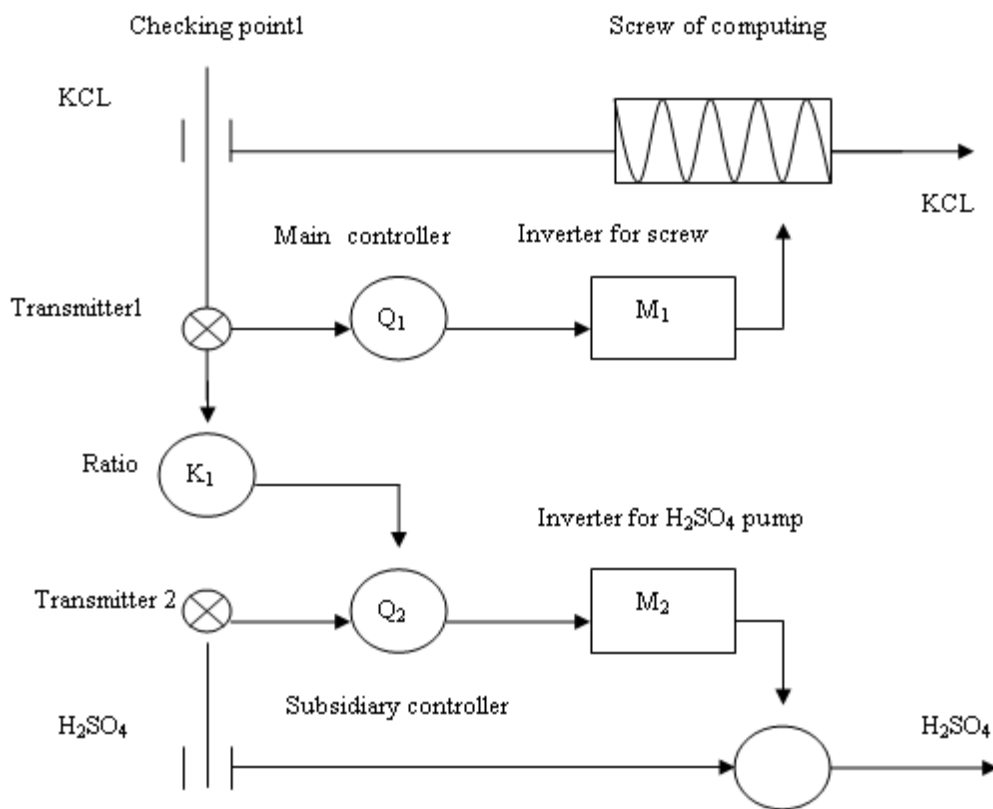


Figure 1. KCL-H₂SO₄ double closed-loop flow Proportional Control system

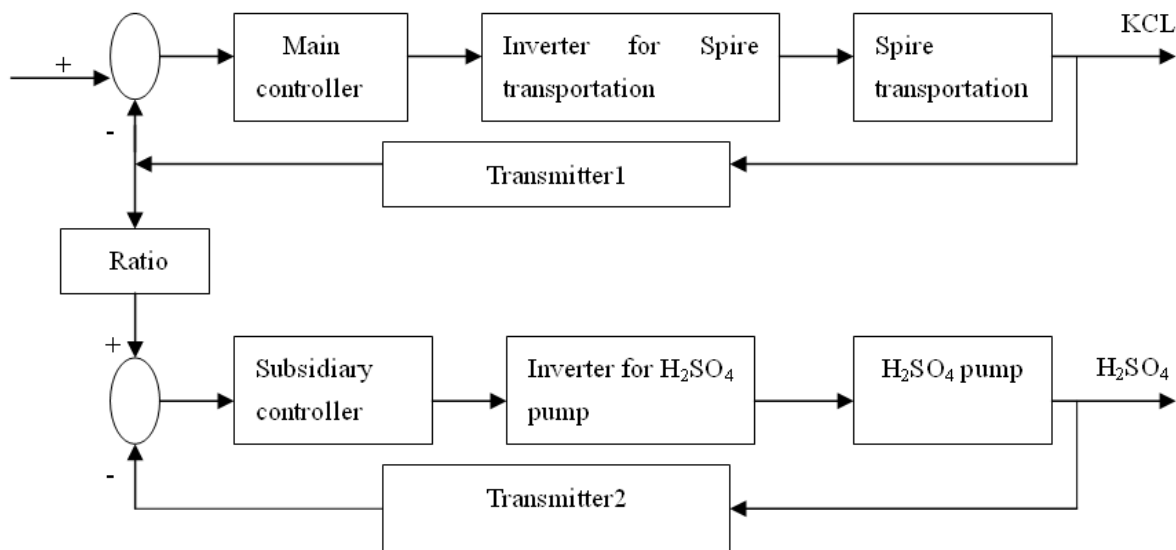


Figure 2. flow Proportional Control system

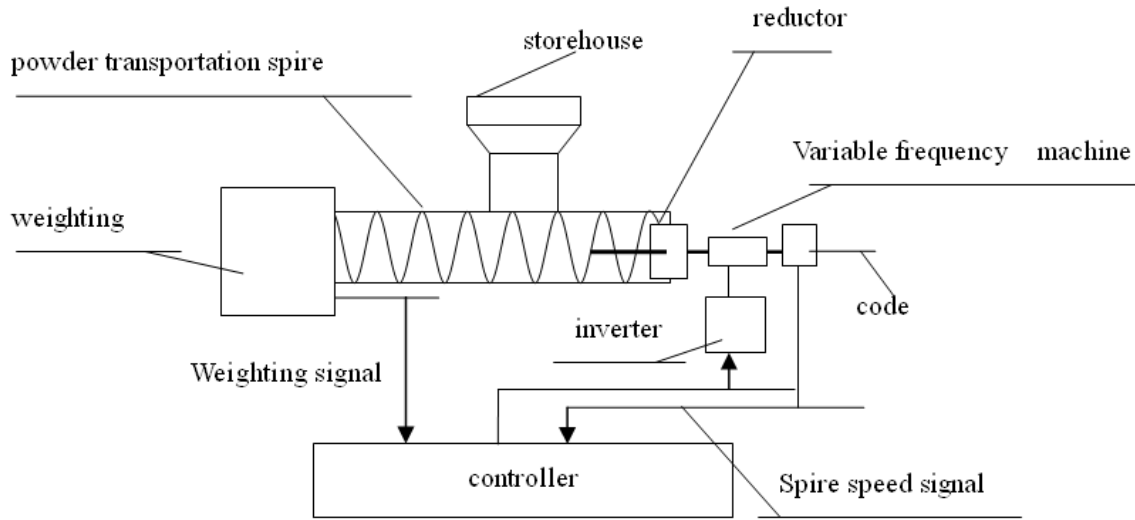


Figure 3. measure spire sketch map



Operation and Combustion Characteristics of a Direct Injection Diesel Engine Fuelled with Esterified Cotton Seed Oil

Murugu Mohan Kumar Kandasamy

School of Mechanical Engineering, SASTRA University

Thanjavur 613402, Tamilnadu, India

E-mail: kmohan2001@rediffmail.com

Sarangan Jeganathan

School of Mechanical Engineering, National Institute of Technology

Trichirappalli 620015, Tamilnadu, India

Rajamohan Ganesan

School of Engineering and Science, Curtin University Technology

Sarawak Campus 98009, Miri, Malaysia

Abstract

Vegetable oils are renewable in nature and can be directly used as fuels in diesel engines. However, their high viscosity and poor volatility lead to reduced thermal efficiency and increased hydrocarbon, carbon monoxide and smoke emissions. Transesterification is one of the methods by which viscosity could be drastically reduced and the fuel could be adopted for use in diesel engine. This Esterified vegetable oil is popularly known as Bio-diesel and that is commercially available in the developed countries due to its distinct advantage over the conventional diesel. In this work, neat cotton seed oil was converted into Bio diesel by the transesterification process and the viscosity was reduced from $21.4 \times 10^{-6} \text{ m}^2/\text{s}$ to $4.8 \times 10^{-6} \text{ m}^2/\text{s}$ (viscosity of the neat Cotton seed oil). A single cylinder water-cooled, direct injection diesel engine developing a power output of 3.7 kW at 1500 rpm was used for the experimental investigations which include combustion, performance and emission characteristics of the engine. Base data was generated for diesel first and subsequently, it was replaced by the Bio diesel and both the results were compared and discussed.

Keywords: Diesel engine, Esterified cotton seed oil, Bio diesel, Esterification, Operation characteristics, Combustion characteristics, Emissions characteristics

1. Introduction

In the modern and fast moving world, petroleum based fuels have become important for a country's development. Products derived from crude oil continue to be the major and critical sources of energy for fuelling vehicles all over the world. However, petroleum reserves are limited and are non renewable. Diesel is mainly consumed in the transport, industrial and agricultural sectors. The cost of transportation affects the economics of all other consumables that reach common people. A country's development is strongly linked to availability of fuels for transportation and power generation. Most of the countries in the world face the major challenge of meeting the high demand of crude oil to meet the growing energy needs. It is therefore, important to have a long-term plan for development of alternative energy sources in a balanced manner by making optimal use of available land and manpower resources. It is important to explore the feasibility of substitution of diesel with an alternative fuel, which can be produced with in the country on a massive scale for commercial utilization. Vegetable oils are considered as good alternatives to diesel as their properties are close to diesel. Thus, they offer the advantage of being to be used in existing diesel engine without any modifications. They have a reasonably high cetane number. The flash point of vegetable oils is high and hence it is safe to use them. Vegetable oils typically have large molecules, with carbon, hydrogen and oxygen being present. They have a structure similar to diesel fuel, but differ in the type of linkage of the chains and have a higher molecular mass and viscosity. The presence of oxygen in vegetable oils raises the stoichiometric fuel air ratio. Contrary to fossil fuels, vegetable oils are free from sulfur and heavy metals. The heating value is slightly lower than diesel. In this

work, the fatty acid methyl esters (Bio diesel) were produced from the neat 'Cotton seed oil' by the Transesterification process. Transesterification of vegetable oils provides a significant reduction in viscosity, thereby enhancing the physical and chemical properties of vegetable oil to improve the engine performance and also the properties of the transesterified oil (Bio diesel) is almost matching with diesel. It has been reported that the methyl and ethyl esters of vegetable oil can result in superior performance than neat vegetable oils. Larry Wagner et al., (1984) studied the effect of soybean oil esters on performance and emissions of a four-cylinder direct injection turbocharged diesel engine. They found that the engine performance with soybean oil esters did not differ to a great extent from that of diesel fuel performance. Clark et al.,(1984) studied the effect of methyl and ethyl esters of soybean oil on engine performance and durability in a direct injection four cylinder diesel engine. They observed that the engine fuelled with soybean esters resulted in a slightly less power combined with an increase in fuel consumption. Emissions were found to be similar to diesel. Nobukazu Takagi and Koichiro Itow (1984) conducted experiments on a single cylinder direct injection diesel engine with rapeseed oil and palm oil as fuels. Ramesh et al.(1989) investigated the performance of a glow plug assisted hot surface ignition engine using methyl ester of rice bran oil as fuel. Normal and nimonic crown pistons were used for their tests. They reported improvement in brake thermal efficiency about 1% when the glow plug is on. The percentage improvement in brake thermal efficiency was more in the case of normal piston compared to nimonic piston. Brake thermal efficiency was higher with nimonic piston at low power outputs than normal piston. They observed reduced ignition delay in both cases with glow plug assistance. No significant changes in hydrocarbon and carbon monoxide emissions with methyl ester of rice bran oil using glow plug ignition were noted. John Einfait and Carroll Goering (1995) used Soy oil methyl ester produced from soybean oil for evaluation as a fuel in a diesel agricultural tractor engine and reported that the engine produced the same power as that with diesel fuel but had higher specific fuel consumption. Perkins and Peterson (1991) conducted a 1000-hour durability test on a compression ignition engine when fueled with methyl ester of winter rapeseed oil. Based upon the evaluation of engine performance, wear and injector deposits as indication of engine durability, they noted that the methyl ester of winter rape oil appeared to be equal to diesel fuel. They also reported that the major disadvantage for the methyl ester of winter rape oil was its cloud and pour points, which eliminate its use in cold weather. Kyle Scholl and Spencer Sorenson (1993) investigated the combustion characteristics of soybean oil methyl ester in a four cylinder naturally aspirated direct injection diesel engine and compared the results with the conventional diesel fuel. Experimental measurements of performance, emissions and rate of heat release were performed as a function of engine load for different fuel injection timings and injection orifice diameters. They found that the overall performance and combustion of soybean methyl ester behaved comparable to diesel fuel.

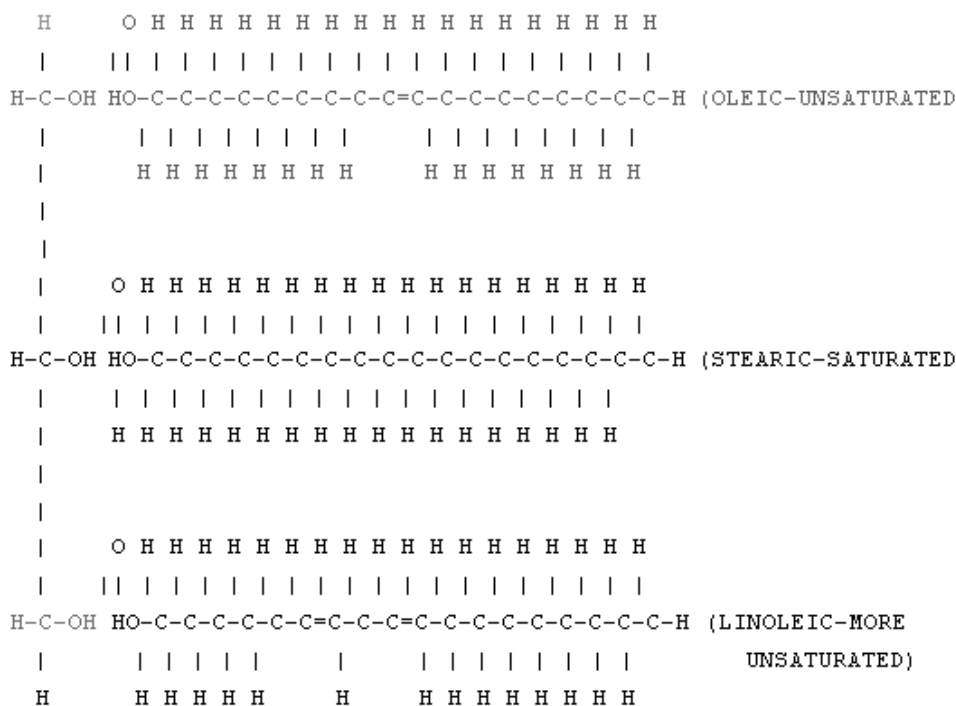
They also found that the methyl ester gave lower HC and smoke emissions than diesel at optimum operating conditions. They observed a longer ignition delay by 2 ° crank angle with the ester than diesel. They also observed that the premixed portion of the combustion process had a lower maximum rate of combustion with the ester as compared to neat diesel. Masjuki and Abdulmuin (1996 a),(1996 b) conducted experiments on a water-cooled direct injection, ISUZU, four-cylinder, four-stroke engine. They reported that palm oil derived fuels result in performance comparable to diesel with improved combustion stability of the engine. They observed that the emission characteristics were good except that CO levels. They suggested that by supplemental intake air preheating, the emissions can be reduced with improved efficiency. Jajoo and Keoti (1997) carried out experiments on a single cylinder diesel engine using rapeseed oil and soybean oil and their methyl esters as fuel and revealed that the engine performance is comparable to that of diesel operation.

Ken Friis Hansen and Michel Grouleff Jensen (1997) conducted several studies on a six cylinder direct injection horizontal turbocharged diesel engine. They used methyl ester of rapeseed oil for their experiments. They found that there was a decrease in hydrocarbon and carbon monoxide emissions but an increase in NO_x and particulate emission. Varaprasad et al. (1997) studied the effect of using Jatropha oil and esterified Jatropha oil on a single cylinder diesel engine. They found that the brake thermal efficiency was higher with esterified Jatropha oil as compared to raw Jatropha oil but inferior to diesel and also reported low NO_x emissions and high smoke levels with neat Jatropha oil as compared to esterified Jatropha oil and diesel. David Chang and Van Gerpen (1998) tested a four cylinder direct injection diesel engine with soybean methyl ester as fuel. They measured the diesel engine particulate emissions with a double dilution tunnel system and they found that the bio diesel fueled diesel engine produced higher fraction of soluble organic material in its exhaust particulate emission. However, hydrocarbon emissions were lowered when the engine was fueled with bio diesel blends. They reported that the soluble organic fraction was increased when the fraction of Biodiesel was increased in the blend. Shaheed and Swain (1999) conducted the experiments on a single cylinder air cooled naturally aspirated direct injection diesel engine using coconut oil and methyl ester of coconut oil and diesel. They reported that the engine performed well on the three fuels except for the initial engine starting problems with coconut oil. Swain and Shaheed (2000) also conducted experiments on a single cylinder direct injection Lister Petter diesel engine with the same oil. They observed that the esters derived from coconut oil have many characteristics similar to diesel fuel with little performance and emission differences. They concluded that the fuel derived from the

coconut oil is a potential alternative for operating a standard diesel engine without any engine modifications. Abdul Moneyem and Van Gerpen (2001) conducted experiments to characterize the effect of oxidized Bio diesel on engine performance and emissions. They used methyl soyate (Bio diesel) for testing a turbocharged direct injection diesel engine. They found that the performance of neat Bio diesel and it's blend with diesel were similar to neat diesel fuel operation. They also found a significant reduction in Bosch smoke number with neat Bio diesel and it's blend when compared with diesel.

Recep Altin et al. (2001) conducted experiments on a single cylinder direct injection diesel engine to evaluate the performance and exhaust emissions using refined sunflower oil, cottonseed oil, soybean oil and their methyl esters. They found little power loss, higher particulate emissions and less NO_x emissions with neat vegetable oils. Kalligeros et al.(2003) conducted experiments on a single cylinder indirect injection Petter diesel engine using olive oil and sunflower oil as fuels in different proportions with marine diesel. They reported lower unburned hydrocarbon, carbon monoxide, particulate and nitrogen oxide emissions with blends than neat vegetable oils.

The ideal diesel fuel is a saturated and non- branched hydrocarbon molecule with carbon number of 14, where as vegetable oil molecules (as shown below) are Triglycerides generally with non branched chains of different lengths and different degrees of saturation with the carbon number of 18 to 57 and it depends on the type of vegetable oils. The vegetable oil contains a substantial amount of oxygen in their structure and so it is naturally oxygenated.



Structure of Vegetable Oil Molecules

2. Production of Bio diesel

2.1 Steps followed for the production of Bio diesel:

- Solvent was prepared by dissolving the calculated amount of NaOH (catalyst) with calculated amount of Methanol for 1 lit. of cotton seed oil
- Measured amount of raw cotton seed oil was taken in the three way conical flask and heated up to 60°C to 65°C
- The prepared solution was added to the heated oil.
- The mixture was continuously stirred throughout the process and was maintained at constant temperature.
- This process was carried out for two hours.
- The conical flask was left for natural cooling for eight hours
- The Glycerin settled at the bottom of the flask and it was separated using the separating funnel.
- The remaining in the flask was the **Ester of cotton seed oil (Bio diesel)**

Fig.1 shows the schematic diagram of the setup for Transesterification process, fig.2 shows the photograph of Bio diesel comparing with the neat cotton seed oil and diesel and the fig.3 shows the photograph of Glycerin that was settled at the bottom of the flask during the process of transesterification. Table 1 show the comparison of some of the important properties of Bio diesel which was produced with neat cotton seed oil and with diesel. It is found that the properties are closely matching with 'United states-ASTM standard' and also with 'German Bio diesel standard'.

Table 1.

Properties	Neat cotton Seed oil	Bio diesel	Diesel	US ASTM *	DIN **
				Specification	specification
Gross calorific value (kJ/kg)	39,982	40,207	43,500	36,000 to 42,000	38,000 to 41,000
Flash Point (°C)	260	120	46	100 to 130	100 to 120
Kinematic viscosity at 50°C (× 10 ⁶ m ² /s)	21.4	4.8	7	1.9 to 6.5	3.5 to 5
Relative density at 27°C (g/cc)	0.9146	0.8813	0.86	0.8 to 0.88	0.8 to 0.85
Sediments (Toluene Insoluble) (%)	0.003	0.005	0.05	0.05 max	-
Sulphur (%w/w)	0.38	0.00	0.25	0.05 max	0.01 max
Cetane Number	35	54.5	45	40 min	49 min
Ash (%w/w)	0.01	0.01	0.01	0.02 max	-

* German Bio diesel standard;

** United States Bio diesel ASTM standard

3. Experimental setup

An experimental set up was made with necessary instruments to evaluate the performance, emission and combustion parameters of the compression ignition engine at different operating conditions. The overall view of the experimental setup is shown in figs.4 & 5 and the specifications of the engine are as given below:

Make	: COMET
No. of Cylinder	: one
Orientation	: vertical
Cycle	: 4 strokes
Ignition System	: compression Ignition
Bore and stroke	: 80 mm × 110 mm
Displacement volume	: 553 cc
Compression ratio	: 18:1
Arrangement of valves	: overhead
Combustion Chamber	: hemi spherical open Chamber (Direct Injection)
Rated power	: 3.5 kW @ 1500 rpm
Cooling Medium	: water cooled

A provision was made to mount a piezoelectric pressure transducer flush with the cylinder head surface in order to measure the cylinder pressure. Fig.6 indicates the view of pressure transducer mounted flush with the cylinder head and data acquisition system. A piezoelectric type pressure sensor was fitted on Diesel injection line to determine the actual start of injection indicated by the needle lift of the injection nozzle and it is shown in fig.7. The engine was coupled to an eddy current dynamometer and a strain gauge based load cell sensor is mounted on the dynamometer to measure the load. This sensor is connected to load transmitter. A Rotary encoder which is an optical sensor was used for speed and crank-angle measurement and it is indicated in fig.8. It will give a voltage pulse exactly when the TDC position was reached. The voltage signals from the optical sensor were fed to an Analog to Digital converter and then to the data acquisition system along with pressure signals for recording.

One Differential pressure transmitter fitted to fuel measuring unit was used for fuel flow and another Differential pressure transmitter was used as air flow transmitter and it senses the differential pressure across the orifice plate. Rota

meters were used for measuring the water flow rate to engine and calorimeter. Temperature sensors were used for measurement of engine and calorimeter water temperatures and they are indicated in fig.9. Thermocouple type temperature sensors were used for measurement of the exhaust gas temperatures.

All the exhaust emission measurements including the smoke were made with the help of an engine exhaust gas analyzer. The probe of the analyzer was fitted in the engine exhaust pipe and all the parameters were measured at different loads in on line mode.

4. Results and discussions

The performance, combustion and emissions characteristics of the engine under variable load conditions have been observed for Bio diesel and compared with diesel.

4.1 Performance Parameters

The variation of **brake thermal efficiency** with power output for Bio diesel and diesel are shown in fig.10. The thermal efficiency is always lower with Bio diesel as compared with diesel. The maximum thermal efficiency of the bio diesel is about 30 % where as it is 32% with diesel at full load. This is due to high density of the Bio diesel (0.8813g/cc) as compared to diesel (0.86g/cc) and affects the mixture formation. This leads to slow combustion and thus the lesser thermal efficiency with Bio diesel. No drop in maximum power is observed with Bio diesel. The variation of **volumetric efficiency** with Bio diesel and diesel are shown in fig.11. The volumetric efficiency with Bio diesel is lower than diesel. It may be noted that the volumetric efficiency curve is closely related to the exhaust temperature curves shown in fig.12.

A higher exhaust temperature leads to a lower volumetric efficiency. This is because the temperature of the retained exhaust gases will be higher when the exhaust gas temperature rises. A high-retained exhaust gas temperature will heat the incoming fresh air and lower the volumetric efficiency. The fig.12 shows the **exhaust gas temperature** and it is more for Bio diesel than diesel particularly at high loads. More dominant diffusion combustion phase is the reason for more exhaust gas temperature for Bio diesel. The maximum temperature of exhaust gas at full load is 430 ° C with the Bio diesel and is 410 ° C with diesel.

4.2 Combustion parameters

The variation of **delay period** is shown in fig.13 and it was calculated based on the dynamic injection timing measured with piezoelectric transducer. The delay period is lower for Bio diesel as compared to diesel. At full load, the delay period for Bio diesel is 5°24' of crank angle and for diesel, it is 5°54' of crank angle from the start of injection. The lower delay period has a higher Cetane rating and is more acceptable as diesel. Better atomization of the fuel droplet leads to minimizing the time for start of combustion and hence there is a reduction in the delay period for Bio diesel. Better atomization of the Bio diesel is possible only by the reduction of viscosity drastically by the Transesterification process. The variation of **peak pressure** is shown in fig.14. The Peak Pressure depends on the amount of fuel taking part in the uncontrolled combustion phase that is governed by the delay period and the spray envelope of the injected fuel. Since the delay period for Bio diesel is lesser than diesel, the fuel taking part in the uncontrolled combustion phase is less and hence the peak pressure is lesser than the diesel for all the load of operations. The peak pressure with Bio diesel is 74 bar and with diesel it is 81 bar at full load.

The **rate of pressure rise** is shown in fig.15 and it is due to the domination effects of the premixed phase of combustion. For the Bio diesel, this effect is less and so the rate of pressure rise is slightly lower than diesel. For Bio diesel, it is 3.6 bar /°CA and for diesel, it is 3.9 bar / ° CA at full load. The **duration of Injection** is shown in fig.16 and there is no considerable change in the duration of Injection with Bio diesel as compared to diesel.

It is 36°24' with Bio diesel and 36° with diesel at full load. The variation is only within 1° to 2° of crank angle. Similarly there is no considerable change in the dynamic injection timing for both the fuels. The **combustion duration** shown in fig.17 was calculated based on the duration between the start of combustion and 90% cumulative heat release. It is seen that the combustion duration is increased with rise in power output with diesel and as well as with Bio diesel due to increase in the quantity of fuel injected. Higher combustion duration is observed with Bio diesel than diesel due to the longer diffusion combustion phase.

4.3 Emission Parameters

The variation of **smoke emission** with power output with Bio diesel and diesel is shown in fig.18. It is less with Bio diesel as compared to diesel. Smoke number is 3.9 for Bio diesel and 4.2 for diesel at full load. Generally the cause for smoke in diesel is due to the presence of heavy petroleum oil residues in it. In the case of Bio diesel, there is no presence of such residues and that resulting in less smoke with Bio diesel. The % of variation in the **carbon monoxide emission** with Bio diesel and diesel is shown in fig.19. It is less with Bio diesel at lower load when compare to diesel, because, the Bio diesel is oxygenated in the molecular structure and that helps in complete combustion to carbon dioxide rather than leading to the formation of Carbon monoxide at lower loads. However CO emission is more at

higher loads for the Bio diesel. It is because of more carbon present in the Bio diesel (18 number of Carbon in one molecule), the oxygen supplied is insufficient even though the oxygen available in the fuel is compensated. This leads to the suffocation and ends up with incomplete combustion. The carbon monoxide emission is 0.15% at lower load and 0.6% at higher loads for Bio diesel. For diesel, it is 0.17% at lower load and 0.4% at higher loads. The variation in the **Hydro carbon emissions** with Bio diesel and with diesel is shown in fig.20. It is found that these emissions are more with Bio diesel as compared to diesel. More quantity of injected fuel and lesser availability of air is the reason for more hydrocarbon emissions. The variation in the **Nitric oxide emission** with Bio diesel and with diesel is shown in the fig.21. It is found to be lower with Bio diesel as compared to diesel at lower loads. At lower loads, it is 84 ppm for Bio diesel and 104 ppm for diesel. This reduction in NO emission is mainly associated with the reduced premixed burning rate following the delay period at lower loads. It may also be noted that the rate of heat release (during the premixed burning phase) and the calculated cylinder gas temperature are lesser at lower loads with Bio diesel as compared to diesel. However at higher loads, there is an increase in the combustion temperature and that leads to more NO emission with Bio diesel as compared to diesel. The variation in the **particulate emissions** with Bio diesel and diesel are shown in fig.22. Particulate emissions are greatly increased in all cases with load. Trends are similar to that of smoke. The particulate emission is found to be more with Bio diesel compared to diesel. The main cause of particulate emission is known to be inadequate mixing of the fuel and air at high loads. Over rich fuel air mixtures in the localized regions of the combustion chamber will lead to particulate emissions. The variation in the **heat release rate** with Bio diesel and with diesel is shown in the fig.23. It is seen that the premixed burning phase, which is associated with a high heat release rate, is most significant with diesel. This is the reason for the thermal efficiency being highest with diesel. The diffusion-burning phase indicated under the second peak is greater for Bio diesel compared to diesel. This is consistent with the expected effects of reduction of air entrainment and fuel air mixing rates. This leads to less fuel being prepared for rapid combustion with Bio diesel after the delay period. Therefore, more burning occurs in the diffusion phase rather than in the premixed phase with Bio diesel. The significantly higher combustion rates during the later stages with Bio diesel leads to high exhaust temperatures and lower thermal efficiency.

5. Conclusions

This work was aimed to evaluate the suitability of Bio diesel as an alternative fuel in a diesel engine by studying the performance, combustion and emission characteristics of the engine. Initially the experiment was conducted at a constant speed of 1500 rev/min under variable load conditions with diesel. In the next phase, the engine was operated with Bio diesel (ester of cotton seed oil). Experiments were conducted at 0%, 25%, 50%, 75% and 100% of the rated load. Based on the results the following conclusions are made.

- Bio diesel leads to better performance with reduced emissions as compared to diesel.
- For Bio diesel, the brake thermal efficiency is inferior to diesel. The maximum brake thermal efficiency of the bio diesel is about 30 % where as it is 32% with diesel at full load.
- Exhaust gas temperature is more for Bio diesel than diesel particularly at high loads.
- The delay period is lower for Bio diesel as compared to diesel.
- The peak pressure is lesser with Bio diesel as compared to diesel for the entire loads of operations.
- Smoke intensity is greatly increased with loads for Bio diesel and as well as for diesel, but however it is lesser with Bio diesel as compared to diesel.
- The carbon monoxide emission is lesser with Bio diesel at lower loads as compared to diesel. However it is more at higher loads.
- The conclusions clearly indicates that the Bio diesel derived from the cotton seed oil can be very well used as an alternative fuel in a diesel engine without any engine modifications.

References

- Abdul Monyem., Jon, H and Van Gerpen. (2001) 'The effect of Biodiesel oxidation on Engine Performance and Emissions', *International Journal of Biomass and Bio Energy*, No.20, pp. 317-325.
- Clark, S.J., Wagner, L., Schorck, M.D. and Piennaar, P.G. (1984) 'Methyl and Ethyl Soybean Esters as Renewable Fuels for Diesel Engines', *Journal of American Oil Chemist Society*, Vol. 61, No.10, pp.1632-1638 .
- David y. Chang and Jon H. Van Gerpen. (1998) 'Determination of Particulate and Hydrocarbon Emissions from Diesel Engines Fueled with Bio diesel', *Society of Automotive Engineers*, Paper No. 982527.
- John Einfalt and Carroll E. Goering (1995) 'Methyl Soyate as a fuel in a Diesel Tractor' *Transactions of American society of automotive engineers*, Vol.85, pp. 70-74.
- Jajoo,B.N and Keoti, R.S. (1997) 'Evaluation of Vegetable Oil as Supplementary fuels for Diesel Engines', *Proceedings of the XV National Conference on I.C. Engines and Combustion*, Anna University, Chennai, Tamil Nadu state, India.

Kyle W Scholl, and Spencer C Sorenson (1993) 'Combustion Analysis of Soybean Oil Methyl Ester in a Direct Injection Diesel Engine', *Society of Automotive engineers*, Paper No. 930934.

Ken Friis Hansen and Michael Grouleff Jensen (1997) 'Chemical and Biological Characteristics of Exhaust Emissions from a DI Diesel Engine Fuelled with Rapeseed Oil Methyl Ester (RME)', *Society of Automotive Engineers*, Paper No. 971689.

Kaligeros, S., Zannikos, F., Stournas, S., Lois, E., Anastopoulod, G., Teas Ch and Sakellaropoulos, F. (2003) 'An Investigation of Using Bio diesel/Marine Diesel blends on the Performance of a Stationary Diesel Engine', *Journal of Biomass and Bio energy*, No.24, pp. 141-149.

Larry E. Wagner., Stanley J. Clark and Mark D. Schrock (1984) 'Effect of Soybean Oil Esters on the Performance, Lubrication Oil and Water of Diesel Engines', *Society of Automotive engineers*, Paper No. 841385.

Masjuki, H., Abdulmuin, M.Z. and Sii, H.S. (1996 a) 'Indirect Injection Diesel Engine Operation on Palm Oil Methyl Esters and Its Emulsions', *Proceedings of Institute of Mechanical Engineers*, No. 211, pp.291 – 299.

Masjuki, H., Abdulmuin M.Z and Sii, H.S. (1996 b) 'Investigation on Preheated Palm Oil Methyl Esters in the Diesel Engine', *Proceedings of Institute of Mechanical Engineers*, No.210, pp.131 – 138.

Nobukazu Takagi, and Koichiro Itow (1984) 'Low Carbon Flower Buildup Low Smoke and Efficient Diesel Operation with Vegetable Oils by Conversion to Monoesters and Blending with Diesel Oil or alcohols', *Society of automotive engineers*, Paper No.841161.

Perkins, L.A. and Peterson, C.L. (1991) 'Durability Testing of Transesterified Winter Rape Oil (*Brassica Napus*) as fuel in Small Bore, Multi Cylinder, DI, CI engine', *Society of Automotive engineers*, Paper No. 911764.

Ramesh, A., Nagalingam, B. and Goparakrishnan, K.V. (1989) 'Performance of Glow Plug Surface Ignition Engine with Methyl ester of Rice Bran Oil as Fuel', *Proceedings of XI National Conference on I.C. Engines and Combustion*, Indian Institute of Technology Madras, Tamil Nadu state, India.

Recep Altin., Selim Cetinkaya and Huseyin Serdas Yucesu. (2001) 'The Potential of Using Vegetable oil Fuels as Fuel for Diesel Engines', *International Journal of Energy Conversion management*, No.42, pp.529 – 538.

Shaheed, A and Swain, E. (1999) 'Combustion Analysis of Coconut Oil and Its Methyl Esters in a Diesel Engine', *Proceedings of Institute of Mechanical Engineers*, Vol 213, Part A, pp. 417-425.

Swain, E and Shaheed, A. (2000) 'An Experimental Study to Evaluate the Use of Coconut Based Fuels as Alternatives to Diesel Oil', *Journal of the Institute of Energy*, No.73, pp. 100-105.

Varaprasad, C.M., Muralikrishna, M.V.S and Prabhakar reddy, C. (1997) 'Investigations on Bio diesel (Esterified *Jatropha Curcus* Oil) in Diesel Engines' *XV National Conference on I.C. Engines and Combustion*, Anna University, Chennai, Tamil Nadu, India.

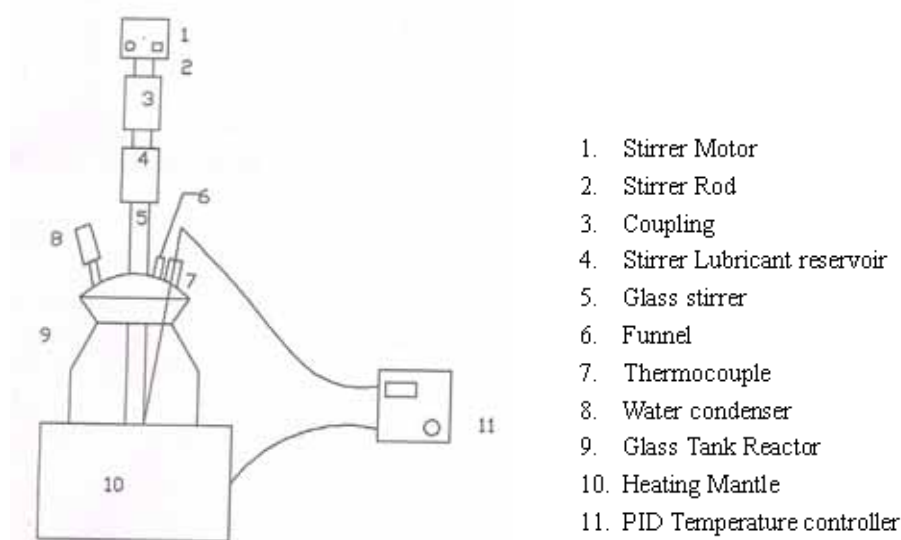


Figure 1. Setup for Transesterification

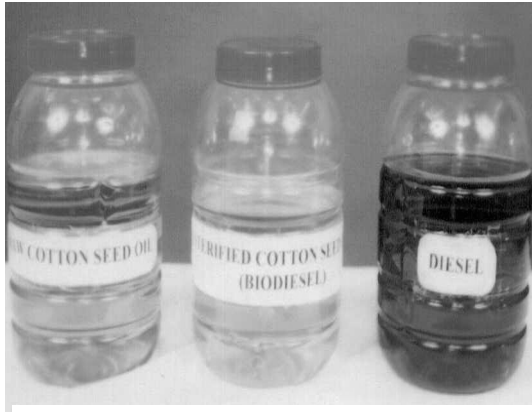


Figure 2. Neat Cotton Seed Oil, Bio Diesel & Diesel (comparison)

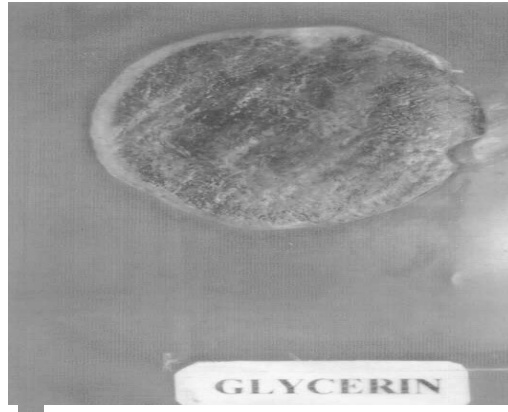


Figure 3. Glycerin (By product)



Figure 4 & 5. Overall View of the Experimental Setup



Figure 6. Pressure Transducer



Figure 7. Injection Sensor

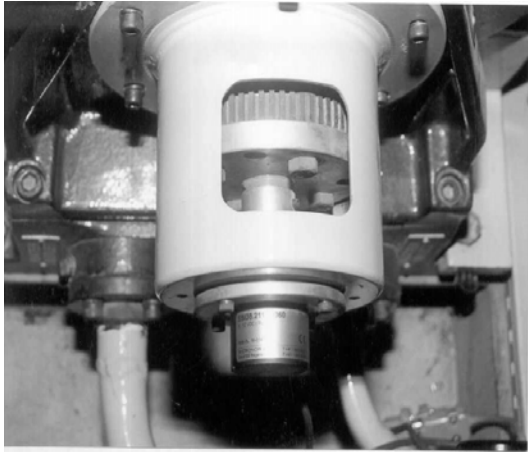


Figure 8. Rotary Encoder (Optical sensor)

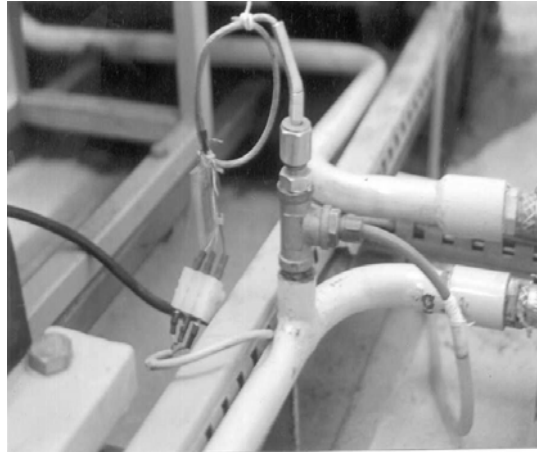


Figure 9. Temperature Sensor for Coolant Water Temperature

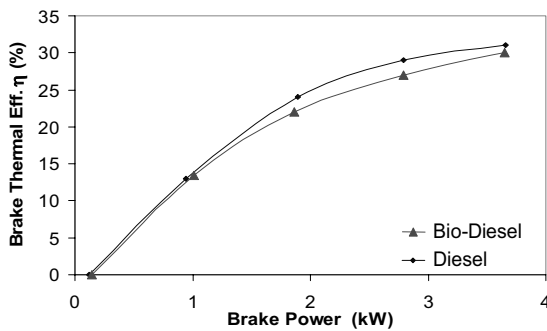


Fig. 10 Brake Power Vs Break Thermal Eff.

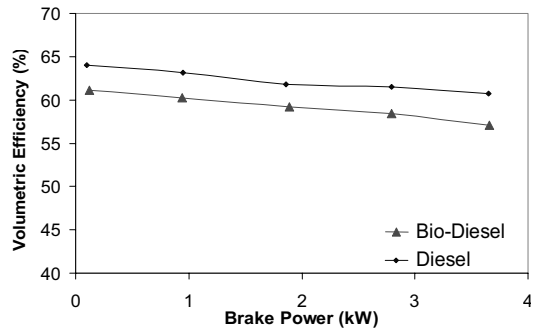


Fig. 11 Brake Power Vs Volumetric Efficiency

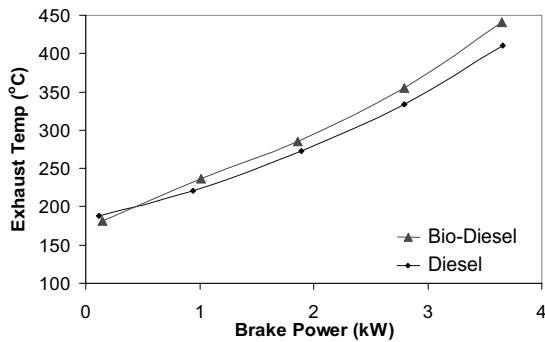


Fig. 12 Brake Power Vs Exhaust Temp

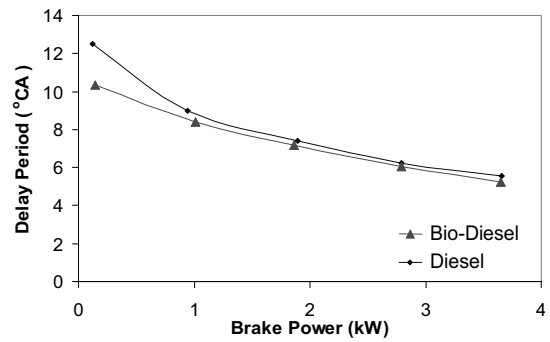


Fig. 13 Brake Power Vs Delay Period

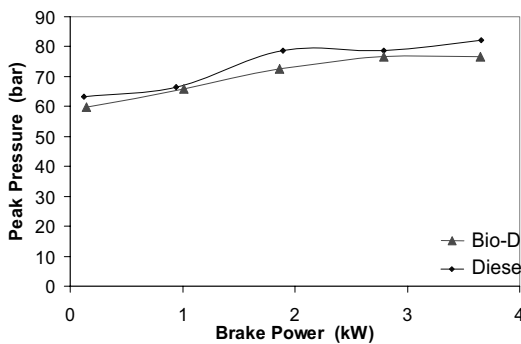


Fig. 14 Brake Power vs Peak Pressure

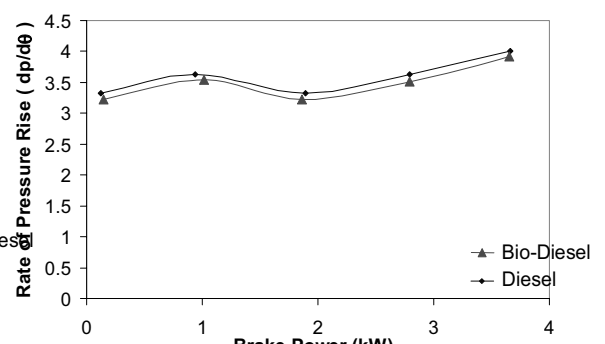


Fig. 15 Brake Power vs Rate of Pressure Rise

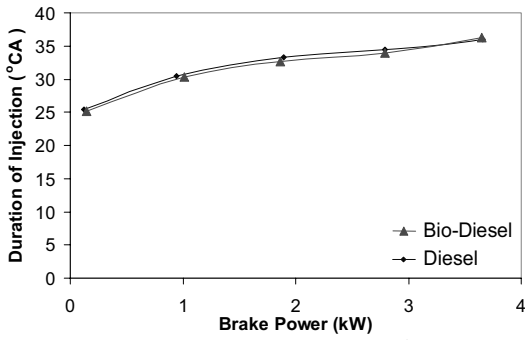


Fig. 16 Brake Power Vs Duration of injection

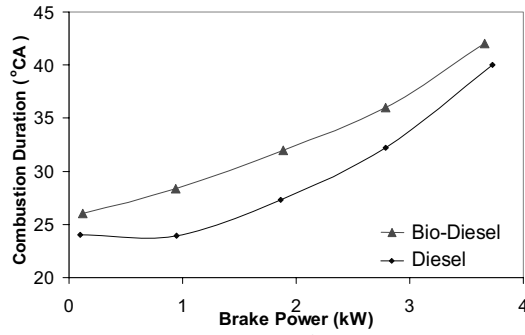


Fig. 17 Brake Power Vs Combustion Duration

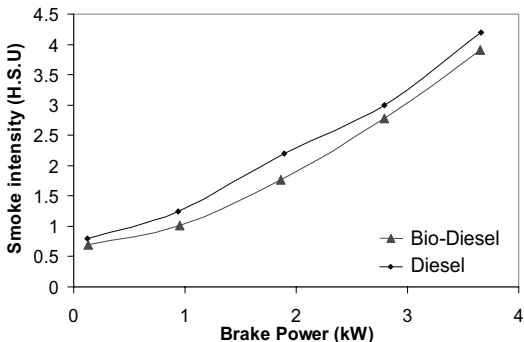


Fig. 18 Brake Power Vs Smoke

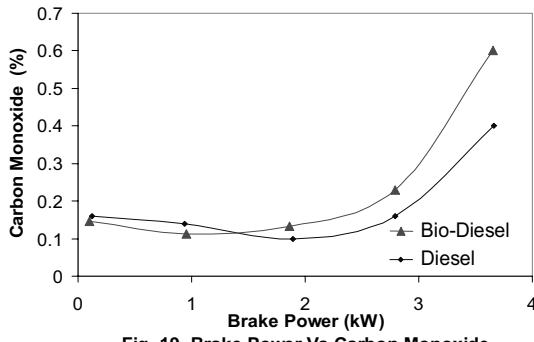


Fig. 19 Brake Power Vs Carbon Monoxide

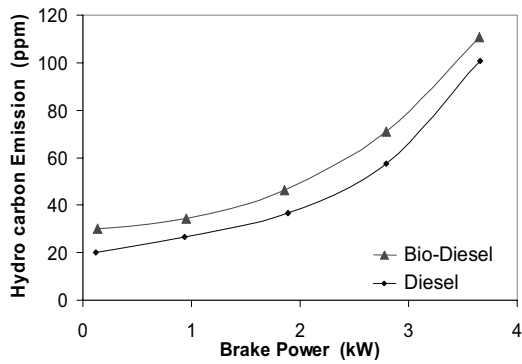


Fig. 20 Brake Power Vs Hydro carbon Emission

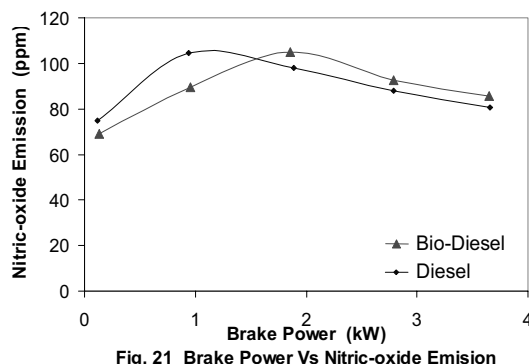


Fig. 21 Brake Power Vs Nitric-oxide Emission

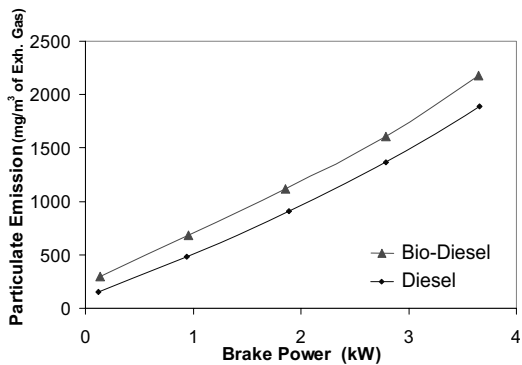


Fig. 22 Brake Power Vs Particulate Emission

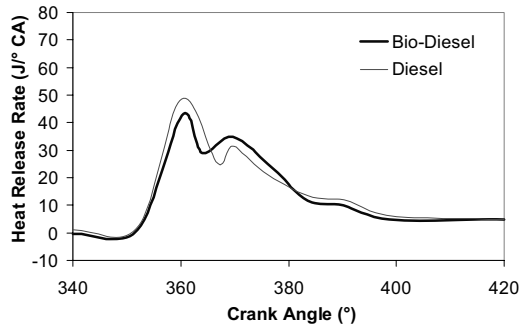


Fig. 23 Crank Angle Vs Heat Release Rate



Study on the Duality between MFP and ACP

Xiaojun Lei

Department of Mathematics

Tongren University

Tongren 554300, China

Tel: 86-856-523-0984 E-mail: xjleitry@163.com

Zhian Liang

Department of Statistics

Shanghai Financial and Economics University

Shanghai 200433, China

Tel: 86-21-6591-3351 E-mail: Zhian L@163.com

Abstract

Under the generalized weak convexity of (F, α, ρ, d) , we studied the results of several sorts of duality type about the problem of multi-objective fractional programming (MFP), extended this results to the generalized arcwise connected hypothesis, established the optimized problem of arcwise connected area (ACP) and the optimal sufficient condition of $\min_{x \in S} f(x) \quad s.t. \quad g(x) \leq 0$ under constraint condition, and gave the duality model, and obtained the conclusions of weak duality and strong duality.

Keywords: Arcwise connected function, Generalized convexity, Weak (strong) duality, Strong Quasi-arc, Optimal solution

1. Introduction

One of important extensions about convexity was the concept of invariant convexity put forward by Hanson in 1981, after that, in twenties years, thirty sorts of generalized convexity functions are introduced, which makes the research contents of the optimized problems become very deep and abundant. The extrusive problem in these problems is the duality problem under the weak convexity concept. In the optimization theory, for an appointed mathematic programming problem, there are many types of duality, and two famous dualities are Wolfe duality (Wolfe, 1961, p.239-244) and Mond-Weir duality (Mond, 1981, p.263-28), and in recent years, the mixed duality has been thought as the type of various optimized problems, and the mixed duality (Aghezzaf, 2000, p.91-101, Aghezzah, 2001, p.617-628, Zi, 1993, p.113-118, Liang, 2001, p.446-461, Mond, 1982, p.105-124, Mukherjee, 2000, p.571-586, Preda, 1992, p.365-377, Xu, 1996, p.621-635, Yang, 2000, p.999-1005, Zhang, 1997, p.29-44).

Generally, when we solute an optimized problem, the feasible area is usually in the area with interior points, but in practical problems, it always doesn't possess this condition, for example, the feasible area of the problem is the following line-type figure without interior point which is seen Figure 1. Its feasible area is connected by curve S. So when we define the function in this feasible area, we can not consider its partial derivative or directional derivative, and the grads of the function. For these problems, in early 1970, Ortega and Rheinboldt (Ortega, 1970) put forward the concept of regional arcwise connection, after that, Avriel and Zang (Avriel, 1980, p.407-435) extended it as various generalized convexities. The arcwise connected function and various generalized functions possess very good local-global extremum property, and in this article, we mainly introduce the duality problem result under the generalized weak convexity of (F, α, ρ, d) introduced by Liang. Z. A, Huang. H. Z. and Purdulos. P. M (Liang, 2003, p.447-471), and extend it into the weak duality and strong duality of generalized arcwise connected function optimized problem (ACP), and give some results.

2. Basic conclusions of MFP duality under generalized weak convexity of (F, α, ρ, d)

Here, we will give the conclusions of several duality problems about MFP.

Supposed

$$(MFP) \quad \min \frac{f(x)}{g(x)} \Delta \left(\frac{f_1(x)}{g_1(x)}, \frac{f_2(x)}{g_2(x)}, \dots, \frac{f_p(x)}{g_p(x)} \right)^T \quad (1-1)$$

$$s.t \quad h(x) \leq 0, \quad x \in X.$$

When $X \subset R^n$ is an open set, $f_i, g_i (i=1,2,\dots,p)$ is the real valued function on X, and h is m dimensional vector value function defined on X, and $M = \{1,2,\dots,m\}$ and $M_0, M_1 \dots M_q$ is a

partition of M, i.e. $\bigcup_{k=0}^q M_k = M, M_k \cap M_l = \emptyset$, when $k \neq l$, so the generalized Mond-Weir duality of MEP is

$$\begin{aligned} \text{Max } & \frac{f(u)}{g(u)} + \lambda_{M_0}^T h_{M_0}(u) e \Delta \left(\frac{f_1(u)}{g_1(u)} + \lambda_{M_0}^T h_{M_0}(u) + \dots + \frac{f_p(u)}{g_p(u)} + \lambda_{M_0}^T h_{M_0}(u) \right)^T \quad (1\text{---}2) \\ \text{s.t. } & \sum_{i=1}^q \tau_i \nabla \frac{f_i(u)}{g_i(u)} + \sum_{j=1}^m \lambda_j \nabla h_j(u) = 0 \\ & \lambda_{M_k}^T h_{M_k}(u) \geq 0, \quad k = 1,2,\dots,q \\ & \tau = (\tau_1, \tau_2, \dots, \tau_p)^T \in R_+^p, \tau > 0, \sum_{i=1}^p \tau_i = 1 \\ & \lambda_{M_k} \in R_+^{|M_k|} \quad k = 0,1,2,\dots,q \quad u \in X \end{aligned}$$

Where, $e = (1,1,\dots,1)^T$ and λ_{M_k} represent column vectors, and their component subscripts belong to M_k .

2.1 Mond-weir duality

$$\begin{aligned} \text{(MFD1) Max } & \frac{f(u)}{g(u)} = \left(\frac{f_1(u)}{g_1(u)}, \frac{f_2(u)}{g_2(u)}, \dots, \frac{f_p(u)}{g_p(u)} \right)^T \quad (2\text{---}1) \\ \text{s.t. } & \sum_{i=1}^q \tau_i \nabla \frac{f_i(u)}{g_i(u)} + \sum_{j=1}^m \lambda_j \nabla h_j(u) = 0 \\ & \lambda^T h(u) \geq 0 \\ & \tau = (\tau_1, \tau_2, \dots, \tau_p)^T \in R_+^p, \tau > 0, \sum_{i=1}^p \tau_i = 1 \\ & \lambda = (\lambda_1, \lambda_2, \dots, \lambda_p)^T \in R_+^m, u \in X \end{aligned}$$

Theorem 2.1 (weak duality) (Liang, 2003, p.447-471): Supposed \bar{x} is a feasible solution of (MFP), and $(\bar{u}, \bar{\tau}, \bar{\lambda})$ is a feasible solution of (MFD1), and if f_i and $-g_i (i=1,2,\dots,p)$ are convex $(F, \alpha_i, \rho_i, d_i)$ on \bar{u} , so $h_j (j=1,2,\dots,m)$ is convex (F, β, ζ_j, c_j) on \bar{u} , and the inequation exists.

$$\sum_{i=1}^p \tau_i \rho_i \frac{\bar{d}_i(\bar{x}, \bar{u})}{\alpha_i(\bar{x}, \bar{u})} + \sum_{j=1}^m \bar{\lambda}_j \zeta_j \frac{c_j^2(\bar{x}, \bar{u})}{\beta(\bar{x}, \bar{u})} \geq 0 \quad (2\text{---}2)$$

Where, $\bar{\alpha}_i(\bar{x}, \bar{u}) = \alpha_i(\bar{x}, \bar{u}) \frac{g(\bar{u})}{g(\bar{x})}$, $\bar{\rho}_i = \rho_i \left(1 + \frac{f_i(\bar{u})}{g_i(\bar{u})} \right)$, $\bar{d}_i(\bar{x}, \bar{u}) = \frac{d_i(\bar{x}, \bar{u})}{g_i^{\frac{1}{2}}(\bar{x})}$, so $\frac{f(\bar{x})}{g(\bar{x})} \neq \frac{f(\bar{u})}{g(\bar{u})}$.

Deduction 2.1 (weak duality) (Liang, 2003, p.447-471): Supposed \bar{x} is a feasible solution of (MFP), and $(\bar{u}, \bar{\tau}, \bar{\lambda})$ is a feasible solution of (MFD1), and if f_i and $g_i (i=1,2,\dots,p)$ are strongly convex $(F, \alpha_i, \rho_i, d_i)$ (or convex (F, α_i)). On \bar{u} , $h_j (j=1,2,\dots,m)$ is strongly convex $\bar{u}(F, \beta, \zeta_j, c_j)$, so $\frac{f(\bar{x})}{g(\bar{x})} \neq \frac{f(\bar{u})}{g(\bar{u})}$.

Theorem 2.2 (strong duality): Supposed \bar{x} is an effective solution of (MFP), and \bar{x} fulfills the restrain condition (GGCQ) (Avriel, 1980, p.407-435), so $(\bar{\tau}, \bar{\lambda}) \in R_+^p \times R_+^m$ exists and makes $(\bar{x}, \bar{\tau}, \bar{\lambda})$ be a feasible solution of (MFD1), and the objective function values on the corresponding points of (MFP) and (MFD1) are equal, and if it fulfills the generalized convex inequation in Theorem 2.1, so $(\bar{x}, \bar{\tau}, \bar{\lambda})$ is an effective solution of (MFD1).

In fact, because \bar{x} is an effective solution of (MFP), and (GGCQ) exists on \bar{x} , as a necessary and effective condition,

$(\bar{\tau}, \bar{\lambda}) \in R_+^p \times R_+^m, \bar{\tau} > 0$ exists and makes $(\bar{u}, \bar{\tau}, \bar{\lambda})$ be a feasible solution of (MFD1). Though the corresponding objective functions of (MFP) and (MFD1) are equal, but if $(\bar{u}, \bar{\tau}, \bar{\lambda})$ is not the sufficient solution of (MFD1), so a feasible solution (x^*, τ^*, λ^*) of (MFD1) must exist and make $\frac{f(\bar{x})}{g(\bar{x})} < \frac{f(x^*)}{g(x^*)}$.

Its result is contradictive with the conclusion of weak duality in Theorem 2.1, so $(\bar{u}, \bar{\tau}, \bar{\lambda})$ is an effective solution of (MFD1).

2.2 Schaible duality

The extended formula of (MFP) Schaible duality (Schaible, 1976, p.452-46 & Schaible, 1976, p.858-867) is

$$\begin{aligned}
 \text{(MFD2)} \quad & \text{Max } \lambda = (\lambda_1, \lambda_2, \dots, \lambda_p)^T \\
 \text{s.t.} \quad & \sum_{i=1}^p \tau_i \nabla_u (f_i(u) - \lambda_i g_i(u)) + \sum_{j=1}^m v_j \nabla h_j(u) = 0 \\
 & f_i(u) - \lambda_i g_i(u) \geq 0 \quad i=1, 2, \dots, p \\
 & v^T h(u) \geq 0, \quad \tau > 0, \sum_{i=1}^p \tau_i = 1 \\
 & \lambda \in R_+^p, \tau \in R_+^p, v \in R_+^{M_h}, u \in X
 \end{aligned}$$

Theorem 2.3 (weak duality) (Liang, 2003, p.447-471): Supposed that \bar{x} is a feasible solution of (MFP), and $(\bar{u}, \bar{\tau}, \bar{\lambda}, \bar{v})$ is a feasible solution of (MFD2), if one of following equation comes into existence.

(1) f_i and $-g_i$ ($i=1, 2, \dots, p$) are convex F, α_i, ρ_i, d_i on \bar{u} , h_j ($j=1, 2, \dots, m$) is convex (F, β, ζ_j, c_j) on \bar{u} , and

□

(2) f_i and $-g_i$ ($i=1, 2, \dots, p$) are convex F, α_i, ρ_i, d_i on \bar{u} , h_j ($j=1, 2, \dots, m$) is convex (F, β, ζ_j, c_j) on \bar{u} , and these vectors $\bar{\tau}, \bar{\lambda}, \bar{v}$ fulfill

$$\sum_{i=1}^p \bar{\tau}_i \rho_i (1 + \bar{\lambda}_i) + \sum_{j=1}^m \bar{v}_j \zeta_j \geq 0 \tag{2---3}$$

So $\frac{f(\bar{x})}{g(\bar{x})} \neq \bar{\lambda}$.

Theorem 2.4 (strong duality) (Liang, 2003, p.447-471): Supposed \bar{x} is an effective solution of (MFP), and \bar{x} fulfills the restrain condition (GGCQ) (Avriel, 1980, p.407-435), so $\bar{\tau} \in R_+^p, \bar{\lambda} \in R_+^p, v \in R_+^m$ exists and makes $(\bar{x}, \bar{\tau}, \bar{\lambda}, \bar{v})$ be a feasible solution of (MFD2), and $\bar{\lambda} = \frac{f(\bar{x})}{g(\bar{x})}$. If all hypotheses in Theorem 2.3 are fulfilled, so the

corresponding $(\bar{x}, \bar{\tau}, \bar{\lambda}, \bar{v})$ is an effective solution of (MFD2).

2.3 Extended Bector duality

Supposed $G(x) = \prod_{i=1}^p g_i(x), \quad G_i(x) = \frac{G(x)}{g_i(x)} \quad (i = 1, 2, \dots, p),$

so (MFP) can be written as the following form

$$\begin{aligned}
 \overline{\text{(MFP)}} \quad & \min \frac{f(x)}{g(x)} = \left(\frac{G_1(x)f_1(x)}{G(x)}, \frac{G_2(x)f_2(x)}{G(x)}, \dots, \frac{G_p(x)f_p(x)}{G(x)} \right)^T \\
 \text{s.t.} \quad & h(x) \leq 0, x \in X.
 \end{aligned}$$

We use the equation of (MFP) from the form of $\overline{\text{(MFP)}}$ to establish the following duality which is called as the extended Bector duality,

$$\begin{aligned}
 \text{(MFD3) Max} & \left(\frac{G_1(u)f_1(u) + v_{M_0}^T(h_{M_0}(u))}{G(u)}, \dots, \frac{G_p(u)f_p(u) + v_{M_0}^T h_{M_0}(u)}{G(u)} \right)^T \quad (2-4) \\
 \text{s.t} & \sum_{i=1}^p \tau_i \nabla_u \frac{G_i(u)f_i(u) + v_{M_0}^T h_{M_0}(u)}{G(u)} + \sum_{k=1}^q \nabla_u v_{M_k}^T h_{M_k}(u) = 0 \\
 & v_k^T h_{M_k}(u) \geq 0 \quad u = 1, 2, \dots, q \\
 & G_i(u)f_i(u) + v_{M_0}^T h_{M_0}(u) \geq 0, \quad i = 1, 2, \dots, p \\
 & \sum_{i=1}^p \tau_i = 1, \tau = (\tau_1, \tau_2, \dots, \tau_p)^T \in R_+^p, \tau > 0 \\
 & u \in X, v_{M_k} \in R_+^{M_k}, k = 1, 2, \dots, q
 \end{aligned}$$

Theorem 2.5 (weak duality) (Liang, 2003, p.447-471): Supposed that \bar{x} is a feasible solution of (MFP), and (u, τ, v) is a feasible solution of (MFD3), and $-G$ is convex (F, α, ρ, d) on u point, $G_i f_i (i = 1, 2, \dots, p)$ is convex F, α, ρ_i, d on u point, and $h_j (j = 1, 2, \dots, m)$ is convex (F, α, ξ_j, d) on u point, and if $\rho \geq \max_{1 \leq i \leq p} \rho_i$ and the following inequation exists.

$$\begin{aligned}
 \sum_{i=1}^p \tau_i \rho_i \left(1 + \frac{G_i(u)f_i(u) + v_{M_0}^T h_{M_0}(u)}{G(u)} \right) + \sum_{j \in M_0} v_j \zeta_j + G(u) \cdot \sum_{k=1}^q \sum_{j \in M_0} v_j \zeta_j & \geq 0 \quad (2-5) \\
 \text{so } \frac{f(x)}{g(x)} & \not\leq \frac{\overline{G(u)}f(u) + u_{M_0}^T h_{M_0}(u)e}{G(u)}
 \end{aligned}$$

Where, $\overline{G(u)} = \text{diag}\{G_1(u) \cdots G_p(u)\}, e \in R^p, e = (1, 1, \dots, 1)$.

Theorem 2.6 (strong duality) (Liang, 2003, p.447-471): Supposed \bar{x} is an effective solution of (MFP), and \bar{x} fulfills the restrain condition (GGCQ) (Avriel, 1980, p.407-435), so $(\bar{\tau}, \bar{v})$ exists and makes $\bar{x}, \bar{\tau}, \bar{v}$ be a feasible solution of (MFD3), and the objective function values of (MFP) and (MFD3) are respectively equal on \bar{x} and $(\bar{x}, \bar{\tau}, \bar{v})$, If the hypotheses and conditions in Theorem 2.5 are fulfilled, so the $(\bar{x}, \bar{\tau}, \bar{v})$ is an effective solution of (MFD3).

3. The optimal condition and duality of generalized arcwise connected function

After we give the weak duality and strong duality of (MFP) under some very weak generalized functions, now we consider the optimized problem which area is arcwise connection.

$$\begin{aligned}
 \text{(ACP)} \quad \min & f(x) \\
 \text{s.t} & x \in X
 \end{aligned}$$

here, $X = \{x \in S; g_j(x) \leq 0, j = 1, 2, \dots, m\}$. $f(x), g_j(x), (j = 1, 2, \dots, m)$ is the real valued function on the set of arcwise connection $S \subseteq R^n$, and to any $x_1, x_2 \in S$ and the arc $H_{x_1 x_2}, f(x)$ and $g_j(x) (j = 1, 2, \dots, m)$ connecting x_1 and x_2 are arcwise derivative about $H_{x_1 x_2}$ on x_2 .

Definition 3.1: Supposed $H_{x_1 x_2}$ is a continual vector value function, i.e. $H_{x_1 x_2} : [0, 1] \rightarrow S$, and $H_{x_1 x_2}(0) = x_1, H_{x_1 x_2}(1) = x_2. x_1, x_2 \in S \subset R^n$ are arcwise connections. If a vector $\nabla^- H_{x_1 x_2}(\lambda_0) \in R^n$ and a vector value function $\alpha : [0, 1] \rightarrow R^n$ exist and fulfill $\lim_{t \rightarrow 0} \alpha(t) = 0$ to make following equation come into existence when $0 \leq \lambda \leq 1$

$$H_{x_1 x_2}(\lambda) - H_{x_1 x_2}(\lambda_0) = (\lambda - \lambda_0) \nabla^- H_{x_1 x_2}(\lambda_0) + (\lambda - \lambda_0) \cdot \alpha(\lambda - \lambda_0). \quad (3-1)$$

So vector $\nabla^- H_{x_1 x_2}(\lambda_0)$ is called as the directional derivative of $H_{x_1 x_2}$ on the point of $\lambda = \lambda_0$, which is got from the following equation

$$\nabla^- H_{x_1x_2}(\lambda_0) = \lim_{\lambda \rightarrow \lambda_0} \{ [H_{x_1x_2}(\lambda) - H_{x_1x_2}(\lambda_0)] / (\lambda - \lambda_0) \}. \tag{3-2}$$

Thus, we can define the arcwise derivative concept of arcwise connected function.

Definition 3.2: Supposed $f(x)$ is the continual real valued function on the arcwise connected set $S \subseteq R^n$, to any one point x in S , $x_0 \in S$, H_{x,x_0} is the arcwise connecting x and x_0 . If x tends towards x_0 along H_{x,x_0} , the following limitation exists.

$$J_{H_{x,x_0}}(x_0) = (\nabla^- H_{x_1,x_2}(1))^T \nabla f(x_0) = \lim_{\lambda \rightarrow 1} \frac{f(H_{x,x_0}(\lambda)) - f(x_0)}{\lambda - 1} \tag{3-3}$$

So we call $f(x)$ is arcwise derivative about H_{x,x_0} on the point of x_0 , and it is marked as $f_{H_{x,x_0}}(x_0)$.

In this way, to $0 \leq \lambda \leq 1$, a continual arcwise connected function (ACF) $f(x)$ on S can be denoted as $f(H_{x_1x_2}(\lambda)) = f(x_2) + (\lambda - 1)f_{H_{x_1x_2}}(x_2) + (1 - \lambda)\bar{\alpha} \cdot (1 - \lambda)$. (3-4)

Here, $\bar{\alpha} : [0,1] \rightarrow R$, and fulfills $\lim_{t \rightarrow 0} \bar{\alpha}(t) = 0$.

Definition 3.3: Supposed $f(x)$ is the continual real valued function on the arcwise connected set $S \subseteq R^n$, to any one point x in S , $x_0 \in S$, the arcwise H_{x,x_0} connecting x and x_0 exists and makes the following containment relationship come into existence.

$$f(x) \leq f(x_0) \Rightarrow f_{H_{x,x_0}}(x_0) \geq 0 \tag{3-5}$$

So we call that $f(x)$ is the puppet arcwise connected function on x_0 which is marked as PACF.

Under the same condition, if the containment relationship is $f(x) \leq f(x_0) \Rightarrow f_{H_{x,x_0}}(x_0) > 0$, so we call $f(x)$ is the strong puppet arcwise connected function on x_0 which is marked as SPACF, and if $f(x) < f(x_0) \Rightarrow f_{H_{x,x_0}}(x_0) > 0$, so we call $f(x)$ is the strict strong puppet arcwise connected function on x_0 which is marked as STPACF.

If $f(x)$ is PACF, SPACF and STPACF on any point of S , so we call $f(x)$ is PACF, SPACF and STPACF on S .

Theorem 3.1 (Zhiun, 2001): Supposed $f(x)$ is the quasi-arcwise connected function QACF on an arcwise connected set $S \subseteq R^n$, if $x_0 \in S$ is a strict local minimum point of $f(x)$, so x_0 is a strict global minimum point of $f(x)$ on S .

Theorem 3.2 (Zhiun, 2001): Supposed $f(x)$ is the strong quasi-arcwise connected function SQACF on an arcwise connected set $S \subseteq R^n$, if $x_0 \in S$ is a strict local minimum point of $f(x)$, so x_0 is the only strict global minimum point of $f(x)$ on S .

Prove: counterevidence. Supposed $f(x)$ is SQACF and $x_0 \in S$ is a local minimum point of $f(x)$, if $\bar{x} \in S$ exists and makes $f(\bar{x}) < f(x_0)$, so the arcwise $H_{\bar{x},x_0}$ connecting \bar{x} with x_0 exists, to any $0 \leq \lambda < 1$, there is

$$f(H_{\bar{x},x_0}(\lambda)) < f(x_0). \tag{3-6}$$

To any neighbor area of x_0 , we can always find λ_0 to make $H_{\bar{x},x_0}(\lambda)$ in this neighbor area when $\lambda_0 \leq \lambda < 1$, that is contradictive with that x_0 is a local minimum point of $f(x)$, so the theorem is proved.

To STQACF, there are following theorems.

Theorem 3.3: Supposed $f(x)$ is the STQACF defined on an arcwise connected set $S \subseteq R^n$, and if $x_0 \in S$ is a strict local minimum point of $f(x)$, so x_0 is the global minimum point of $f(x)$ on S .

Theorem 3.4: Supposed $f(x)$ is the real valued continual function on an arcwise connected set $S \subseteq R^n$, $x_0 \in S$ is the point to fulfill $\nabla f(x_0) = 0$, and if $f(x)$ is STPACF, so x_0 is the global minimum point of $f(x)$ on S . If $f(x)$ is SPACF, so x_0 is the only strict global minimum point of $f(x)$ on S .

Prove: supposed $f(x)$ is STPACF, $x_0 \in S$ is the point to fulfill $\nabla f(x_0) = 0$, so to any $x \in S$ and corresponding arcwise $H_{x,x'}$, there is

$$f_{H_{x,x_0}}(x_0) = (\nabla^{-} H_{x,x_0}(v) \nabla f(x_0)) = 0.$$

Thus, from the definition of STPACF, we can obtain $f(x) \geq f(x_0)$, i.e. x_0 is the global minimum point of $f(x)$ on S , and if $f(x)$ is SPACF, so from definition, we can obtain $f(x) > f(x_0)$. To any $x \in S, x \neq x_0$ comes into existence, i.e. x_0 is the only global minimum point of $f(x)$ on S .

Theorem 3.5: supposed in the problem (ACP), $X = \{x \in S, g_j(x) \leq 0, j = 1, 2, \dots, m\}$ is the feasible area, $f(x), g_j(x), j = 1, 2, \dots, m$ is arcwise derivative on the arcwise connected set $S \subseteq R^n$, and if x^* is the optimal solution of (ACP), and $f_{H_{x,x^*}}(x^*)$ and $(g_i)_{H_{x,x^*}}(x^*)$ are convex functions about x , so $r_0^* \in R, r^* \in R^m$ exists and makes following equation come into existence to any $x \in S$.

$$r_0^* f_{H_{x,x^*}}(x^*) + r^{*T} (g_I)_{H_{x,x^*}}(x^*) \leq 0 \tag{3---7}$$

$$r^{*T} g(x^*) \leq 0 \tag{3---8}$$

$$(r_0^* r^*) \geq 0 \tag{3---9}$$

Here, $I := I(x^*) = \{j \mid g_j(x^*) = 0\}, J := J(x^*) = \{j \mid g_j(x^*) < 0\}$.

Prove: first, we prove the equation group

$$f_{H_{x,x^*}}(x^*) > 0 \tag{3---10}$$

$$(g_i)_{H_{x,x^*}}(x^*) > 0 \tag{3---11}$$

has no solution in S .

counterevidence, if $x \in S$ exists and is a solution of the equation group, and because $f_{H_{x,x^*}}(x^*)$ and $(g_i)_{H_{x,x^*}}(x^*)$ exist, so to any $0 \leq \lambda \leq 1$

$$f(H_{x,x^*}(\lambda)) = f(x^*) + (\lambda - 1)f_{H_{x,x^*}}(x^*) + (1 - \lambda)\alpha(1 - \lambda) \tag{3---12}$$

$$g_i(H_{x,x^*}(\lambda)) = g_i(x^*) + (\lambda - 1)(g_i)_{H_{x,x^*}}(x^*) + (1 - \lambda)\alpha_i(1 - \lambda) \tag{3---13}$$

$$\text{here, } \alpha : [0,1] \rightarrow R. \lim_{t \rightarrow 0} \alpha(t) = 0 \tag{3.--14}$$

$$\alpha_i : [0,1] \rightarrow R. \lim_{t \rightarrow 0} \alpha_i(t) = 0 \tag{3.--15}$$

from (3.10), (3.11), (3.14) and (3.15), we can obtain, to enough big λ markas $\lambda_0 < \lambda < 1$

$$f_{H_{x,x^*}}(x^*) - \alpha(1 - \lambda) > 0$$

$$(g_i)_{H_{x,x^*}}(x^*) - \alpha_i(1 - \lambda) > 0 \quad i \in I$$

thus, from (3.10) and (3.11), to $\lambda_0 < \lambda < 1$, there are

$$f_{H_{x,x^*}}(\lambda) - f(x^*) < 0 \tag{3.--16}$$

$$(g_i)_{H_{x,x^*}}(x^*) - g_i(x^*) < 0 \quad i \in I \tag{3.--17}$$

Because $g_j, j \in I$ is arcwise derivative and continual on x^* , and the arcwise $H_{x,x^*}(\lambda)$ is also the continual function about λ , so $\lim_{\lambda \rightarrow 1} g_j(H_{x,x^*}(\lambda)) = g_j(x^*) < 0$.

That means $\lambda_j^*, j \in J$ exists, and when $\lambda_j^* \leq \lambda < 1, g_j(H_{x,x^*}(\lambda)) < 0 \tag{3.--18}$.

Supposed $\lambda^* = \max\{\lambda_0, \lambda_j^*\}$, so from (3.16), (3.11), (3.18), to $\lambda^* < \lambda < 1$, we can obtain $H_{x,x^*}(\lambda) \in X$, and

$f(H_{x,x}(\lambda)) - f(x^*) < 0$. That is contradictive with that x^* is the optimal solution of (ACP), so the equation group (3.10) and (3.11) has no solution.

Because $f_{H_{x,x^*}}(x^*)$ and $(g_l)_{H_{x,x^*}}(x^*)$ are convex function about x , so $r_0^* \in R, r_i^* \in R^m$ which are not zero completely exist and make flowing equation come into existence to any $x \in S$.

$$r_0^* f_{H_{x,x^*}}(x^*) + r_l^{x^T} (g_l)_{H_{x,x^*}}(x^*) \leq 0.$$

Let $r_j^* = 0$, so the theorem is proved.

Now, we establish the Mond-Weir duality of (ACP), and give the theorems of weak duality and strong duality.

$$\begin{aligned} \text{(ACPD)} \quad & \text{Max } f(u) \\ \text{s.t.} \quad & r_0 f_{H_{x,u}}(u) + r^T g_{H_{x,u}}(u) \leq 0 \end{aligned} \quad (3.--19)$$

$$\sum_{j=0}^m r_j g_j(u) \geq 0 \quad (3.--20)$$

$$u \in S \quad (r_0, r) \geq 0, r_0 \in R, r \in R^m \quad (3.--21)$$

Theorem 3.6 (weak duality): supposed x is the feasible solution of (ACP), (u, r_0, r) is the feasible solution of (ACPD), and if $f(x)$ is STPACF on u point, $\sum_{j=0}^m r_j g_j(u)$ is SPACF on u ,

so
$$f(x) \geq f(u).$$

Prove: reduction to absurdity, if $f(x) < f(u)$, because $f(x)$ is PACF on u point, from definition, there is

$$r_0 f_{H_{x,u}}(u) \geq 0 \quad (3---22).$$

If $r_0 > 0$, so the inequation strictly comes into existence, and because x is the feasible solution of (ACP), (u, r_0, r) is the feasible solution of (ACPD), and we can obtain

$$\sum_{j=1}^m r_j g_j(x) \leq \sum_{j=1}^m r_j g_j(u) \quad (3.--23)$$

$$\sum_{j=1}^m r_j g_j(u) \text{ is SPACF on } u, \text{ so}$$

$$\left(\sum_{j=1}^m r_j g_j(u)\right)_{H_{x,u}}(u) \geq 0 \quad (3.--24).$$

If some $r_j > 0, j = 1, 2, 3, \dots, m$, so the inequation strictly comes into existence, thus, from (3.22) and (3.24), we can obtain

$$r_0 f_{H_{x,u}}(u) + r^T g_{H_{x,u}}(u) > 0 \quad (3.--25).$$

That is contradictive with (3.19), so $f(x) \geq f(u)$.

Theorem 3.7 (strong duality): supposed x^* is the optimal solution of (ACP), $f_{H_{x,x^*}}(x^*)$ and $(g_l)_{H_{x,x^*}}(x^*)$ are convex functions about x , so $r_0^* \in R, r^* \in R^m$ which are not zero completely exist and make (x^*, r_0^*, r^*) be the feasible solution of (ACPD), and the objective function values of (ACP) and (ACPD) are equal on x^* . If to every feasible (u, r_0, r) of (ACPD), $f(x)$ is STPACF on u point, $\sum_{j=1}^m r_j g_j(u)$ is SPACF on u , so (x^*, r_0^*, r^*) is the optimal solution of (ACPD).

Prove: because x^* is the optimal solution of (ACP), so from theorem 3.1, $r_0^* \in R, r^* \in R^m$ exist and make (x^*, r_0^*, r^*) is the feasible solution of (ACPD), so the objective function values of (ACP) and (ACPD) are equal on x^* . If (x^*, r_0^*, r^*) is not the optimal solution of (ACPD), so the feasible solution of (ACPD) (u, r_0, r) exists and makes

$$f(u) > f(x^*) \quad (3\text{---}26).$$

Because $f(x)$ is STPACF on u point, $\sum_{j=1}^m r_j g_j(u)$ is SPACF on u , (3.22) is contradictive with theorem 3.4, so (x^*, r_0^*, r^*) is the optimal solution of (ACPD).

References

- Aghezzaf, B. and Hachimi, M. (2000). Generalized Convexity and Duality in multi-objective Programming Problems. *Journal of Global Optimization*. No.18. p.91-101.
- Aghezzah, B. and Hachimi, M. (2001). Sufficiency and Duality in Multi-objective Programming Involving Generalized (F, ρ) -convexity. *Journal of Mathematical Analysis and Applications*. No.258. p.617-628.
- Avriel, M. Zang, I. (1980). Generalized Arcwise Connected Sets and Functions and Characterization of Cocal-global Minimum Properties. *Journal of Optimization Theory and Applications*. vol.32. p.407-435.
- Liang Z.A, Huang H.Z, Purdulos. P.M. (2003). Efficiency Conditions and Duality for a Class of Multi-objective Fractional Programming Problems. *Journal of Global Optimization*. No.27. p.447-471.
- Liang, Z. and Ye, Q. (2001). Duality for a Class of Multi-objective Control Problems with Generalized Invexity. *Journal of Mathematical Analysis and Applications*. No.256. p.446-461.
- Mond, B. and Weir, T. (1982). Duality for Fractional Programming with Generalized Convexity Conditions. *Journal of Information and Optimization Sciences*. No.3(2). p.105-124.
- Mond, B. and Weir, T. (1981). *Generalized Concavity and Duality, in Generalized Convexity in Optimization and Economics*. Schaible, S. and Ziemba, W.T. (Eds), Academic Press. New York. p.263-280.
- Mukherjee, R.N. and Rao, C.P. (2000). Mixed Type Duality for Multi-objective Variational Problems. *Journal of Mathematical Analysis and Applications*. No.252. p.571-586.
- Ortega. I.M. and Rheinboldt. W.C. (1970). *Iterative Solutions of Nonlinear Equations in Several Variables*. Academic Press. New York.
- Preda, V. (1992). On Efficiency and Duality for Multi-objective Programs. *Journal of Mathematical Analysis and Applications*. No.166. p.365-377.
- Schaible, S. (1976). Duality in Fractional Programming: a Unified Approach. *Operations Research*. No.24. p.452-46.
- Schaible, S. (1976). Fractional Programming, I: Duality. *Management Science*. No.22. p.858-867.
- Wolfe, P. (1961). A Duality Theorem for Nonlinear Programming. *Quarterly of Applied Mathematics*. No.19. p.239-244.
- Xu, Z. (1996). Mixed Type Duality in Multi-objective Programming Problems. *Journal of Mathematical Analysis and Applications*. No.198. p.621-635.
- Yang, X.M. Teo, K.L. and Yang, X.O. (2000). Duality for a Class of Non-differentiable Multi-objective Programming Problems. *Journal of Mathematical Analysis and Applications*. No.252. p.999-1005.
- Zhang, Z. and Mond, B. (1997). Duality for a Non-differentiable Programming Problem. *Bulletin of the Australian Mathematical Society*. No.55. p.29-44.
- Zhiun Liang, Hong Xuan Huang, P.M. Purdulos. (2001). Optimality Conditions for a Class of Fractional Programming. *Journal of Optimization Theory and Applications*. No.110(3).
- Zi, Z. (1993). Duality Theorems for a Class of Generalized Convex Multi-objective Programming Problems. *Acta Scientiarum Naturalium Universita-tis Nei Mongol*. No.24(2). p.113-118.

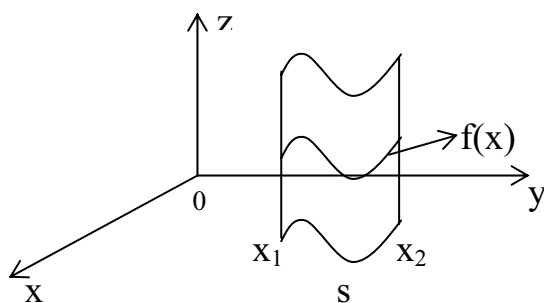


Figure 1. A Line-type Figure without Interior Point



UPM-APSB AISA Airborne Hyperspectral Technology for Managing Mangrove Forest in Malaysia

Kamaruzaman Jusoff

Yale University, Centre for Earth Observation (CEO)

Environmental Science Centre, 21 Sachem St, New Haven CT 06511, USA

Tel: 203-676-7761 E-mail: jusoff.kamaruzaman@yale.edu

The research is financed by Universiti Putra Malaysia and Aeroscan Precision (M) Sdn Bhd (Sponsoring information)

Abstract

Mangrove forests are one of the most productive and bio-diverse wetlands environments on earth. In Malaysia, Forestry Department of Peninsular Malaysia (FDPM) has always been fully committed to the implementation of the sustainable forest management practices and in line with current concerns such as climate change, conservation of biodiversity and Tsunami, have brought about a heightened expectation on the political, socio-economic, ecological and environmental well-being of the country. Thus, managing mangrove forests is very challenging to the department and a precise geospatial database is urgently required. The objectives of this paper are to assess the capability of UPM-APSB's AISA airborne hyperspectral imaging sensor for developing a geospatial database through an individual mangrove species mapping and to determine the wavelength regions that define the inherent spectral characteristics amongst mangrove species. A total of nine groups of mangrove species spectral separability were identified in Port Klang, Selangor namely *Lumnitzera littorea*, *Rhizophora mucronata*, *R. stylosa*, *Sonneratia alba*, *Avicennia officinalis*, *R. apiculata*, *Bruguiera parviflora*, *B. gymnorhiza*, *B. cylindrical* and *S. caseolaris*. The species were easily identified and separated in the NIR range (700 nm to 900 nm) with the following spectral values namely (a) 1,750-6,000: *B. cylindrical*, (b) 2,000-7,750: *B. gymnorhiza*, (c) 1,875-8,250: *B. parviflora*, (d) 1,875-5,500 : *A. officinalis*, (e) 1,625-6,250 : *S. caseolaris*, (f) 1,875-5,250: *S. alba*, (g) 1,750-7,500: *R. apiculata*, (h) 2,000-8,000: *R. stylosa*, (i) 2,200-7,000: *R. mucronata*. Results of this study indicated that the mangrove species could only be identified at the near infrared (NIR) wavelength (700 nm to 900 nm) and not in the visible (VIS) spectrum. With such a capability, the sensor should be in a position to provide a geospatial database of the Malaysian mangroves for Tsunami management and other purposes of interests. Future management of mangrove forests in P.Malaysia should then adopt an integrated approach by further refining the current management and incorporating latest findings and updated latest geospatial information through more vigorous airborne hyperspectral data acquisition on mangrove forest. With the future geospatial database developed from the sensor, the National Forestry Policy and other policies related to mangrove forests management can be revised from time to time to match latest prevailing conditions and requirement. The future success in developing a mangrove geospatial database using UPM-APSB's AISA data by FDPM will in fact contribute to the sustainability of the wetlands in Malaysia which is crucial to the survival and future health of our Mother Earth.

Keywords: Mangrove, Airborne sensing, Hyperspectral, Mapping, Management, Tsunami

1. Introduction

Mangrove forests are one of the most productive and bio-diverse wetlands environments on earth. The importance of mangrove forests in providing invaluable goods and services both in economics and environmental terms are well understood and documented (Dato' Hj. Dahlan, 2007). In Peninsular Malaysia, mangrove forests forms one of the major wetland types which have been identified as one of the key life support systems on earth. Mangroves in P. Malaysia are found mainly on the sheltered west coast that borders the Straits of Melaka in the states of Kedah, Perak, Selangor and Johor. Major near-shore islands, including the Kelang islands in Selangor and Pulau Kukup in Johore are also predominantly colonized by mangroves. Small patches of mangrove forests occur along the rocky shores and they include those found in Pulau Langkawi, Kedah; in Pulau Pangkor, Perak; and in Port Dickson, Negeri Sembilan. In the south, mangroves are found in the estuaries of Sungai Pulai and Sg. Johor which drain into the straits of Johor, and the remaining mangroves are found along the straits of Johore. On the east coast, mangrove forests are mostly confined to

sheltered estuaries of the Kelantan Delta and Tok Bali, Kelantan (Kasawani *et. al.*, 2007), Kemaman river in Terengganu, Bebar in Pahang. The total area of mangrove forests in Peninsular Malaysia at the end of 2006 is estimated to be 107,802 ha of which 82,091 ha has been gazetted as Permanent Reserved Forests (PRFs). Perak has the largest mangrove reserves, followed by Johore and Selangor. Mangrove reserves of Matang (Perak), South Johor (Johor) and Kelang (Selangor), together constitute 74 percent of the mangrove forest reserves. The importance of managing mangrove forests using hierarchy analysis goes beyond their status as the habitat of many endangered flora and fauna species (Nur Ilayana and Kamaruzaman, 2007). They are a valuable natural resource with distinctive diversity, high intrinsic natural productivity and unique habitat value. Mangrove forests provide invaluable goods and services both in economics and environmental terms. Apart from the production of poles, charcoal and fuel wood, the mangrove ecosystem supports a wide range of functions such as coastline protection, assimilation of waste, source of food, shelter and sanctuary for fauna, spawning and breeding ground for marine life and also recently proven as a barrier to significantly reduce the height and force of the waves of the tsunami. The mangrove forests can be an idyllic retreat for nature and wildlife lovers, photographers, bird-watchers or anyone who wants to relax and appreciate the beauty of the mangrove environment and its diverse flora and fauna. The meandering rivers and rivulets add to the peaceful environment especially to those escaping the tension of city life. Fireflies found at river estuaries have been a major ecotourism attraction, such as in Kampong Kuantan, Selangor (Wan Faridah *et. al.*, 2007); Kampong Yakyoh, Trengganu; Kelantan Delta, Tumpat; Sungai Lebam, Johor; and Kuala Linggi, Negeri Sembilan/Melaka. Traditionally, the coastal communities living within or at the fringes of the mangrove forests have been dependent on the mangrove forests for their livelihood. Mangrove forests are a major source of fishery resources. The mudflats are habitats for various types of shellfish, where many species of fish, prawns and other marine fauna spawn and feed. Local communities have been relying on the mangrove forests for consumable plants and medicinal herbs (Amjad and kamaruzaman, 2007). Yet, these unique coastal tropical forests environment are among the most threatened habitats in the world, for instance the degradation of Indus Delta mangroves in Pakistan (Amjad *et. al.*, 2007).

Mangroves act as “bio-shield” as they act as a barrier to the coastal waves, but the impact caused by the tsunamis was so devastating that it has resulted in the destruction of many mangrove trees along the southeastern coast lines. An obvious environmental impact of the Tsunami is the physical damage to the mangroves that has resulted from waves and backwash. The deposit of silt may lead to the clogging of pores of the aerial roots of mangroves and cause total destruction of the plant species. The degree and extent of damage of the mangrove is not known. Their loss can certainly prove to be disastrous in terms of coastline ecosystem functions. An integrated comparative approach to mangrove vegetation mapping using advanced remote sensing and GIS technologies has been well reported by many researchers Aschbacher *et. al.*, 1995; Amjad *et. al.*, 2007; and Kasawani *et.al.*, 2007). For Tsunami-affected areas, as all other disaster-affected areas, utilization of hyperspectral sensing data, in particular airborne hyperspectral imaging technology can offer a real-time synoptic view for quick detection, quantification and monitoring in real-time. Moreover, remote sensing and GIS can be used to model the impact of disasters such as Tsunami. The benefits of spectral imaging have been addressed in university research, especially in Malaysia for more than four years. Several airborne instruments especially UPM-APSB's AISA sensor have been available for applications development and studies (Kamaruzaman, 2006); in addition, new airborne instruments with refined capabilities have been recently flown or are nearing completion. The use of airborne instruments is a natural way to develop algorithms and techniques. Typically, the image resolution is determined by instrument design and aircraft altitude and this can be varied to understand resolution impacts on phenomenological processes. In addition, aircraft systems allow opportunistic collections because of their scheduling flexibility with respect to weather. Satellite systems, on the other hand, permit broader, recurring views to address larger scale and regional issues. Until now, there have been no space-based hyperspectral instruments to provide this option. Hyperspectral imaging is the simultaneous collection of images covering many narrow, contiguous wavelength bands. From each pixel in the image spectral responses that are indicative of what material is exposed on the Earth's surface can be extracted. Absorption features in these spectra are determined by chemical composition and physical structure and as such can be used to identify a wide range of materials. Subtle variations in composition or structure lead to shifts in position and shape of absorption features which allows the differentiation of many similar substances and the depth of absorption features that provide the measure of abundance. These capabilities are what make airborne hyperspectral imaging such a powerful tool in remote sensing (Kamaruzaman, 2006). The objective of this paper is therefore to demonstrate the capabilities and usefulness of UPM-APSB's AISA airborne hyperspectral imaging technique for future geospatial database development towards sustainable management of the mangroves with a specific individual species mapping case study in Port Klang, Selangor, Malaysia.

2. Methodology

2.1 Description of the study area

Few area of interest (AOIs) was selected in this study covering Sabah and Peninsular Malaysia. However, in this paper only Port Klang mangrove forests located in Klang River and Northport of Klang in the state of Selangor have been selected (Fig.1). The geographical position of Port Klang mangrove forest is located at latitudes 2°59'24" N-2°59'12" N

and longitudes 101°22'36" E-101°23'12" E. The study area comprises of four major families of mangrove species (Avicenniaceae, Rhizophoraceae, Bruguiera and Sonneratiaceae). A total of 19 samples of mangrove trees were randomly selected for this study. The mangrove species that were randomly selected in the area includes *Rhizophora mucronata* (Bakau Kurap), *Rhizophora stylosa* (Bakau), *Rhizophora apiculata* (Bakau Minyak), *Bruguiera parviflora* (Lenggadai), *Bruguiera gymnorhiza* (Tumu), *Bruguiera cylindrical* (Bakau Putih), *Sonneratia caseolaris* (Berembang), *Sonneratia alba* (Perepat), *Lumnitzera littorea* (Teruntum Merah) and *Avicennia officials* (Api-api Ludat).

<Fig. 1 A map of Peninsular Malaysia showing the location of study site (in red circle) >

2.2 Systems overview of UPM-APSB's AISA hyperspectral airborne sensing technology

UPM-APSB'S AISA airborne hyperspectral system is a commercial hyperspectral sensor product that was manufactured by Finnish Company SPECIM, Spectral Imaging Ltd. and is operated by Forest Geospatial Information & Survey Lab (FGISL)/Aeroscan Precision (M) Sdn. Bhd. in Lebu Silikon, Universiti Putra Malaysia to acquire hyperspectral imaging data from the sky about mangrove canopy (Fig.2). This sensor is a small, lightweight (15 kg) portable instrument and easy to handle. Recent enhancements to the hardware and software of the Caligeo system have produced a significant reduction in the integration time, which has improved its overall spectral and spatial capabilities. The swath width of the aircraft is 360 m with a 10% overlap and Field of View (FOV) that will be flying in cross track with the direction of 20° and can produce a spatial ground resolution from 1 km altitude approximately 1 m at a flight speed of 120 knots (60 m/s). UPM-APSB's AISA airborne hyperspectral sensor is capable of collecting data within a spectral range between 430 to 1,100 nm and have 286 spectral channels. Current operational collection configurations range from 10 to 70 spectral bands depending on the aircraft speed, altitude and mission goals.

<Fig. 2 A complete UPM-APSB's AISA airborne hyperspectral sensor system >

The UPM-APSB's AISA sensor system also incorporates the Fiber Optic Downwelling Irradiance System (FODIS). The FODIS allows for the concurrent measurement of downwelling and upwelling radiance by the UPM-APSB's AISA sensor head. A diffuse collector installed on the top of the plane is connected to the UPM-APSB's AISA head via fiber optic cable and collects downwelling irradiance in the same bandwidth configurations as the areas being imaged. The calibration of the FODIS coupled with the UPM-APSB's AISA sensor allows for the calculation of apparent at-platform reflectance.

2.3 Data pre and advance processing

In order to provide accurate location of the remotely sensed data, an Inertial Navigation System (INS) and Differential GPS (DGPS) are integrated into the UPM-APSB's AISA sensor suite. The INS and UPM-APSB's AISA data streams are combined in the collection computer to provide frame by frame geo-referencing of the imagery. Pitch, roll, and yaw are encoded with the DGPS information to provide accurate locations of areas of interest on the ground. The UPM-APSB's AISA pre-processing software (CaliGeo) provides for the automatic geometric correction, rectification, mosaicking, and calculation of radiance or apparent at-platform reflectance (FODIS ratio). The program uses the DGPS and attitude information from the INS to perform the geometric, geo-referencing and mosaicking operations. Automated batch processing provides for rapid turnaround times for data delivery. To ensure the accurate measurement and calculation of radiance and "reflectance", the UPM-APSB's AISA system is frequently calibrated using's own NIST traceable integrating sphere. The generated calibration files were used by the CaliGeo software to output images in either radiance (mW/cm²/sr/nm/ms – times a scaling factor) or apparent reflectance. Hyperspectral imaging data is typically formatted into cubes in which the base of the cube is a two-dimensional spatial image of the observed scene at a given wavelength and the height of the cube is built up of many 2-D image layers, each from a different spectral channel. The resultant cubes are typically very large.

ENVI 4.0 which combines a complete image-processing package with the most advanced yet easy-to-use spectral tools was used for the digital image analysis in this study. This powerful amalgam creates a complete data analysis and visualization environment perfect for today's advanced earth science courses. The ease of use, ability to handle airborne hyperspectral data, powerful algorithms and flexible parameters make ENVI 4.0 an excellent choice for hyperspectral analysis. In the data analysis process, factors such as the sensor and attitude alignments, accuracies of the attitude measurement system, DGPS, ground control points and the digital elevation model were all required to be taken into consideration. This ancillary data, in combination with the hyperspectral data (in the 400 nm to 1,100 nm band range, depending on the application requirements), adds up to more than two gigabytes of data amassed during each operational remote sensing flight. In addition, multiple flights are routinely required to scan the entire area under study, further compounding the volume of data until complete images, sometimes as large as 50 gigabytes, are created. ENVI's spectral analysis tools, for example the spectral angle mapper and unmixing algorithms, to analyse the data includes an extensive spectral library for mangrove forest species, as well as masking and classification routines which complement ENVI's many other image processing and data analysis routines were fully utilized in this study. Additional mangrove

forest analysis algorithms were developed using IDL and incorporated with ENVI.

3. Results and discussion

3.1 Development of spectral signatures for individual mangrove forest species mapping and identification

The spectral libraries for 19 randomly selected mangrove trees at Port Klang using analysis image from UPM-APSB's AISA airborne sensor through ENVI software were obtained. From the 19 samples that were randomly selected, a total of nine mangrove species was identified and mapped using the UPM-APSB's AISA sensor (Fig.3). Through the visible (VIS) light region (650 - 680 nm), mangrove forest tree is very low in spectral reflectance, with the exception of small rise in the green. The spectral profiles for nine species from 19 selected trees showed different spectral profile and wavelength absorption because each tree species emitted or radiated varying VIS and Near Infrared (NIR) light at different wavelength. In this study, different spectral patterns were observed from different mangrove species. These results encourage us to further study mangrove areas in the tropics as well as to acquire information on local distribution of different mangrove species for sustainable management and conservation in preparation for the second Tsunami, if any. Fig. 3 shows that the wavelength range between 450-700 nm absorbed sunlight below 2,000 values and all emittance at this range did not show much different from each other. In the wavelength range of 700 nm to 800 nm, there are increased of spectral value from 1,750 to nearly 8,500. The spectral profiles of 19 selected trees were inseparable within this wavelength range because the intensity of solar energy reflected by trees is in dependent on the chlorophyll's ability to absorb the red and blue energy and the spongy layer to reflect the NIR energy. Perhaps, this is the reason why multi-spectral based satellites do not have such capability to identify individual mangrove tree species (Kamaruzaman, 2006; Kamaruzaman and Kasawani, 2007; and Kasawani *et. al.*, 2007).

<Fig. 3 The spectral signature profile of nine mangrove species developed using the UPM-APSB's AISA sensor >

The trend of spectral profiles for nine species from 19-selected trees depends on the color of the canopy. The arising colors from the image showed that those four major colors can be separated in order to determine the dominant families of mangroves species (Fig.3). From the range of major colours (red, orange, green and yellow) they could then be distributed into nine different colours with various bands. The red canopy from AISA image can only be divided into one type of red (dark red) while the orange canopy could extract three more types of orange (dark orange, intermediate orange and light orange). A total of 10 of tree species were registered in the NIR region approximately at 700-900 nm wavelengths. These include families from *Rhizophora*, *Bruguiera*, *Avicennia* and *Sonneratia*. As displayed in on the electromagnetic spectrum that covers approximately 450-700 nm, the spectral profiles look similar. However, in the NIR region of the spectrum, the spectral profiles can be separated from each other.

3.2 Limited geospatial information in managing mangrove forests of Malaysia

There is limited geospatial information or documentation on mangrove degradation and destruction along the Malaysian coastlines. Similarly, many statements have been made about the impact on biological diversity loss, but there are lacks of scientific data or evidence especially real-time remote sensing geospatial database to support these statements. However, shrinking mangrove areas resulting from developmental decisions of the past, as well as signs of strain on the remaining mangroves provides evidence of threat to this ecosystem (Kasawani *et. al.*, 2007). Being a fragile ecosystem, mangroves tend to fluctuate as a result of slight changes in the natural environment. Rapid development has led to clearing of mangrove areas to make way for urban and infrastructure development, beach resorts and aquaculture ponds. Industries and factories situated near the rivers and streams might discharge their effluent into the water systems, polluting and choking the riverine habitat, and eventually adversely affecting the aquatic biodiversity. The disruption of mangrove functions as part of our wetland ecosystem has a high cost: economically, socially and ecologically. The disturbance of their natural balance can destroy critical gene pools required for medical and agricultural purposes, affecting their ability to protect the coastline naturally and ruined their use for educational and recreational purposes. Constant sedimentation has endangered a variety of fishes and other marine species, particularly the corals. Destruction of mangroves led to a dramatic loss to the commercial and recreational fishing industry, coastal erosion, and endangered many floral and faunal species.

The mangrove ecosystem is a sensitive ecosystem that has continued to be affected by the rapid economic growth of the country. The familiar development-environment frictions have always been a major concern. Population pressures and the increasing demand for land continue to pose threat to the coastal and marine resources. Mangrove forests have been the most vulnerable, under severe pressure and the first to be cleared when the need for land arises. There have been perceptions that mangrove areas are considered wasteland, thus, converting mangrove to other uses will fetch a higher financial returns. To many, mangroves are considered an eyesore that need to be cleared, while to some, mangroves are a waterfront that need to be developed, failing to recognize the essential functions of mangroves in maintaining the coastal ecosystem. Another issue is jurisdiction between federal and state government. Matters related to land use and natural resources remains within the exclusive jurisdiction of the state. The vast natural resources sectors such as forests, fishery, wildlife, mining and agriculture are under different agencies/authority with separate sets of regulatory

laws, which at times creates overlaps in prescriptive and enforcement jurisdiction. The establishment of the National Forestry Council has successfully tackled this issue at policy level, and the various committees formed at the federal and state levels has helped to further improve towards conservation, sustainable use, management and development of the mangroves. Public awareness regarding mangroves and their conservation is on the rise. But some still do not appreciate the role of mangroves to the environment and quality of life. Despite the many benefits and functions, mangroves is seen not much more than timber, charcoal and woodchips, Indirect benefits offered by mangroves are easily forgotten and set aside when quick profits can be generated by converting mangroves to other uses. Absence of proper evaluation on mangrove forests results in the undervaluation of the mangrove forests. This in turn, has sent the wrong signals to the market. Therefore, there is need for a comprehensive valuation of our mangrove forests. More applicable inputs from research are needed.

3.3 Implications on the management of mangrove forests and Tsunami

Managing mangrove forests has been very challenging especially in combating the next Tsunami. The policy and management have great impact on political, social, economic, ecological and environmental (particularly Tsunami) well-being of the country. Forestry Department Peninsular Malaysia (FDPM) holds the responsibility and obligation in managing and safeguarding the Malaysian's mangrove resources. FDPM has taken steps to designate mangrove forest reserves to ensure they are efficiently and sustainably managed while preparing for the unpredictable natural disaster, Tsunami along the targeted Malaysian coastline as the first priority. In this particular preparation, UPM-APSB's AISA airborne hyperspectral imaging data which can be automatically inputted into a GIS-ready format should be able to locate the most suitable sites for Tsunami-warning tower installation. Factors that were taken into consideration in locating the sites include the risk of the area for tsunami, effectiveness of tower working range and the towers must not block the good view of scenery could be easily planned using this near real-time data. In addition to the sustainable management of mangrove forests along the coastlines of Malaysia, airborne hyperspectral images are also extremely useful and beneficial to Tsunami warning management in term of accuracy, quality, up to datedness, timely availability and cost effectiveness.

Mangrove forest reserves are managed with the overall goal of conserving and managing the sustainability of forest through sustainable management, and maintaining its important roles in the national economy and environmental stability (Dato Hj Dahlan, 2007). This goal was approved by the National Forestry Council through the National Land Council in 1992 and is binding for the states in Peninsular Malaysia. Large mangrove areas were excised for residential, agricultural and industrial purposes. These are in direct conflict with the ecologically sound multiple-use management system and prompted an urgent need for the formulation of a national mangrove management plan to ensure rational management and utilization as well as resolving conflicts in resource utilization by the various sectors. It is expected that UPM-APSB's AISA airborne hyperspectral system technology should be able to provide an updates on the existing mangrove four broad classifications of the Malaysian mangrove forest namely, (a) Protection Forest for ensuring favorable climatic and physical conditions of the country, safeguarding of water resources, soil fertility, environmental quality, conservation of biological diversity and the minimization of damage by floods and erosion to rivers and agricultural land (ha), (b) Production Forest for the supply in perpetuity at reasonable rates of all forms of forest produce which can be economically produced within the country and are required for agricultural, domestic and industrial purposes as well as for export (ha), (c) Amenity Forest for the conservation of adequate forest areas for recreation; eco-tourism and in promoting public awareness in forestry (ha), and (d) Research and Education forest for the conduct of research, education and conservation of biological diversity (ha) (Dato Hj Dahlan, 2007). Certainly, this broad classification can be easily mapped, monitored, quantified and updated in near real-time and precision with the UPM-APSB's AISA airborne hyperspectral imaging data as per the State Forestry Department's demand and request.

3.4 Future strategy in managing mangrove forests

FDPM have been successful in managing and conserving the mangrove forests in Peninsular Malaysia since the early 1900s. However, there is room for further improvement with the use of airborne hyperspectral sensing technology. It is therefore possible to revise the NFP and other related policies from time to time (pending on airborne request and schedule) to match prevailing conditions and requirements, and to ensure the realization of its multi-functions in perpetuity. The co-operation and co-ordination of relevant agencies will be fostered with respect to specific objectives in safeguarding the mangrove ecosystems for conservation and management of Tsunami. Future management of mangrove forests in P. Malaysia will continue to adopt an integrated approach by further refining the current management approach and incorporating latest findings and updated geospatial information through more vigorous airborne hyperspectral imaging data capture and acquisition on mangrove forests. The remaining mangrove forests will be mapped, quantified, classified and protected to ensure its biological diversity remained intact and not lost in the name of development. Disruption to the mangrove ecosystems and functions must cease, the diversity of remaining mangroves must be retained, and where possible rehabilitation, restoration and re-creation of mangroves habitats must continue to be pursued for Tsumani.

4. Conclusion

There is no doubt that FDPMP recognizes the significant role of mangroves and is fully committed to ensure that the Malaysian mangrove resources are well-managed, sustained, utilized, conserved and preserved for the benefits of present and future generations. It is expected that with the newly introduced UPM-APSB's AISA airborne hyperspectral imaging technology, FDPMP will move a step forward and take a more positive approach by giving increasing emphasis on the geospatial database development for conservation aspects of mangroves forest management. The future success in the sustainable management of mangrove forests by FDPMP using a geospatial database of mangroves will in fact contribute to the sustainability of the wetlands in Malaysia which is crucial to the survival and future health of our Mother Earth. Further investigation on the use of UPM-APSB's AISA airborne hyperspectral sensor technology for different management applications of mangrove forests is recommended to assess the full reliability of the system.

References

- Amjad, A. Shah and Kamaruzaman Jusoff. (2007). Mangrove conservation through community participation in Pakistan: The case of Sonmiani Bay. The 5th WSEAS International Conference on Environment, Ecosystems and Development (EED'07), Puerto De La Cruz, Tenerife, Canary Islands, Spain, December 14-16, 2007.7p.
- Aschbacher, J.K., Ofren, R.B., Delsol, J.P., Suselo, T.B., Vibulsresth, S.K. and Charrupat, T.K. (1995). An integrated comparative approach to mangrove vegetation mapping using advanced remote sensing and GIS technologies: Preliminary results. *Hydrobiologia*. 295, 285–294.
- Amjad, A. Shah, Kasawani, I., and Kamaruzaman, J. (2007). Degradation of Indus Delta mangroves in Pakistan. *In: Procs/CD of International Seminar on Wetlands & Sustainability*, 4-6 September, 2007, Puteri Pacific Hotel, Johor Bharu, Johor, Malaysia. pp.347-360.
- Dato' Hj. Dahlan Hj. Taha. (2007). Policy and management of mangrove forests in Peninsular Malaysia. A keynote paper presented at The International Seminar on Wetlands & Sustainability (ISWS'07), 4-6 September, 2007, Puteri Pacific Hotel, Johor Bharu, Johor, Malaysia. 10p.
- Kamaruzaman Jusoff. (2006). UPM-APSB's AISA airborne hyperspectral imaging for individual mangrove mapping in Port Klang. *In: Procs. National Seminar on Science, Technology & Social Science STSS2006*, 30-31 May, 2006, Swiss Garden Resort & Spa, Kuantan, Pahang, Malaysia. pp.751-759.
- Kamaruzaman J. and Kasawani, I. (2007). Spectral signatures of some mangrove species in Malaysia. The 5th WSEAS International Conference on Environment, Ecosystems and Development (EED'07), Puerto De La Cruz, Tenerife, Canary Islands, Spain, December 14-16, 2007.10p.
- Kasawani, I., Kamaruzaman J., and Nurun Nadhirah, M.I. (2007). A study of forest structure, diversity index and above-ground biomass at Tok Bali Mangrove Forest, Kelantan, Malaysia. The 5th WSEAS International Conference on Environment, Ecosystems and Development (EED'07) Puerto De La Cruz, Tenerife, Canary Islands, Spain, December 14 -16, 2007.9p.
- Kasawani, I., Najiha S. Amjad, A. S., and Kamaruzaman, J. (2007). Wetland cover changes in Kuala Trengganu District using LandsatTM imagery. *In: Procs/CD of International Seminar on Wetlands & Sustainability*, 4-6 September, 2007, Puteri Pacific Hotel, Johor Bharu, Johor, Malaysia. pp.111-118.
- Nur Ilayana Mohd Zukki and Kamaruzaman Jusoff. (2007). Aplikasi proses analisis hierarki untuk pengurusan persis hutan paya bakau. (*In Malay*). A Poster Paper presented at the *Bengkel Hutan Pesisiran Pantai Negara: Kesedaran dan Tindakan Bersama*, 5-7 November 2007. Residence Resort Paka, Terengganu Darul Iman, Malaysia. 5p.
- Wan Faridah Akhmal W. Jusoh, Kamaruzaman Jusoff and Zelina Zaiton Ibrahim. (2007). Meningkatkan kesedaran bakau melalui eko-pelancungan kelip-kelip. (*In Malay*). A Poster Paper presented at the *Bengkel Hutan Pesisiran Pantai Negara: Kesedaran dan Tindakan Bersama*, 5-7 November 2007. Residence Resort Paka, Terengganu Darul Iman, Malaysia. 5p.



Figure 1. A map of Peninsular Malaysia showing the location of study site (in red circle)



Figure 2. A complete UPM-APSB's AISA airborne hyperspectral sensor system

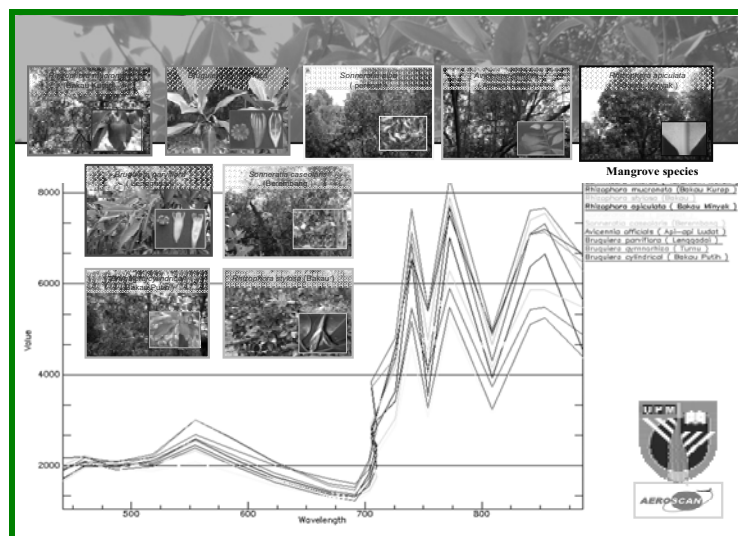


Figure 3. The spectral signature profile of nine mangrove species developed using the UPM-APSB's AISA sensor



The Quality Test to Tarim River Sluice Concrete by the Rebound Method

Xindong Zhang & Yue Han

College of Water Resources and Architectural Engineering

Tarim University

Alar City 843300, China

Tel: 86-997-478-6700 E-mail: zxdhy@yahoo.cn

Abstract

The nondestructive examination (NDE) used for concrete deflection is a new method of quality testing for concrete and it is characterized by rapid measurement, high precision and low cost. In this article, we introduce the basic principle and the development application of the rebound method. Taking the engineering project in Tarim Dam as an example, we use the rebound method to test the concrete structure in the Tarim River sluice, introduce the test method and approach of the rebound method, and analyze the test result. The result indicates that the nondestructive examination based on the concrete rebound method is an effective method with simple operation, easy operation, convenient use and high computation precision to test the quality of the concrete with large volume and achieve the requirement of the project.

Keywords: The rebound method, Nondestructive examination (NDE), Concrete, Quality test

1. Introduction

With the process of time, the problems of structure security induced by low standard, aging and the gradual weakening of structure function after long-term using are increasingly serious for old buildings. The repair and strengthening for the existing buildings can not only save their intrinsic characters, but possess considerable economic benefits such as small investment, little influence and quick efficiency and large social benefits. However we should implement the appraisal of reliability for the structure of the existing building before repair, alteration and strengthening, and the intensity of concrete is one of key factors to decide the strength performance and reliability for the structure of concrete (Tang, 2000, p.57-59). The test technology of concrete structure can be divided into the local breakage method and the nondestructive method according to its influencing degree to the structure. The local breakage method would induce local breakages for the concrete structure, and it is restricted by many factors such as high expenses and small range inspection. The nondestructive method is popular by extensive engineering technical personnel because of non-destruction, simple instrument, convenient operation, repetitive test for concrete structure, and the test with large range. So in this article, we mainly discuss the rebound nondestructive test technology of the concrete, and introduce the principle and characters of the test technology combining with the actual condition of the Tarim River sluice, which can offer references for the diagnoses of the bearing capacity and endurance of original structure and prepare for future works.

2. The test of concrete by the rebound method

2.1 Development and application of the rebound method

The rebound method was invented by engineers of Switzerland, and it is the witnessed test technology of structured concrete which calculates the pressive strength through measuring the surface rigidity of the concrete (Wu, 2003). Since the technology came out, it has been applied in the application of construction project for half century. Though for a long time, a series of instruments used in the nondestructive test of concrete had been developed in foreign and domestic practices, and various new test technologies have been deeply studied, but the rebound method has kept its predominant status all along in the nondestructive test domain of concrete because the instrument has simple structure and the economic and applicable test method with high efficiency and high test precision is easy to be grasped. With the development of the rebound method, the technology exerts large function in the quality test of concrete project, and it has been extensively applied in many industries such as construction, highway, traffic, water conservation and railway.

2.2 Test method and principle of the rebound method

The rebound method uses a heavy hammer drove by a spring to strike the surface of the concrete through the resilient pole, and measures the distance of the heavy hammer which is rebounded back, and takes the rebound value (the ratio

between the rebound distance and the initial length of the spring) as the relative index of the intensity to calculate the intensity of the concrete. The rebound value reflects the elasticity and plasticity of the concrete to some extent, and it has necessary association with the intensity of the concrete, and we can establish the relationship equation between the rebound value and the intensity of the concrete, i.e. the strength cure. Usually, because the surface rigidity of the concrete by carbonization increases to make the rebound measured higher, and different carbonization depths have different influencing degrees to the rebound value. Large numbers of researches and locale test indicate that the carbonization depth reflect the comprehensive influence including the age of the age and the environment of the concrete, so we should take the carbonization depth as another parameter for the measuring curve of strength.

3. The test of concrete intensity for the sluice of Tarim River by the rebound method

3.1 Introduction of the project

The Tarim River Sluice Division Pivotal Project is located in the middle reaches of the Akshu River in the town of Baishenairike of the county of Awat, and it is the total diversion pivotal project in the north farming irrigation area and the south farming irrigation area of Xinjiang Corps Farming First Division. The Tarim sluice mainly includes the release sluice, the north in-sluice and the south in-sluice, and the upper reaches and the lower reaches watercourse repair segments. The sluice has 32 holes, every hole is 6 meters, and the total net width is 192 meter, and the span is 223 meters. The project was firstly established in April of 1971, and completed and operated in June of 1972. To enhance the defending ability of the project, the government invested 9.1 million Yuan in 1992 to strengthen the drainage dike, training dike and spur dike. The construction of the project enhances the irrigation rate in the irrigation area of Tarim River, effectively controls the corrosion of flood to shores, reduces much mud and sand, discharge the flood of 2.63 billion m³ to the lower reaches of Tarim River every year, and exerts large benefits for the ecological construction for the farming development in the irrigation area.

3.2 The concrete test for the sluice of Tarim River

3.2.1 The test of concrete intensity for the sluice of Tarim River

According to the regulations of “Technical Specification for Inspection of Concrete Compressive Strength by Rebound Method (JGJ/T23-92)”, the test adopts the @-3000 concrete rebound meter which is inspected by the measure department. We use the rebound meter strikes the pouring face and the side face, and every measured area is about 20cm×20cm, and in all rebound values, we respectively delete three maximum values and three minimum values and get the mean in the surplus 10 rebound values, so we can confirm the pressive strength according to the rebound values and the carbonization depth in the area.

3.2.2 The carbonization depth test for the sluice concrete of Tarim River

We adopt 500ml phenolphthalein solvent of 1% to confect the phenolphthalein alcohol solvent to measure the carbonization degree of the bridge pier. To obtain exact carbonization value, we should measure several groups to get the mean value.

3.3 Data processing

The results of data processing are seen in Figure 1 and Figure 2.

3.4 Test analysis of the rebound method

At the same time and under the same condition, we measure the rebound value by the @-3000 rebound meter with same standard, and from the test result, the maximum value of Tarim River sluice is 57.6MPa, and the minimum value is 33.0MPa, and the former is 1.75 times of the latter, but the mean value is about 47MPa, which indicates the rebound distance is large when the rebound hammer strikes the carpolite (especially for big carpolite), and the distance is small when the rebound hammer strikes the mortar, and the distance would be smaller when pores exist in mortar. When the even values have small differences in the measure area, it proves that the construction quality was better, the construction method was exact, the construction technology was reasonable and the construction level was higher.

4. Conclusions

The nondestructive examination based on the concrete rebound method is an effective method with simple operation, easy operation, convenient use and high computation precision, and it can completely fulfill the requirement of the civil engineering. We adopt the test technology based on the concrete rebound method to evaluate the sluice of Tarim River, and the result can offer references for the diagnoses of the bearing capacity and endurance of original structure and prepare for future works.

References

Tang, Yeqing & Wan, Molin. (2000). *Building Reconstruction and Disease Treatment*. Beijing: China Architecture and Building Press. p.57-59.

Wu, Xinxuan. (2003). *Handbook of Non-destructive Testing Techniques of Concrete*. Beijing: China Communications Press.

Zhang, Junzhe. (1989). *Application of Undamaged Concrete Checking and Measuring Techniques*. Beijing: Science & Technology Press.

Zhao, Shangchuan & Zhao, Guofan. (2001). Prediction of Remaining Service Life of Existing Concrete Structures Based on Reliability. *Building Science*. No.3(5). p.41-44.

Table 1. Concrete test data of Tarim River sluice

Record of concrete test by the rebound method																			
No.	Rebound value Ri																		carbonization depth
measure area	R1	R2	R3	R4	R5	R6	R7	R8	R9	R10	R11	R12	R13	R14	R15	R16	Rm	f_{cu}^c	di(mm)
1	55	58	59	53	43	60	53	60	46	49	56	57	46	58	62	55	55.3	57.4	4
2	42	50	49	44	42	48	50	50	48	55	45	46	53	50	47	46	47.9	43.0	4
3	59	57	50	55	53	59	62	61	52	51	59	47	52	41	57	59	55.4	57.6	4
4	48	46	41	48	46	49	56	41	41	48	48	47	49	51	48	46	47.4	42.1	4
5	43	48	47	43	53	54	49	54	50	39	40	40	41	38	48	49	45.8	39.3	4
6	58	54	48	57	54	55	58	51	54	33	64	53	54	51	54	54	54.0	54.7	4
7	55	53	48	61	42	41	39	42	43	45	40	46	44	45	47	48	45.0	37.9	4
8	49	56	61	53	53	57	54	60	53	43	58	58	49	56	45	56	54.5	55.8	4
9	54	59	44	46	52	54	53	51	54	55	52	50	53	52	51	49	52.2	51.1	4
10	55	54	58	52	52	53	55	55	50	52	42	56	54	52	54	43	53.3	53.3	4
11	50	42	42	48	57	44	46	41	40	43	57	42	47	50	43	49	45.4	38.6	4
12	45	40	62	56	47	51	58	54	50	60	44	56	57	52	43	56	52.4	51.5	4
13	47	49	51	44	55	58	51	49	58	53	52	58	56	38	48	51	51.5	49.8	4
14	47	44	44	46	47	55	51	40	52	56	53	60	47	58	50	52	50.0	46.9	4
15	43	38	46	41	41	47	41	36	43	46	43	42	38	36	44	44	42.0	33.0	4

Table 2. Test result of Tarim River sluice

Intensity computation (Mpa)						Intensity evaluation (MPa)
Standard deviation	7.96	Minimum	33.0	Even value	47.5	34.4



Simulation of a Four-Car Elevator Operation Using MATLAB

Saw Soon King & Omrane Bouketir

School of Electrical and Electronic Engineering

University of Nottingham, Malaysia Campus

Jalan Broga 43500 Semenyih Selangor, MALAYSIA

Tel: 60-3-8924-8159 E-mail: omrane@nottingham.edu.my

Abstract

The design and simulation of a four-cars-elevator controller in a nine storey building is described in this paper. The design and simulation were accomplished using MATLABTM fuzzy logic toolbox. The logic of the controller of a multi-car elevator has to be designed in such a way that the average waiting time is minimized while keeping the energy consumption of the system optimum. This is a multi-criteria optimization problem in stochastic environment and is best approached through Artificial Intelligent techniques. The work here focuses mainly on extracting the rules to minimize factors (i.e. waiting time, travelled distance and riding time) in order to minimize the energy consumed by the system. In this paper a detailed algorithm is presented to achieve the multiple objectives of minimizing the waiting time and the distance travelled simultaneously. This was accomplished by distributing different weightage to different quantities and then minimizing a combined cost. A simulator has been built with interactive GUI in Matlab to evaluate the efficacy of the algorithm.

Keywords: Elevator, Fuzzy Logic, Membership Function, Optimization, Simulator

1. Introduction

Elevators are often a requirement in new buildings with multiple floors throughout the world. In high rise buildings, there is a need for intelligent elevator control system in order to obtain optimum performance.

Usually a high rise building contains more than one elevator to increase the optimization of the elevator performance. When a few hall requests are registered, the elevator controller will decide which of the elevator will serve which of the incoming hall requests. Therefore the controller plays an important role in determining the time for which the passengers have to wait before the elevator arrives (waiting time). The waiting times of the passenger for an elevator to arrive or to serve their request are often heard as complaints by the passengers. Consequently the controller will reduce the waiting time of the passenger. However, in the process of reducing the waiting time, other quantities like the time spent by the people in the elevator (riding time) and the total distance travelled by the elevator increases, which is also unwanted. Therefore an intelligent elevator control system is required to solve this problem of optimization of multiple objectives. The multiple objectives in the current controller design are minimization of waiting time and distance travelled simultaneously.

However, an optimum solution to this problem is not known yet (Crites and Barto, 1998), or perhaps not possible due to its stochastic nature. In (Crites and Barto, 1998) Reinforcement Learning (RL) algorithms have been demonstrated to be powerful heuristic methods for addressing large-scale control problems and have been applied to elevator group control. A team of RL agents, each of which is responsible for controlling one elevator car was used. The team receives a global reward signal which appears noisy to each agent due to the effects of the actions of the other agents, the random nature of the arrivals and the incomplete observation of the state. The results demonstrated the power of multi-agent RL on a very large scale stochastic dynamic optimization problem of practical utility. Other works in this area based on fuzzy logic can be found in (Tan et al., 1997), (Kim et al., 1998), (Marja-Liasa, 1998), (Wang et al., 1999), (Koehler & Ottiger, 2002) and (Tanuj, 2004).

In this paper a detailed algorithm is presented to achieve the multiple objectives of minimizing the waiting time and the distance travelled simultaneously. This was accomplished by distributing different weightage to different quantities and then minimizing a combined cost. A simulator has been built with interactive GUI in Matlab to evaluate the effectiveness of the algorithm.

2. Elevator Configuration

The number of the elevators was fixed to stress more on the group control of elevators rather than the selection of

optimum number of elevators. Most of the features are easy to understand. Thus, some basic features of the elevators have been adopted as follows:

- The building has 9 floors (1-9), 4 elevators which are independent of each other operationally but controlled by a common supervisory group controller based on fuzzy logic.
- The elevator travels in a fixed constant speed which is 1.5 meters per second. The inter-floor distance between each floor is selected to be 3 meters, so the elevator will only take 2 seconds to move from one floor to another. For each stops, the elevator will take 6 seconds to allow passengers to board or to alight the car.

3. Traffic Generation

The traffic generation for the hall requests is produced and generated in such a way that it mimics real life situations. It is well known that the real world stochastic processes like arrival of users for a service follow a Poisson distribution. For this case, the stochastic process is the arrival of passengers for the elevator services.

The probability that there are exactly x occurrences that take place during a fixed amount of time-interval is given by:

$$P(x, \lambda) = \frac{e^{-\lambda} \lambda^x}{x!} \quad (1).$$

The traffic generation for this elevator system is divided into 5 different modes:

1. busy mode, 2. moderate mode, 3. up-peak mode, 4. down-peak mode, and 5. off-peak mode. The traffic for each mode is created using the random integer generator ("randint") in MATLAB. In up-peak mode, all the hall requests are registered at the ground floor while in down-peak mode, all the car request's destination is to the ground floor. On the other hand, for other traffic modes, their hall requests are generated randomly from the ground floor to the highest floor. Table 1 describes specifications of the 5 different modes and their respective arrival rates.

3.1 Input and Output Parameters

In order to achieve good performance, the elevator fuzzy logic controller uses 3 parameters as the control input and one parameter for output. These parameters represent the criteria or objective to be optimized in this elevator system. The input variables for the elevator system are:

Waiting time: is the total time that the passenger has to wait before an elevator serves his/her request.

Travelling distance: is the total distance travelled by an elevator before reaching a request from present state. Minimizing the distance means minimizing the energy consumed by the system.

Loading: is the number of passengers in an elevator. This is to have an idea about the load of each elevator so the controller can decide which car may serve a request.

Whereas the output variable is:

Priority: Output of the fuzzy logic controller, where the elevator (among the four) with the highest value of priority will be assigned.

3.2 Estimation of the Range for Input Variables

The range of the inputs for the elevator system have been estimated and found to be:

- Maximum waiting time is when the request is from the 9th floor and there is a request in every floor.

The expected waiting time is expressed in terms of number of floors and number of stops since the constant speed of the elevator is 1.5 meter per second which is in agreement to existing systems (Tanuj, 2004) while the height of each floor is 3 meter (inter-floor distance = 3 meters). Therefore the elevator takes only two second to travel from one floor to another. For each elevator stops, it takes approximately 6 seconds to unload or to load passengers. So the expression for calculating the waiting time is:

$$ewt = 6 * ns + 2 * nf; \text{ where:}$$

ewt : expected waiting time

ns : number of stops

nf : number of floors between car position and the request.

- Maximum distance required to be travelled if from the ground floor to the ninth floor is 21 meters.

The expected distance is equivalent to the number of floors that a particular elevator has to travel to reach the request under consideration and assuming that there are no new requests assigned to this elevator during the duration for the elevator to travel to the request. The maximum value which is 24 occurs when the hall request is at the 9th floor while the elevator is situated at the ground floor (1st floor). So the expression for calculating the distance is:

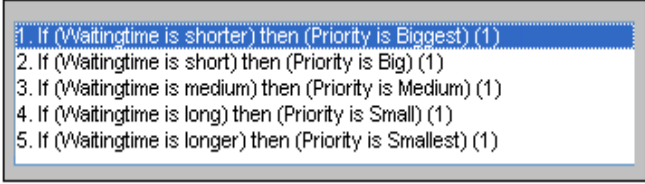
$ed=3*nf$ where:

nf : number of floors between car position and the request.

4. Membership Functions and Fuzzy Sets

The membership function that is used for each quantity for the input variables is triangle function. For each quantity, a total of five membership functions were used. As for the output variable 3 triangle membership functions and 2 trapezoids function are used. Figure 1 shows the membership function for waiting time input

There are 4 different types of fuzzy rule sets constructed with each to minimize a respective parameter. One of the fuzzy rules set minimizes waiting time, other set minimizes the distance travelled by the elevators, third set minimizes the loading and the last set minimizes all of them simultaneously. A sample of the first set is given in the passage below.



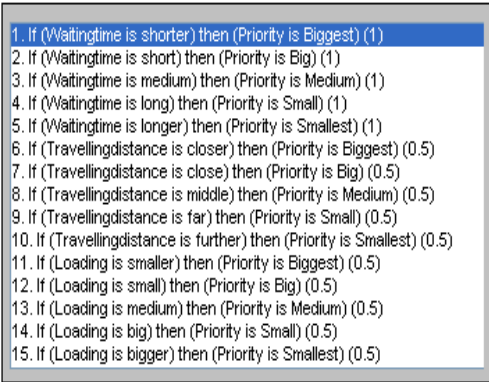
```

1. If (Waitingtime is shorter) then (Priority is Biggest) (1)
2. If (Waitingtime is short) then (Priority is Big) (1)
3. If (Waitingtime is medium) then (Priority is Medium) (1)
4. If (Waitingtime is long) then (Priority is Small) (1)
5. If (Waitingtime is longer) then (Priority is Smallest) (1)

```

There are only 5 rules used and all of the rules have the same weightage which is one.

In the last set there are altogether 15 IF/THEN rules. All rules are described in one dimensional space for each input and output as shown below:



```

1. If (Waitingtime is shorter) then (Priority is Biggest) (1)
2. If (Waitingtime is short) then (Priority is Big) (1)
3. If (Waitingtime is medium) then (Priority is Medium) (1)
4. If (Waitingtime is long) then (Priority is Small) (1)
5. If (Waitingtime is longer) then (Priority is Smallest) (1)
6. If (Travellingdistance is closer) then (Priority is Biggest) (0.5)
7. If (Travellingdistance is close) then (Priority is Big) (0.5)
8. If (Travellingdistance is middle) then (Priority is Medium) (0.5)
9. If (Travellingdistance is far) then (Priority is Small) (0.5)
10. If (Travellingdistance is further) then (Priority is Smallest) (0.5)
11. If (Loading is smaller) then (Priority is Biggest) (0.5)
12. If (Loading is small) then (Priority is Big) (0.5)
13. If (Loading is medium) then (Priority is Medium) (0.5)
14. If (Loading is big) then (Priority is Small) (0.5)
15. If (Loading is bigger) then (Priority is Smallest) (0.5)

```

The number appearing at the end of each rule indicates the rule's weight. Every rule has a weight which ranges from 0 to 1. Rules with higher weight will have a higher priority. The input waiting time is of the highest priority since the rule weight for it is 1.0 which is higher as compared to the other input variables. Based on the rules above, the fuzzy logic-based elevator will optimize the minimization of waiting time before considering the other quantities.

The rules above try to minimize all objectives simultaneously with the input variable of waiting time given the highest priority followed by loading and distance according to the different weightage assigned to them.

The fuzzy output which is priority indicates the suitability of a particular elevator to be assigned to a particular hall request. Depending on the fuzzy inputs and the rule bases, the output fuzzy set, 'priority' is computed using Mamdani inference scheme.

5. Rules Implementation in MATALB

Here extracts from the overall source code developed in MATLAB are given.

5.1 Traffic Generation

```

65 %===== Traffic Generation =====
66 % To choose the traffic mode
67 traffic_mode = input('Traffic : 1 for busy(peak), 2 for moderate and 3 for off-peak')
68 while (traffic_mode > 3) & (traffic < 1) % will ask user to input again if input is out of the 1-3 range
69     traffic_mode = input('1 for busy(peak), 2 for moderate and 3 for off-peak')
70 end
71 n1 = 0;
72 for c = 1:1:300
73
74     if c > n1
75
76         if traffic_mode == 1
77             interval = randint(1,1,[4,8]) % 1 input in 4-8 seconds ,38-75 inputs in 5 mins
78         elseif traffic_mode == 2
79             interval = randint(1,1,[6,20]) % 1 input in 6-20 seconds ,15-50 inputs in 5 mins
80         elseif traffic_mode == 3
81             interval = randint(1,1,[20,40]) % 1 input in 20-40 seconds,8-15 inputs in 5 mins
82         end
83         c1 = randint(1,1,[1+n1,interval+n1]) % "generates an output of 1 x 1 integer matrix and the output is
84             % limited by the range given in the square bracket"
85         n1 = n1 + interval
86     end
87
88     if c == c1
89
90         hall_requestx(1,c) = randint(1,1,[1,9])

```

5.2 Calculation of Waiting Time and Travelled Distance

```

182 - elseif status(1,d) == -1 & direction_of_hall_requestx(1,c) == 2 & move_car_position(1,d) >= hall_requestx(1,c)
183
184 -     if hall_requestx(1,c) >= max_carcall(1,d) % hall request is above the highest car request for an elevator
185
186 -         waiting_time(1,d) = abs(hall_requestx(1,c) - car_position(1,d))
187
188 -         distance(1,d) = 3*(abs(hall_requestx(1,c) - car_position(1,d)))
189
190 -         a = readfis('Fuzzy_rules'); % To read a fuzzy inference system from Fuzzy_rules.fis file
191 -         priorities(1,d) = evalfis([waiting_time(1,d) distance(1,d) loading(1,d)],a)
192 -         % evalfis = To perform fuzzy inference calculation to obtain the priorities value
193 -         elseif (hall_requestx(1,c) > min_carcall(1,d)) & (hall_requestx(1,c) < max_carcall(1,d))
194 -             % hall request is between the lowest and the highest car request
195 -             waiting_time(1,d) = abs(hall_requestx(1,c) - car_position(1,d)) + (3*(no_of_car_callb(1,d)))
196
197 -             distance(1,d) = 3*(abs(hall_requestx(1,c) - car_position(1,d)))
198
199 -             a = readfis('Fuzzy_rules');
200 -             priorities(1,d) = evalfis([waiting_time(1,d) distance(1,d) loading(1,d)],a)
201
202 -         elseif hall_requestx(1,d) <= min_carcall(1,d) % hall request is below the lowest car request
203
204 -             waiting_time(1,d) = abs(hall_requestx(1,c) - car_position(1,d)) + (3*no_of_car_callc(1,d))
205 -             no_of_car_callc = 0;
206 -             distance(1,d) = 3*(abs(hall_requestx(1,c) - car_position(1,d)))
207
208 -             a = readfis('Fuzzy_rules');
209 -             priorities(1,d) = evalfis([waiting_time(1,d) distance(1,d) loading(1,d)],a)
210
211 -     end

```

5.3 Moving Status Assignment

```

404 - for z = 1:1:4
405 -     if loading(1,z) ~= 20           % Condition is satisfied if the loading for an elevator is not maximum (i.e. loading = 20)
406 -         if car_assignment(1,z) >= 1 % Condition is satisfied if the car assignment for a elevator is more than 0
407 -             if move_car_position(1,z) ~= 0
408 -                 for e = 1:1:5
409 -                     if unloading(z,:) == 0 % Condition is satisfied if an elevator has unload all of its passengers aboard
410 -                         % ===== An elevator has reach an active hall request & its direction is going up ===== %
411 -                         if (move_car_position(1,z) == hall_request(e,z)) & (hall_request(e,z) ~= 0) & direction_of_hall_requestx(1,c) == 1
412 -                             moving_status(1,z) = 1 % elevator has an active request above the present car position
413 -                             status(1,z) = 0 % elevator is set to stationary
414 -                         % ===== An elevator has reach an active hall request & its direction is going down ===== %
415 -                         elseif (move_car_position(1,z) == hall_request(e,z)) & (hall_request(e,z) ~= 0) & direction_of_hall_requestx(1,c) == 2
416 -                             moving_status(1,z) = -1 % elevator has an active request below the present car position
417 -                             status(1,z) = 0 % elevator is set to stationary
418 -                         % ===== An elevator has an active hall request above the present car position ===== %
419 -                         elseif (hall_request(e,z) > move_car_position(1,z)) & (hall_request(e,z) ~= 0)
420 -                             moving_status(1,z) = 1 % elevator has an active request above the present car position
421 -                             status(1,z) = 1 % elevator moving up
422 -                         % ===== An elevator has an active hall request below the present car position ===== %
423 -                         elseif (hall_request(e,z) < move_car_position(1,z)) & (hall_request(e,z) ~= 0)
424 -                             moving_status(1,z) = -1 % elevator has an active request below the present car position
425 -                             status(1,z) = -1 % elevator moving down
426 -                     end
427 -                 end
428 -             end
429 -         end
430 -     end
431 - end
432 - end

```

Definitions of some variables used in the source code are as follows:

car assignment; it is an array of dimension 1 x 4. At the start, all the 4 values are set to zero since there is no hall request being registered. Once a hall request is assigned to an elevator, for instance if elevator 1 is being assigned to a hall request, car_assignment(1,1) will be set to 1 which means the first row and the first column of the array car_assignment will be set to 1.

```

car_assignment =

     1     0     0     0

```

car position (move_car_position); it is also an array of dimension 1 x 4 and its value is only from 1 to 9 which represents the floors in the building. In the example below, elevator 1 is located at 1st floor, elevator 2 is positioned at the 4th floor, elevator 3 is situated at the 7th floor and lastly elevator 4 is placed at the 9th floor.

```

car_position =

     1     4     7     9

```

hall_request; represents the hall requests that are active or registered. Similar to the car position, the values varies from 1-9. The array's column size is determined by the number of hall requests served by a particular elevator. If there are 3 hall requests assigned to an elevator, then the array size would be 3 x 4. Example below shows that the 3 hall requests for elevator 1 are at the 2nd floor, 4th floor and 7th floor.

```

hall_request =

     2     0     0     0
     4     0     0     0
     7     0     0     0

```

direction_of_hall_request; this variable represents the direction of the hall requests that are registered or active. Similar to the hall request, it has the same array size as the hall request. An up button is represented by '1' while a down button is represented by '2'. In the example below a 3 hall requests with the desire of moving upwards are registered for elevator 1 and a hall request moving downwards is active for elevator 2.

direction_of_hall_request =

```

1    2    0    0
1    0    0    0
1    0    0    0

```

status; also of dimension 1 x 4 and it represents the status of each elevator and it could be either 0, 1 or -1 for each elevator corresponding to idle, up and down respectively. Value below shows that elevator 1 is moving up, elevator 2 moving down while elevator 3 and 4 are idle.

status =

```

1   -1    0    0

```

loading; represents the number of people inside an elevator and it has an array size of 1 x 4. The maximum capacity of an elevator is 23 persons (1500Kg). The loading value below shows that there are currently 20, 4 and 13 people in elevator 1, 2 and 3 respectively

loading =

```

20    4    13    0

```

moving_status; it is of dimension 1 x 4 and it represents whether there are hall request or car request that are still active for a particular elevator. If there are still hall request that have not been served and the request are above the car position, then it will be 1. Similarly if the request is below the car position then it will be -1. If an elevator has served all of its requests, then it will be 0. Example below shows that elevator 1 and 4 has served all of its requests while elevators 2 and 3 still have active requests below and above them respectively

moving_status =

```

0   -1    1    0

```

Carcall; it represents the car requests that are active or registered and it has an array size of 4 x 9. Each row represents each elevator and each column represents each floor in the building where the first row represents elevator 1 and so on. The numbers shown below represent the active car requests and their corresponding floors.

CARCALL =

```

1  NaN  NaN  NaN    5  NaN  NaN    8  NaN
NaN  NaN    3  NaN  NaN  NaN  NaN  NaN  NaN
NaN    2  NaN  NaN  NaN    6  NaN  NaN  NaN
NaN  NaN  NaN  NaN  NaN  NaN  NaN  NaN  NaN

```

Unloading; It represents the number of people that is supposed to leave the elevator at a specific floor. It has the same dimension as **Carall** which is 4 x 9. Similar to CARCALL, each row represents each elevator and each column represents the number of people leaving the elevator at a specific floor where the first row represents elevator 1 and the first column represents the first floor and so on. The numbers shown in figure 3.21 below represents the number of people leaving the elevator at the corresponding floors.

unloading =

```

5  NaN  NaN  NaN    4  NaN  NaN    2  NaN
NaN  NaN   17  NaN  NaN  NaN  NaN  NaN  NaN
NaN   12  NaN  NaN  NaN    4  NaN  NaN  NaN
NaN  NaN  NaN  NaN  NaN  NaN  NaN  NaN  NaN

```

6. Results and Discussions

The simulation was run for 5 different traffic patterns using the four different fuzzy rule sets. For each traffic pattern, two quantities which are **average waiting time** and **average distance** were evaluated for different arrival rates ranging

from 5 to 38 hall requests per 5 minutes using four different fuzzy set rules with each trying to minimize their respective parameters.

Each simulation case was run for a simulated time of 1 hour for each traffic pattern. The averages obtained are based on the number of hall requests registered within the 1 hour simulation time. The traffic patterns are busy, moderate, up-peak, down-peak, off-peak and constant whereby their specification were defined in Table 1. The results are shown in Tables 2, 3, 4 and 5. Graphical representations of the obtained results are shown in figures 2, and 3.

From the results shown in the tables and the figures, it can be seen that the waiting time is minimum when the waiting time minimization logic is used. Similarly, distance travelled is minimum when the distance minimization logic is chosen for all five traffic patterns. Minimization of distance travelled is basically means minimization of energy consumption. The least the elevator travel, the least the energy is needed to move the elevators. As for the minimization for loading, it has the highest value of averages for both the waiting time and distance travelled in all traffic modes because it only concentrates of minimizing the number of passengers in the elevator instead of the waiting time or distance which is the main concern in this system. Another important conclusion; is that the logic that minimizes all parameters simultaneously (optimum) produces good result because its averages stays close to the minimum value of the logic that minimizes the concerned quantities.

The average value for both waiting time and distance travelled decreases as the traffic reduces from busy to moderate and finally to off-peak. This is due to the reduction of arrival rate for each traffic whereby busy has the highest arrival rates followed by moderate and lastly off-peak.

7. Conclusion

A fuzzy logic-based controller of a four-car elevator was presented in this paper. A description of the configuration of the elevator including its design features, its inputs and outputs parameters were given. A set of fuzzy rules was drawn based on practical considerations; mainly minimization of waiting time and energy consumption. The simulation and execution of these rules using MATLAB showed the effectiveness of the controller in minimizing the waiting time compared to the works in the literature. However a hardware implementation is be accomplished in order to ascertain the simulation results.

References

- Crites, R. & Barto, A. (1998). Elevator group control using multiple reinforcement learning agents. *Machine Learning*: 33, 235-262.
- Kim, C. Kyoung, A., Kwang, H.L., and Kim, J.o. (1998). Design and Implementation of a Fuzzy Elevator Group Control System. *IEEE Transactions on Systems, Man and Cybernetics*, Part A: Systems and Humans: 28, 277-287.
- Koehler, J. & Ottiger, D. (2002). An AI-based approach to destination control in elevators. *AI Magazine*: 23(3), 59-79.
- Marja-Liisa, S. M. (1997). Elevator Group Control with Artificial Intelligence", KONE Corporation, Helsinki University of Technology, *Systems Analysis, Laboratory, Research Reports*, A67, October 1997.
- Tan K.K. Marzuki K., & Rubiyah Y. (1997). Intelligent Elevator Control By Ordinal Structure Fuzzy Logic Algorithm: *Proc. of ICARCV 97*, Singapore.
- Tanuj A. (2004). Intelligent Control of Group of Elevators. *Dual Degree Report*, Indian Institute of Technology Bombay, Mumbai, India.
- Wang, Y.-H., Hsia, K.-H., and Huang, Y.-P. (1999). Elevator Group Control with Fuzzy Logic and Genetic Algorithms. *Journal of the Chinese Fuzzy Systems Association*: 5(2), 25-34.

Table 1. Modes of Traffic Generation

Traffic Mode	Interval	Arrival Rate	Hall request generation	Car request generation
Busy	1 hall request in every 8 – 12 seconds	25 – 38 hall requests per 5 minutes	floor 1-9	floor 1-9
Moderate	1 hall request in every 10 – 20 seconds	15 – 30 hall requests per 5 minutes	floor 1-9	floor 1-9
Up-peak	1 hall request in every 12 – 30 seconds	10 – 25 hall requests per 5 minutes	floor 1	floor 2-9
Down-peak	1 hall request in every 12 – 30 seconds	10 – 25 hall requests per 5 minutes	floor 2-9	floor 1
Off-peak	1 hall request in every 12 – 30 seconds	10 – 25 hall requests per 5 minutes	floor 1-9	floor 1-9
Constant	Interval is selected manually ranging from 8 – 60 seconds	Arrival rate ranging from 5 – 38 hall request per 5 minutes	floor 1- 9	floor 1-9

Table 2. Averages for minimizes waiting time only for 5 traffic mode

Traffic mode	Busy	moderate	Up-peak	Down-peak	Off- peak
Total waiting time (s)	1128	574	1232	1034	301
Total distance (m)	2259	1426	2864	2109	886
Total loading	3493	2300	1727	1594	1725
Average waiting time (s)	3.14	2.32	7.29	6.30	1.75
Average distance (s)	6.29	5.77	16.95	12.86	5.15
Average loading	10	9	10	10	10
Total number of input	359	247	169	164	172

Table 3. Averages for minimizes distance only for 5 traffic mode

Traffic mode	Busy	moderate	Up-peak	Down-peak	Off- peak
Total waiting time (s)	1364	706	1440	1044	353
Total distance (m)	2172	1385	2660	2019	807
Total loading	3104	2383	1941	1533	1650
Average waiting time (s)	3.80	2.86	8.37	6.29	2.02
Average distance (s)	6.05	5.61	15.47	12.16	4.61
Average loading	9	10	11	9	9
Total number of input	359	247	172	166	175

Table 4. Averages minimizes loading only for 5 traffic mode

Traffic mode	Busy	moderate	Up-peak	Down-peak	Off- peak
Total waiting time (s)	2340	1396	1336	1144	832
Total distance (m)	3978	2562	3057	2175	1656
Total loading	3473	2420	1856	1708	1841
Average waiting time (s)	6.41	5.92	7.68	6.69	4.89
Average distance (s)	10.90	10.86	17.57	12.72	9.74
Average loading	10	10	11	10	11
Total number of input	365	236	174	171	170

Table 5. Averages for minimizing all parameters simultaneously for 5 traffic mode

Traffic mode	Busy	moderate	Up-peak	Down-peak	Off- peak
Total waiting time (s)	1220	690	1308	1162	317
Total distance (m)	2226	1482	2746	2214	816
Total loading	3273	2416	1998	1683	1816
Average waiting time (s)	3.40	2.79	7.69	6.60	1.88
Average distance (s)	6.20	6.00	16.15	12.58	4.83
Average loading	9	10	12	10	11
Total number of input	359	247	170	176	169

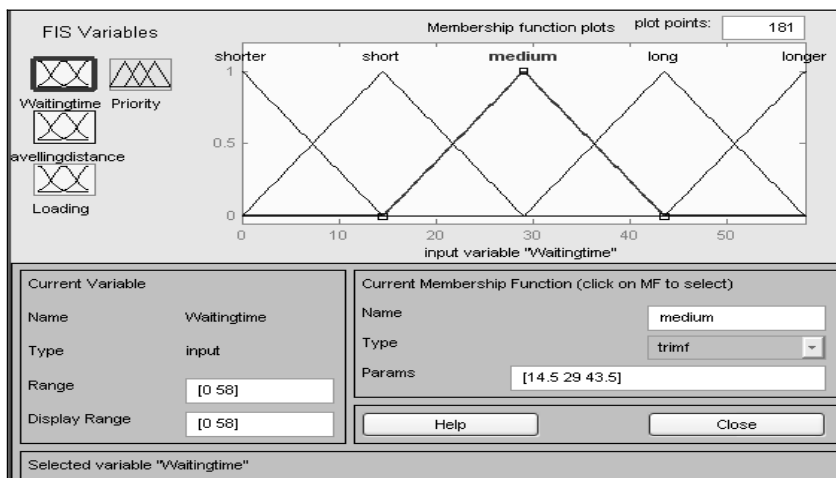


Figure 1. membership function for waiting time input

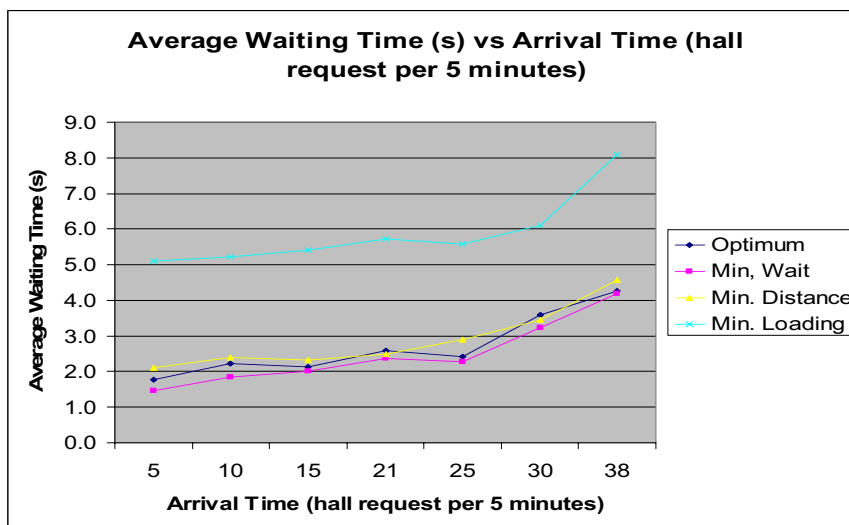


Figure 2. Averages for waiting time at various constant arrival rates

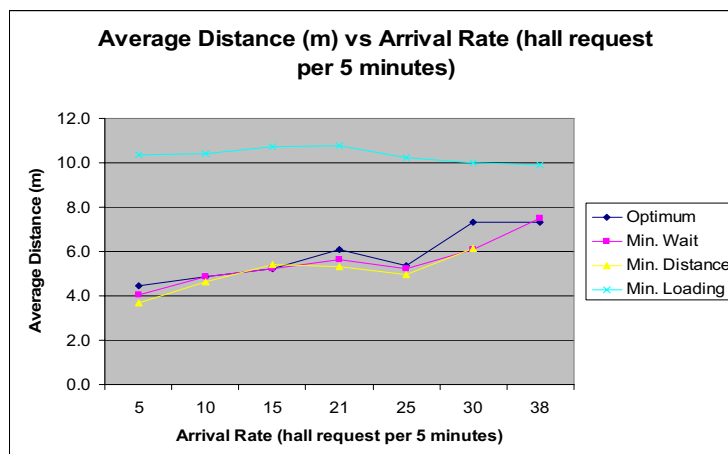


Figure 3. Averages for distance at various constant arrival rates



Analysis of Factors to Influence Single Yarn Strength CV Value

Dan Shen & Yi Zhang
Tianjin Polytechnic University
Tianjin 300160, China
E-mail: shendan27@163.com

Abstract

The single yarn strength CV value is one important index to measure the quality of yarn. Taking pure cotton and polyester cotton blended yarn as research objects, in this article, we systematically analyze the effects of some factors such as raw material blended ratio, yarn unevenness and twist unevenness on single yarn strength CV value, and use the mathematic analysis method to obtain the relationships between various influencing factors with single yarn strength value, and the result possesses directional meanings to enhance the quality of yarn in actual production.

Keywords: Yarn, Single yarn strength CV value, Yarn unevenness, Twist unevenness

The single yarn strength CV value is one important index to measure the quality of yarn. At present, certain deficiencies still exist to improve the yarn strength CV in China textile enterprises, and some enterprises can not achieve the national standards in the index and induce the demotion of yarn. The single yarn strength CV value influences not only the production efficiency of working procedures such as machine weaving and knitting, but also the appearance quality of finished products. Therefore, it is a necessary work to analyze the influencing factors of the single yarn strength CV value and discuss the measures to reduce the finished yarn single strength CV value in order to enhance the quality of the finished yarn.

1. Experiment

1.1 *Experimental equipments and experimental conditions*

Experiment materials: carded polyester cotton blended yarn T/C 80/20 13tex, T/C 90/10 13tex, combed polyester cotton blended yarn T/CJ 40/60 13tex, T/CJ 65/35 13tex.

Experiment equipments: single-yarn strength tester, Uster III yarn evenness tester, Y331 twist tester, one ten-thousandth electronic scale, oven.

Sampling method: sampling in the spinning locale (including the raw material and sample yarn), and every group quantity is confirmed by the national standards GB 3916-83, GB/T 398-83.

Experiment conditions: balanced sample in the room with constant temperature and constant wetness which can fulfill the condition of the primary standard atmosphere, and implementing evaluations of single yarn strength, yarn evenness, single yarn twist and single yarn hectometer weight.

1.2 *Experiment results*

1.2.1 Single yarn strength CV value test to the yarns with different blended ratios

The results are seen in Table 1.

1.2.2 Yarn evenness CV value, hectometer weight CV value and twist CV value test to the yarns with same blended ratio

In order to make clear the relationships between the yarn evenness CV value which reflects the thickness unevenness of the short segment of the yarn, the single yarn hectometer weight CV value which reflects the thickness unevenness of the long segment of the yarn, and the yarn twist unevenness ratio with the single yarn strength CV value, we choose the single yarn T/CJ 65/35 13tex to implement various tests, and the results are seen in Table 2.

2. Experiment results and analysis

2.1 *The relationship between the blended ratio and single yarn strength CV value*

From Table 1, the blended ratios of the carded polyester cotton blended yarn are different, so the single yarn strength CV values are different, and the single yarn strength CV value of T/C 90/10 13tex is smaller than the value of T/C 80/20 13tex. The reason is that the content of short fiber in the cotton string before blending is more, and with the increase of cotton fiber content, the fiber length tidiness in the blended material deteriorates, and because the carder yarn lacks short fiber ridding function, so in the extension process, the fiber shift points are dispersive, and the move distance warp

is large, so the yarn evenness is relatively bad and its single strength CV value is big.

However, the blended ratios of the combed polyester cotton blended yarn are different, so the single yarn CV values are different, and the single yarn strength CV value of T/CJ 40/60 13tex is smaller than the value of T/CJ 65/35 13tex. The blended ratios of these two sorts are near the critical blended ratio, and they are combed polyester cotton blended yarns with low short cotton fiber rate, so the reason to induce the difference of single strength CV value is not the short fiber rate, but the blended evenness degree of two sorts of fiber in the cotton strings. Some researches indicate that for the blended spinning of cotton and chemical fiber, when the proportions of two fiber contents are equal, the blended unevenness rate is minimum, and the proportions are more different, they are more difficult to be blended (Shi, 2003, p.36-40). Because the content proportion differences of these two sorts of fiber in T/CJ 40/60 13tex are relatively small, and the blended unevenness rate is small, so its single yarn strength CV value is small.

2.2 The relationships among single yarn evenness CV value, twist CV value and hectometer weight CV value with single yarn strength CV value

In order to make clear the relationships between three influencing factors and the single strength CV value, we use the single linear correlation analysis method to analyze the result, and use the software of SPSS, the correlative coefficient r and the significance level t in the statistics to implement the significance test.

The statistics points out that if $|r| < r_{0.05}$, the correlation coefficient is not significant, and if $r_{0.05} \leq |r| \leq r_{0.01}$, the correlation coefficient r is significant, and if $|r| \geq r_{0.01}$, the correlation coefficient is very significant.

2.2.1 The relationship between yarn evenness CV value and single yarn strength CV value

According to the data in Table 2, we adopt the single linear correlation analysis to analyze the relationship between single yarn evenness CV value and single strength CV value, and the result is seen in Table 3.

From Table 3, we can obtain the regression equation:

$$y = -6.911 + 1.017x.$$

Where, y is the single strength CV value, x is the yarn evenness CV value.

The correlation coefficient r is 0.927, from table we can get $r_{0.01} = 0.834$. $|r| \geq r_{0.01}$, which indicates that the single yarn evenness CV value and the single strength CV value present significant positive correlative, that is to say, the yarn evenness CV value is bigger, the single strength CV value is bigger. The result further shows the evenness CV value which reflects the unevenness of short segment of the yarn is bigger, the thin nodes and the thick node of the yarn are more, which will certainly increase the yarn strength and make the difference of yarn strength bigger (Liu, 1989). Therefore, the decrease of yarn evenness CV value can reduce the single yarn strength CV value.

2.2.2 The relationship between twist CV value and single yarn strength CV value

From the data in Table 2, we adopt the single linear correlation analysis to analyze the relationship between twist CV value and single strength CV value, and the result is seen in Table 4.

From Table 4, we can obtain the regression equation:

$$y = 4.717 + 1.096x.$$

Where, y is the single strength CV value, x is the twist CV value.

The correlation coefficient $r = 0.921 > 0.834 = r_{0.01}$, which presents very significantly positive correlation, that is to say, the unevenness of the twist is bigger, the single strength CV value is bigger. Therefore, the decrease of the twist unevenness rate possesses important meaning to reduce the single strength CV value.

2.2.3 The relationship between hectometer weight CV value and single yarn strength CV value

The yarn hectometer weight CV value, i.e. the thickness unevenness of long segment, is the important factor to influence the strength among pipe yarns. Some experiences showed that usual think yarn weight unevenness rate must be stabilized in 2%, and can avoid that the paroxysmal CV value exceeds the standard (Yu, 2002, p.22-25). However, sometimes the single strength CV value is high, but the hectometer weight unevenness rate doesn't change, because the yarn segment in which the "paroxysmal strength" occurs always is about half meter, which requires that when we reduce the unevenness of long segment of the thin yarn, we also should reduce the unevenness of the segment with about half meter.

The analysis result is seen in Table 5.

From Table 5, we can obtain the regression equation:

$$y = 7.461 + 0.798x.$$

Where, y is the single strength CV value, x is the hectometer weight CV value.

The correlation coefficient $r = 0.841 > 0.834 = r_{0.01}$, which presents very significantly positive correlation, that is to say, the single strength CV value increases with the increase of hectometer weight CV value. Therefore, the decrease of hectometer weight CV value has important meanings to reduce the single strength CV value.

2.2.4 The relationships among three influencing factors

From the regression equations established between three factors with single strength CV value and the obtained correlation coefficients, we can get:

$$r_{\text{evenness}} > r_{\text{twist}} > r_{\text{hectometer weight}}$$

That shows the yarn evenness CV value has the most important influence to the single strength CV value, then the twist CV value is the second one, and then the hectometer weight CV value.

We utilize the SPSS software to implement correlation analysis between every two factors, and the results are seen in Table 6, Table 7 and Table 8.

From above analysis, the twist CV value, the hectometer CV value and the yarn evenness CV value are highly significant, the correlation coefficients are all above 0.9. Therefore, in the twist CV value, the hectometer CV value and the yarn evenness CV value, the yarn evenness CV value is the root of all problems, so to improve the yarn evenness CV value can not only reduce the twist CV value and the hectometer CV value, but also these three factors can exert functions to improve the single strength CV value together.

3. Conclusions

(1) The blended ratio of polyester cotton blended yarn influences the single yarn strength CV value, and with the increase of cotton fiber content of the carded polyester cotton blended yarn, the single strength CV value increases, and when the blended ratio of the combed polyester cotton blended yarn is close the critical blended ratio, the single strength CV value is smaller.

(2) Three influencing factors including the yarn evenness CV value, the twist CV value, the hectometer weight CV value are all positive correlative with the single strength CV value, and $r_{\text{evenness}} > r_{\text{twist}} > r_{\text{hectometer weight}}$, and the correlation coefficients among three factors are all above 0.9, and they are high correlative. To improve the yarn evenness CV value can not only reduce the twist CV value and the hectometer CV value, but more important, these three factors can exert functions to improve the single strength CV value together.

References

- Liu, Rongqing, Chen, Baiting & Zhuduo. (1989). *The Theory and Practice of Yarn Evenness Degree*. Beijing: Textile Industry Press.
- Shi, Taoran & Zhaobo. (2003). Experimental Analysis of Factors Affecting Single Yarn Breaking Strength CV. *Cotton Textile Technology*. No.31(3). p.36-40.
- Yu, Guilin. (2002). Cause and Control Measures of Yarn Hairiness and Twist Unevenness. *Cotton Textile Technology*. No.30(4). p.22-25.

Table 1. Single yarn strength CV values of the yarns with different blended ratios

Sort	Carded polyester Cotton blended yarn		Combed polyester Cotton blended yarn	
	T/C 80/20 13tex	T/C 90/10 13tex	T/CJ 40/60 13tex	T/CJ 65/35 13tex
Single strength/cN	301.2	344.0	183.5	237.7
Single strength CV/%	10.38	8.71	8.97	10.11

Note: Data in Table 1 are averages from the data of 60 sub-samples.

Table 2. The relationships between three factors and single yarn strength CV

Item	Group							
	1	2	3	4	5	6	7	8
Yarn evenness CV/%	15.23	15.76	15.77	15.90	16.08	16.31	16.60	16.85
Twist CV/%	3.61	3.72	4.04	4.25	4.43	4.64	4.76	4.90
Hectometer weight CV/%	1.59	1.79	1.88	2.69	2.83	2.91	2.99	2.99
Single strength CV/%	8.85	8.90	8.97	9.01	9.74	9.58	10.02	10.31

Note: Data in Table 2 are averages from the data in former 8 groups of 30 sub-samples.

Table 3. Analysis result between yarn evenness CV and single yarn strength CV

Item	Non-standardization coefficient		Standardization coefficient	T	Level of significance
	B	Standard error	Beta		
Yarn evenness CV	-6.911	2.696	0.927	-2.564	0.043
	1.017	0.168		6.602	0.001

Note: The attributive variable is the single yarn strength CV, and B indicates the uncertain coefficient value and the constant value.

Table 4. Analysis result between twist CV and single yarn strength CV

Item	Non-standardization coefficient		Standardization coefficient	T	Level of significance
	B	Standard error	Beta		
Yarn evenness CV	4.717	0.817	0.921	5.776	0.001
	1.096	0.189		5.793	0.001

Note: The attributive variable is the single yarn strength CV.

Table 5. Analysis result between hectometer weight CV and single yarn strength CV

Item	Non-standardization coefficient		Standardization coefficient	T	Level of significance
	B	Standard error	Beta		
Hectometer weight CV	7.461	0.528	0.841	14.121	0.001
	0.798	0.210		3.806	0.001

Note: The attributive variable is the single yarn strength CV.

Table 6. The relationship between yarn evenness CV and twist CV

Item	Non-standardization coefficient		Standardization coefficient	T	Level of significance
	B	Standard error	Beta		
Yarn evenness CV	-9.817	1.831	0.953	-5.360	0.002
	1.017	0.168		6.602	0.001

Note: The attributive variable is the twist CV.

Table 7. The relationship between yarn evenness CV and hectometer weight CV

Item	Non-standardization coefficient		Standardization coefficient	T	Level of significance
	B	Standard error	Beta		
Yarn evenness CV	-13.708	3.734	0.870	-3.672	0.010
	1.007	0.232		4.332	0.005

Note: The attributive variable is the hectometer weight CV.

Table 8. The relationship between twist CV and hectometer weight CV

Item	Non-standardization coefficient		Standardization coefficient	T	Level of significance
	B	Standard error	Beta		
Twist CV	-2.660	0.688	0.950	-3.863	0.008
	1.192	0.159		7.474	0.000

Note: The attributive variable is the hectometer weight CV.



Sorption Kinetic Studies of Medical Grade Activated Carbon Prepared from Papaya Seeds

J.G. Collin (Corresponding author) & Mei P. Lee

Industrial Chemistry Programme

School of Science & Technology

Universiti Malaysia Sabah

88999 Kota Kinabalu

Sabah, Malaysia

Tel: 60-88-320-000 x 2117 E-mail : collin@ums.edu.my

The research is financed by the Centre for Management of Research and Conference, Universiti Malaysia Sabah (Grant No. B-09-01-01-ER/U131)

Abstract

The aim of this investigation was to determine the adsorption behavior and kinetics of methylene blue in aqueous solution on activated carbons prepared from papaya seeds by way of the two stage activation method in self-generated atmosphere using a muffle furnace. The optimised activated carbon, AK7, had a sorption kinetic that complied with the pseudo-second order kinetics and was fitted well to Langmuir isotherm model. The highest adsorption capacity of 97.09 mg g⁻¹ was obtained when the samples (AK7) were subjected to activation temperature of 500°C for 60 minutes with the percentage of methylene blue removal efficiency of 99.5%.

Keywords: Papaya seeds, Activated carbon, Sorption studies

1. Introduction

Activated carbons are versatile adsorbents with a wide range of applications that concerns principally with the removal of impurity species by adsorption from the liquid or gas phase. They also find use as catalyst support, in waste water treatment, in sugar syrup purification, in air pollution control as well as in the pharmaceutical and chemical industries. Many researchers have prepared activated carbon from various carbonaceous precursors (Gergova 1994) such as various grain sorghum (Diao 2002), fruits stones, rice and peanut husk (Ahmedna 2000), wood (Anuar 2002, Anuar 2001), wheat straw (Ahmedna 2000), coconut and oil palm shell (Collin 2005, Collin 2006), etc. Activated carbon is also the most commonly used support in first aid process of detoxification, owing mainly to its highly porous structure and high surface area. In medical application, adsorption kinetic is an important consideration, as fast acting adsorbents can prevent poison from further being taken in by the gastrointestinal track. Adsorption kinetics depends on the surface area and porosity of the charcoal prepared. Activated carbons are highly effective in removing both natural and synthetic toxins in the gastrointestinal tract. It is also use to treat animals for drug overdose and helps prevent the absorption of most poisons or drugs by the stomach and intestines (Boyd 1999). When toxic substances enter the human or animal digesting system, activated carbon can attached the toxic molecule onto its surface. Because activated carbon is not digested, it stays inside the intestine tract and eliminates the toxin when the person or animal has a bowel movement (Vale 1993). Laxative medicine that stimulates bowel movement is sometimes given together with the activated carbon to shorten the amount of time taken for the carbon to move through the colon system and reduce the possibility of constipation and reabsorption of the toxin thorough the wall of intestine. The selection method of preparation and precursor was explained in our previous paper (Collin : CARBON 2006). In order to prepare activated carbon for medical use, the precursors must come from vegetable source and be low in ash content (Jankowska 1991). There is no international standard for medicinal activated carbon. Different pharmacopoeias specify the use of different compound (Methylene blue, Iodine, phenol and others) to determine acceptable adsorptive capacities of activated carbon. Literature survey showed little or no interest of these authors in preparing and characterizing medical grade activated carbon on a laboratory scale. Most efforts were towards the preparation for commercial and general use activated carbons. This led to a few queries. First, is it possible to prepare medical grade activated carbon under normal

activated carbon producing scale from papaya seeds? Second, how effective is the prepared activated carbon in removing arsenic from an aqueous system? Papaya seeds are agriculture by-product that currently has no economic value; can offer an inexpensive and economic gain-able source activated carbon. In spite of its abundant availability and ease of gain, this precursor has received little attention from researchers to exploit its potential as to date. A number of activation methods have been reported in the literature using H_3PO_4 as an activating agent. The chemical nature of activated carbon significantly influences its adsorptive, electrochemical, catalytic, and other properties. However, few papers reported on the effects on chemical preparation conditions and preparation methods on the carbon. Generally, activation methods can be classified as single-stage or two-stage activation process carried out either in an inert medium or self-generated atmosphere (Collin : CARBON 2006). Since medical grade activated carbon are mostly employed in liquid phase of livestock's body fluid, it is essential to test its adsorption capacity in the same phase. This work describes the evaluation of activated carbons prepared from papaya seeds, by comparing the methylene blue adsorption kinetics of H_3PO_4 impregnated activated carbons in aqueous systems.

2. Experimental

The papaya seeds were collected daily from a local fruit stall in Kota Kinabalu, Sabah, Malaysia. After cleaning and processing it into activated charcoals using a muffle furnace, liquid phase adsorption studies were conducted. The chamber of muffle furnace consists of small vapor column with a small opening to the atmosphere, where decomposition of the precursors occurs in a mixture of initial existing atmosphere and gaseous decomposition produced during the process. Each of the samples was pretreated with phosphoric acid to precursor weight ratio of 1.0, 1.5, and 2.0 respectively (Collin : CARBON 2006) as shown in table 1. In both semi carbonization and activation processes, the samples were exposed to heat straightaway after the furnace temperature reached desire temperature. Since temperature progression was not the focus of the study, heating rate can be neglected. Desiccators served as the storing means while waiting for the furnace to attain the desired temperature. Leaching processes were crucial steps to remove the soluble ash formed during the activation process. Ash consisted mainly of oxides and some smaller portion of sulphates, carbonates, iron, aluminium, calcium, sodium and other metal and their compounds (Jankowska 1991). In the preparation of medical grade activated carbon, the content of heavy metal should be minimized; therefore it is advisable to remove the ash beforehand. Ash is commonly removed by leaching the activated carbon with acids (Jankowska 1991). As the samples were pretreated with phosphoric acid, refluxing the samples with distilled water was sufficient to remove the ash. The end product was characterized for percentage of yield, pH value, moisture and ash content, which was presented in our previous paper (Collin : CARBON 2006). In this paper, we present the sorption kinetics and sorption isotherm of the prepared carbon.

2.1 Methylene blue adsorption isotherm

The adsorption isotherms of methylene blue onto activated carbon were studied by applying the linear Langmuir equation 1

$$\frac{C_e}{Q_e} = \frac{1}{Q_m} C_e + \frac{1}{Q_m \cdot K_L} \quad (1)$$

and the Freundlich equation 2

$$\log Q_e = \log K_F + \frac{1}{n} \log C_e \quad (2)$$

Where C_e is the amount of adsorbate in the solution at equilibrium, Q_e is amount of methylene blue adsorbed by activated carbon, Q_m is the amount of adsorbate adsorbed to form monolayer coverage, and K_L , n and K_F are the equation constants (Rahman 2003).

2.2 Removal efficiency of methylene blue

The adsorption behavior of the activated carbon were studied by evaluating the removal efficiency, R_E , of methylene blue, calculated as equation 3

$$R_E = \frac{(C_o - C_e)}{C_o} \times 100 \quad (3)$$

Where C_o is the initial concentration of aqueous solution of methylene blue and C_e is the amount of adsorbate in the solution at equilibrium, R_E is expressed in term of percentage (Rahman 2003).

2.3 Iodine adsorption kinetics

0.1g of sample was added to a 0.25 L Erlenmeyer flask containing 10mgdm^{-3} aqueous solution of iodine. The flask was kept in a thermostat shaker at 30°C for 45 minutes. The content was gravity filtered and the concentration of the iodine determined. The procedure was extended to 60, 90, and 120 minutes. The kinetics and dynamics of adsorption of iodine on activated carbon was studied by applying the Lagergren first order and pseudo-second order rate equations that have

been most widely used for the adsorption of an adsorbate from an aqueous solution, which are expressed by the equations 4 and 5 respectively

$$\log(q_e - q_t) = \log q_e - \frac{k_{ad}}{2.303} t \quad (4)$$

$$\frac{t}{q_t} = \frac{1}{k_{ad} q_e^2} + \frac{1}{q_e} t \quad (5)$$

where q_e and q_t are the amount of dye adsorbed per unit mass of the adsorbent (in mgg^{-1}) at equilibrium time and time t , respectively, and k_{ad} is the rate constant.

2.4 Nitrogen adsorption by using BET method

BET isotherms were determined from the adsorption and desorption capacity of the activated carbons placed in inert atmosphere of nitrogen gas. It is assumed that the nitrogen molecules will form a single layer filling the pores on the surface of the activated carbon, which is known as the adsorption process. When the pressure in the chamber is gradually reduce, the single layer of molecule will leave the surface of the activated carbon, which is known as the desorption process.

3. Results and discussion

Methylene blue is a relatively large molecule and is often employed as an adsorbate in the liquid phase adsorption. It is a type of basic dye which is cationic (positively charged) and will therefore react with material that is negatively charged. Thus, it serves as a model compound for adsorption of medium size organic compounds from aqueous solutions (Stavropoulos 2005). It also indicates the specific surface area of the carbon which results from the existence of pores of dimension greater than 1.5nm (Jankowska 1991). Figure 1 shows the chemical structure of methylene blue molecule.

3.1 Methylene blue adsorption isotherm

The adsorption capacity of methylene blue using different impregnation ratio of phosphoric acid was shown in figure 2. In the impregnation ratio of 1.0, 1.5, 2.0, the loadings were very close, but still the trend suggested a continuous increase with the increasing of dye concentration. From figure 3, it is observed that the adsorption capacity of AK5 was higher than AK1. This indicates that the increase in activation temperature is proportionate to the adsorption capacity of methylene blue. These trends were consistent with the study done by Lafi (Lafi 2001). Figure 4 illustrates the relationship between the activation time and the adsorption capacity of methylene blue. Increasing the activation time could lead to pore damaged, severely affecting the carbons ability to adsorb the methylene blue as the activation time was increased from 30 to 90 minutes. When the adsorption data of AK1 to AK9 were tested using equation 1 and 2, they demonstrated compliance to the Langmuir model as indicated by its relatively higher linear correlation coefficients. The values of R^2 were all between 0.96 and 0.99 which indicating a good mathematical fit as shown in Table 2. The Langmuir adsorption model is a typical model for monolayer adsorption and was adapted to model isotherms and calculate the methylene blue (MB) adsorption capacities of the prepared activated carbons (Stavropoulos 2005). Table 2 summarizes the parameters of the methylene blue adsorption for Langmuir model and Freundlich model from AK1 to AK9. The highest adsorption capacity was AK 7 which was 97.09 mg g^{-1} , while the lowest was AK3 which was 52.91 mg g^{-1} . This may be due to the porosity of the activated carbon where AK 7 yielded the highest percentage of micropore; 86.87% as shown in Table 4, proving that adsorption capacity is proportionate to the surface area of the activated carbon (Lafi 2001). A ratio of surface area accessible to MB compared to BET surface area (S_{MB}/S_{BET}) is also given in the Table 2. Taking the surface area of methylene blue (S_{MB}° to be $1.93 \text{ m}^2 \text{ mg}^{-1}$), the surface area of the activated carbons accessible to methylene blue (S_{MB}) was calculated according to equation 6.

$$S_{MB} = S_{MB}^{\circ} \times q_m \quad (6)$$

Where q_m is the amount adsorbed per unit mass of adsorbent corresponding to complete coverage of the adsorption site, calculated from the slope of linear Langmuir isotherm (Stavropoulos 2005).

Pore sizes create limited accessibility of methylene blue molecule in activated carbon. From table 2, the surface area, estimated by methylene blue adsorption, increased with activation temperature by comparing AK2 and AK6 which was $94.61 \text{ m}^2 \text{ g}^{-1}$ and $155.65 \text{ m}^2 \text{ g}^{-1}$ respectively. Higher temperature impelled the opening and enlargement of the pores, which increased the uptake of methylene blue. Besides that, the surface area estimated by the N_2 adsorption isotherms showed higher values than the surface area estimated by Langmuir isotherms. This was due to the size of N_2 molecule, which has a much smaller molecular cross-section than the methylene blue molecule. Therefore, N_2 adsorption can enter not only the mesopores, but also the micropores. The ratio of S_{MB}/S_{BET} indicates the fraction of porosity accessible to methylene blue molecule. AK 4 showed a larger S_{MB} compared to S_{BET} , therefore, might indicated that the adsorption mechanism was not limited to the porous nature. The S_{MB}/S_{BET} ratio for AK 5 and AK 9 showed that the methylene blue

only accessed about 17% and 18% of the total porosity of the carbon. This low coverage of internal surface area confirmed once again the microporosity character of the activated carbon since methylene blue adsorbs in mesopores (Stavropoulos 2005).

3.2 Removal efficiency of methylene blue

Figure 5 shows the removal efficiency of methylene blue versus initial concentration of methylene blue. The percentage of removal efficiency for all activated carbons was within the range of 68% to 99%. Figure 5 indicates that AK2, AK3 and AK4 had a low efficiency to remove the methylene blue. This trend indicates that longer activation time of the precursors which was prepared at 400°C with 1.5 impregnation ratio, may damaged the pore and affect its ability to remove methylene blue. AK7 had the highest removal efficiency of methylene blue, which was 99.5%.

3.3 Iodine adsorption kinetics

The iodine adsorption kinetics for the activated carbons studied in this work were presented in table 3. It was observed that the adsorption capacity followed the pseudo-second order model as indicated by its near relative high linear correlation. Researchers (Molino-Sabio 2004) indicated that this adsorption capability was due to the influence of the phosphoric acid to the porosity development in the carbon, which led to a more heterogeneous pore distribution. This is important for the fast uptake of adsorbates or toxic substances that enter the body as heterogeneous pore distribution enhances the surface area and serves as a pathway to the inner pores of the carbon. Phosphoric acid impregnation also helps to clean up the carbon surface groups that will hamper the electrostatic binding forces between the surfaces of the carbon and the adsorbates, thus, improving adsorption rate. Acid impregnated carbons are negatively charged (sometimes referred to as L-type carbons), therefore are most suitable to adsorb positively charged adsorbates. However some researchers (Ibezim 1999) have determined that the performance of some types of activated carbons can be severely hampered by acidic conditions in the gastrointestinal contents.

3.4 Adsorption isotherm of BET

Figure 6 shows the BET adsorption isotherms of the activated carbons were Langmuirian in shape and being typical type I isotherm with open hysteresis in the BDDT (Brunauer, Deming, Deming, Teller isotherm) classification, which is characteristic of adsorption on a microporous adsorbent. It tends monotonically to the limiting adsorption associated with a complete monolayer (Anuar 2004). These findings were corroborated by other researches (Youssef 2005, Yang 2003, Castro 2000, Guo 1998). The highest adsorption capacity was obtained by AK 9 whereas the lowest adsorption capacity was AK 4. This was due to its physical properties where the AK 4 produced the lowest BET surface area, micropore surface area, micropore volume.

3.5 Porosity of activated carbons

BET and micropore surface area, micropore volume, average pore diameter and percentage of micropore of activated carbon are given in table 4. Although the highest BET surface area of activated carbon was the sample AK9 which had $895.7\text{m}^2\text{g}^{-1}$, but, AK 5 yielded the highest for micropore surface area and micropore volume which was $687.5\text{m}^2\text{g}^{-1}$ and 0.276cc g^{-1} respectively. Contrary, the lowest was AK4 which was $198.5\text{m}^2\text{g}^{-1}$ and $168\text{m}^2\text{g}^{-1}$. Moreover, the micropore volume of activated carbon was between 0.07ccg^{-1} and 0.27ccg^{-1} and its average pore diameter was between 19Å to 21Å. The impregnated activated carbon of AK6 produced the highest average pore diameter with 21.3 Å while the impregnated activated carbon of AK7 produced the lowest average pore diameter with 18.4Å. The percentage of micropore showed that the H_3PO_4 impregnated activated carbon produced the highest percentage at 86.9%. This showed that the majority of the pores were micropores and a significant amount of pores have been enlarged to either mesopores or macropores. Therefore it was possible to suggest that the chemical activators had an effect in increasing pore sizes.

(a) Effect of Impregnation Ratio of H_3PO_4 on Porosity Development

Increased impregnation ratio was associated with an increased development in BET surface area as shown in table 4. An approximate decreased in micropore surface area, micropore volume and percentage of micropores appeared with respectively increased in impregnation ratio from 1.0, 1.5 to 2.0 (table 1) which was AK8, AK6, AK9 respectively. These results were generally consistent with results reported by Girgis 1999. This was due to the intense chemical attack of the highly concentrated H_3PO_4 , which collapsed the micropore and produced the development of meso and macroporosity (Molino-Sabio 2004).

(b) Effect of Activation Temperature on Porosity Development

Increasing the temperature from 400°C to 500°C progressively increased the BET surface area, micropore surface area and micropore volume. It can be observed by comparing the sample between AK1 and AK5 or AK2 and AK6 which was activated in 30 and 45 minutes respectively with 1.5 impregnation ratios. These results were consistent with the research done by other researchers (Castro 2000, Jagtoyen 1998, Solum 1995, Hayashi 2000). Therefore, a lower activation temperature produced microporous carbons (Diao 2002).

(c) Effect of Activation Time on Porosity Development

However when the activation duration was lengthened from 30 to 45 minutes, the BET surface area, micropore surface area and micropore volume also increased. But increasing the activation duration from 45 to 90 minutes caused the BET surface areas, micropore surface area and micropore volume to decrease. This trend was entirely consistent with the research done by (Diao 2002). This indicates that the pore structure of the carbon developed over a duration of 30 to 45 minutes would caused some of the pores to enlarge or even collapse, thus reducing the BET surface area and micropore surface area and micropore volume (Diao 2002).

4. Conclusion

In conclusion, this study showed that the use of dehydrating agent of H_3PO_4 and the two-stage self-generated atmosphere method played a major role in shaping and transforming papaya seeds into activated carbon with well-developed porosity and high adsorption capacity. Due to the activated carbon produced with carbonization and followed by physical activation in an open system (without gas control), only low temperature is needed to complete the decomposition of organic constituents. Generally, lower yield of activated papaya seeds were produced as the pyrolysis temperature and time increased. Activated carbons produced from papaya seed were basic due to the washing process. The activated carbons which were prepared by this method have been proven to be strongly effective in removing methylene blue dye in aqueous solution. It yielded a majority of micropores structure in which the percentage of micropore was between 82% and 87% with the average pore diameter of 19 to 21Å. The kinetic studies indicated that all the prepared activated carbons fitted well in Langmuir isotherms with pseudo-second order model. Besides being an adsorbent for aqueous based impurities, these activated carbons have a potential to be used in pharmaceutical or in medical industries as no toxic chemicals were involved in the activation process. Therefore it is hoped that papaya seeds will provide a clean, cheap and efficient precursor to prepare medical grade activated carbons for the purpose of gastrointestinal decontamination.

Acknowledgements

This research was supported by the Centre for Management of Research and Conference, University Malaysia Sabah (Grant No. B-09-01-01-ER/U131) and is gratefully acknowledged. The authors would also like to express deepest gratitude to Prof. Datin Dr. Maryati Mohamed, Director of the Institute for Tropical Biology and Conservation, UMS, for the use of certain scientific instruments.

References

- Ahmedna M., Marshall W.E, and Rao R.M. (2000). Surface properties of granular activated carbons from agricultural by-products and their effects on raw sugar decolorization. *Bioresource Technology*, 71, 103-112.
- Ahmedna M., Marshall W.E and Rao R.M. (2000). Production of granular activated carbons from select agricultural by-products and evaluation of their physical, chemical and adsorption properties. *Bioresource Technology*, 71, 113-123.
- Anuar, K., Collin, G. J., Zulkarnain, Z., Hussein, M. Z., Haron, M.J. and Abdullah, A. H. (2001). Preparation and characterizations of activated carbon from Resak wood (*Vatica Hullettii*). *Research Journal of Chemistry and Environment*, 5, 21-24.
- Anuar, K., Collin, G. J., Zulkarnain, Z., Hussein, M. Z., Haron, M.J. and Abdullah, A. H. (2002). Preparation and characterization of activated carbon from Resak wood (*Vatica Hullettii*): surface area and porosity studies. *Oriental Journal of Chemistry*, 18, 43-46.
- Anuar, K., Collin, G. J., Kuang, D., Zulkarnain Zainal, Mohd. Zobir Hussien, Abdul Halim Abdullah, and Jamaluddin Daud, (2004). Activated carbons from oil palm shells (*elaeis guineensis*)-preparation and characterization. *Malaysian Journal of Analytical Sciences* 8 (1), 130-134.
- Boyd R. and Hanson J. (1999). Prospective single blinded randomised controlled trial of two orally administered charcoal preparations. *Journal of Accident and Emergency Medicine* 16, 24-25.
- Castro, J.B., Bonelli, P.R., Cerrella, E.G, and Cukierman, L., (2000). Phosphoric acid activation of agricultural residues and bagasse from sugar cane: influence of the experimental condition on adsorption characteristics of activated carbons. *Ind. Eng. Chem. Res.* 39, 4166-4172.
- Collin G. J., Hasnul F. M. Z., and Siti F. D., (2005), Treatment of landfill leachate in Kayu Madang, Sabah: Textural and Chemical Characterization (Part 1), *Malaysian Journal of Analytical Sciences*, 10, 1-6.
- Collin G. J., Fauziah H. A. A., Hasnul F. M. Z., and Siti F. D., (2006). Treatment of landfill leachate in Kayu Madang, Sabah: Porosity and Adsorption Studies (Part 2), *Asian Chemistry Letters*, 10(3 & 4), 89-94.
- Collin G. J., Awang B., Ng K.W., and Lee M. P., (2006) Development and study of medical grade activated carbon from papaya (*carica papaya*) seeds: Textural and Characterization (Part 1). Proceeding of the International Carbon Conference, CARBON 2006, The Robert Gordon University, Aberdeen, Scotland.

- Diao Y., Walawender W.P., Fan L.T. (2002). Activated carbons prepared from phosphoric acid activation of grain sorghum. *Bioresource Technology*, 81, 45-52.
- Gergova, K., Petrov, N., Eser, S. (1994). Adsorption properties and microstructure of activated carbons produced from agricultural by-products by steam pyrolysis. *Carbon*, 32, 693-702.
- Girgis, B. S. and Ishak, M. F., (1999). Activated carbon from cotton stalks by impregnation with phosphoric acid. *Materials Letters* 39, 107-114.
- Guo, J., and Lua, A. C., (1998). Characterization of chars pyrolyzed from oil palm stones for the preparation of activated carbons. *Journal of Analytical and Applied Pyrolysis* 46, 113-125.
- Hayashi, J., Kazehaya, A., Muroyama, K., and Watkinson, A. P., (2000). Preparation of activated carbon from lignin by chemical activation. *Carbon* 38, 1873-1878.
- Ibezim, E.C., Ofoefule, S.I., Ejahalaka, C.N.C and Orisakwe, O.E., (1999). In-vitro adsorption of ciprofloxacin on activated carbon and talc. *American Journal Therapeutic* 6, 199-201.
- Jagtoyen, M., and Derbyshire, F., (1998). Activated carbons from yellow poplar and white oak by H₃PO₄ activation. *Carbon* 36 (7-8), 1085-1097.
- Jankowska, H., Swiatkowski, and Choma, J. (1991). Active Carbon, Elis Horwood Ltd.
- Lafi W.K., (2001). Production of activated carbon from acorns and olive seeds. *Biomass and Bioenergy* 20, 57-62.
- Molino-Sabio, M., and Rodriguez-Reinoso, F., (2004). Role of chemical activation in the development of carbon porosity. *Colloids and Surfaces A: Physicochem. Eng. Aspects* 241, 15-25.
- Rahman, I.A. and Saad, B., (2003). Utilization of guava seeds as a source of activated carbon for removal of methylene blue from aqueous solution. *Malaysian Journal of Chemistry* 5, 8-14.
- Solum, M. S., Pugmire, R. J., Jagtoyen, M., and Derbyshire, F., (1995). Evolution of carbon structure in chemically activated wood. *Carbon* 33, 1247-1250.
- Stavropoulos, G.G. and Zabaniotou, A.A., (2005). Production and characterization of activated carbon from olive-seed waste residue. *Microporous and Mesoporous Materials* 82, 79-85.
- Vale J.A. and Proudfoot A.T., (1993), How useful is activated charcoal? *British Medical Journal*, 306, 78-79.
- Yang, T., and Lua, A. C., (2003). Characteristics of activated carbons prepared from pistachio-nut shells by potassium hydroxide activation. *Microporous and Mesoporous Materials* 63, 113-124.
- Youssef, A. M., Radwan, N. R. E., Abdel-Gawad, I., and Singer, G. A. A., (2005). Textural properties of activated carbons from apricot stones. *Colloids and Surfaces A: Physicochem. Eng. Aspects* 252, 143-151.

Table 1. Preparation parameters of activated carbons AK1 to AK9.

Sample	Ratio of Impregnation	Semi- carbonization		Activation	
		Temperature (°C)	Time (min)	Temperature (°C)	Time (min)
AK 1	1.5	200	15	400	30
AK 2	1.5	200	15	400	45
AK 3	1.5	200	15	400	60
AK 4	1.5	200	15	400	90
AK 5	1.5	200	15	500	30
AK 6	1.5	200	15	500	45
AK 7	1.0	200	15	500	60
AK 8	1.0	200	15	500	45
AK 9	2.0	200	15	500	45

Table 2. Methylene blue adsorption kinetics for activated carbons AK1 to AK9.

Sample	Langmuir Model					Freundlich Model		
	R ²	K _L	q _m , mgg ⁻¹	S _{MB} m ² g ⁻¹	S _{MB} /S _{BET}	R ²	K _F	n
AK 1	0.97	0.496	81.30	156.91	0.27	0.83	3.95	1.86
AK 2	0.96	1.943	49.02	94.61	0.15	0.60	4.21	5.21
AK 3	0.99	1.853	52.91	102.11	0.19	0.59	4.29	5.03
AK 4	0.99	1.303	54.05	104.32	0.53	0.53	4.19	4.86
AK 5	0.99	2.288	74.07	142.96	0.17	0.83	4.98	3.21
AK 6	0.99	2.067	80.65	155.65	0.22	0.71	5.24	2.21
AK 7	0.99	4.120	97.09	187.38	0.24	0.94	7.17	1.72
AK 8	0.99	5.218	83.33	160.83	0.23	0.76	6.26	2.25
AK 9	0.99	4.680	85.47	164.96	0.18	0.69	6.20	2.38

Table 3. Iodine adsorption kinetics for activated carbons AK1 to AK9

Lagergren kinetics				
Sample	First order	Pseudo second order		
	R ²	R ²	k _{ad} (min g mg ⁻¹)	q _e (mg g ⁻¹)
AK1	0.9040	1.0000	19.68504	0.1193
AK2	0.8789	0.9998	454.5455	0.0048
AK3	0.5932	0.9993	416.6667	0.0042
AK4	0.8789	0.9999	384.6154	0.0078
AK5	0.8954	0.9997	333.3333	0.0042
AK6	0.9763	0.9997	294.1176	0.0072
AK7	0.8954	0.9998	212.7660	0.0018
AK8	0.9334	0.9994	270.2703	0.0015
AK9	0.9763	0.9997	208.3333	0.0272

Table 4. Porosity data of the activated carbons AK1 to AK9.

Sample	BET surface area (m ² g ⁻¹)	Micropore surface area (m ² g ⁻¹)	Micropore volume (cc g ⁻¹)	Average pore diameter (Å)	Micropore (%)	Iodine Number (m ² g ⁻¹)
AK1	585.9055	498.9877	0.199241	19.9508	85.17	150.9
AK2	638.6633	521.4834	0.208899	19.4113	81.65	268.2
AK3	547.6578	456.4519	0.182578	19.7493	83.35	212.3
AK4	198.4713	168.0074	0.066648	19.8076	84.65	106.2
AK5	822.8388	687.4916	0.276198	18.5601	83.55	380.0
AK6	713.7507	588.9832	0.237155	21.3555	82.52	229.1
AK7	775.5432	673.7001	0.269542	18.3874	86.87	363.2
AK8	694.2739	602.0462	0.241316	18.5343	86.72	296.2
AK9	895.6582	553.6766	0.222338	19.6096	61.82	217.9

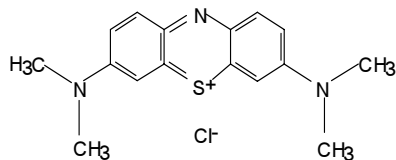


Figure 1. Chemical structure of methylene blue.

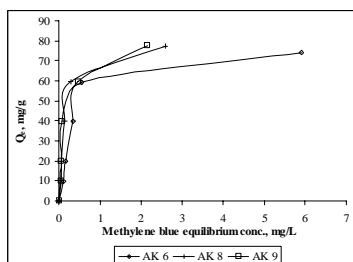


Figure 2. Adsorption isotherms with different impregnation ratio.

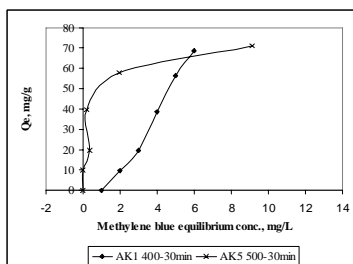


Figure 3. Adsorption isotherms with different activation temperature.

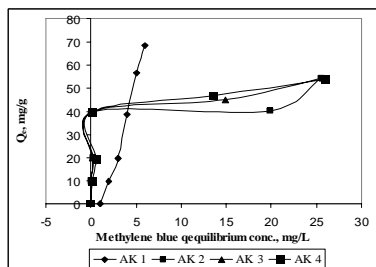


Figure 4. Adsorption isotherms with different activation time.

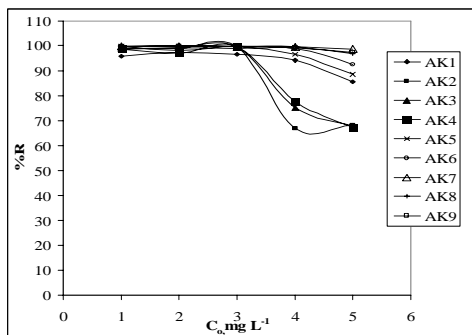


Figure 5. Removal efficiency of methylene blue

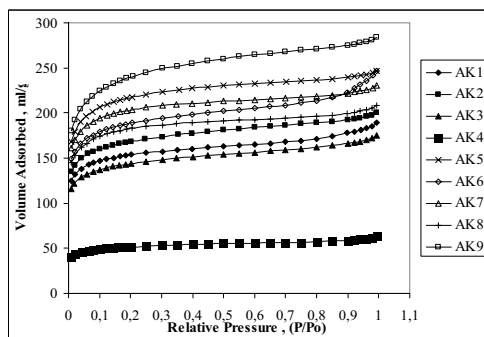


Figure 6. BET adsorption isotherm



Study on the GMRES (m) Method of Krylov Subspace and Its Application

Silin Bai & Jianping Liu
College of Science
Yanshan University
Tangshan 066004, China

Abstract

The Krylov subspace GMRES (m) method is the programming arithmetic based on the projection method. Now, it has become into the excellent arithmetic to solve the linear problem with large scale, and it also can be applied in the nonlinear programming problems. In this article, we translate the nonlinear optimization problems into the non-smooth equations to solve them. We put forward the iterative method of Newton-GMRES to solve the non-smooth equations, and for large-sized problem, this method is especially applied. And the samples also prove the validity of this method.

Keywords: Non-smooth Equations, Newton-GMRES method

It is the important task to solve the large-sized nonlinear programming problem in the computation mathematics and the scientific engineering computation. The Krylov subspace method is used more in recent twenty years, and it is a sort of iterative method based on the projection method which is applied extensively. The common subspace arithmetic includes FOM, IOM, GMERS and conjugate gradient method and Lanczos, CG, B iGGSTAB aiming at the symmetric array, and some excellent arithmetic have entered into the tool box of MATLAB. In this article, we apply the Krylov subspace GMRES arithmetic in the typical Newton's method, and obtain the Newton-GMRES method which has very important function to solve large-sized nonlinear programming problems.

Many nonlinear programming problems such as nonlinear optimal problems and nonlinear variational inequalities can be translated into non-smooth equations to solve. Therefore, the non-smooth equation offers a general frame to solve these problems in fact. The solutions of the non-smooth equation are extensively noticed, and one new research hotspot in the nonlinear programming domain forms (Hrker et al. 1990, IP et al, 1992, Pang et al, 1990, 1993, Qi et al, 1993a, 1993b).

For the solution of the nonlinear equation,

$$p(x) = 0 \tag{1.1}$$

here, $F: R_n - R_n$ is a nonlinear mapping. When F is continual and differentiable, one usual method to solve the equations (1.1) is the Newton's method (Ortega et al, 1970).

$$x_{k+1} = x_k - F'(x_k)^{-1} F(x^k) \tag{1.2}$$

Many effective methods to solve the equations are related with the Newton's methods such as Quasi-Newton Methods and so on.

Suppose that F is not a smooth map, but a local map, so $F'(x)$ may not exist, so we can not use the equation (1.2) to solve the non-smooth equations (1.1). If $\partial F(x_k)$ is the generalized Jacobi of $F(x)$ on x_k , i.e. $\partial F(x_k) \text{Co} \left\{ \lim_{\substack{x_i \rightarrow x \\ x_i \in D_F}} F'(x_i) \right\}$, we can use the generalized Jacobi of $F(x)$ to replace F (Qi, et al, 1993b), and it can offer a

sort of generalized Newton Method to solve the non-smooth equations.

$$x_{k+1} = x_k + V_k^{-1}(x_k) \tag{1.3}$$

Where, $V_k \in \partial F(x_k)$. It proves the local super-linear convergence of the generalized Newton Method when $F(x)$ is half-smooth.

In actual application, when we use the equation (1.3) to solve the non-smooth problem, V_k is very difficult to be

estimated especially for large-sized problems. In addition, it is the problem how to effectively solve $V_k d_k + F(x^k) = 0$ to deserve us to deeply study.

For the GMRES arithmetic and other Krylov subspace iterative methods to solve the linear equations, we only need the product of the matrix V_k and the vector u , and needn't directly compute the matrix of V_k . Therefore, under the non-smooth condition, we can use $F'(x_k, u) \approx \frac{F(x_k + \delta u) - F(x_k)}{\delta}$ to approximately replace $V_k d_k$. Combining with the arithmetic (1.3), we can obtain a sort of nested algorithm to solve the equation (1.1). The algorithm can not only overcome the difficulty to compute V_k , but also effectively solve the equation (1.1).

Many scholars considered the Krylov subspace iterative method of nonlinear equations (Peter et al, 1987), we they only limited the problem in the smooth condition. In this article, we consider the non-smooth condition, which is the generalization for the smooth condition. Because the generalized Jacobi is difficult to be estimate, so this Newton-GMRES arithmetic is very applicable.

1. Nonlinear Newton-GMRES method

Now, we offer a sort of Newton-GMRES iterative arithmetic to solve non-smooth equations.

Step 1. Supposed that $\varepsilon > 0, \{\varepsilon_k\} \varepsilon_k > 0 \varepsilon_k \rightarrow 0$.

Select initial approximate $x_0 \in R^n, k = 0$.

Step 2. Supposed that $q_0 = (F(x_k + \sigma_0^{(k)} d_0) - F(x_k)) / \sigma_0^{(k)}$, and $d^{(0)}$ is one approximate solution of the linear equations (1.4). $r^{(0)} = -F(x_k) - q_0, \beta^{(0)} = \|r^{(0)}\|, u_1 = r^{(0)} / \beta^{(0)}, j = 0$.

Step 3. $j = j + 1$

$$q_{j+1} = (F(x_k + \sigma_j^{(k)} u_j) - F(x_k)) / \sigma_j^{(k)}$$

$$W_{j+1} = q_{j+1} - \sum_{i=1}^j h_{ij} u_i$$

$$h_{ij} = (q_{j+1}, u_i) \quad i = 1, \dots, j$$

$$h_{j+1,j} = \|W_{j+1}\|$$

$$u_{j+1} = W_{j+1} / h_{j+1,j}$$

Define the Hessenberg matrix $(j+1) \times j, h_j$, and its nonzero unit is h_{ij} .

To solve the minimization problem,

$$\min_{y \in R} \|\beta^{(0)} e_1 - \overline{H_j} y\| \tag{2.1}$$

Where, $e_1 = (1, 0, \dots, 0)^T$ is the unit vector with $j+1$ dimensions. Note y_j is one solution of the equation (2.1).

$$d^{(j)} = d^{(0)} + u_j y_j \quad u_j = [u_1, u_2 \dots u_j]$$

Compute the residual

$$\rho_j = \|r^{(j)}\| = \|F(x_k) + (F(x_k + \sigma_j^{(k)} d^{(j)}) - F(x_k)) / \sigma_j^{(k)}\|$$

Step 4. If $\rho_j \leq \varepsilon_k$ or $j = n$, so next, or else turn to Step 3.

Step 5. Supposed that $x_{k+1} = x_k + d^{(j)}$,

If $\|F(x_{k+1})\| \leq \varepsilon$, then end, or else, turn to Step 2.

Generally, in the computation of value, we take $d_0 = (0, \dots, 0)^T$,

$$V_{(x)} u = (F(x + \sigma u) - F(x)) / \sigma \tag{2.2}$$

$$\sigma = \sqrt{\varepsilon} \frac{\|x\|}{\|u\|} \tag{2.3}$$

ε is a value close to the precision of the machine. In the flowing value computation, we take $\varepsilon = 10^{-8}$.

2. Examples

Many actual problems can be translated into non-smooth equations to solve. For the problem of nonlinear complementarity problem, seek $x \in R_n$ to make

$$x \geq 0, H(x) \geq 0, x^T H(x) = 0 \quad (2.4)$$

and prove the problem is equivalent to the nonlinear equations

$$F(x) = \min(x, H(x)) = 0 \quad (2.5).$$

Example: Seek $x \geq 0$, $H(x) \geq 0$, $x^T H(x) = 0$,

where, $H(x) = c(x) + A(x) + b$

$$c(x) = (c_1(x_1), c_2(x_2), \dots, c_n(x_n))$$

$$c_i(x_i) = 10 \arctan(x_i) \quad i = 1, 2, \dots, n$$

$$M = \begin{bmatrix} 2.5 & -1 & & & & \\ -1 & 2.5 & -1 & & & \\ & -1 & 2.5 & -1 & & \\ & & \dots & & & \\ & & & -1 & 2.5 & -1 \\ & & & & -1 & 2.5 \end{bmatrix}$$

$$b = \left(-\frac{n}{2}, -\frac{n}{2} + 1, \dots, -\frac{n}{2} + n - 1 \right)^T$$

This question is equivalent to the solution of the following equations.

$$F(x) = \min(x, H(x)) = 0$$

The appointed stop standard is $\|F(x)\| \leq 10^{-6}$. For the problems with different sizes, its iterative steps are in Table 1, where x_0 is the appointed initial value, and D_n is the dimension number of the question.

References

- Harker P T & Xiao B. (1990). Newton's Method for the Nonlinear Complementarity Problem: A B2 Differentiable Equation Approach. *Math. Prog.* No.48. p.339-357.
- Ip CM, Kyparisis J. (1992). Local Convergence of Quasi-Newton Methods for B2 Differentiable Equation Approach. *Math. Prog.* No.56. p.71-90.
- Ortega JM & Rheinboldt WC. (1970). *Iterative Solution of Nonlinear Equations in Several Variables*. New York: Academic Press.
- Pang J S. (1990). Newton's Methods for B2 Differentiable Equations. *Math. Oper. Res.* No.15. p.311-341.
- Pang J S & Qi, L. (1993). Nonsmooth Equations: Motivation and Algorithms. *SIAMJ. Opti.* No.3. p.443-465.
- Peter N, Brown. (1987). Local Convergence Theory for Combined Inexact Newton/Finite Difference Projection Methods. *SIAMJ. Numer. Anal.* No.24. p.407-433.
- Qi, L. (1993). Convergence Analysis of Some Algorithms for Solving Nonsmooth Equations. *Math. Oper. Res.* No.18. p.227-244.
- Qi, L & Sun J. (1993). A Nonsmooth Version of Newton's Method. *Math. Prog.* No.58. p.353-367.

Table 1. The steps of iteration method of different scale problem

x_0	$(1, \dots, 1)$	$(1, 0, \dots, 1, 0)$	$(1, 0 \dots 0, 1)$	$(1, 1, 0 \dots 0, 1, 1)$	$(1, 0 \dots 0110 \dots 01)$
$D_n = 50$	15	11	9	9	9
$D_n = 100$	8	9	8	8	8
$D_n = 200$	7	9	10	8	10
$D_n = 500$	8	10	9	9	8



Experimental Studies on Disposal of Various Industrial Solid Wastes

K.Senthilkumar (Corresponding Author)

Department of Chemical Engineering

Erode Sengunthar Engineering College

Thudupathi, Erode-638057, Tamilnadu, India

Tel: 91-4294-232-701 E-mail: ukxen2003@yahoo.co.in

V. Sivakumar

Department of Chemical Engineering

Kongu Engineering College

Perundurai, Erode-638052, Tamilnadu, India

Tel: 91-4294-225-026 E-mail: drvsivakumar@yahoo.com

P. Akilamudhan

Department of Chemical Engineering

Erode Sengunthar Engineering College

Thudupathi, Erode-638057, Tamilnadu, India

Tel: 91-4294-232-701 E-mail: akilamudhan@yahoo.co.in

Abstract

In the present study, solid waste from various industries has been collected and characterized. Based on the nature and composition of solid waste, the possible chemical composition is evaluated and value added products are prepared. Methods for conversion of solid wastes into building materials such as bricks and concrete blocks have been described. Mixing of solid waste in various proportions with red soil also carried out as pot experiment. From the results of various tests on final product, it is concluded that solid waste can be used suitably to produce bricks with 25-30% of sludge, for concrete blocks with 45-50% of sludge. By applying this type of alternative, solid waste could be disposed off in a better way without affecting the existing environment.

Keywords: Solid waste, Solid waste management, Sludge disposal, Environmental engineering

1. Introduction

Based on the quality of liquid effluent, textile house is one of the leading and most polluting industrial sectors in India. To treat this waste water, adsorption and coagulation techniques are used by the most of textile effluent treatment plants. The textile solid waste, brownish in color, contains mainly iron, chloride, sulphate and a few traces of other substances, all coming from different sections and type of dyes used in the textile industries. The solid waste from the glass industries will be grey in color. In general, sludge generation and accumulation are the most serious problems faced by the treatment plants. Due to its chemical and mineral content, these industrial solid wastes are found to be hazardous in the view of environmental consideration (Khan 1994). Unsafe disposal of the solid waste may cause harmful effects on the environment & human beings (Giri and Bhattacharya, 1991, Raviprasath et al, 2003). Hence, solid waste management should be given primary importance before things become too convoluted (Kumaravelan and Anandan, 2004). The conventional techniques for sludge disposal like compositing, land filling, agricultural utility, open dumping and thermal techniques are found to have some drawbacks such as land losing its fertility, possible contamination of under ground water, requirement large surface area for storage and high cost of disposal.

To overcome the drawbacks of the existing sludge disposal methods, an attempt has been made to dispose the solid sludge waste from textile house, glass industry and thermal industries (all are located at Erode, India). The employment of waste sludge to produce valuable products is considered to be the most advanced trend in solid waste management

for the environmental damages can be reduced or overcome and the cost is can be considerably reduced without necessitating heavy establishments. The present work analyses the feasibility of producing building materials like bricks and concrete blocks. The experimental work was carried out at our college (Erode Sengunthar Engg. College, Erode, India). The solid wastes collected are subjected to chemical analysis to get the nature and chemical composition of the sludge. An attempt has been made to study the possibility of mixing the solid wastes in various proportions with red soil or other conventional raw materials to produce the building materials. Mixing solid wastes in various proportions with red soil was carried out as pot experiments. To obtain the quality of bricks compressive strength, water holding capacity and efflorescence test were carried out.

2. Materials and Methods

2.1 Materials

Sludge after the solar evaporation was taken from textile house, glass and thermal industry. All the reagents used for finding the characteristics of the sludge are of A.R. Grade.

2.2 Analysis of Sludge

The solid waste was evaluated based on its various characteristics of loss of ignition and insoluble residue; iron, sulphate, calcium, aluminium and silica were analyzed as per the standard methods (Vogel, 1961, APHA, 1991, Arnold et. al, 1992).

2.3 Manufacture of bricks

The most common bricks are one of the oldest building materials and it is extensively used at present as a leading material of construction because of its durability, strength, low cost and easy availability of raw materials. The conventional bricks are manufactured by four distinct operations like preparation of clay, molding, drying and burning. The sludge was dried in order to remove the moisture. Then it was mixed with various binding materials and water in the ratio 1:0.25. Fly ash was used as binding materials. In preparation of brick, the composition of textile house sludge, glass industry sludge, thermal industry waste (fly ash) and red soil were made in various proportions. The sludge was mixed in various proportions with the red soil forming a murrice. The mixture was then made in to brick shape using a brick mold made of cast iron having the dimensions 22 cm x 10 cm x 6 cm. The wet brick was put in the open air for atmospheric drying for about 8 days. Then the bricks were arranged and burnt in a lime kiln at a temperature around 950-1200 °C. The burnt bricks were then subjected to various tests.

2.4 Manufacture of concrete blocks

Normally 8 kg of coarse aggregates, 4 kg of sand, 2 kg of cement and sufficient amount of water were mixed with water-cement ratio of 0.45 and 0.5. The concrete mixture was filled in the mould in layers approximately 5 cm deep. The mixture was tamped with the help of a standard rod. The specimens were kept in cold water for 24 hours. After the mould is removed, the specimen is subjected to curing for about 3-7 days. In the present study, 4 kg of aggregates was replaced by waste concrete aggregates, 2 kg of sand was replaced by glass industry waste and 1 kg of cement was replaced by fly ash and powder solid glass waste.

2.5 Tests on Burnt Bricks

Various properties of burnt bricks like compressive strength, water holding capacity, efflorescence test, flexural strength and compacting factor test for concrete blocks were carried out as per the standard procedures (Rangola, 2002, BIS-1077-1957).

2.6 Recovery of Iron Oxide

Since, in the textile waste sludge, the amount of Iron Oxide present is 30.18 %, an attempt has been made to recover this. 0.250 kg of the textile solid sludge was taken in 1000 ml beaker and 1:1 Hydrochloric acid (HCl) was added in such a way that the level of the acid was 0.05 m above the solid. The contents were boiled for 10-15 minutes and allowed to settle. The supernatant liquid was filtered. The above procedure was repeated 5 to 6 times to leach the iron completely and Iron was precipitated in the filtrate by Hydroxide Method (Vogel, 1961). The precipitate was dried and ignited. This iron may be used in paint industry.

3. Results and Discussion

For bricks manufactured from individual and combination of various industrial sludge, various tests like compressive strength, water holding capacity, flexural strength; efflorescence test and for concrete blocks compacting factor test were conducted and results have given in Table 2, 3, 4, and 5. Maximum allowable values for the bricks are given in Table 6. From the analysis results of various solid wastes (given in Table 1), it found that these sludge is considered to be suitable for the production of building materials such as bricks and concrete blocks. The work mainly focused on using sludge to replace red soil/clay in the manufacture of bricks and sand/ aggregates/cement in the manufacture of

concrete blocks. From the tabulated results it is clear that sludge can be replaced up to 25-30% in the manufacture of bricks that does not affect physical and chemical properties of bricks. But in the manufacture of concrete blocks, compaction factor test results (Flexural strength of concrete blocks: Breaking point of concrete block =0.22 m) and flexural strength of concrete blocks shows that 45-50% of sludge can be replaced.

4. Conclusion

Solid waste from various industries (textile house, glass and thermal industry) has been collected and characterized. These solid waste were obtained can be utilized in the production of building materials. From the results, it is concluded that solid waste sludge can be replaced up to 25-30% to produce bricks and 45-50% to produce concrete blocks. The bricks produced with 25-30 % sludge were observed to have good compressive strength and water holding capacity, which meets the specifications recommended. As the present disposal methods are found to be hazardous, a highly eco-friendly method has been formulated for the conversion of solid wastes into value-added products like building bricks and concrete blocks. This promising alternate disposal method thus paves a better way to dispose the solid wastes from various industries on one side and provides a means to utilize the solid wastes for useful purpose, on the other.

References

- APHA, (1991). *Standard Methods for Examination of water and wastewater*, American Public Health Association, Washington D.C.,
- Arnold, E. Greenberg, Lenore, Desceri, S., Andrew, Saaton, D. (1992). *Standard methods for the examination of water and wastewater*, 18th Edn.
- Bureau of Indian Standard, BIS-1077-1957.
- Giri, A. K., Bhattacharya, A. K. (1991). Characterization of solid waste generation in Wazirpur area of Delhi, *J. Ecotoxicol. Env. Monit.* 9(1), 51-61.
- Khan, R.R., (1994), Environmental Management of Municipal solid waste, *Indian J. Environ. Prot.* 149 (1), 26-30
- Kumaravelan, R. Anandan, P. (2004). *Principles of Environmental Engineering*, 1st Edn. SciTech Publishers Ltd., Chennai. 3.16-3.17.
- Rangola, S. C. (2002). *Engineering Materials*, 28th Edn. Charotar Publishing House, 39-41.
- Raviprasath, P., Sastry, G. S. R., Sharma, P. N. (2003), Studies on the Characterization and Utilization of Solid Waste from a Battery Manufacturing Industry, *Pollution Research*, 22 (1), 73-75.
- Vogel, A. I. (1961., *Text book of Inorganic Analysis*, 3rd Edn., Longman Green & Co. Ltd., London.

Table 1. Composition of the various industrial sludge (wt %)

Element	Red soil	Textile house sludge	Glass industry sludge	Thermal plant waste	Cement
Alumina	27.0	2.0	0.0002	30.36	6.0
Calcium	-	26.67	-	3.04	55.0
Ferric oxide	01.0	30.18	0.0002	3.34	3.5
Magnesium	05.0	3.5	-	0.93	7.5
Org. matter	05.0	-	-	-	-
Silica	62.0	5.0	45.13	50.41	22.0
Sodium	-	3.65	12.96	3.07	1.0
Sulphate	-	1.714	-	1.71	2.0
Others	-	27.286	41.9098	7.14	3.0

Table 2. Analysis of textile house waste- red soil blended bricks (wt. %)

Textile house waste %	Red soil				Fly ash*		
	%	Compressive strength (N/mm ²)	water holding capacity (%)	Efflorescence	%	Compre-ssi ve strength (N/mm ²)	water holding capacity (%)
80	20	-	15.90	Slight	20	0.925	14.50
70	30	-	15.50	Slight	30	0.875	15.95
60	40	0.52	14.85	Slight	40	-	>18
50	50	0.81	14.00	Slight	50	-	>18
40	60	1.20	13.75	Slight	-	-	-
30	70	4.55	12.95	Slight	-	-	-

*For all Fly ash composition efflorescence test is: serious

Table 3. Compaction factor and flexural strength test on concrete blocks

Water- cement ratio	Compaction factor	Flexural strength
0.4	0.73	Breaking point = 0.22 m
0.45	0.74	

Table 4. Analysis of textile house sludge-glass industry sludge-red soil blended bricks

Textile house waste %	Glass industry waste %	Red soil %	Compressive strength (N/mm ²)	Water holding capacity (%)	Efflorescence
5	5	90	9.225	8.95	Nil
5	10	85	8.995	10.50	Nil
5	15	80	8.125	10.95	Slight
5	20	75	6.850	11.25	Slight
10	10	80	7.125	10.25	Nil
10	5	85	8.850	10.15	Nil
10	15	75	6.225	11.50	Slight
10	20	70	5.445	11.25	Slight
15	10	75	4.125	11.50	Slight
15	15	70	3.850	11.95	Slight

Table 5. Analysis of industrial wastes of textile-glass -thermal-red soil blended bricks

Textile waste %	Glass waste %	thermal waste %	Red soil %	Compressive strength (N/mm ²)	Water holding capacity (%)	Efflorescence
5	5	5	85	9.885	8.22	Nil
5	5	10	80	10.150	8.62	Nil
5	10	5	80	9.50	8.79	Nil
10	10	10	70	7.55	10.11	Slight
10	5	5	80	8.15	9.15	Nil
10	10	5	75	7.125	9.92	Nil
10	5	10	75	7.75	9.87	Nil
15	5	5	75	7.17	9.90	Nil
15	10	5	70	6.99	11.10	Slight
15	15	5	65	5.20	11.95	Slight
15	10	10	65	5.35	11.04	Slight
20	5	5	70	5.55	9.94	Nil

Table 6. Maximum allowable values for the bricks

S. No.	Test type	Maximum allowable value
1.	Compressive strength	7 to 14 N/mm ² (BIS-1077-1957)
2.	Water absorption	20% dry brick wt.
3.	Hardness	Sufficiently hard
4.	Structure	Homogenous, Free from defects
5.	Efflorescence test	White deposit on surface, up to 10%- slight, up to 50%- moderate, greater than 50%- serious



A System Matrix Equations over an Arbitrary Skew Field

Youcai Xue

School of Science

Zhejiang University of Science and Technology

318, Liuhe Rod, Hangzhou 310023, China

Tel: 86-571-8507-0705 E-mail: xue_jian2008@sina.com

Abstract

In this paper, we give a practical solving method and an expression of general solutions of a system matrix equations $A_1XB_1 = C_1$ and $A_2XB_2 = C_2$ over an arbitrary skew field by using some matrix techniques and elementary operations on matrices.

Keywords: skew field, System matrix equations, Elementary operations on matrices

1. Introduction

It is well known that matrix equation is one of important contents of matrix study. In [1] an expression of general solutions of the matrix equation $AXB=CXD$ over an arbitrary skew field was given. In this paper we consider the mentioned system matrix equations $A_1XB_1 = C_1$ and $A_2XB_2 = C_2$ over an arbitrary skew field and give an expression of general solutions and a practical solving method of the matrix equation by using some matrix techniques and elementary operations on matrices with entries from an arbitrary skew field.

Throughout this paper we denote an arbitrary skew field by F , the set of all $m \times n$ matrixes over F by $F^{m \times n}$, the set of all matrices in $F^{m \times n}$ with rank r by $F_r^{m \times n}$, a $m \times m$ identity matrix by I_m , the rank of matrix A by $\text{rank}A$.

Now we introduce the following known lemmas.

Lemma 1.1^[2] Let $A \in F^{m \times n}$. Then $\text{rank}A=r$ if and only if there exist $P \in F_m^{m \times m}$ and $Q \in F_n^{n \times n}$ such that

$$PAQ = \begin{bmatrix} I_r & 0 \\ 0 & 0 \end{bmatrix}$$

Lemma 1.2^[3] Suppose P and Q be invertible matrices over F . If the multiplication of matrices can be performed, then $\text{rank}A = \text{rank}PA = \text{rank}AQ = \text{rank}PAQ$ for any matrix A with entries from F .

Lemma 1.3^[4] Let $A \in F_r^{r \times r}$. Then

$$\text{rank} \begin{bmatrix} A & B \\ C & D \end{bmatrix} = r + \text{rank}(D - CA^{-1}B)$$

Lemma 1.4^[5] Let $A \in F^{n \times n}$. Then the following conditions are equivalent:

- (i) A is invertible;
- (ii) A is a product of elementary matrices;
- (iii) $\text{rank}A=n$

Lemma 1.5^[5] Let $A \in F^{m \times n}$, E_m (resp. E_n) be the elementary matrix obtained by performing an elementary row[resp. column] operation T on I_m (resp. I_n). Then $E_m A$ (resp. $A E_n$) is the matrix obtained by performing the operation T on A .

2. Main Results

Now we consider the matrix equation

$$\begin{cases} A_1XB_1 = C_1 \\ A_2XB_2 = C_2 \end{cases} \tag{1}$$

where $A_1 \in F_r^{m \times n}, A_2 \in F_t^{p \times n}, B_1 \in F_s^{l \times k}, B_2 \in F_w^{l \times q}, C_1 \in F^{m \times k}, C_2 \in F^{p \times q}$.

(1) is equivalent to the following systems matrix equations

$$\begin{cases} PA_1QQ^{-1}XV_0^{-1}V_0B_1Q_0 = PC_1Q_0 \\ VA_2QQ^{-1}XV_0^{-1}V_0B_2U = VC_2U \end{cases} \tag{2}$$

Where $P \in F_m^{m \times m}, Q \in F_n^{n \times n}, Q_0 \in F_k^{k \times k}, V \in F_p^{p \times p}, U \in F_q^{q \times q}, V_0 \in F_l^{l \times l}$.

Theorem 2.1 For matrices A_1, A_2, B_1, B_2 in (1), there exist

$P \in F_m^{m \times m}, Q \in F_n^{n \times n}, Q_0 \in F_k^{k \times k}, V \in F_p^{p \times p}, U \in F_q^{q \times q}, V_0 \in F_l^{l \times l}$, such that

$$(i) \quad PA_1Q = \begin{bmatrix} I_r & 0 \\ 0 & 0 \end{bmatrix} \begin{matrix} r \\ m-r \end{matrix}, VA_2Q = \begin{bmatrix} 0 & 0 & I_{r_2} & 0 \\ I_{r_1} & 0 & 0 & 0 \\ 0 & 0 & 0 & 0 \end{bmatrix} \begin{matrix} r_2 \\ r_1 \\ p-r_1-r_2 \end{matrix};$$

$$(ii) \quad V_0B_1Q_0 = \begin{bmatrix} I_s & 0 \\ 0 & 0 \end{bmatrix} \begin{matrix} s \\ l-s \end{matrix}, V_0B_2U = \begin{bmatrix} 0 & I_{s_2} & 0 \\ 0 & 0 & 0 \\ I_{s_1} & 0 & 0 \\ 0 & 0 & 0 \end{bmatrix} \begin{matrix} s_2 \\ s-s_2 \\ s_1 \\ l-s-s_1 \end{matrix}$$

Where $r_1 + r_2 = t, s_1 + s_2 = w$.

Proof We proof (ii). It follows from Lemma 1.1 that there exist $V_1 \in F_l^{l \times l}, Q_1 \in F_k^{k \times k}$ such that

$$V_1B_1Q_1 = \begin{bmatrix} I_s & 0 \\ 0 & 0 \end{bmatrix} \begin{matrix} s \\ l-s \end{matrix} \tag{3}$$

Let $V_1B_2 = \begin{bmatrix} W_1 \\ W_2 \end{bmatrix}$, where $W_1 \in F^{s \times q}, W_2 \in F^{(l-s) \times q}$. For W_2 , there exist $V_2 \in F_{l-s}^{(l-s) \times (l-s)}, Q_2 \in F_q^{q \times q}$, such that

$$V_2W_2Q_2 = \begin{bmatrix} I_{s_1} & 0 \\ 0 & 0 \end{bmatrix} \begin{matrix} s_1 \\ l-s-s_1 \end{matrix} \tag{4}$$

Let $W_1Q_2 = [W_{11} \quad W_{12}]$, where $W_{11} \in F^{s \times s_1}, W_{12} \in F^{s \times (q-s_1)}$. It follows from Lemma 1.2 and 1.3 that

$$\begin{aligned} \text{rank} B_2 &= \text{rank} \begin{bmatrix} I_s & 0 \\ 0 & V_2 \end{bmatrix} V_1B_2Q_2 = \text{rank} \begin{bmatrix} I_s & 0 \\ 0 & V_2 \end{bmatrix} \begin{bmatrix} W_1Q_2 \\ W_2Q_2 \end{bmatrix} = \text{rank} \begin{bmatrix} W_1Q_2 \\ V_2W_2Q_2 \end{bmatrix} \\ &= \text{rank} \begin{bmatrix} W_{11} & W_{12} \\ I_{s_1} & 0 \\ 0 & 0 \end{bmatrix} = s_1 + \text{rank} W_{12} \end{aligned}$$

Hence $\text{rank} W_{12} = s - s_1 \equiv s_2$

For W_{12} there exist $V_3 \in F_s^{s \times s}$ and $Q_3 \in F_{q-s_1}^{(q-s_1) \times (q-s_1)}$ such that

$$V_3W_{12}Q_3 = \begin{bmatrix} I_{s_2} & 0 \\ 0 & 0 \end{bmatrix} \begin{matrix} s_2 \\ s-s_2 \end{matrix} \tag{5}$$

Let

$$V_0 = \begin{bmatrix} V_3 & (-V_3W_{11}, 0)V_2 \\ 0 & V_2 \end{bmatrix} V_1, Q_0 = Q_1 \begin{bmatrix} V_3^{-1} & 0 \\ 0 & I_{k-s} \end{bmatrix}, U = Q_2 \begin{bmatrix} I_{s_1} & 0 \\ 0 & Q_3 \end{bmatrix}$$

by (3)~(5)

$$V_0B_1Q_0 = \begin{bmatrix} V_3 & (-V_3W_{11}, 0)V_2 \\ 0 & V_2 \end{bmatrix} V_1B_1Q_1 \begin{bmatrix} V_3^{-1} & 0 \\ 0 & I_{k-s} \end{bmatrix} = \begin{bmatrix} I_s & 0 \\ 0 & 0 \end{bmatrix}$$

$$\begin{aligned}
 V_0 B_2 U &= \begin{bmatrix} V_3 & (-V_3 W_{11}, 0) V_2 \\ 0 & V_2 \end{bmatrix} V_1 B_2 Q_2 \begin{bmatrix} I_{s_1} & 0 \\ 0 & Q_3 \end{bmatrix} = \begin{bmatrix} V_3 W_1 Q_2 + (-V_3 W_{11}, 0) V_2 W_2 Q_2 \\ V_2 W_2 Q_2 \end{bmatrix} \begin{bmatrix} I_{s_1} & 0 \\ 0 & Q_3 \end{bmatrix} \\
 &= \begin{bmatrix} 0 & V_3 W_{12} \\ I_{s_1} & 0 \\ 0 & 0 \end{bmatrix} \begin{bmatrix} I_{s_1} & 0 \\ 0 & Q_3 \end{bmatrix} = \begin{bmatrix} 0 & V_3 W_{12} Q_3 \\ I_{s_1} & 0 \\ 0 & 0 \end{bmatrix} = \begin{bmatrix} 0 & I_{s_2} & 0 \\ 0 & 0 & 0 \\ I_{s_1} & 0 & 0 \\ 0 & 0 & 0 \end{bmatrix}
 \end{aligned}$$

Similarly, (i) may be shown.

Let

$$\text{(iii)} \quad \left\{ \begin{aligned}
 Q^{-1} X V_0^{-1} &= \begin{bmatrix} X_{11} & X_{12} & X_{13} & X_{14} \\ X_{21} & X_{22} & X_{23} & X_{24} \\ X_{31} & X_{32} & X_{33} & X_{34} \\ X_{41} & X_{42} & X_{43} & X_{44} \end{bmatrix} \begin{matrix} r_1 \\ r - r_1 \\ r_2 \\ n - r - r_2 \end{matrix} \\
 P C_1 Q_0 &= \begin{pmatrix} G_1 & G_2 \\ G_3 & G_4 \end{pmatrix} r = \begin{pmatrix} \begin{pmatrix} G_{11} & G_{12} \\ G_{21} & G_{22} \end{pmatrix} & G_2 \\ & G_3 & G_4 \end{pmatrix} \\
 V C_2 U &= \begin{pmatrix} E_{11} & E_{12} & E_{13} \\ E_{21} & E_{22} & E_{23} \\ E_{31} & E_{32} & E_{33} \end{pmatrix} \begin{matrix} r_1 \\ r_2 \\ r_3 \end{matrix} \\
 & \quad \quad \quad \begin{matrix} s_2 & s - s_2 & s_1 & l - s - s_1 \\ s_1 & s_2 & k - s & \end{matrix}
 \end{aligned} \right.$$

Theorem 2.2 Let $P, U, Q, Q_0, V, V_0, E_{ij} (i, j = 1, 2, 3), G_{ij} (i, j = 1, 2), G_k (k = 1, 2, 3, 4)$ be matrices mentioned in theorem 2.1 and (iii). Then (1) has solution if and only if $X_{ij} = G_{ij} (i, j = 1, 2), X_{33} = E_{11}, X_{31} = E_{12}, X_{13} = E_{21}, X_{11} = E_{22} = G_{11}, G_i = 0 (i = 2, 3, 4) E_{j3} = E_{3j} = 0 (j = 1, 2, 3)$ Whence the general solution of (1) is

$$X = Q \begin{bmatrix} G_{11} & G_{12} & E_{21} & X_{14} \\ G_{21} & G_{22} & X_{23} & X_{24} \\ E_{12} & X_{32} & E_{11} & X_{34} \\ X_{41} & X_{42} & X_{43} & X_{44} \end{bmatrix} V_0 \tag{6}$$

where,

$$\begin{aligned}
 X_{14} &\in F^{r_1 \times (l - s - s_1)}, X_{23} \in F^{(r - r_1) \times s_1}, X_{24} \in F^{(r - r_1) \times (l - s - s_1)}, X_{32} \in F^{r_2 \times (s - s_2)}, \\
 X_{34} &\in F^{r_2 \times (l - s - s_1)}, X_{41} \in F^{(n - r - r_2) \times s_2}, X_{42} \in F^{(n - r - r_2) \times (s - s_2)}, X_{43} \in F^{(n - r - r_2) \times s_1}, \\
 X_{44} &\in F^{(n - r - r_2) \times (l - s - s_1)}
 \end{aligned}$$

are all any matrices over F with corresponding orders.

Proof For (1), i.e. for (2), by (iii), (2) is equivalent to the following systems matrix equations

$$\left\{ \begin{aligned}
 \begin{pmatrix} I_r & 0 \\ 0 & 0 \end{pmatrix} \begin{pmatrix} X_{11} & X_{12} & X_{13} & X_{14} \\ X_{21} & X_{21} & X_{21} & X_{21} \\ X_{31} & X_{32} & X_{33} & X_{34} \\ X_{41} & X_{42} & X_{43} & X_{44} \end{pmatrix} \begin{pmatrix} I_s & 0 \\ 0 & 0 \end{pmatrix} &= \begin{pmatrix} \begin{pmatrix} G_{11} & G_{12} \\ G_{21} & G_{22} \end{pmatrix} & G_2 \\ & G_3 & G_4 \end{pmatrix} \\
 \begin{pmatrix} 0 & 0 & I_{r_2} & 0 \\ I_{r_1} & 0 & 0 & 0 \\ 0 & 0 & 0 & 0 \end{pmatrix} \begin{pmatrix} X_{11} & X_{12} & X_{13} & X_{14} \\ X_{21} & X_{21} & X_{21} & X_{21} \\ X_{31} & X_{32} & X_{33} & X_{34} \\ X_{41} & X_{42} & X_{43} & X_{44} \end{pmatrix} \begin{pmatrix} 0 & I_{s_2} & 0 \\ 0 & 0 & 0 \\ I_{s_1} & 0 & 0 \\ 0 & 0 & 0 \end{pmatrix} &= \begin{pmatrix} E_{11} & E_{12} & E_{13} \\ E_{21} & E_{22} & E_{23} \\ E_{31} & E_{32} & E_{33} \end{pmatrix}
 \end{aligned} \right. \tag{7}$$

(7) i.e.

$$\left(\begin{array}{c} \left(\begin{array}{cc} X_{11} & X_{12} \\ X_{21} & X_{22} \end{array} \right) & 0 \\ 0 & 0 \end{array} \right) = \left(\begin{array}{c} \left(\begin{array}{cc} G_{11} & G_{12} \\ G_{21} & G_{22} \end{array} \right) & G_2 \\ & G_3 & G_4 \end{array} \right) \tag{8}$$

$$\left(\begin{array}{c} \left(\begin{array}{ccc} X_{33} & X_{31} & 0 \\ X_{13} & X_{11} & 0 \\ 0 & 0 & 0 \end{array} \right) & \left(\begin{array}{ccc} E_{11} & E_{12} & E_{13} \\ E_{21} & E_{22} & E_{23} \\ E_{31} & F_{32} & E_{33} \end{array} \right) \end{array} \right)$$

This proof is completed.

To sum up the above results, we obtain the detailed steps of solving (1):

(i) Let $L = \begin{bmatrix} B_1 & B_2 & I_l \\ I_k & I_q & 0 \end{bmatrix}$, we apply a sequence of elementary row operations on the first l rows of G and apply a sequence of elementary column operations on the first k columns of L and obtain the following form

$$L_1 = \left(\begin{array}{c} \left(\begin{array}{cc} \Lambda & 0 \\ 0 & 0 \end{array} \right) & \left(\begin{array}{c} W_1 \\ W_2 \end{array} \right) & V_1 \\ Q_0 & I_q & 0 \end{array} \right)$$

Where, Λ is a non-degenerate upper (or lower) triangular matrix. Then, we apply a sequence of elementary row operations on the first s rows of L_1 and apply a sequence of elementary column operations on the next q columns of L_1 again till we obtain the following form

$$L_2 = \left(\begin{array}{c} \left(\begin{array}{cc} I_s & 0 \\ 0 & 0 \end{array} \right) & \left(\begin{array}{ccc} 0 & I_{s_2} & 0 \\ 0 & 0 & 0 \\ I_{s_1} & 0 & 0 \\ 0 & 0 & 0 \end{array} \right) & V_0 \\ Q_0 & U & 0 \end{array} \right)$$

(ii) Let $M = \begin{bmatrix} A_1 & I_m \\ A_2 & I_p \\ I_n & 0 \end{bmatrix}$, we apply a sequence of elementary row operations on the first m rows of M and apply a sequence

of elementary column operations of the first n columns of M and obtain

$$M_1 = \left(\begin{array}{c} \left(\begin{array}{cc} \Omega & 0 \\ 0 & 0 \end{array} \right) & P \\ \left(\begin{array}{cc} D_1 & D_2 \end{array} \right) & I_p \\ Q_1 & 0 \end{array} \right)$$

Where, Ω is a non-degenerate upper (or lower) triangular matrix. Then, we apply a sequence of elementary column operations on the first r columns of M_1 and apply a sequence of elementary row operations on the next p rows of M_1 again till we obtain the following form

$$M_2 = \left(\begin{array}{c} \left(\begin{array}{ccc} I_s & 0 & \\ 0 & 0 & \end{array} \right) & P \\ \left(\begin{array}{cccc} 0 & 0 & I_{s_1} & 0 \\ I_{s_2} & 0 & 0 & 0 \\ 0 & 0 & 0 & 0 \end{array} \right) & V \\ Q & 0 \end{array} \right)$$

(iii) By theorem 2.2, we can discuss the all solution circumstances of (1) and obtain an expression of general solutions if it has solution.

References

- Xue You-cai, A matrix equation $AXB=CXD$ over an arbitrary skew field, *J. of Engineering Math.* 15:1(1998), 139-142.
- Xie Bang-jie, Self-conjugate matrices and determinant over the quaternion field, *J. Natural Science of Jilin University*, 2(1980),19-35.
- Xie Bang-jie, Matrices and two types of generalized Jordan's form over a ring and a skew field, *J. Natural Science of Jilin University*, 1(1978), 21-46.
- Tu Bexun, Generalized inverses of matrices over a p-skew field, *Acta. Math.Sinica*, 29:2(1986), 246-248.
- T.W.Hungerford, *Algebra*, Springer-verlag, New York, in 1980.30:5(1987), 688-694.



Error Estimates to A Kind of Boundary Value Problem about An Elliptic Differential Equation with Variable Coefficient

Rao Li, Yiming Chen, Yong Li & Wei Guan

College of Science

Yanshan University

Qinhuangdao, 066004, China

E-mail: lirao123@yahoo.com.cn

Abstract

A kind of boundary value problem about a second-order elliptic differential equation with variable coefficient is discussed indirectly by transforming it as the second kind of variational inequality form. Using regularization method, the variational inequality is formulated as an equal variational equation, which can be made discrete by the finite element method. Abstract error estimate and the error estimates of the approximation are derived under the energy norm and L^2 -norm.

Keywords: Variational inequality, Error estimate, Finite element analysis, Elliptic differential equation

1. Problem Statement

Suppose $\Omega \in R^n$ is a bounded open domain, Γ is the sufficiently smooth boundary of Ω , and n is the outward normal to Γ , $meas(\Gamma) > 0$; $V = \{u \in H^1(\Omega), u \geq 0\}$; $K \subset V$; Where

$$a(u, v) = \int_{\Omega} \sum_{i,j=1}^n \alpha_{ij}(x) \frac{\partial u}{\partial x_j} \frac{\partial v}{\partial x_i} dx + \int_{\Omega} \beta(x) uv dx, j(v) = g \int_{\Gamma} \alpha_{ij}(x) |v| ds, g \text{ is a positive constant; } \langle f, v \rangle = \int_{\Omega} f v dx, f \in L^n(\Omega).$$

In this paper, we discuss the boundary value problem about a second-order elliptic type differential equation with variable coefficient as follows:

$$\begin{cases} - \sum_{i,j=1}^n \frac{\partial}{\partial x_i} \left[\alpha_{i,j}(x) \frac{\partial u(x)}{\partial x_j} \right] + \beta(x) u(x) = f(x) & \text{in } \Omega \\ \left| \frac{\partial u}{\partial n_A} \right| \leq g & \text{on } \Gamma \\ u \frac{\partial u}{\partial n_A} + g|u| = 0 & \text{on } \Gamma \end{cases} \quad (1)$$

The coefficients and the solution u in (1) satisfy:

- (i) Exist $a > 0$, such that $\sum_{i,j=1}^n \alpha_{ij}(x) \xi_i \xi_j \geq a \sum_{i=1}^n \xi_i^2, a.e. x \in \Omega, \forall \xi \in R^n$.
- (ii) $\alpha_{ij}(x) \in L^\infty(\Omega), \alpha_{ij}(x) = \alpha_{ji}(x), \beta(x) \in L^\infty(\Omega), \frac{\partial u}{\partial x_j} n_j = \frac{\partial u}{\partial n_A} \in H^{-\frac{1}{2}}(\Gamma)$.

We had proven the variational inequality problem that is equal to problem (1), as follows:

$$\begin{cases} \text{find } u \in V, \text{ such that} \\ \langle a(u, v - u) + j(v) - j(u) \rangle \geq \langle f, v - u \rangle \forall v \in V \end{cases} \quad (2)$$

And the variational inequality exists only one solution. (Chen, 2008)

Problem (2) originates from many physics and engineering reality. The variational inequality includes an

indifferentiable functional. Using the regularization method (Chen, 2008), and making use of the differentiable function (R. Ding, 2005, pp.121-124), this problem was formulated as an equal variational equation. We will construct approach by finite element method and give the abstract error estimate and the error estimates of the approximation under the energy norm and L^2 -norm. For better dissertating, regularization about the variational inequality (2) and the process of solving the equal variational equation (Chen, 2008) will be iterated in the next part briefly.

2. Regularization method and the equal problem

Using regularization method, we construct the differentiable functional $j_\epsilon(v) = g \sum_{i,j=1}^n \int \alpha_{ij}(x) \psi_\epsilon(v) ds$ to substitute

$j(v) = g \sum_{i,j=1}^n \alpha_{ij}(x) |v| ds$ approximately, where

$$\psi_\epsilon(\xi) = \int_0^\xi \varphi(t) dt = \begin{cases} g\xi - \frac{1}{2}\epsilon g^2, & \xi \geq \epsilon g \\ \frac{\xi^2}{2\epsilon}, & |\xi| \leq \epsilon g \\ -g\xi - \frac{1}{2}\epsilon g^2, & \xi \leq -\epsilon g \end{cases} \tag{3}$$

And

$$\varphi(t) = \begin{cases} g, & \xi \geq \epsilon g \\ \frac{t}{\epsilon}, & |\xi| \leq \epsilon g \\ -g, & \xi \leq -\epsilon g \end{cases} \tag{4}$$

Easily we know that $\lim_{\epsilon \rightarrow 0} \psi_\epsilon(v) = g|v|$. Problem (2) can be substituted approximately by the problem:

$$\begin{cases} \text{find } u \in V, \text{ such that} \\ a(u, v - u) + j_\epsilon(v) - j_\epsilon(u) \geq \langle f, v - u \rangle \quad \forall v \in V \end{cases} \tag{5}$$

We can easily prove that $j_\epsilon(v)$ is convex, differentiable and $\lim_{\epsilon \rightarrow 0} j_\epsilon(v) = j(v)$.

The following theorem is quoted from the article (Chen, 2008), we give it directly without proof.

Theorem 1 Suppose u and u_ϵ are the solutions of problem (2) and (5) respectively, then when $\epsilon \rightarrow 0$, u_ϵ converges to u strongly.

In the following we consider the equal form to variational inequality (5).

Let $v = u \pm tw, t > 0, w \in V$ in (5), then we have

$$\pm a(u, w) + g \sum_{i,j=1}^n \int \alpha_{ij}(x) \left[\frac{\psi_\epsilon(u \pm tw) - \psi_\epsilon(u)}{t} \right] ds \geq \pm \langle f, v \rangle$$

Let $t \rightarrow 0^+$, we have

$$\lim_{t \rightarrow 0^+} \frac{\psi_\epsilon(u \pm tw) - \psi_\epsilon(u)}{t} = \pm \psi'_\epsilon(u) w = \pm \varphi(u) w$$

Then the solution $u \in V$ of problem (5) satisfies

$$a(u, v) + g \sum_{i,j=1}^n \int \alpha_{ij}(x) \varphi(u) v ds = \langle f, v \rangle \quad \forall v \in V \tag{6}$$

So we obtain the equal variational form (6) to problem (5).

3. The finite element approach and the error estimate

In order to carry on the stability estimate and the error analysis, we give the following lemma and the deduction at first. C is used to express constant in the paper, and the identical letter appears in different place may express different constants.

Lemma 1 Function $\varphi(t)$ is defined as (4), then $\varphi(t) \in H^1(-\infty, +\infty)$ and satisfies Lipschitz and monotony conditions as

follow:

$$|\varphi(u) - \varphi(v)| \leq \frac{1}{\varepsilon} |u - v| \quad \forall u, v \in R \tag{7}$$

$$(\varphi(u) - \varphi(v))(u - v) \geq 0 \quad \forall u, v \in R \tag{8}$$

Deduction 1 The solution of problem (6) exists uniquely and satisfies the following stability:

$$\|u\|_1 \leq C \|f\| \tag{9}$$

Proof The solution of problem (5) exists uniquely. Form the equivalence between (5) and (6), we know that problem (6) has only one solution. Following we prove the stability estimate. Take $v = u$ in (6), and take notice of $\varphi(0) = 0$ form (9), by lemma 1, we have $\varphi(u)u \geq 0$, also by $g > 0, \alpha_{ij} \geq 0 a.e. on \Gamma$, we can obtain $a(u, u) \leq \langle f, u \rangle$. Additionally, as the bilinear form $a(u, u)$ is compulsive, we can obtain the stability estimate.

Suppose J_h is a regular triangulation in Ω , $V_h \subset V$ is the corresponding linear finite element space. Marking $\|u\|_E = \sqrt{a(u, u)}$ to express the energy norm. Consider the following finite element approximation problem about problem (6).

$$\begin{cases} \text{find } u_h \in V_h, \text{ such that} \\ a(u_h, v_h) + g \sum_{i,j=1}^n \int_{\Gamma} \alpha_{ij}(x) \varphi(u_h) v_h ds = \langle f, v_h \rangle \quad \forall v_h \in V_h \end{cases} \tag{10}$$

Just like deduction 1, we can obtain the existence and uniqueness of the solution of (10), and the solution similarly satisfies the stability estimate (9). Abstract error estimate about solutions of (6) and (10) will be given in the next part.

Theorem 2 Suppose u and u_h are the solutions of problem (6) and (10) respectively, then we have error estimates under the energy norm and L^2 -norm as follows:

$$\|u - u_h\|_E \leq C \inf_{v_h \in V_h} \left\{ \|u - v_h\|_E + g \sum_{i,j=1}^n \|\alpha_{ij}(x)\|_1 \|u - v_h\|_{L^2(\Gamma)} \right\} \tag{11}$$

$$\|u - u_h\|_{L^2(\Omega)} \leq C \sum_{i,j=1}^n \|\alpha_{ij}(x)\|_1 \sup_{q \in L^2(\Omega)} \left\{ \frac{1}{\|q\|} \inf_{v_h \in V_h} \| \omega - v_h \|_E \right\} \|u - u_h\|_E \tag{12}$$

For assigned $q \in L^2(\Omega)$, $\omega \in V$ is the unique solution of the following elliptic problem (17).

Proof To perform subtraction between (6) and (10), we can obtain

$$a(u - u_h, v_h) + g \sum_{i,j=1}^n \int_{\Gamma} \alpha_{ij}(x) [\varphi(u) - \varphi(u_h)] v_h ds = 0 \quad \forall v_h \in V_h \tag{13}$$

From this expression, using the compulsive character of the bilinear form $a(u, u)$, we have

$$\begin{aligned} \mu_0 \|u - u_h\|_E^2 &\leq a(u - u_h, u - u_h) \\ &= a(u - u_h, u - v_h) - g \sum_{i,j=1}^n \int_{\Gamma} \alpha_{ij}(x) [\varphi(u) - \varphi(u_h)] (v_h - u_h) ds \\ &= a(u - u_h, u - v_h) - g \sum_{i,j=1}^n \int_{\Gamma} \alpha_{ij}(x) [\varphi(u) - \varphi(u_h)] (v_h - u) ds \\ &\quad - g \sum_{i,j=1}^n \int_{\Gamma} \alpha_{ij}(x) [\varphi(u) - \varphi(u_h)] (u - u_h) ds \end{aligned} \tag{14}$$

By Lemma 1, the bounded character of $a(u, u)$ and trace theorem, we can obtain

$$\begin{aligned} \mu_0 \|u - u_h\|_E^2 &\leq \mu_1 \|u - u_h\|_E \|u - v_h\|_E + \frac{1}{\varepsilon} g \sum_{i,j=1}^n \int_{\Gamma} \alpha_{ij}(x) |u - u_h| |v_h - u| ds \\ &\leq \mu_1 \|u - u_h\|_E \|u - v_h\|_E + C \frac{1}{\varepsilon} g \sum_{i,j=1}^n \|\alpha_{ij}(x)\|_1 \|u - u_h\|_E \|v_h - u\|_{L^2(\Gamma)} \quad v_h \in V_h \end{aligned} \tag{15}$$

Thus we obtain the error estimate expression (11).

In order to derive the error estimate under L^2 norm, for discretionally assigned $q \in L^2(\Omega)$, we first introduce the following auxiliary problem

$$\begin{cases} -\sum_{i,j=1}^n \frac{\partial}{\partial x_i} \left[\alpha_{i,j}(x) \frac{\partial \omega(x)}{\partial x_j} \right] + \beta(x)\omega(x) = q & \text{in } \Omega \\ \frac{\partial \omega}{\partial n_A} + \gamma(x)\omega = 0 & \text{on } \Gamma \end{cases} \quad (16)$$

Where $\gamma(x) = \frac{\varphi(u) - \varphi(u_h)}{u - u_h}$. The equal variational form of problem (16) is

$$\begin{cases} \text{find } \omega \in V, \text{ such that} \\ A(\omega, v) = \langle q, v \rangle \quad \forall v \in V \end{cases} \quad (17)$$

Where, $A(\omega, v) = a(\omega, v) + \sum_{i,j=1}^n \int_{\Gamma} \gamma \alpha_{ij}(x) \omega v ds$. We may know by lemma 1 that $\gamma(x) \in L^\infty(\Omega)$ and satisfies

$$0 \leq \gamma(x) \leq \frac{1}{\varepsilon} \quad x \in \bar{\Omega} \quad (18)$$

By $A(\omega, v)$, expression (18) and trace theorem, we know that the bilinear form $A(\cdot, \cdot)$ satisfies compulsive and bounded conditions in V , so the solution of problem (17) exists unequally.

Let $v = e = u - u_h$ in (17), using expression (13), the definition of $\gamma(x)$, lemma 1 and trace theorem, for $\forall v_h \in V_h$, we can obtain

$$\begin{aligned} (e, q) &= a(e, \omega) + g \sum_{i,j=1}^n \int_{\Gamma} \gamma \alpha_{ij}(x) \omega e ds = a(e, \omega - v_h) + a(e, v_h) + g \sum_{i,j=1}^n \int_{\Gamma} \gamma \alpha_{ij}(x) \omega e ds \\ &= a(e, \omega - v_h) - g \sum_{i,j=1}^n \int_{\Gamma} \alpha_{ij}(x) [\varphi(u) - \varphi(u_h)] v_h ds + g \sum_{i,j=1}^n \int_{\Gamma} \gamma \alpha_{ij}(x) \omega e ds \\ &= a(e, \omega - v_h) + g \sum_{i,j=1}^n \int_{\Gamma} \alpha_{ij}(x) [\varphi(u) - \varphi(u_h)] (\omega - v_h) ds \\ &\leq \mu \|e\|_E \|\omega - v_h\|_E + C \frac{1}{\varepsilon} g \sum_{i,j=1}^n \|\alpha_{ij}(x)\|_1 \|u - u_h\|_E \|\omega - v_h\|_E \end{aligned}$$

By the haphazardness of $q \in L^2(\Omega)$ and $v_h \in V_h$, we have expression (12). The proof finished.

By problem (20) and the compulsory condition of $A(\omega, v)$, we can obtain the following lemma:

Lemma 2 When Ω is a convex region or a full smooth bounded domain, the solution of problem (17) $\omega \in V \cap H^2(\Omega)$ and satisfies the stability estimate $\|\omega\|_2 \leq C \|q\|$.

In order to obtain the error estimate, we define interpolation operator $\Pi_h : C^0(\bar{\Omega}) \rightarrow V_h$ as follow: for $\forall v \in C^0(\bar{\Omega})$, $\Pi_h v \in V_h$ such that $\Pi_h v(P) = v(P)$, \forall dissection node $P \in \bar{\Omega}$.

By the above conclusions, theorem 2, lemmas 2 as well as the finite element interpolation theory, we can obtain conclusions about the error estimate as follows.

Theorem 3 Suppose $u \in V$ is the solution of problem (7) and $u_h \in V_h$ is the solution of (10), then when $u \in H^{1+\alpha}(\Omega)$, $\alpha \geq 0$, the following error estimates come into existence:

$$\|u - u_h\|_E \leq Ch^\alpha \left(\|u\|_{1+\alpha} + gh^{\frac{1}{2}} \sum_{i,j=1}^n \|\alpha_{ij}(x)\|_1 \|u\|_{H^{\frac{1}{2}+\alpha}(\Gamma)} \right) \quad (19)$$

$$\|u - u_h\|_{L^2(\Omega)} \leq Ch^{1+\alpha} \sum_{i,j=1}^n \|\alpha_{ij}(x)\|_1 \left(\|u\|_{1+\alpha} + gh^{\frac{1}{2}} \sum_{i,j=1}^n \|\alpha_{ij}(x)\|_1 \|u\|_{H^{\frac{1}{2}+\alpha}(\Gamma)} \right) \quad (20)$$

Proof Let $v_h = \Pi_h u$ in the abstract error estimate expression (11), then

$$\begin{aligned} \|u - u_h\|_E &\leq C \inf_{v_h \in V_h} \left\{ \|u - v_h\|_E + g \sum_{i,j=1}^n \|\alpha_{ij}(x)\|_1 \|u - v_h\|_{L^2(\Gamma)} \right\} \\ &\leq C \left\{ \|u - \Pi_h u\|_E + g \sum_{i,j=1}^n \|\alpha_{ij}(x)\|_1 \|u - \Pi_h u\|_{L^2(\Gamma)} \right\} \end{aligned} \quad (21)$$

By the finite element interpolation theory^[3], for $u \in H^{1+\alpha}(\Omega)$, $\alpha \geq 0$, we have

$$\|u - \Pi_h u\|_E \leq C_0 h^\alpha \|u\|_{1+\alpha}, \quad \|u - \Pi_h u\|_{L^2(\Gamma)} \leq C_1 h^{\frac{1}{2}+\alpha} \|u\|_{H^{\frac{1}{2}+\alpha}(\Gamma)}$$

Substitute them into the right margin of (21), and then we have the error estimate (19).

Let $v_h = \Pi_h \omega$ in (12) and using lemma 2, we have

$$\begin{aligned} \|u - u_h\|_{L^2(\Omega)} &\leq C \sup_{q \in L^2(\Omega)} \left\{ \frac{1}{\|q\|} \inf_{v_h \in V_h} \|\omega - v_h\|_E \right\} \sum_{i,j=1}^n \|\alpha_{ij}(x)\|_1 \|u - u_h\|_1 \\ &\leq Ch \sup_{q \in L^2(\Omega)} \left\{ \frac{1}{\|q\|} \|\omega\|_2 \right\} \sum_{i,j=1}^n \|\alpha_{ij}(x)\|_1 \|u - u_h\|_E \leq Ch \sum_{i,j=1}^n \|\alpha_{ij}(x)\|_1 \|u - u_h\|_E \end{aligned}$$

Additionally by (19) which have been proved above, we can obtain expression (20). The proof finished.

4. Conclusions

The variational equation equal to the variational inequality is made discrete by finite element method, which made the interpolation computation directly to the original variational inequality simplified. The existence, uniqueness and stability of the finite element solution are given. The abstract error estimate is established, and error estimate under the energy norm and L^2 norm is given. The finite element analysis about the variational inequality problem narrated in the paper is consummated.

References

- Chen Y. M. and Li R.. "The Existence and Uniqueness of the Solution for a kind of Second Order Elliptic Differential Equation of Variable Coefficient". Third international conference on innovative computing, information and control. China. 2008.
- Ding R. and Qian F. B.. "Regularization and finite element approximation for fourth-order variational inequality of the second kind." Journal of Lanzhou University (Natural Sciences). 2005. pp. 121-124.
- Ciarlet P. G. *The finite element method for elliptic problems*. North-Holland. Amsterdam. 1978.
- Glowinski R, Lions J. L. and Tremolieres R. *Numerical analysis of variational inequality*. Amsterdam. North-Holland Publishing Company. 1981.

Acknowledgement

This work is supported by the Nature Science Foundation of Hebei province in China (E2007000381).



The Choice of AC Electricity Bridge Adjustment Parameters

Zaiqi Fu, Changji Shan, Yuhui Luo & Xungang Yang

Department of Physics

Zhaotong Teacher's College

Zhaotong 657000, China

Tel: 86-870-215-3826 E-mail:zhxfzq@126.com

Abstract

It is set forth that how to choose adjustment parameters in the plural plane coordinate figure by the relation of Electricity Bridge's balance condition and adjustment parameters.

Keywords: Adjustment parameters, Choice, Balance

On the discussion of AC electricity bridge in some schoolbooks and correlated datum, it has been put forward that how to choose some quantities as adjustment parameters or the selected adjustment parameters from the observed quantities which have been discriminated reading. The new viewpoint is brought forward that how to choose the adjustment parameters by the point of view of adjustment velocity.

1. The Balance Condition of AC Electricity Bridge

The balance process of AC electricity bridge is decided by the change of eqn(1). Because Z_1, Z_2, Z_3, Z_4 are composed of resistance, capacitance and inductance which are parallel connection or in series, except the observed parameters, the others quantities can be regarded as adjustment parameters.

$$P=Z_2Z_3-Z_1Z_4=a+jb \quad (1)$$

It is shown by eqn(1) that the two quantities at least are chosen as adjustment parameters for a and b=0 together. If three or the more quantities are chosen, then adjustment times is nimety, the balance process can be very much trouble. In the most things, two quantities are chosen as adjustment parameters.

The selections have more groups. Some groups can not attain the balance of electricity bridge; some groups may attain the aim, but nimety. It is the best choice that not only some groups may attain the balance but also the adjustment times are few. The article will set forth how to choose correct adjustment parameters quickly through the frequent used AC electricity bridge.

2. The Quickly Chosen of AC Electricity Bridge Adjustment Parameters

At the balance point of electricity bridge, the relation of a, b and adjustment parameters may be expressed by parallel beeline family^[3]. The more nearly 90° of two parameter beeline angle, the more quickly of balance speed. It can be shown that which parameter beeline are perpendicularity or parallelism one another. The best choice is two parameters of perpendicularity, not parallelism. Without parameters of perpendicularity, the best seemliness choice is two parameters which angle is rather big.

2.1 Capacitance Electricity Bridge

According to Fig.2, it is shown the expression formula of a and b are eqn(2) and eqn(3) separated by the eqn(1). The beelines of each parameters are shown in Fig.3. It is the best choice that R_2 and C_2 are adjustment parameters, as shown in Fig.3.

$$a=R_xR_3-R_4R_2 \quad (2) \quad b=\frac{R_4}{C_2\omega}-\frac{R_3}{C_x\omega} \quad (3)$$

2.2 Inductance Compare Electricity Bridge

According to Fig.4, it is shown the expression formula of a and b are eqn(4) and eqn(5) separated by the eqn(1). The beelines of each parameters are shown in Fig.5. It is the best choice that R_2 and L_2 are adjustment parameters, as shown in Fig.5.

$$a=R_xR_3-R_2R_4 \quad (4) \quad b=L_xR_3\omega-L_2R_3\omega \quad (5)$$

2.3 Schering Electricity Bridge

According to Fig.6, it is shown the expression formula of a and b are eqn(6) and eqn(7) separated by the eqn(1). The beelines of each parameters are shown in Fig.7. Because the angle of R_3 and C_3 is rather big, it is the best choice that R_3 and C_3 are

adjustment parameters ,as shown in Fig.7.

$$a = \frac{R_x R_3}{1 + (R_3 C_3 \omega)^2} - \frac{R_3^2 C_3 \omega}{C_x \omega [1 + (R_3 C_3 \omega)^2]} \quad (6)$$

$$b = \frac{R_2}{C_4 \omega} - \frac{R_x R_3^2 C_3 \omega}{1 + (R_3 C_3 \omega)^2} - \frac{R_3}{C_x \omega [1 + (R_3 C_3 \omega)^2]} \quad (7)$$

2.4 Maxwell Electricity Bridge

According to Fig.8,it is shown the expression formula of a and b are eqn(8) and eqn(9) separated by the eqn(1).The beelines of each parameters are shown in Fig.9.Because the angle of R_3 and C_3 is rather big,it is the best choice that R_3 and C_3 are adjustment parameters ,as shown in Fig.9.

$$a = \frac{R_3 (R_x + R_3 C_3 \omega^2 L_x)}{1 + (R_3 C_3 \omega)^2} - R_2 R_4 \quad (8) \quad b = \frac{R_3 (L_x \omega - R_x R_3 C_3 \omega)}{1 + (R_3 C_3 \omega)^2} \quad (9)$$

For the complex AC Electricity Bridge, it is difficult to ascertain the relation which a and b change with some parameter varying. At the time ,it may be judged by the software of origin.

3. Conclusion

First, the each parameters are done in the coordinate chart of a and jb,then according to the angle between the beelines,it is a convenience method to choose perpendicularity or bigger angle as the adjustment parameter.

References

- Chen, Tianxiang. (2005).High Precision $\tan\delta$ Online Measure on Electricity Bridge's Balance Principle. *High Voltage Technique*.vol.31(1).pp.42—44
- Chen, Xin.(2004).The Improvement of AC Electricity Bridge Experiment.*College Physics Experiment*. vol.17(4).pp.9—11.
- Li, Yao.(2002).The balance of Adjustment AC Electricity Bridge Quickly. *College Physics Experiment*. vol.15(3).pp.38—39
- Liang, Bo. (2006).The Neglect Question In the Schering Electricity Bridge's Testing.*The Chinese Testing technique*.vol.3 (22).pp.90—92
- Lin, Lijuan.(2006).Making Use of Ray Separate Magnifying signal To Design the AC Electricity Bridge. *College Physics*.vol.25 (2).pp.43—45
- Liu, Yun.(2003).The Analysis and Application In the Electricity Bridge Sensitivity and Bridge Circuitry. *Journal of Shan Xi Science College*.vol.21(5).pp.56—58
- Ou, Xinda.(2004).The relation of Schering Electricity Bridge's Testing Range and Location Selection. *Northwest Electric Power Technique*.vol.3.pp.95—96
- Qin,Zhenhuang. (2003).*Electrotechnician*,Beijing: China Higher Education Press.
- Yang,Shu-wu. (2000).*Common Physics Experiment*,Beijing: China Higher Education Press.
- Zhang, Gongming.(2008).The discussion of Electricity Bridge Characteristic and Definition.*Chinese Measurement*.vol. 2.pp.69—71
- Zhang, Jing.(2005).The parameter measure and Electricity Bridge meter on L-C-R. *Electron Quality. Testing Technique* .vol.7.pp.15—16
- Zheng, Jiaxiang &Lu, Yuxin. (1982).*Electron Measure Principle*.Beijing: National Defence Industry Press.

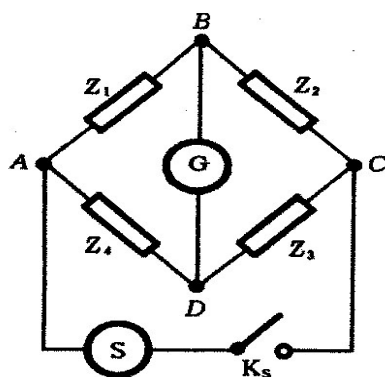


Figure 1. Electricit Bridge Circuitry

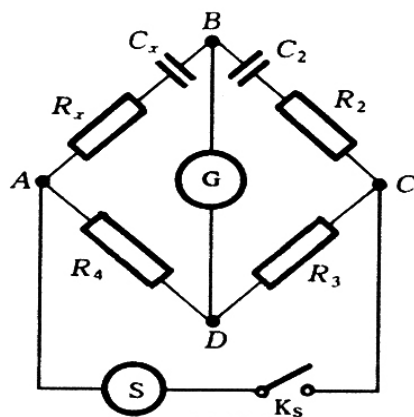


Figure 2. Capacitance electricity bridge

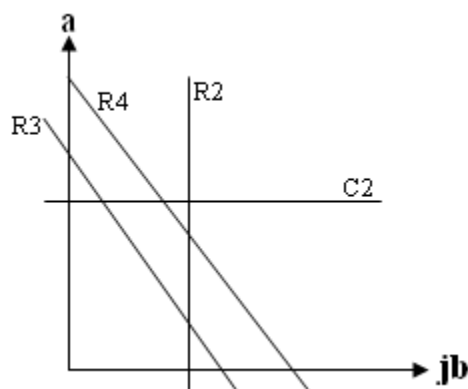


Figure 3. The beeline chart of Capacitance electricity bridge parameter

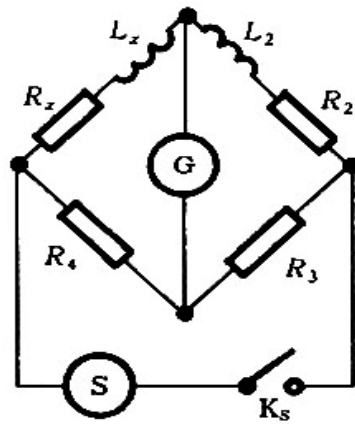


Figure 4. Inductance Compare Electricity Bridge

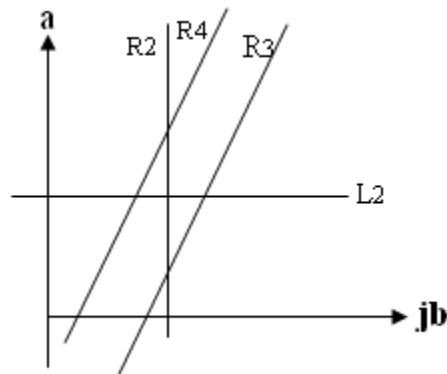


Figure 5. The beeline chart of Inductance Compare bridge parameter

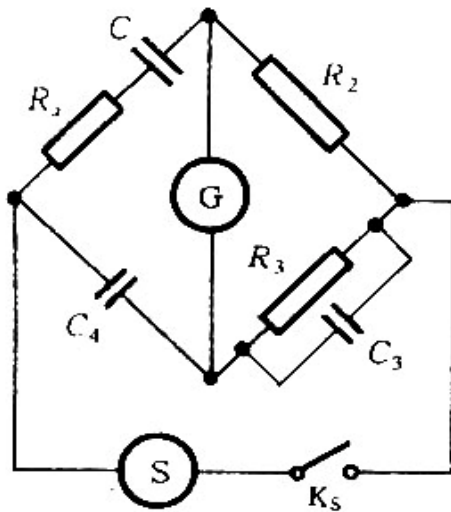


Figure 6. Schering Electricity Bridge

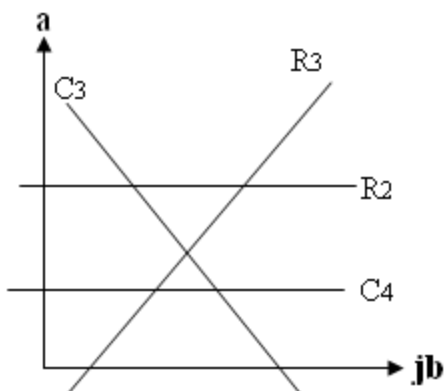


Figure 7. The beeline chart of Schering Electricity Bridge Parameter

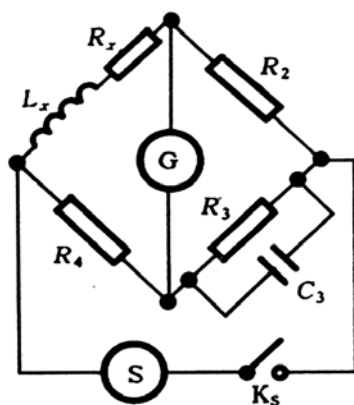


Figure 8. Maxwell Electricity Bridge

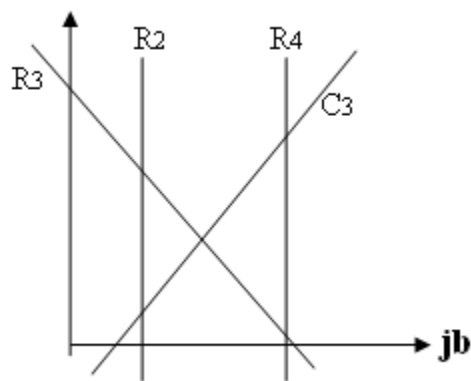


Figure 9. The beeline chart of Maxwell Electricity Bridge Parameter



Artificial Neural Network Based Rotor Position Estimation for Switched Reluctance Motor

L.Jessi Sahaya Shanthi(Corresponding Author)

Department of Electrical and Electronics Engineering
Thiagarajar College of Engineering, Madurai-625 015, India
E-mail: ljsee@tce.edu

R.Arumugam

Department of Electrical and Electronics Engineering
SSN College of Engineering, Chennai, India

Y.K.Taly

Head,Control Instrumentation Division of Bhabha Atomic Research Centre (BARC),Mumbai, India

S.B.Nandha Kumar

Department of Electrical and Electronics Engineering
Thiagarajar College of Engineering, Madurai-625 015, India

Abstract

Switched Reluctance Motor (SRM) is becoming popular as a variable speed industrial drive. But the requirement of position sensor to synchronize the rotor position with phase currents makes the SRM drive circuit complex and unreliable. With the advent of high speed digital signal processors, it is possible to implement algorithms to estimate the rotor position based on the electrical signals in motor windings. In addition to this, the latest graphical user interface software aids to reduce the time for the development of control algorithms. This paper presents the simulation study of an artificial neural network(ANN) based algorithm for rotor position estimation from phase voltage and current of a four phase SRM using VISSIM version 6.0B software. Based on the simulation results, a particular artificial neural network (ANN) is selected and checked for real time implementation.

Keywords: Switched reluctance motor, Rotor position estimation, Artificial neural network, VISSIM version 6.0B

1. Introduction

The Switched Reluctance Motor (SRM) drives have been receiving attention as variable speed industrial drives due to its simple construction, low manufacturing cost, fault tolerance, absence of magnets, rotor conductors and brushes, reduced maintenance requirements, rugged behavior, and large torque output over very wide speed range. The SRM drives can also deliver servo-drive performance equivalent to dc brushed motors. During the twenty years, the study of Switched Reluctance Motor (SRM) has made rapid progress. It has many fine features, such as simple and robust structure with no windings on the rotor, maximum operating speed and the ability of operating at high rotor temperatures. The simple power electronic converter requirement, the fault tolerant capability and the high torque per inertia ratio are the very specific advantages of SRM drives. The primary disadvantages of SRM drives are the rotor position sensing requirements and the higher torque ripple compared to other machines [1]-[10].

In aerospace applications, the design engineers of motor drive system for the fuel delivery system are concentrating on SRM drives because of the basic need of designing a compact and minimum weight system [9]. However, rotor position sensing plays a vital role in SRM drives, as commutation signals for the converter are derived from the position sensor signals. The position sensor unit adds to the system cost and dimensions and impair the drive reliability. To design a reliable and compact controller for SRM drives, the position sensor unit should be eliminated. Implementing the sensorless scheme using the fast acting digital signal processors makes the overall system reliable, compact and accurate [10].

2. Rotor Position Estimation Methods

Several sensorless rotor position estimation methods have been patented and published for sensorless control of SRM drives. All of these methods use the instantaneous phase inductance variation information in some way to detect the rotor position indirectly. As the flux linkage - rotor position - current characteristics vary significantly between the aligned and unaligned positions of the doubly salient stator and rotor poles, it is possible to estimate the rotor position indirectly in SRM drives [5] - [8]. The methods can be broadly classified into two categories: (i) Non-intrusive methods, where position information is obtained from terminal measurements of voltages and currents and associated computations, and (ii) Intrusive (Active probing) methods, where low level high-frequency signals are injected into an idle phase to determine the position dependent, unsaturated phase inductance characteristics.

The Non-intrusive methods rely on the machine characteristics for estimating the rotor position. The following are the various Non-intrusive methods: (i) The model based estimator technique (ii) The flux linkage/current method and (iii) The mutual voltage method [7]. For these methods the terminal measurements of phase voltage or mutual voltage and current are used as inputs for an estimator to obtain the rotor position. In model based estimator technique, the feedback gains of the observer are dependent on the input variables, i.e. phase current and voltage measurements. The rotor position is obtained as an estimated state variable from the observer [6]. In the flux linkage -current method, the terminal measurements are applied in the following equation to obtain the phase flux linkage,

$$\psi = \int (v - R * i) \cdot dt \tag{1}$$

Where Ψ is phase winding flux linkage, v is voltage across the phase winding, R is phase winding resistance and i is phase current. The various sensorless rotor position estimation methods suggested in the literature have their own merits and demerits depending on their principle of operation. Ideally, it is desirable to have a sensorless scheme, which uses only terminal measurements and does not require additional hardware [7].

Recently a number of papers have been published in the area of artificial neural network for motion control. Application of artificial neural network for position estimation in SRM drives is also studied by many researchers. In an earlier ANN based non intrusive rotor position estimation work, the estimation error is usually bounded on $[- 5^\circ, + 5^\circ]$ [1]. And the method deserves consideration as a candidate for integration in to practical SRM drive systems. Based on the works in [1] and [2] the simulation study of an artificial neural network(ANN) based algorithm for rotor position estimation from phase voltage and current of a four phase SRM using VISSIM version 6.0B software is done and the results are shown. In this paper, the nonlinear characteristics of SRM are discussed. Different architectures of artificial neural network are tuned for phase flux linkage and phase current waveforms as input and rotor position as output. The different ANN structures are trained for the same data. The trained ANN structure with minimum error is verified experimentally.

3. The Nonlinearised dynamic model of SRM

The switched reluctance machine is a doubly salient machine with unequal number of rotor and stator poles. Windings of diametrically opposite stator poles are connected in series to form one phase of the machine. As the switched reluctance machine is a doubly salient machine, its electromagnetism characteristic has high saturation effect [2]. This makes the model highly nonlinear and the simulation work includes more nonlinear functions.

The SRM's voltage balance equation is,

$$V_k = R_k * i_k + \frac{d\psi_k(i_k, \theta)}{dt} \tag{2}$$

Where V_k is the applied voltage to the k^{th} phase, R_k is the phase resistance, i_k is the stator current passing through the k^{th} phase and $\psi_k(i_k, \theta)$ is the flux linkage at the k^{th} phase.

The SRM's mechanical equation is

$$T_c = J \frac{d^2\theta}{dt^2} + D \frac{d\theta}{dt} + T_L \tag{3}$$

Where T_c is the total electro mechanical torque produced, J is the moment of inertia of the drive, D is the viscous friction coefficient and T_L is the load torque. Then,

$$\psi_k = \psi_k(i_k, \theta) \tag{4}$$

$$v_k = R_k i_k + \frac{\partial \psi_k}{\partial i_k} \cdot \frac{di_k}{dt} + \frac{\partial \psi_k}{\partial \theta} \cdot \frac{d\theta}{dt} \tag{5}$$

$$\begin{aligned}
 &= R_k i_k + \left(L_k + i_k \frac{\partial L_k}{\partial i_k} \right) \frac{di_k}{dt} + i_k \frac{\partial L_k}{\partial \theta} \frac{d\theta}{dt} \\
 &= R_k i_k + \left(L_k + i_k \frac{\partial L_k}{\partial i_k} \right) \frac{di_k}{dt} + i_k \frac{\partial L_k}{\partial \theta} \cdot \omega
 \end{aligned} \tag{6}$$

From equation no.(6), i_k can be expressed

$$i_k = \int \frac{di_k}{dt} \cdot dt = \int \frac{V_k - R_k i_k - i_k \omega \cdot \frac{\partial L_k}{\partial \theta}}{\left[L_k + i_k \cdot \frac{\partial L_k}{\partial i_k} \right]} dt \tag{7}$$

In the above equations (6) and (7) inductance related terms are substituted in terms of

$$L_k = L_0 + P(\theta) \cdot Q(i_k) \tag{8}$$

Where

$$P(\theta) = a_0 + \sum_{r=1}^n a_r \sin(b_r \theta - \Phi_r), \tag{9}$$

$$Q(i) = [(1 - c_1 i_k) / c_2] \sin(i_k - c_3) \tag{10}$$

The wave shaping constants a_r , b_r and Φ_r are chosen according to the inductance profile of an 8/6 motor with respect to rotor position at constant current. The constants c_1 , c_2 and c_3 are chosen according to the nonlinear relation of phase inductance with current. And L_0 is the minimum unaligned inductance which is dependent on rotor pole height.

Torque can be expressed as,

$$T_{ek} = \frac{\partial w_k}{\partial \theta} \quad / \quad i_k = \text{Constant}$$

Where w_k is the magnetic co-energy of winding.

$$\begin{aligned}
 &= \frac{\partial \int_0^{i_k} \psi_k(\theta, i_k) di_k}{\partial \theta} \\
 T_{ek} &= \frac{\partial \int_0^{i_k} L_k(\theta, i_k) i_k di_k}{\partial \theta} \tag{11}
 \end{aligned}$$

$$T_e = \sum_{k=1}^4 T_{ek}$$

Hence torque output can also be got in terms of inductance as in equation (11).

Figure.1 VISSIM based model of SRM and flux estimator

The four phase, 8/6 pole SRM is modeled based on the equations (1) – (11). The VISSIM based SRM model and its output waveforms are shown in Fig.1. The individual phase models are grouped to get the over all model. The flux linkage estimation algorithm is simulated for the four phases. The simulation study enhances the analysis of flux linkage estimation for different excitation patterns. The results shown are for turn on degree of 7.5 degree mechanical with respect to unaligned position of phase A and turn off degree of 22.5 degree mechanical.

4. Simulation model of ANN based rotor position estimator

The Vissim block diagram for ANN based rotor position estimation is shown in Fig.2. The flux linkage and current values for four phases are collected in the flux-current.dat file for one electrical cycle. It is equivalent to 60 degree mechanical. The flux linkage- current - rotor position for the four phases are the ANN training data. The various ANN structures are trained for the same data. By trial and error method, it is found that the ANN with one hidden layer and twenty neurons per layer provided minimum error. The neural network setup in VISSIM is shown in Fig.3 and Fig.4. The learning method used is back propagation with momentum. The learn rate selected is 0.8 and momentum selected is 0.8. The various ANN structures are run in parallel and errors are compared.

Figure.2 ANN based rotor position estimation using VISSIM

5. Simulation Results

The different ANN structures are trained for the same set of flux linkage-current-rotor position data. The different structures are the following,

Case 1: Number of hidden layers=2, Number of neurons per layer = 10, Method=Back Propagation, Learn rate=0.5 and weight=0.5.

Case 2: Number of hidden layers=1, Number of neurons per layer = 30, Method=Back Propagation, Learn rate=0.5 and weight=0.5.

Case 3: Number of hidden layers=1, Number of neurons per layer = 20, Method=Back Propagation with momentum, Momentum=0.7, Learn rate=0.7 and weight=0.5.

Case 4: Number of hidden layers=1, Number of neurons per layer = 20, Method=Back Propagation with momentum, Momentum=0.5, Learn rate=0.5 and weight=0.8.

Case 5: Number of hidden layers=1, Number of neurons per layer = 20, Method=Back Propagation with momentum, Momentum=0.8, Learn rate=0.8 and weight=0.8.

Figure.3 Neural net setup information for Case 4

Figure.4 Neural net setup information for case 5

From the simulation results, ANN structure with case 5 is the best for training the flux linkage-current-rotor position data. The position estimation error using this ANN structure is bounded on $[-2.4^\circ, +1.2^\circ]$ mechanical.

In Fig.5 the rotor position estimation results for two different ANNs (case 4 and case 5) are shown. In Fig.6 the rotor position estimation error results for two different ANNs (case 4 and case 5) are shown for comparison. From the SRM model designed, the flux linkage and current of four phases are studied and verified for different commutation angles. The results shown are for turn on degree of 7.5 degree mechanical with respect to unaligned position of phase A and turn off degree of 22.5 degree mechanical. The model has simulation step time limitation. The maximum value of simulation step time is 0.001seconds.

Figure.5 Rotor Position vs Time for two different ANNs (case 4 and case 5)

Figure.6 Error vs Time for two different ANNs (case 4 and case 5)

6. Experimental Setup and results

The following Fig.7 shows the experimental setup of power circuits to drive the 8/6 SRM and Fig.8 shows the reflective type position sensor setup used to produce the commutation signals for the control of SRM with position sensor. The online information of flux linkage-current-position is collected through Vissim-GUI working environment with position sensor setup. The Texas Instruments Digital Signal Processor TMS320F2812 is used with Vissim-GUI working environment.

The hall effect voltage and current sensors are used with signal conditioner circuits to feed the phase voltage-current information to ADC of DSP. Based on the values of phase voltage-current data, the phase flux linkages are calculated based on equation (1). The flux linkage-current-position data is collected in .dat files. The different neural networks can be trained with the collected data through .dat files. The errors can be compared. In this paper, comparison between only two ANNs are produced. The network with minimum error can be selected for real time application. The ANN with minimum error is checked for real time application. It is working for only low speeds.

Fig.7 Experimental setup of 8/6 SRM Converter circuits(left) and voltage-current sensors setup(right)

Fig.8 Reflective type sensors used to produce commutation signals

7. Conclusion

The results obtained from the VISSIM based ANN rotor position estimator are compared with the actual rotor position. The minimum estimation error is bounded on $[-2.4^\circ, +1.2^\circ]$ for the ANN structure with case 5. The simulation work is very much useful in the analysis of flux linkage – current for different turn on, turn off angles and to select the structure of ANN. Using the ramp generator block in VISSIM the different commutation signals can be generated. The reset integrator block is used to evaluate flux linkage from phase voltage and phase currents. The flux linkage - current - rotor position data is tuned in the neural network. This paper provides enough research material for analyzing the nonlinearised model and to estimate rotor position with various ANN structures using VISSIM. The structure with minimum error can be selected for real time application. The results obtained are experimentally checked only for low speed position sensorless control of SRM.

Acknowledgement

With out the blessings of Almighty, the support of management and staff members of Thiagarajar College of

Engineering this research work is not possible. The research work is supported by Bhabha Atomic Research Centre, Mumbai, India. The motor used in this research is from Bhabha Atomic Research Centre, Mumbai, India. The encouragement from Board of Research in Nuclear Sciences (BRNS), Department of Atomic Energy, India is gratefully acknowledged.

References

- Arthur V.Radun, "High Power Density Switched Reluctance Motor Drive for Aerospace Applications", IEEE trans. Ind. Applicat., vol.28,No.1,January/February 1992.
- Erkan Mese and David A.Torrey, "An Approach for Sensorless Position Estimation for Switched Reluctance Motors Using Artificial Neural Networks", IEEE Transactions on Power Electronics, vol.17, no.1, January 2002.
- Fabio Filicori, Corrado Guarino LoBianco, Alberto Tonielli, "Modeling and Control strategies for a Variable Reluctance Direct-Drive Motor", IEEE Transactions on Industrial Electronics, Vol. 40, No.1, February 1993.
- G.Suresh, B.Fahimi, K.M.Rahman, M.Ehsani "Analysis of Amplitude Modulation Methods for Sensorless SRM Drives", IEEE PESC Conference Records,1998.
- G.Suresh, B.Fahimi, K.M.Rahman, M.Ehsani "Inductance Based Position Encoding for sensorless SRM drives" IEEE Proc. Pp.832-837Apr 1999.
- Khwaja M.Rahman, Steven E.Schulz, "High Performance Fully Digital Switched Reluctance Motor Controller for Vehicle Propulsion", IEEE Trans. Ind. Applicat., vol.38, No.4, July/August 2002.
- MStiebler andke Liu, "An Analytical Model of Switched Reluctance Machines" IEEE Transactions on Energy Conversion, Vol.14, December 1999.
- Tom Perl, Iqbal Husain, Malik Elbuluk, "Design Trends and Trade offs for Sensorless Operation of Switched Reluctance Motor Drives", IEEE Conference Records, 1995.
- Wenzhe Lu, AliKeyhani, "Sensorless Control of Switched ReluctanceMotors Using Sliding Mode Observers", IEEE Proc.pp.69- 72 2001.
- YulongCui, XiangWang, Chaoying Liu, Jiaomin Liu, "The Simulation Study Of Switched Reluctance Motor's Non Linearized Model", Proc. of Second International Conference On Machine Learning And Cybernetics Page No 2720-2725, November 2003.

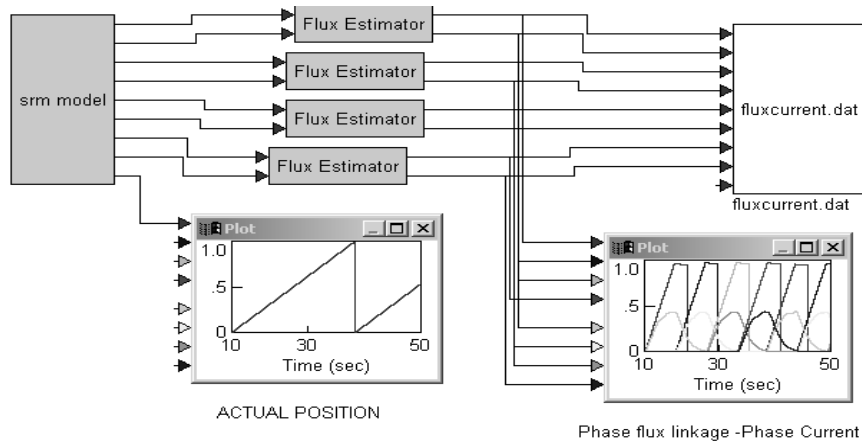


Figure 1. VISSIM based model of SRM and flux estimator

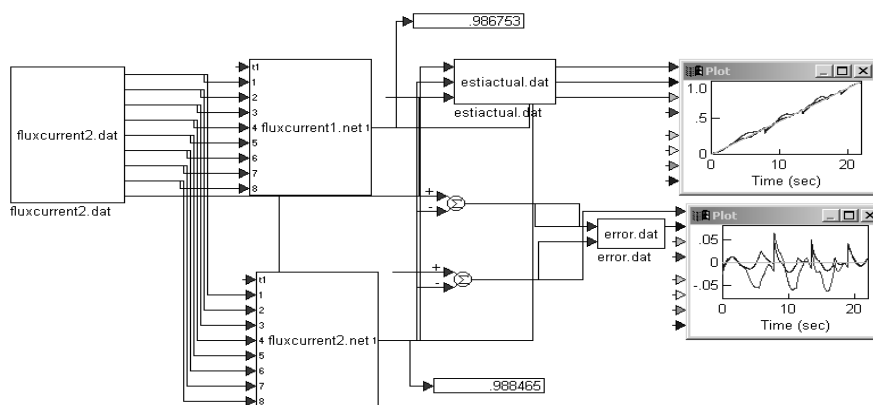


Figure 2. ANN based rotor position estimation using VISSIM

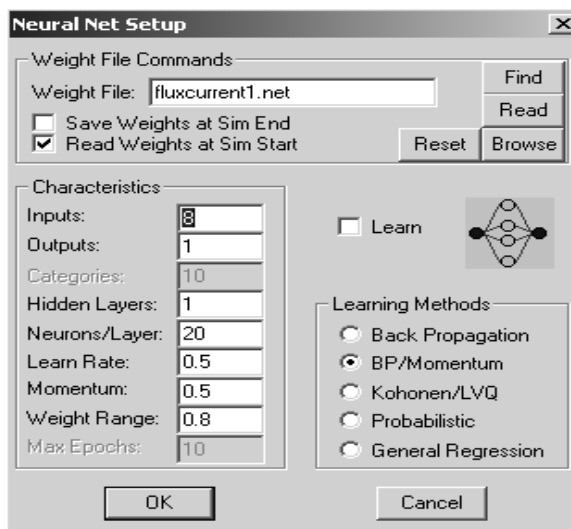


Figure 3. Neural net setup information for Case 4

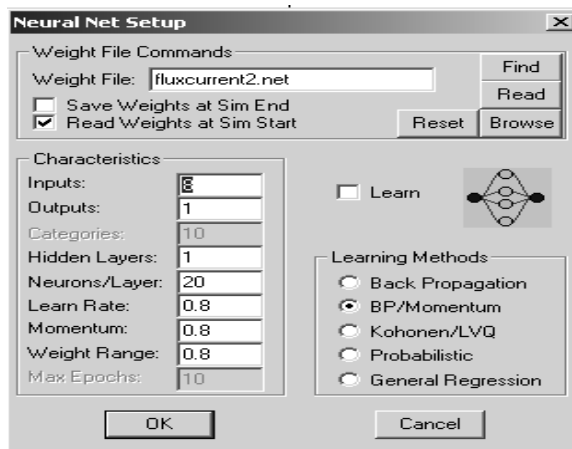


Figure 4. Neural net setup information for case 5

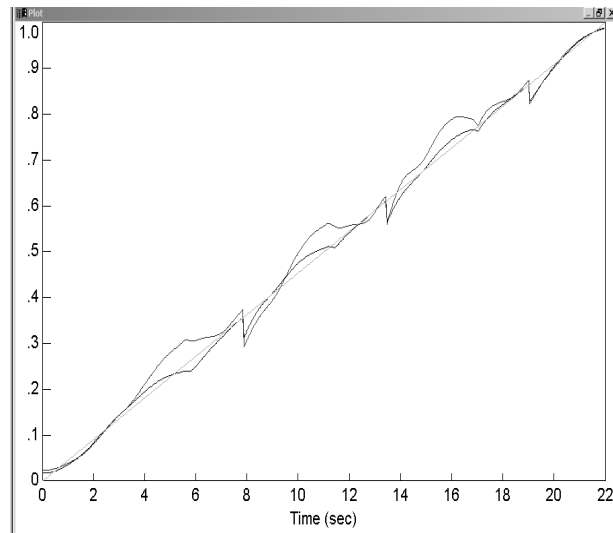


Figure 5. Rotor Position vs Time for two different ANNs (case 4 and case 5)

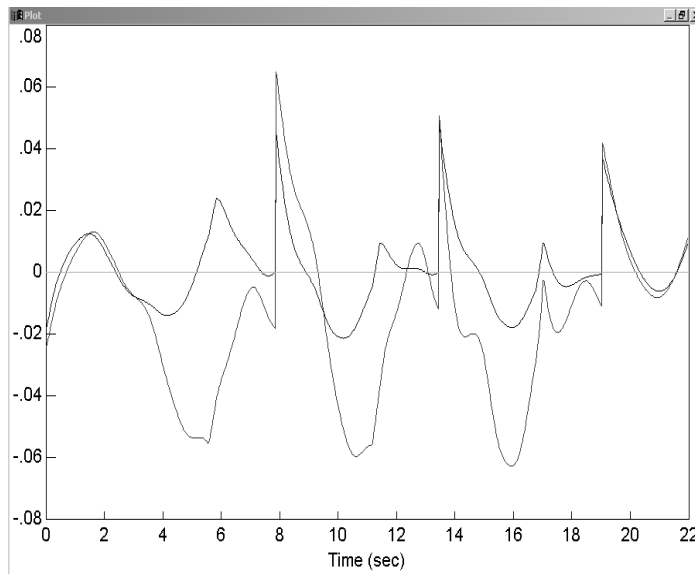


Figure 6. Error vs Time for two different ANNs (case 4 and case 5)

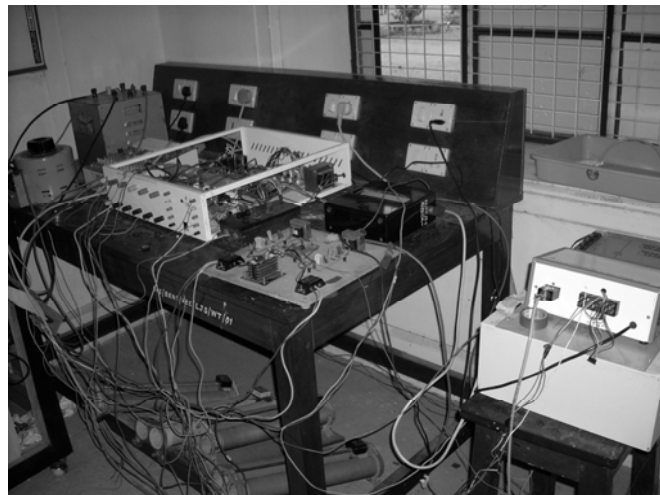


Figure 7. Experimental setup of 8/6 SRM Converter circuits(left) and voltage-current sensors setup(right)

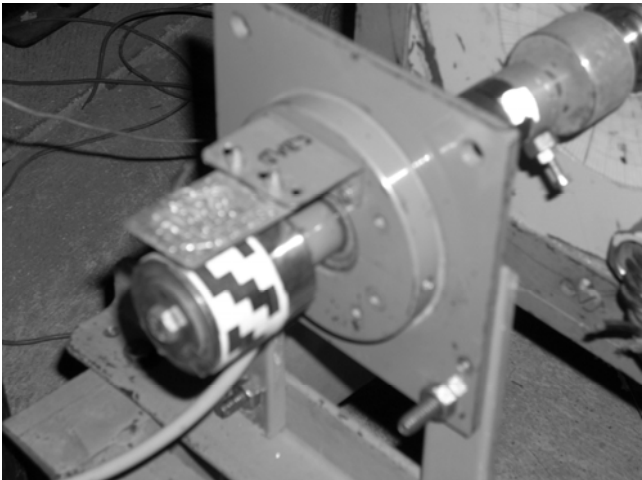


Figure 8. Reflective type sensors used to produce commutation signals



Synthesis Study of Nucleus-cell Style High-property

Water-absorbent Polymer

Cuirong Zhang, Shucui Mao & Zhenyu Jia

Institute of Green Chemical Engineering

Zhongkai Agriculture Engineering College

Guangzhou 510230, China

Abstract

In this paper, MBA was used as crosslinker, SiO₂ and carboxymethyl cellulose as the nucleus-maker, nucleus-cell style SAP was synthesized by AA-AM-AMPS three-member copolymerization. The multiple of water-absorbent by SAP could reach 1150 times by the optimization of the technological conditions. Nucleus-cell style SAP has a good command of fluidity and wet-resistance, it can keep its fluidity 15 hrs after exposure under the air with the humidity of 84%. The best proportion of AA, AM, AMPS is 13:3:4, and the best content of SiO₂ is 0.8%.

Keywords: Water-absorbent polymer, Nucleus-cell style, Step-crosslinking

Water-absorbent polymer, a kind of function material, can absorb water weigh as hundreds times even thousands times as themself. SAP has been applied in industry, agriculture, medical and treatment, gardening, etc. SAP developed very fast in nearly years. Different kinds of SAP have been prepared, such as synthesized polymers, amyllum species, cellulose species, etc. SAPs from modified amyllum or cellulose can be biodegraded but are easy to corrupt and conglomerate. Their heat resistance, water-keeping performance and gel intensity are poor. Also preparation process is complicated. Two kinds of technology were used to make SAP by acryl acid. One was solution polymerization (disc polymerization) process; the other was reversal-phase suspension polymerization process. At present, SAP made by solution polymerization was of poor moisture proof and was prone to absorb moisture at ambient temperature and at usual relative humidity in practically application. This make it inconvenient to apply, store, transport, packing, produce and machining. Even make it incapable to use. A kind of core-shell high-quality SAP had been synthesized by reverse-phase suspending polymerization in this work. Monomers ratio and other process conditions were studied. FTIR and High power microscope were used to observe core-shell forming and association.

1. Experimental

1.1 Materials

Acryl acid(AA), Acrylamide(AM), 2-acrylamide-2-methyl-propane sulfoacid sodium (AMPS), N,N-methylene-bis-acrylamide(MBA), ammonium persulfate(APS), hydrosulfite of sodium, sodium hydroxide, cyclohexane, surfactant(SP-85, OP-7), carboxymethyl cellulose. All were chemically pure. Silicon dioxide(superfine powder-700 mesh size) was supplied by Chengdu chemical plant.

1.2 Procedure

First, AA was neutralized by NaOH solution and neutralization degree reached 80-85%; second, some AM, AMPS, cross-linker MBA as well as initiator solution were added in and were stirred to get A solution(water phase). Composite surfactant (SP-85:OP-7=1:1) were added in cyclohexane phase and were stirred to disperse enough, so B solution was gotten. B solution was placed into a four-neck flask and was stirred, and then 95% A was added in slowly. They reacted one hour at certain temperature. Then residual A solution as well as cross-linker, cellulose, SiO₂ was added in the flask too. The reaction went on for another three hours. After filtration and separation quickly, product was washed by methanol and was dried to get granular polymer.

1.3 structure and properties test

(1) Test of water- absorbent speed (whirlpool method): pour water in beakers; put beakers on magnetic stirring apparatus; turn on it and muddler make water whirlpool. Pour 0.5g SAP into water and record time by stopwatch until whirlpool disappears. Find out the relationship between water-absorbent and the time.

(2)multiple test of absorbing and solution (net method): put 1g SAP in beakers. Put 0.9% NaCl solution, 0.9% CaCl₂

solution, distilled water, tap water, and soil lixivium etc into beaker respectively. When SAP absorbs liquid balance, excrement liquid is filtered by 100-mesh net. Weight and work out the absorbing & solution multiple.

$$Q=(W1-W2)/M \quad (1)$$

In formula: Q- absorbing & solution multiple; W1-SAP weigh after absorbing(g); W2- net weigh(g); M-SAP weigh(g).

(3) fluidity test(angle of repose): samples in filler flow to horizontal desktop spontaneously. Test samples' angle of repose. Fluidity is poor if the angle is greater than 45° , and fluidity is good if it is smaller than 45° .

(4) test of humidity resistance: judge samples' humidity resistance by test their hygroscopic capacity at different time and moisture condition.

(5) observe samples' morphologies by high-quality microscope.

(6) FTIR : FTIR was got by NiColet-170SX instrument after samples were dealt with KBr by pressed disc method.

2. results and discussion

2.1 monomers affection on SAP'S properties

Figure 1 presented that water-absorbent multiple decreased and salt water-absorbent multiple increased, while degree of cross linking, degree of neutralization and reaction temperature kept invariable with AM monomer's increasing. AM contained amido which belonged to non-ion hydrophilic group and was of strong property of salt-resistance. With amido increasing, -N-H-O-hydrogen bonds tended to form between polymer chains within network structure. Cohesive energy increased. Intensity increases and water-absorbent multiple decreased. With AMPS monomer's ratio increasing, salt-absorbent ratio and water-absorbent ratio increased accordingly. -SO₃H was strong hydrophilic ionic group. With its ratio increasing, ionicity of SAP network increased too. The osmotic pressures both in network and out network increased, and then water-absorbent increased accordingly. Ion in solvent had important influence on water-absorbent performance of SAP. The influence of Ca²⁺ was stronger than Na⁺ at the same concentration. Ca²⁺ entered into SAP net and was easy to form complex compound with carboxylic radical, which reduced repulsion between anions, so increased elastic behaviour of gelatum made water-absorbent multiple of SAP decrease. In thermodynamics opinion, Flory quantitatively stated how water-absorbent performance of SAP related to ion concentration in solvent, charge density of polymer, degree of cross linking and the appetency of groups in net to water. With degree of cross linking increasing, water-absorbent multiple decreased; with ion concentration in solvent increasing, water-absorbent multiple decreased too. In order to improve water-absorbent multiple and water-absorbent speed, strong hydrophilic groups including hydrophilic non-ionic groups could be introduced in polymer. Experimental results accorded with that theory basically. Of its performances, water-absorbing multiple, water-absorbing speed, gel intensity and salt resistance were mostly pursued by people and also were considered in actual application. According to molecule designing opinion, copolymerization of two members or three members even several members was valid way to improve SAP performances. When any two components of AA, AM and AMPS copolymerized, the most water-absorbing multiple was 916 times. While three components copolymerized, it increased to 1150 times.

Figure1 showed that water-absorbing speed rate curve of core-shell SAP was "S" shape. Shell made speed rate slower at the beginning. When shell split, water entered in quickly. Proper thickness of shell didn't influence water-absorbing multiple and speed rate. The shell could protect SAP against moisture. During the process of water-absorbing, SAP surface carried through hydration ionization firstly. More was hydration ionization degree, more would water-solubility increase. sol came into being and ion film did simultaneously, which held back water's penetration and influenced water-absorbing speed rate, so ionic group content couldn't be more, otherwise water-absorbing multiple would decrease. Amido was of stronger hydrophilicity and formed hydrogen bond with water molecule, which increased the hydrophilicity and improved water-absorbing speed rate greatly. Core-shell SAP could achieve water-absorbing saturation in 10 minutes.

Figure 2 showed that moisture absorption speed of core-shell SAP was slower at the incipient stage in humidity atmosphere, which was mostly due to consumed time for polymer hydration and molecule chain stretching. As long as polymer chains stretched out, water-absorbing speed would accelerate. In the case of the protection of shell, water-absorbing speed stayed slow because of poor affinity between water molecules and SAP. That was why core-shell resin owned better humidity resistance than general polymer. At 84% relative humidity, core-shell SAP could keep better fluidity after 15 hours at ambient temperature. Angles of repose were test to compare fluidity. That of Core-shell SAP was 36° and that of non-core-shell production was 44° .

2.2 temperature's influence on synthesis

It could be seen form figure 3 that polymerization reaction kept stable and water-absorbing multiple was small at low temperature. When temperature rose to 70°C , water-absorbing multiple of SAP achieved the highest peak. After that, water-absorbing multiple went down with temperature's continuous rising. Synthesising SAP belonged to free radical polymerization and exothermic reaction, while initiator's decomposing belonged to endothermic reaction. At low

temperature initiator decomposed slowly. Their concentration and initiating efficiency were low, too. Cessation reaction and growth reaction was a pair of competitive reaction. The former activation energy (about 8.5-17kg/mol) was lower than the latter's (about 17-34 kg/mol). Low temperature would make monomers' residual large and polymer molecular weigh small, which would have influence on water-absorbing multiple of SAP. Although suspending liquid could eliminate heat, AA polymerization was exothermic reaction, when temperature rose, initiator composed fast and initiating efficiency improved to make core temperature high. This made AA self-polymerize and cross-link, so that polymer clew couldn't stretch and water-absorbing multiple decreased. Figure 2 displayed that monomers' residual decreased with temperature rising at various temperature, which accorded with the above conclusion.

2.3 degree of neutralization's influence

Figure 4 indicated that water-absorbing multiple of SAP became larger with degree of neutralization increasing when other condition stayed unchanged. When degree of neutralization achieved 85% liquid-absorbing multiple reached the peak. Since the acidity of -SO₃H group was stronger than that of -COOH, when AMPS was added in the neutralized AA solution, AMPS would react with sodium acrylate and -COOH would be released, so in fact neutralization in general polymer was smaller than the data calculated on AA, which could be seemed as the concentration of AA increased. Reaction activity of AA was stronger than that of acrylate, AM and AMPS, so AA likely self-cross link, which made swelling capacity of polymer net decrease and water-absorbing multiple as well as water-solubility become small. When neutralization exceeded 85%, would -COONa group increase. This reduced self-cross linking, but water-solubility increased, so water-absorbing multiple and speed would reduce too.

2.4 Influence of addition of SiO₂ on the effect on SAP core-forming

Table 3 presented that humidity-resistance time of SAP increased with addition of SiO₂ but the correlation was not direct proportion. When SiO₂ quantity was little, particle surface of SAP couldn't be covered fully. When SiO₂ quantity reached 0.8%, the complete film formed and humidity-resistance performance was promoted greatly. The addition quantity of SiO₂ was not very large, so its influence on water-absorbing multiple and speed rate was little.

2.5 FTIR analyses

Figure 5 showed that Si-O stretching vibration was at 1108 cm⁻¹ and flexural vibration was at 474cm⁻¹. Vibration peaks of -OH and Al-O occurred at 3412cm⁻¹ and 619cm⁻¹ respectively since the purity of SiO₂.

Figure 6 showed that 1570cm⁻¹ peak came from C=O stretching vibration of amide group and carboxyl. Dissymmetric stretching vibration of S=O occurred at 1330cm⁻¹ and its stretching vibration was at 1058cm⁻¹. 3412cm⁻¹ peak of -OH mean that -SO₃H existed. 1174cm⁻¹ and 513cm⁻¹ peaks represented stretching vibration and flexural vibration of Si-O respectively, which indicated that SiO₂ was grafted at SAP surface and formed shell.

2.6 SAP morphology observation by microscope

Figure 7 showed that SAP made from reversal-phase suspending process were uniform spheres. Figure 8 presented the morphology after water-absorbing. Shell was obvious and it broke up after water-absorbing. Figure 9 showed the SAP morphology from solution polymerization processing. The powder products derived from massive products when they were cracked. Most particles were irregular.

Conclusion

- When MBA was used as cross-linker and SiO₂ was used as the nucleus-maker, SAP was synthesized by AA-AM-AMPS three-member copolymerization in reversal-phase suspending processing. The SAP possessed better water-absorbing capability. The water-absorbing multiple of SAP under the processing of optimizing the technological conditions could reach 1150 times. SAP possessed good fluidity and humidity-resistance. It could keep some fluidity after exposure to the air with 84% humidity for 15 hours.
- No agglomeration and no adhesion occurred in the preparation processing. Hard operating process was overcome. The particles of SAP were uniform.
- Under the preparation processing, temperature should be controlled from low to high. This could control the polymerization reaction effectively.

References

- Cuiyingde,Guojianwei,Liaoliewen. Journal of Chemical Industry[J], 2001,52(7):601~605
- Guojianwei, Cuiyingde,Kangzheng. Fine Chemicals[J], 2001, 6: 348~350
- Jacek K, Dutkiewicz. Journal of Biomedical Material[J],2002,63(3):373~381
- Longmingce,Wangpeng,Dengdong, Chemical communications[J], 2002, 10: 705~709
- Qiuhaixia,Yujiumu,Lintong. Chemical communications[J], 2003, 9: 598~605

Wangxiaodong, Wangyuan, Chemical engineer[J], 2001: 4:1~3

Zhouliming, Gaodechuan, Wangtiemin, Journal of Donghua University [J], 2001, 27(1): 10~12

Table 1. Influence of Monomer composition to absorbent resin (SAP) performance

Content of Monomer components W(AA+AM+AMPS)%	Distilled water absorption rate g/g	Salt water (0.9%) absorption rate g/g	CaCl ₂ (0.9%) absorption rate g/g	Tap water absorption rate g/g	Leaching of soil absorption rate g/g
100+0+0	683	58	42	487	284
90+3+5	846	103	57	531	323
85+6+10	917	112	66	663	416
80+10+10	913	136	83	727	518
75+10+15	1020	148	96	786	542
70+15+15	1080	156	102	834	584
65+15+20	1150	230	113	897	672
60+15+25	830	211	106	710	524
50+25+25	610	88	62	580	390
90+0+10	720	89	58	716	462
80+0+20	857	109	88	792	503
70+0+30	916	112	99	842	594
90+10+0	586	67	46	513	281
80+20+0	537	74	64	488	228
70+30+0	469	83	71	420	206

Table 2. Monomer AA remains measures in SAP at different temperatures

Temperature (°C)	40	50	60	70	80	85
Monomer Residual (ppm)	630	447	325	240	188	160

Table 3. Influence of SiO₂ joins quantity to SAP coring effect and performance

No	Amount of Joinning SiO ₂ (%)	Fangshi Continue time (h)	Absorbent water rate (g/g)	Absorbent Water speed (g/s)	note
1	0.2%	0.8	1143	6	
2	0.4%	3	1157	8.5	
3	0.6%	7	1146	9	
4	0.8%	20	1150	9	
5	1.0%	22	1138	10	

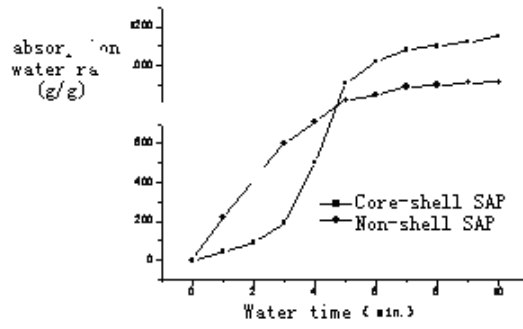
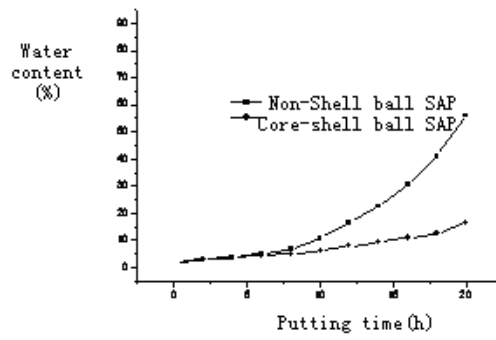


Fig1 Absorbing water speed of SAP



Note: The relative humidity of 84%
Fig2 Moisture absorption performance of SAP

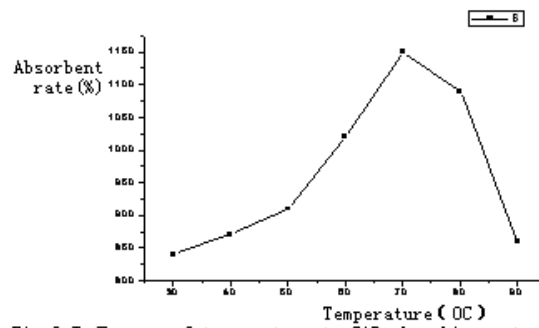


Fig 3 Influence of temperature to SAP absorbing water percentage

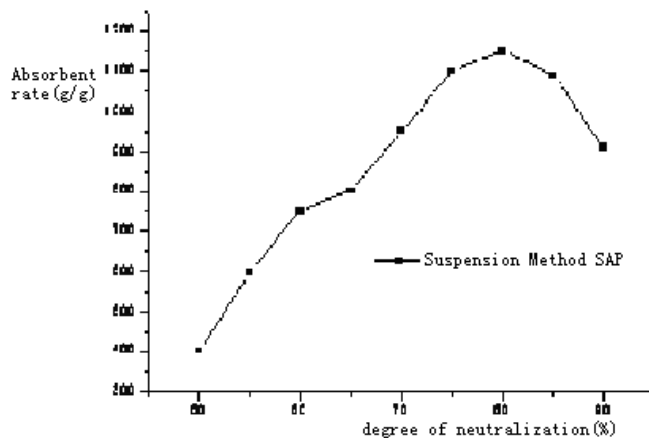


Fig 4 influence of neutral to SAP absorbing water percentage

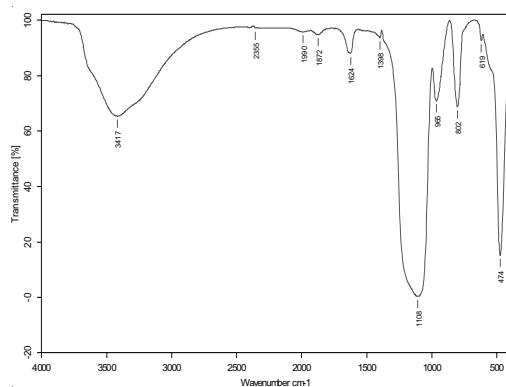


Figure 5. Infrared light spectrogram of SiO₂

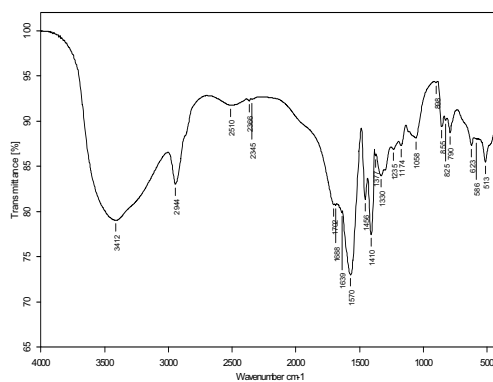


Figure 6. Infrared light spectrogram of SiO₂ superficial stem grafting SAP

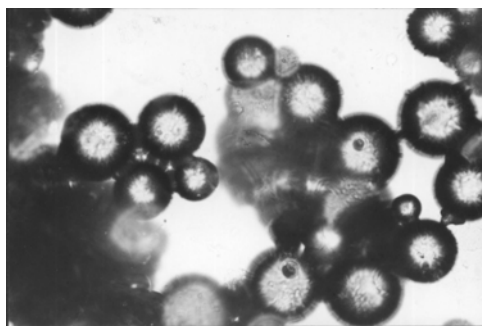


Figure 7. High power microscope chart of SAP by opposition suspension method preparation



Figure 8. Chart after nuclear shell SAP absorbing water



Figure 9. SAP microscope chart by solution polymerization preparation



An N-Component Series Repairable System with Repairman

Doing Other Work and Priority in Repair

Jiaying Yang

Department of Science, Yanshan University

Qinhuangdao 066004, China

E-mail: jiaaying_yang27@163.com

Xianyun Meng

Department of Science, Yanshan University

Qinhuangdao 066004, China

Weiyan Guo

Acheng collage, Harbin Normal University

Yanqin Guan

Department of Science, Yanshan University

Qinhuangdao 066004, China

Taotao Wang

Department of Science, Yanshan University

Qinhuangdao 066004, China

Supported by the Foundation for the natural science of Hebei province of China (A2005000301).

Supported by the Plan Projects of Hebei Education Office (No.2007323).

Abstract

In this paper, we discussed the reliability of an N-unit series repairable system with the repairman doing other work and priority in repair. In this system, it is assumed that the working time distributions of the n components and the arrival interval time distributions of the customers which are out of the system are both exponential and the components in system is given priority in repair. It is also assumed that the repair time distributions of the n components and the service time distributions of the customers are both general continuous distributions. After repair, components are "as good as new". Under these assumptions, using a supplementary variable technique and Laplace transform technique, some important reliability indices such as the system availability, the idle probability of the repairman and the rate of service for customers are derived. Our problem is to determine whether or not given the priority to components in repairing such that the benefit of the system is maximized.

Keywords: Reliability, Supplementary technique, Generalized Markov process

1. Introduction

In order to improve the interest of the system, the supervisor always arranges the repairman service for the customers out of system. Under this condition and assumptions that the working time distributions are exponential and the repair time distributions and the time distribution of the repairman doing other work are both general continuous distributions, by using supplementary technique and vector Markov process, the reliability indices have been obtained and the benefits of the model discussed (Su, B.H., 1994, pp.34-39). Later the number of the customers has been introduced. LIU R.B. and TANG Y.H. (2005, pp.493-496) assumed that the working time and the arrival interval time have exponential distribution while others to be general continuous distributions. By using the supplementary variable method, the vector Markov process and the tool of the Laplace transform, some reliability indexes of the system have been derived and the benefit of the system discussed. HU L.M., WU J.B. and TIAN R.L. (2007, pp.47-50) have been introduced the assumption that each unit had two types of failure. They have obtained the reliability indices of the system. Zhang Y.L. and Wang G. J.(2006,pp.278 - 295) introduced the priority in use in a deteriorating cold standby repairable system.

While it isn't always maximizing the interest of system that repairman is servicing for customers out of system, the repair work of the components maybe delayed for the repairman doing other work. The purpose of this paper is to apply the priority repair model to an n-component series repairable system with the repairman doing other work. Now we may assume that the units after repair is "as good as new" and the units have priority in repair. Furthermore, we assume that the working time of the components and the arrival interval time customers are both exponentially distributed and others generally distributed.

2. Model

We study an n-component series repairable system with repairman doing other work and priority in repair by making the following assumptions:

Assumption 1. Initially, the n components are all new and work in double harness while the repairman is idle.

Assumption 2. When one component is on repairing, the others will stop working and not go wrong. The system is failing now.

Assumption 3. If and only if when the n components are all working and the customer doesn't arrive, the repairman is idle. If and only if when the n components are all working, the customers will be likely to arrival. The customer won't arrive, when one component is repaired or the repairman is serving for one customer and another customer is waiting for service. When one customer is waiting for service and one component goes wrong, the customer will leave. And the component is repaired immediately, while the customer served will be waiting for service. The customer will be served after the repair over and the service before is valid.

Let X_i and Y_i be, respectively, the working time and the repair time of the component $i, i = 1, 2, \dots, n$. We assume that the distributions of X_i and $Y_i (i = 1, 2, \dots, n)$ are, respectively,

$$F_i(t) = 1 - \exp(-\lambda_i t),$$

$$G_i(t) = \int_0^t g_i(x) dx = 1 - \exp(-\int_0^t \mu_i(x) dx),$$

Where $t \geq 0, \lambda_i > 0, \mu_i > 0; i = 1, 2, \dots, n$.

Let H be the service time of the customer. We assume that the distribution of H is

$$H(t) = \int_0^t h(x) dx = 1 - \exp(-\int_0^t d(x) dx).$$

Let V be the time between repairman start idle and the arrival of the first customer and between the arrival of the first customer and the second one. We assume that the distribution of V is

$$V(x) = 1 - \exp(-cx).$$

Where $t \geq 0, c > 0$.

Assumption 4. Assume that $X_i, Y_i (i = 1, 2, \dots, n), H$ and V are independent.

3. The system analysis

Let $\{S(t), t \geq 0\}$ be a stochastic process characterized by the following mutually exclusive events:

$\{S(t) = 0\}$: n components are all working and the repairman is idle.

$\{S(t) = 1i\}$: The component i is repaired, $i = 1, 2, \dots, n$.

$\{S(t) = 2\}$: n components are all working, the repairman is serving for the customer.

$\{S(t) = 3\}$: n components are all working, the repairman is serving for one customer and the another waiting for service.

$\{S(t) = 4i\}$: the component i is repaired, the customer is waiting for service, $i = 1, 2, \dots, n$.

Then $\{S(t), t \geq 0\}$ is a stochastic process with state space $\Omega = \{0, 1i, 2, 3, 4i; i = 1, 2, \dots, n\}$. The set of working states is $W = \{0, 2, 3\}$ and the set of failure states is $F = \{1i, 4i; i = 1, 2, \dots, n\}$. According to the model assumptions, $\{S(t), t \geq 0\}$ is not a Markov process. However, it can be extended to a generalized Markov process by introducing a supplementary variable. Let $X_i(t)$ be the repair time of the component i used at time $t, i = 1, 2, \dots, n$. Let $Y(t)$ be the service time of the customer used. Then $\{S(t), X_i(t), Y(t), t \geq 0; i = 1, 2, \dots, n\}$ constitutes a generalized Markov process.

The state marginal probability of the system at time t are defined by

$$P_0(t) = P\{S(t) = 0\};$$

$$P_{1i}(t, x)dx = P\{S(t) = 1i, x \leq X_{1i}(t) < x + dx\}, i = 1, 2, \dots, n;$$

$$P_2(t, y)dy = P\{S(t) = 2, y \leq Y(t) < y + dy\};$$

$$P_3(t, y)dy = P\{S(t) = 3, y \leq Y(t) < y + dy\};$$

$$P_{4i}(t, x, y)dx = P\{S(t) = 4i, x \leq X_i(t) < x + dx, Y(t) = y\}, i = 1, 2, \dots, n.$$

According to the model assumptions and the supplementary variable technique, we can obtain the following differential equations for the system. By straightforward probability arguments, for example, we have

$$P_0(t + \Delta t) = P_0(t)(1 - \Lambda \Delta t - c \Delta t) + \sum_{i=1}^n \int_0^\infty \mu_i(x) \Delta t P_{1i}(t, x) dx + \int_0^\infty d(y) \Delta t P_{1i}(t, y) dy + o(\Delta t) \text{ where } \Lambda = \sum_{i=1}^n \lambda_i, \text{ Letting}$$

Δt tend to zero, we can get

$$\left(\frac{d}{dt} + \Lambda + c\right)P_0(t) = \sum_{i=1}^n \int_0^\infty \mu_i(x) P_{1i}(t, x) dx + \int_0^\infty d(y) P_2(t, y) dy; \tag{1}$$

In the same way, we have

$$\left(\frac{\partial}{\partial t} + \frac{\partial}{\partial x} + \mu_i(x)\right)P_{1i}(t, x) = 0, i = 1, 2, \dots, n; \tag{2}$$

$$\left(\frac{\partial}{\partial t} + \frac{\partial}{\partial y} + \Lambda + c + d(y)\right)P_2(t, y) = \sum_{i=1}^n \int_0^\infty \mu_i(x) P_{4i}(t, x, y) dx; \tag{3}$$

$$\left(\frac{\partial}{\partial t} + \frac{\partial}{\partial y} + \Lambda + d(y)\right)P_3(t, y) = cP_2(t, y); \tag{4}$$

$$\left(\frac{\partial}{\partial t} + \frac{\partial}{\partial x} + \mu_i(x)\right)P_{4i}(t, x, y) = 0, i = 1, 2, \dots, n; \tag{5}$$

The boundary conditions are

$$P_{1i}(t, 0) = \lambda_i P_0(t), i = 1, 2, \dots, n; \tag{6}$$

$$P_2(t, 0) = cP_0(t) + \int_0^\infty d(y) P_3(t, y) dy; \tag{7}$$

$$P_3(t, 0) = 0; \tag{8}$$

$$P_{4i}(t, 0, y) = \lambda_i P_2(t, y) + \lambda_i P_3(t, y); \tag{9}$$

The initial conditions are

$$P_0(0) = 1, P_{1i}(0) = 0, i = 1, 2, \dots, n, P_2(0) = 0, P_3(0) = 0, P_{4i}(0) = 0, i = 1, 2, \dots, n.$$

The system differential equations using Laplace transforms are obtained as follows:

$$(s + \Lambda + c)P_0^*(s) = P_0^*(0) + \sum_{i=1}^n \int_0^\infty \mu_i(x) P_{1i}^*(s, x) dx + \int_0^\infty d(y) P_2^*(s, y) dy; \tag{10}$$

$$\left(\frac{d}{dx} + s + \mu_i(x)\right)P_{1i}^*(s, x) = 0, i = 1, 2, \dots, n; \tag{11}$$

$$\left(\frac{d}{dy} + s + \Lambda + c + d(y)\right)P_2^*(s, y) = \sum_{i=1}^n \int_0^\infty \mu_i(x) P_{4i}^*(s, x, y) dx; \tag{12}$$

$$\left(\frac{d}{dy} + s + \Lambda + d(y)\right)P_3^*(s, y) = cP_2^*(s, y); \tag{13}$$

$$\left(\frac{d}{dx} + s + \mu_i(x)\right)P_{4i}^*(s, x, y) = 0, i = 1, 2, \dots, n; \tag{14}$$

Together with the borderline conditions and the initial conditions, this system of equations can be solved to yield:

$$P_0^*(s) = \frac{\sum_{i=1}^n \lambda_i \hat{G}_i(s) + c [1 - \hat{H}(w) + \hat{H}(s + \Lambda + c)]}{(w + c) \left(\sum_{i=1}^n \lambda_i \hat{G}_i(s) + c \right) - c(s + \Lambda + c) \hat{H}(w) + cw \hat{H}(s + \Lambda + c)}; \tag{15}$$

$$P_{1i}^*(t, x) = \lambda_i P_0^*(s) e^{-sx} \bar{G}_i(x), i = 1, 2, \dots, n; \tag{16}$$

$$P_2^*(s, y) = P_2^*(s, 0) \frac{\sum_{i=1}^n \lambda_i \hat{G}_i(s)}{\sum_{i=1}^n \lambda_i \hat{G}_i(s) + c} \left(e^{\left(\sum_{i=1}^n \lambda_i \hat{G}_i(s) + c\right)y} + \frac{c}{\sum_{i=1}^n \lambda_i \hat{G}_i(s)} \right) e^{-(s + \Lambda + c)y} \bar{H}(y); \tag{17}$$

$$P_3^*(s, y) = P_2^*(s, 0) \frac{c}{\sum_{i=1}^n \lambda_i \hat{G}_i(s) + c} \left(e^{\left(\sum_{i=1}^n \lambda_i \hat{G}_i(s) + c\right)y} - 1 \right) e^{-(s + \Lambda + c)y} \bar{H}(y); \tag{18}$$

$$P_{4i}^*(s, x, y) = P_2^*(s, 0) e^{-sy} \bar{H}(y) e^{-sx} \bar{G}_i(x), i = 1, 2, \dots, n; \tag{19}$$

Where
$$P_2^*(s, 0) = \frac{c \left(\sum_{i=1}^n \lambda_i \hat{G}_i(s) + c \right)}{w \left(\sum_{i=1}^n \lambda_i \hat{G}_i(s) + c \right) - c(s + \Lambda + c) \hat{H}(w) + cw \hat{H}(s + \Lambda + c)}; \tag{20}$$

$$w = s + \Lambda - \sum_{i=1}^n \lambda_i \hat{G}_i(s).$$

4. Reliability indices

4.1 system availability and system rate of occurrence of failure

By the definition, the system availability at t is given by

$$A(t) = P(\text{the system is working at time } t) = P(N(t) \in W) = P_0(t) + \sum_{k=2}^3 \int_0^t P_k(t, y) dy.$$

The Laplace-transform of A(t) is

$$A^*(s) = P_0^*(s) + \int_0^\infty P_2^*(s, y) dy + \int_0^\infty P_3^*(s, y) dy$$

Where, according to (15), (17), (18) and (20), thus

$$A^*(s) = \frac{\left(\sum_{i=1}^n \lambda_i \hat{G}_i(s) + c - c \hat{H}(w) + c \hat{H}(s + \Lambda + c) \right) + \frac{c}{w} (s + \Lambda + c) (1 - \hat{H}(w))}{(w + c) \left(\sum_{i=1}^n \lambda_i \hat{G}_i(s) + c \right) - c(s + \Lambda + c) \hat{H}(w) + cw \hat{H}(s + \Lambda + c)} \tag{21}$$

Where $w = s + \Lambda - \sum_{i=1}^n \lambda_i \hat{G}_i(s)$. Using Tauberian theorem, the stay state availability or the limiting availability of the system is given by

$$A = \lim_{t \rightarrow +\infty} A(t) = \lim_{s \rightarrow 0^+} s A^*(s) = \frac{1}{1 + \sum_{i=1}^n \frac{\lambda_i}{\mu_i}} \tag{22}$$

Let $W_f(t)$ be the rate of occurrence of failure or the failure frequency of the system at time t.

Hence

$$M_f(t) = \int W_f(x) dx.$$

According to Lam [6], we have

$$W_f(t) = \sum_{i=1}^n \left[\lambda_i P_0(t) + \int_0^{\infty} \lambda_i P_2(t, y) dy + \int_0^{\infty} \lambda_i P_3(t, y) dy \right] = \Lambda A(t).$$

The Laplace transform of $W_f(t)$ is given by

$$W_f^*(s) = \sum_{i=1}^n \left[\lambda_i P_0^*(s) + \int_0^{\infty} \lambda_i P_2^*(s, y) dy + \int_0^{\infty} \lambda_i P_3^*(s, y) dy \right] = \Lambda A^*(s). \tag{23}$$

Using Tauberian theorem, the stay state failure frequency of the system is given by

$$W_f = \lim_{t \rightarrow +\infty} W_f(t) = \lim_{s \rightarrow 0^+} s W_f^*(s) = \frac{\Lambda}{1 + \sum_{i=1}^n \frac{\lambda_i}{\mu_i}}. \tag{24}$$

4.2 The idle time probability of the repairman

Clearly, the repairman will be idle if and only if the components are all working and no customer is arrival. Thus, the idle time probability of the repairman at time t is given by

$$I(t) = P_0(t)$$

The Laplace transform of $I(t)$ is $I^*(s) = P_0^*(s)$.

Using Tauberian theorem, the stay state failure frequency of the system is given by

$$I = \lim_{t \rightarrow +\infty} I(t) = \lim_{s \rightarrow 0^+} s I^*(s) = \frac{\Lambda + c \hat{H}(\Lambda + c)}{\left(1 + \sum_{i=1}^n \frac{\lambda_i}{\mu_i}\right) \left(\Lambda + c \hat{H}(\Lambda + c)\right) + \frac{c}{d} (\Lambda + c) \sum_{i=1}^n \frac{\lambda_i}{\mu_i}}. \tag{25}$$

4.3 The rate of occurrence of the repairman serving for customer

Let $N(t)$ be the number of the customer served during a given time $(0, t]$, then according Lam[6], we have

$$N(t) = \int D_s(x) dx$$

Where $D_s(t)$ is the rate of occurrence of the repairman serving for customer or the serving frequency of the repairman at time t.

According to Lam [6], we have

$$D_s(t) = \int_0^{\infty} d(y) P_2(t, y) dy + \int_0^{\infty} d(y) P_3(t, y) dy$$

The Laplace transform of $D_s(t)$ is given by

$$\begin{aligned} D_s^*(s) &= \int_0^{\infty} d(y) P_2^*(s, y) dy + \int_0^{\infty} d(y) P_3^*(s, y) dy \\ &= \frac{c \left(\sum_{i=1}^n \lambda_i \hat{G}_i(s) + c \right) \hat{H}(s + \Lambda - \sum_{i=1}^n \lambda_i \hat{G}_i(s)) P_0^*(s)}{\sum_{i=1}^n \lambda_i \hat{G}_i(s) + c - c \left[\hat{H}(s + \Lambda - \sum_{i=1}^n \lambda_i \hat{G}_i(s)) - \hat{H}(s + \Lambda + c) \right]}. \end{aligned}$$

Using Tauberian theorem, the stay state number of the customer served by the repairman per unit time is given by

$$N = \lim_{t \rightarrow +\infty} D_s(t) = \lim_{s \rightarrow 0^+} s D_s^*(s) = \frac{c(\Lambda + c)}{\left(1 + \sum_{i=1}^n \frac{\lambda_i}{\mu_i}\right) \left[\Lambda + \frac{c}{d} (\Lambda + c) + c \hat{H}(\Lambda + c)\right]}. \tag{26}$$

5. The system benefit analysis

In this section, our objective is to determine whether or not given the priority to components in repairing such that the benefit of the system is maximized. Let x_1' be the working reward per unit time of the system, x_2' be the average cost

each time of the system, and x'_3 be the average reward of serving for one customer. Based on the assumptions, the stay state average reward per unit time of the system is

$$y_1 = Ax'_1 - W_f x'_2 + Dx'_3 = \frac{(x'_1 - \Lambda x'_2) \left[\Lambda + \frac{c}{d} (\Lambda + c) + \hat{H}(\Lambda + c) \right] + c(\Lambda + c)x'_3}{\left(1 + \sum_{i=1}^n \frac{\lambda_i}{\mu_i} \right) \left[\Lambda + \frac{c}{d} (\Lambda + c) + \hat{H}(\Lambda + c) \right]} \quad (27)$$

In order to solve the our problem, it is necessary to introduce some conclusion and assumption that LIU, Ren – bin, TANG, Ying – hui & LUO Chuan – yi (2005) have studied. In this paper, let x_1 be the working reward per unit time of the system, x_2 be the average cost each time failure of the system, and x_3 be the average reward of serving for one customer. Clearly, for one system, the x'_1 and x'_3 will be, respectively, same to the x_1 and x_3 while the x'_2 will be different from x_2 , because the x_2 include the cost produced by waiting repair. So the equation will be changed to

$$y_1 = Ax_1 - W_f x'_2 + Dx_3 = \frac{(x_1 - \Lambda x'_2) \left[\Lambda + \frac{c}{d} (\Lambda + c) + \hat{H}(\Lambda + c) \right] + c(\Lambda + c)x_3}{\left(1 + \sum_{i=1}^n \frac{\lambda_i}{\mu_i} \right) \left[\Lambda + \frac{c}{d} (\Lambda + c) + \hat{H}(\Lambda + c) \right]}$$

The stay state average reward per unit time of the system in Lam [2] is

$$y_0 = \frac{(x_1 - \Lambda x_2) \left[1 + \frac{c}{\Lambda} \cdot \frac{1 - \hat{H}(\Lambda)}{1 - \hat{H}(\Lambda) + \hat{H}(\Lambda + c)} \right] + \frac{cx_3}{1 - \hat{H}(\Lambda) + \hat{H}(\Lambda + c)}}{1 + \frac{c}{d} \cdot \frac{1}{1 - \hat{H}(\Lambda) + \hat{H}(\Lambda + c)} + \sum_{i=1}^n \frac{\lambda_i}{\mu_i} \cdot \frac{c}{\Lambda} \cdot \frac{1 - \hat{H}(\Lambda)}{1 - \hat{H}(\Lambda) + \hat{H}(\Lambda + c)}}.$$

whether or not the components given the priority in repairing will depend on the result of the equation $y_1 - y_0$: the component will be given priority in repair when the result of equation $y_1 - y_0$ is positive number, while the component will not be given priority in repair when the result of equation $y_1 - y_0$ is negative. In this way the benefit of the system will be maximized.

References

- Su, B.H. (1994). a model of n-unit series repairable systems with a repairman doing other work[J]. *Journal of Shijiazhuang Railway Institute*. 7(4). 34-39.
- LIU, R.B., TANG, Y. H, & LUO C.Y (2005). An N - unit series repairable system with a repairman doing other work [J]. *Journal of Natural Science of Heilongjiang University*. 22(4). 493-496.
- HU, L.M., WU, J.B. & TIAN R.L. (2007). Series repairable system with two types of failure and a repairman doing other work [J]. *Journal of Yanshan University*, 31(1). 47-50.
- Zhang, Y.L. & Wang G.J. (2007). a deteriorating cold standby repairable system with priority in use[J]. *European Journal of Operational Research* .183. 278 - 295.
- MENG, X.Y., LIU, Y., CHEN, G.J., LIU, L.C., YIN, R.L & YUAN, L. (2006). Reliability analysis of warm standby repairable of two components with continuous lifetime switch and priority [J]. *Journal of Yanshan University*. 30(1). 52-56.
- Shi, D.H. (1985). a new method for calculating the mean failure numbers of a repairable system during $(0, t]$ [J]. *Acta Mathematicae Applicatae Sinica*. 8(1). 101-110.



Periodic Solutions of Higher Order with Restoring Terms Delay Functional Differential Equation with Neutral Type

Haiqing Wang
School of Science
Tianjin Polytechnic University
Tianjin 300160 China
E-mail: haiqingwang@tjpu.edu.cn

Abstract

Using the theory of coincidence degree, the authors have studied the existence of periodic solutions of a type of higher order with restoring terms delay functional differential equations with neutral type, and some new results for the existence of periodic solutions have been obtained.

Keywords: Delay functional differential equation, Coincidence degree, Periodic solutions

1. Introduction and Lemma

The functional differential equation with time delay, because of its wide application, has long been a main subject of common concern. But because the argument in complex time delay may depend on condition itself or variation rate, it is difficult to predict the property of the solution to the functional differential equation with complex deviating argument. It brings such big difficulty to our research work that in a long period of time the research of this equation progressed slowly. In recent years with further development of nonlinear functional analysis and algebra-ictopology, people have already had some achievement on the research of this equation. This paper mainly study periodic solutions of the following kind:

$$x^{(m)}(t) + a(t)x^{(m)}(t - \tau) + f(x(t - \sigma))\dot{x}(t - \sigma) + b(t)g(x(t - \tau)) + c(t)x(t - \tau) = p(t) \quad (1)$$

Lemma ^[7] Let X, Y be Banach space, $L : D_L \subset X \rightarrow Y$ is a Fredholm mapping of index 0 $P : X \rightarrow X, Q : Y \rightarrow Y$ are continuous mapping projector; Ω is an open bounded set in X ,

and $N : \bar{\Omega} \times [0, 1] \rightarrow Y$ is L -Compact on $\bar{\Omega}$, further more suppose:

- (a) $Lx \neq \lambda N(x, \lambda), \forall x \in D_L \cap \partial\Omega, \lambda \in (0, 1);$
- (b) $QN(x, 0) \neq 0, \forall x \in \text{Ker}(L) \cap \partial\Omega;$
- (c) $\text{deg}(QN(x, 0), \text{Ker}(L) \cap \Omega, 0) \neq 0.$

then the equation $Lx = N(x, 1)$ has at least one solution in $\bar{\Omega}$. Where deg is Brouwer degree.

2. Main Results and Proof of Theorems

Theorem: Suppose f, a, b, c, g, p are continuous for their variables respectively; There exists T , such that $p(t+T) = p(t), a(t+T) = a(t), b(t+T) = b(t) > 0, 0 < |a(t)| < a_1 < 1,$

$$c(t+T) = c(t) < 0, a_m = \max_{t \in \mathbf{R}} \{ |a^m(t)| \} < c_0 = \min_{t \in \mathbf{R}} \{ |c(t)| \} \leq c_1 = \max_{t \in \mathbf{R}} \{ |c(t)| \} < \frac{1 - a_1}{T^m},$$

$a(t) \in C^m(\mathbf{R}, \mathbf{R})$ and further more suppose are as follows,

a. $\exists 0 < M < \frac{1 - a_1 - c_1 T^m}{T^{m-1}}, \forall x \in \mathbf{R}, |f(x)| \leq M,$

b. $\exists A > 0, \forall x \in \mathbf{R}, |g(x)| \leq A;$

c. $\forall 0 \neq x \in \mathbf{R}, xg(x) < 0$

then Eq.(1) has at least one T-periodic solution.

Proof of Theorem : In order to use continuation theorem to obtain T-periodic solution of Eq.(1), we firstly make some required preparations. Let $X = \{x \in C^{m-1}(\mathbf{R}, \mathbf{R}) \mid x(t+T) = x(t)\}$

$Y = \{y \in C(\mathbf{R}, \mathbf{R}) \mid y(t+T) = y(t)\}$ and the norm of X is $\|x\| = \max_{0 \leq i \leq m-1} \{ |x^{(i)}|_{\infty} \}$, there $|x^{(0)}|_{\infty} = |x|_{\infty} = \max_{t \in \mathbf{R}} \{ |x(t)| \}$, $|x^{(i)}|_{\infty} = \max_{t \in \mathbf{R}} \{ |x^{(i)}(t)| \}$, $i = 1, 2, \dots, m-1$, $\|y\| = \max_{t \in \mathbf{R}} \{ |y(t)| \}$, then the X and Y with this norm are Banach space.

Firstly, we study the priori bound of T-periodic solution of the following equation

$$x^{(m)}(t) + \lambda a(t)x^{(m)}(t - \tau) + \lambda f(x(t - \sigma))\dot{x}(t - \sigma) + \lambda b(t)g(x(t - \tau)) + \lambda c(t)x(t - \tau) = \lambda^2 p(t) \tag{1.1}$$

Suppose that $x = x(t) \in X$ is an arbitrary T-periodic solution of Eq.(1.1), put $x(t)$ into (1.1) and then integrate both sides of (1.1) on $[0, T]$, so yield

$$\int_0^T [a(t)x^{(m)}(t - \tau) + b(t)g(x(t - \tau)) + c(t)x(t - \tau)]dt = \lambda \int_0^T p(t)dt$$

we easily get :

$$(-1)^m \int_0^T a^{(m)}(t)x(t - \tau)dt + \int_0^T b(t)g(x(t - \tau))dt + \int_0^T c(t)x(t - \tau)dt = \lambda \int_0^T p(t)dt$$

so there exists a $t_0 \in [0, T]$, such that:

$$(-1)^m a^{(m)}(t_0)x(t_0 - \tau) + b(t_0)g(x(t_0 - \tau)) + c(t_0)x(t_0 - \tau) = \lambda p(t_0)$$

$$\text{i.e. } |c(t_0)x(t_0 - \tau)| = |\lambda p(t_0) - (-1)^m a^{(m)}(t_0)x(t_0 - \tau) - b(t_0)g(x(t_0 - \tau))|$$

$$\text{so } |c_0 x(t_0 - \tau)| \leq p_1 + a_m |x(t_0 - \tau)| + b_1 A$$

$$\text{i.e. } |x(t_0 - \tau)| \leq \frac{b_1 A + p_1}{c_0 - a_m} \triangleq A_1 \text{ where } b_1 = \max_{t \in \mathbf{R}} \{ |b(t)| \}, p_1 = \max_{t \in \mathbf{R}} \{ |p(t)| \}$$

$$\text{let } t_0 - \tau = nT + t_1, n \in \mathbf{N}, t_1 \in [0, T], \text{ so } |x(t_1)| = |x(t_0 - \tau)| \leq A_1$$

In view of $\forall t \in [0, T], x(t) = x(t_1) + \int_{t_1}^t \dot{x}(s)ds$, we have

$$|x(t)| = \left| x(t_1) + \int_{t_1}^t \dot{x}(s)ds \right| \leq A_1 + \int_{t_1}^t |\dot{x}(s)|ds \leq A_1 + \int_0^T |\dot{x}(t)|dt$$

$$\text{i.e. } |x^{(0)}|_{\infty} = |x|_{\infty} \leq A_1 + \int_0^T |\dot{x}(t)|dt \tag{1.2}$$

Noting $x(t) = x(t+T)$, so there must exist numbers $\xi_i \in (0, T)$, such that $x^{(i)}(\xi_i) = 0$, there $i = 1, 2, 3, \dots, m-1$.

For $\forall t \in [0, T], x^{(i)}(t) = x^{(i)}(\xi_i) + \int_{\xi_i}^t x^{(i+1)}(s)ds = \int_{\xi_i}^t x^{(i+1)}(s)ds$, we have

$$|x^{(i)}(t)| = \left| \int_{\xi_i}^t x^{(i+1)}(s)ds \right| \leq \int_0^T |x^{(i+1)}(t)|dt \leq T \int_0^T |x^{(i+2)}(t)|dt$$

$$\leq T^2 \cdot \int_0^T |x^{(i+3)}(t)|dt \leq \dots \leq T^{m-(i+1)} \int_0^T |x^{(i+m-i)}(t)|dt = T^{m-(i+1)} \int_0^T |x^{(m)}(t)|dt,$$

$$\text{i.e. } |x^{(i)}|_{\infty} \leq T^{m-(i+1)} \int_0^T |x^{(m)}(t)|dt, i = 1, 2, \dots, m-1 \tag{1.3}$$

Combining (1.2),(1.3), we get

$$|x^{(0)}|_{\infty} = |x|_{\infty} \leq T^{m-1} \int_0^T |x^{(m)}(t)|dt \tag{1.4}$$

By (1.1), we get

$$\int_0^T |x^{(m)}(t)|dt \leq \int_0^T |-\lambda a(t)x^{(m)}(t - \tau) - \lambda f(x(t - \sigma))\dot{x}(t - \sigma)|dt + \int_0^T |-\lambda b(t)g(x(t - \tau)) - \lambda c(t)x(t - \tau) + \lambda^2 p(t)|dt$$

Combining the condition a and b, we easily obtain

$$\int_0^T |x^{(m)}(t)|dt \leq a_1 \int_0^T |x^{(m)}(t - \tau)|dt + M \int_0^T |\dot{x}(t - \sigma)|dt + c_1 \int_0^T |x(t - \tau)|dt + TAb_1 + Tp_1$$

$$\text{i.e. } \int_0^T |x^{(m)}(t)| dt \leq a_1 \int_0^T |x^{(m)}(t)| dt + MT|\dot{x}|_\infty + c_1 T|x|_\infty + TAb_1 + TP_1 \tag{1.5}$$

Noting (1.3), (1.4) and (1.5), we observe

$$\int_0^T |x^{(m)}(t)| dt \leq a_1 \int_0^T |x^{(m)}(t)| dt + MT \cdot T^{m-2} \int_0^T |x^{(m)}(t)| dt + c_1 T(A_1 + T^{m-1} \int_0^T |x^{(m)}(t)| dt) + TAb_1 + TP_1 \tag{i.e.}$$

$$(1 - a_1 - MT^{m-1} - c_1 T^m) \int_0^T |x^{(m)}(t)| dt \leq TAb_1 + TP_1 + c_1 TA_1$$

$$\text{so } \int_0^T |x^{(m)}(t)| dt \leq \frac{TAb_1 + TP_1 + c_1 TA_1}{1 - a_1 - MT^{m-1} - c_1 T^m} \tag{1.6}$$

Noting(1.3),(1.5)and(1.6), we have

$$|x^{(0)}|_\infty = |x|_\infty \leq A_1 + T^{m-1} \cdot \frac{TAb_1 + TP_1 + c_1 TA_1}{1 - a_1 - MT^{m-1} - c_1 T^m} = A_1 + \frac{T^m (Ab_1 + p_1 + c_1 A_1)}{1 - a_1 - MT^{m-1} - c_1 T^m} \triangleq \omega_0$$

$$|x^{(i)}|_\infty \leq T^{m-(i+1)} \cdot \frac{TAb_1 + TP_1 + c_1 TA_1}{1 - a_1 - MT^{m-1} - c_1 T^m} = \frac{T^{m-i} (Ab_1 + p_1 + c_1 A_1)}{1 - a_1 - MT^{m-1} - c_1 T^m} \triangleq \omega_i, i = 1, 2, \dots, m-1$$

Let $\omega = \max_{0 \leq i \leq m} \{\omega_i + 1\}$, and we take $\Omega = \{x | x \in X : \|x\| < \omega\}$, then Ω is an open and bounded set in X .

Let $L : D_L \subset X \rightarrow Y : x \rightarrow Lx = x^{(m)}(t)$;

$N : X \times I \rightarrow Y : x \rightarrow N(x, \lambda) = -a(t)x^{(m)}(t - \tau) - f(x(t - \sigma))\dot{x}(t - \sigma) - b(t)g(x(t - \tau)) - c(t)x(t - \tau) + \lambda p(t)$, then the corresponding equation of $Lx = \lambda N(x, \lambda)$ is Eq.(1.1).

Now, we define projection operators as follows,

$$P : X \rightarrow \text{Ker}(L) : x \rightarrow Px = \frac{1}{T} \int_0^T x(t) dt ; \quad Q : Y \rightarrow Y / \text{Im}(L) : y \rightarrow Qy = \frac{1}{T} \int_0^T y(t) dt$$

obviously, P, Q are continuous operator, $\text{Im}(P) = R = \text{Ker}(L), \text{Ker}(Q) = \text{Im}(L)$, and it is easy to prove that L is a Fredholm mapping of index 0 and N is L -Compact on $\bar{\Omega}$.

From the above discussion and the construction of Ω , we have known that $\forall x \in D_L \cap \partial\Omega$

$\lambda \in (0, 1)$, therefore the condition (a) of lemma holds.

For arbitrary $x \in \text{Ker}(L) \cap \partial\Omega, \|x\| = \omega$, by the definition of Q, N , we have

$$\begin{aligned} QN(x, 0) &= \frac{1}{T} \int_0^T [-a(t)x^{(m)}(t - \tau) - f(x(t - \sigma))\dot{x}(t - \sigma) - b(t)g(x(t - \tau)) - c(t)x(t - \tau)] dt \\ &= -\frac{1}{T} \int_0^T b(t)g(x(t - \tau)) dt - \frac{1}{T} \int_0^T c(t)x(t - \tau) dt \end{aligned}$$

$$\begin{aligned} \text{so } xQN(x, 0) &= -\frac{1}{T} x \int_0^T b(t)g(x(t - \tau)) dt - \frac{1}{T} x \int_0^T c(t)x(t - \tau) dt \\ &= -\frac{1}{T} xg(x) \int_0^T b(t) dt - \frac{1}{T} x^2 \int_0^T c(t) dt > 0 \end{aligned}$$

therefore the condition (b) of lemma holds.

Make a transformation $H(x, \mu) = \mu x + (1 - \mu)QN(x, 0), \forall x \in \partial\Omega \cap \text{Ker}(L), \mu \in [0, 1]$

$$\begin{aligned} \text{We have } xH(x, \mu) &= \mu x^2 + x(1 - \mu)QN(x, 0) \\ &= \mu x^2 - (1 - \mu) \frac{1}{T} g(x)x \int_0^T b(t) dt - (1 - \mu) \frac{1}{T} x^2 \int_0^T c(t) dt > 0 \end{aligned}$$

so $H(x, \mu) \neq 0$, i.e. $H(x, \mu) \neq 0$ is a homotopy, $\text{deg}(QN(x, 0), \text{Ker}(L) \cap \Omega, 0) = \text{deg}(I,$

$\text{Ker}(L) \cap \Omega, 0) = \text{deg}(I, R \cap \Omega, 0) \neq 0$, where I is identity mapping and the condition (c) of lemma holds.

From above all, the requirements of lemma are all met, so Eq. (1) has at least one T-periodic solution under the condition of theorem 1, so far the proof of theorem is completed.

References

Gaines R E and Mawhin J L. Coincidence degree and nonlinear differential equations [c]. *Lecture*

Notes Math, springer-verlag, 1977, 568

Liu Xiping, Jia Mei and Ge Weigao. Periodic solutions to a type of Duffing equation with complex deviating argument[J], *Appl. Math. J. Chinese Univ. Ser. A* 2003,18(1):51-56

Mari P O and Zanolin F. Boundary value problems for forced nonlinear equations at resonance.

Lecture Notes in Math, 1151. Ordinary and Partial Differential Equation. Berlin: springer-verlag, 1984, 285~294

Mawhin J and Ward J J R. Nonuniform nonresonance conditions at the two first eigenvalues for forced periodic solutions of forced Liénard and Duffing equations. *Rocky Mountain J Math*, 1982,12(4):643~654

Pascale E, and Iannacci R. Periodic solution of a generalized Liénard equation with delay,. *Lecture Notes Math, 1017. Berlin: Springer-Verlag*, 1983, 148~156

Xiang Zigui, Liu Changmao, and Huang Xiankai. On Periodic Solutions of Delay Li é nard Equations[J], *Journal of Jishou University (National Science Edition)*, 1998,19(4):35-40

Zheng Zuxiu, Theory of Functional Differential Equation [M]. *Hefei: Anhui education press*, 1994



Existence of Nonoscillatory Solution of High Order Linear Neutral Delay Difference Equation

Shasha Zhang, Xiaozhu Zhong, Ping Yu, Wenxia Zhang & Ning Li

Department of Mathematics

Yanshan University

Qinhuangdao 066004, China

E-mail:shashazm@163.com

Supported by the Foundation for the natural science of Hebei province of China (Z2007431)

Abstract

Consider the high order neutral delay difference equation with positive and negative coefficients $\Delta^{l+1}[x(n) + px(n - \tau)] + R_1(n)x(n - \delta_1) - R_2(n)x(n - \delta_2) = o$

Where $p \in R; \tau \in N(1); \delta_1, \delta_2 \in N; \{R_1(n)\}, \{R_2(n)\}$ are positive real sequences. A sufficient condition for the existence of the eventually positive solution of the above equation is set forward in terms of $\sum_{n=1}^{+\infty} n^i R_i(n) < +\infty, i = 1, 2, n \in N(n_0)$. This result got rid of a quite strong tentative of existing literature, which improve the relevant theorem.

Keywords: Positive and negative coefficients, Neutral difference equation, Eventually positive solution

1. Introduction

Nowadays, as the rapid development of computer science, automation technology, biology and numerical research, neutral delay differential equations oscillation study attracts the attention of many scholars, and some research achievements have been taken in this area. At the same time, a difference equation with positive and negative coefficients attracting more attention becomes a new study field. However, only a few research results have been achieved in this field, and rare results on bounded positive solutions in neutral delay difference equation with positive and negative coefficients. Reference studies the existence of positive solutions in second-order neutral delay difference equation with positive and negative coefficients $\Delta^2[x(n) + px(n - \tau)] + R_1(n)x(n - \delta_1) - R_2(n)x(n - \delta_2) = o$, and gets a sufficient condition for the existence of positive solutions in this equation. Another reference promotes it to the higher order, that is, it focuses on following $l+1$ order difference equation with positive and negative coefficients $\Delta^{l+1}[x(n) + px(n - \tau)] + R_1(n)x(n - \delta_1) - R_2(n)x(n - \delta_2) = o$ (1)

Where $l \in z^+; p \in R; \tau \in \{1, 2, \dots\}; \delta_1, \delta_2 \in \{0, 1, 2, \dots\}; \{R_1(n)\}, \{R_2(n)\}$ are positive real sequences.

For convenience, now the basic concepts and marks in this paper are listed as follows:

“ Δ ” Said for the forward difference operator $\Delta y(n) = y(n+1) - y(n)$; Z Said for the set composing by all integer; R Said for the real number set. Set $a \in Z$, and $N(a) = \{a, a+1, \dots\}, N = N(0), \{x(n)\}$ is named as the solution of difference equation (1) when the $\{x(n)\}$ satisfied the equation (1). When $n \in N(M)$, and $x(n) > 0$, $\{x(n)\}$ is eventually positive solution which means that positive integral M exists. When positive integral M existed, where $n \in N(M)$, and $x(n) < 0$, $\{x(n)\}$ is eventually negative solution. Oscillation refers to that $\{x(n)\}$ are neither eventually positive nor eventually negative, otherwise it called as nonoscillation.

Lemma 1 Assume

$$(i) \sum_{n=1}^{+\infty} n^i R_i(n) < +\infty, i = 1, 2, n \in N(n_0) \quad (2)$$

(ii) There exists a large enough positive integer T_1 , to every $a > 0$ and $n > T_1$ hold, where $aR_1(n) - R_2(n) \geq 0$ (3)

(iii) $p \neq \pm 1$ (4)

hold, then Equation (1) has an eventually positive solution.

The proofing processes could be found in references.

2. Main results and proof

Among the sufficient conditions for the existence of nonoscillatory solution in differential equation(1), the condition (3) may look too restrictive; we will delete the strong condition (3), permit $p = 1$, to get the overall sufficient condition for existence of eventually positive solution on the p value in equation (1).

Theorem 1 Consider the difference equation with positive and negative coefficients

$$\Delta^{l+1}[x(n) + px(n - \tau)] + R_1(n)x(n - \delta_1) - R_2(n)x(n - \delta_2) = o$$

Where $l \in \mathbb{Z}^+$; $p \in \mathbb{R}$; $\tau \in \mathbb{N}(1)$; $\delta_1, \delta_2 \in \mathbb{N}$; $R_1(n), R_2(n) \in C([n_0, \infty), \mathbb{R}^+)$

If condition (2) is hold, where $p \neq -1$, then equation (1) has an eventually positive solution.

Proof: Let the B_N be the Banach space which is composed of all bounded real sequences $x = x(n)$ in $\mathbb{N}(n_0)$, define sup norm $\|x\| = \sup x(n)$. The proof of Theorem 1 will be divided into five claims.

Claim 1. $p = 1$

From condition (2), choose a large enough positive integer $N > (n_0)$, so that when $n > N$,

$$\sum_{k=n}^{+\infty} k^l R_1(k) \leq \frac{1}{l+2} \tag{5}$$

$$\sum_{k=n}^{+\infty} k^l R_2(k) \leq \frac{1}{l+2} \tag{6}$$

hold. Define a subset as $A = \{x \in B_N : l \leq x(n) \leq l+2, n \in \mathbb{N}(n_0)\}$, then it is easy to see A is a bounded, closed, and convex subset of B_N .

Define a mapping $T : A \rightarrow B_N$ as follows

$$Tx(n) = \begin{cases} (l+1) + \sum_{i=1}^{+\infty} \sum_{j_{i-2}=n+(i-1)\tau}^{n+li\tau-1} \sum_{j_{i-3}=j_{i-2}}^{+\infty} \cdots \sum_{j_1=j_2}^{+\infty} \sum_{k=j_1}^{+\infty} \sum_{s=k}^{+\infty} (s-k+1) \cdot \\ [R_1(s)x(s-\delta_1) - R_2(s)x(s-\delta_2)] & n \geq N \\ Tx(N) & n_0 \leq n < N \end{cases} \tag{7}$$

Clearly, Tx is continuous. Next we will prove that T is a self-mapping in A . When $n \geq N, \forall x \in A$, by using (5) and (7), we have

$$\begin{aligned} Tx(n) &\leq (l+1) + \sum_{i=1}^{+\infty} \left[\sum_{j_{i-2}=n+(i-1)\tau}^{n+li\tau-1} + \sum_{j_{i-2}=n+(i-1)\tau}^{n+(i-1)\tau-1} \right] \sum_{j_{i-3}=j_{i-2}}^{+\infty} \cdots \sum_{j_1=j_2}^{+\infty} \sum_{k=j_1}^{+\infty} \sum_{s=k}^{+\infty} (s-k+1)R_1(s)x(s-\delta_1) \leq \\ &(l+1) + (l+2) \sum_{i=1}^{+\infty} \sum_{j_{i-2}=n+(i-1)\tau}^{n+li\tau-1} \sum_{j_{i-3}=j_{i-2}}^{+\infty} \cdots \sum_{j_1=j_2}^{+\infty} \sum_{k=j_1}^{+\infty} \sum_{s=k}^{+\infty} (s-k+1)R_1(s) = \\ &(l+1) + (l+2) \sum_{j_{i-2}=n}^{+\infty} \sum_{j_{i-3}=j_{i-2}}^{+\infty} \cdots \sum_{j_1=j_2}^{+\infty} \sum_{k=j_1}^{+\infty} \sum_{s=k}^{+\infty} (s-k+1)R_1(s) \leq \\ &(l+1) + (l+2) \sum_{s=n}^{+\infty} s^l R_1(s) \leq (l+1) + (l+2) \times \frac{1}{l+2} = l+2 \end{aligned}$$

Furthermore, in view of (6) and (7), we have:

$$Tx(n) \geq (l+1) - (l+2) \sum_{s=n}^{+\infty} s^l R_2(s) \geq (l+1) - (l+2) \times \frac{1}{l+2} = l$$

Clearly, when $n_0 \leq n < N$, we have $l \leq x(n) \leq l+2$, thus $Tx \in A$ which means that T is the self- mapping in A .

Next we will prove that T is a contraction mapping in A . When $n > N$, for every $x_1, x_2 \in A$, we have:

$$|Tx_1(n) - Tx_2(n)| \leq \left| \sum_{i=1}^{+\infty} \sum_{j_{i-2}=n+(i-1)\tau}^{n+li\tau-1} \sum_{j_{i-3}=j_{i-2}}^{+\infty} \cdots \sum_{j_1=j_2}^{+\infty} \sum_{k=j_1}^{+\infty} \sum_{s=k}^{+\infty} (s-k+1) \cdot \right.$$

$$\left. R_1(s) [x_1(s - \delta_1) - x_2(s - \delta_2)] \right| \leq$$

$$\sum_{j_{i-2}=n}^{+\infty} \sum_{j_{i-3}=j_{i-2}}^{+\infty} \cdots \sum_{j_1=j_2}^{+\infty} \sum_{k=j_1}^{+\infty} \sum_{s=k}^{+\infty} (s-k+1) R_1(s) \|x_1 - x_2\| \leq$$

$$\sum_{s=n}^{+\infty} s^l R_1(s) \|x_1 - x_2\| \leq \frac{1}{l+2} \|x_1 - x_2\|$$

Where $q = \frac{1}{l+2}$, so that $|Tx_1(n) - Tx_2(n)| \leq q \|x_1 - x_2\|$.

Clearly, when $n_0 \leq n < N$, we have $|Tx_1(n) - Tx_2(n)| \leq q \|x_1 - x_2\|$. Thus T is a contraction mapping in A .

Above all, according to Banach contraction mapping, T has a fixed point on A such that $Tx = x$. And $x = \{x(n)\}$ satisfies equation (7), so we have

$$x(n) + x(n - \tau) = (2l + 4) + \sum_{i=1}^{+\infty} \sum_{j_{i-2}=n+(i-1)\tau}^{n+li\tau-1} \sum_{j_{i-3}=j_{i-2}}^{+\infty} \cdots \sum_{j_1=j_2}^{+\infty} \sum_{k=j_1}^{+\infty} \sum_{s=k}^{+\infty} (s-k+1) \cdot$$

$$[R_1(s)x(s - \delta_1) - R_2(s)x(s - \delta_2)] =$$

$$(2l + 4) + \sum_{j_{i-2}=n}^{+\infty} \sum_{j_{i-3}=j_{i-2}}^{+\infty} \cdots \sum_{j_1=j_2}^{+\infty} \sum_{k=j_1}^{+\infty} \sum_{s=k}^{+\infty} (s-k+1) [R_1(s)x(s - \delta_1) - R_2(s)x(s - \delta_2)]$$

To get the $l + 1$ order difference equation from the above equation,

$$\Delta^{l+1} [x(n) + x(n - \tau)] + R_1(n)x(n - \delta_1) - R_2(n)x(n - \delta_2) = 0$$

Thus, the fixed point $\{x(n)\}$ is a positive solution of equation (1). This completes the proof of Claim 1.

Claim 2. $0 \leq p < 1$

From condition (2), choose a sufficiently large positive integer $n_1 \geq \max \{T_1, n_0 + \delta\}$, where $\delta = \max \{\tau, \delta_1, \delta_2\}$, so that

$$\sum_{n=n_1}^{+\infty} n^l R_1(n) \leq \frac{M_2 - (1-p)}{M_2} \tag{8}$$

$$\sum_{n=n_1}^{+\infty} n^l R_2(n) \leq \frac{1-p - pM_2 - M_1}{M_2} \tag{9}$$

$$\sum_{n=n_1}^{+\infty} n^l [R_1(n) + R_2(n)] < 1-p \tag{10}$$

hold. Where M_1 and M_2 are positive constant, $1 - M_2 < p \leq \frac{1 - M_1}{1 + M_2}$.

Let $A = \{x \in B_N : M_1 \leq x(n) \leq M_2, n \in N(n_0)\}$, then it is easy to see A is a bounded, closed, and convex subset of B_N .

Define a mapping $T: A \rightarrow B_N$ as follows

$$Tx(n) = \begin{cases} 1 - p - px(n - \tau) + \sum_{s=n}^{+\infty} C_{s+l-n}^l [R_1(s)x(s - \delta_1) - R_2(s)x(s - \delta_2)] & n \geq n_1 \\ Tx(n_1) & n_0 \leq n < n_1 \end{cases} \quad (11)$$

Clearly, Tx is continuous. Next we will prove that T is a self- mapping in A .

When $n \geq n_1$, and $\forall x \in A$, by using (8) and (11), we have

$$Tx(n) \leq 1 - p + \sum_{s=n}^{+\infty} C_{s+l-n}^l R_1(s)x(s - \delta_1) \leq 1 - p + M_2 \sum_{s=n}^{+\infty} s^l R_1(s) \leq 1 - p + \frac{M_2(M_2 - (1 - p))}{M_2} = M_2$$

Furthermore, in view of (9) and (11), we have:

$$Tx(n) \geq 1 - p - px(n - \tau) - \sum_{s=n}^{+\infty} C_{s+l-n}^l R_2(s)x(s - \delta_2) \geq 1 - p - pM_2 - M_2 \sum_{s=n}^{+\infty} s^l R_2(s) \geq 1 - p - pM_2 - \frac{M_2(1 - p - pM_2 - M_1)}{M_2} = M_1$$

Clearly, when $n_0 \leq n < n_1$, we have $M_1 \leq x(n) \leq M_2$. Thus $Tx \in A$ which means that T is the self- mapping in A .

Next we will prove that T is a contraction mapping in A . When $n > n_1$, for every $x_1, x_2 \in A$, we have:

$$\begin{aligned} |Tx_1(n) - Tx_2(n)| &\leq |-px_1(n - \tau) + px_2(n - \tau)| + \\ &\sum_{s=n}^{+\infty} C_{s+l-n}^l R_1(s) |x_1(s - \delta_1) - x_2(s - \delta_1)| + \\ &\sum_{s=n}^{+\infty} C_{s+l-n}^l R_2(s) |x_1(s - \delta_2) - x_2(s - \delta_2)| \leq \\ &p \|x_1 - x_2\| + \|x_1 - x_2\| \sum_{s=n}^{+\infty} s^l (R_1(s) + R_2(s)) = \\ &\|x_1 - x_2\| \left[p + \sum_{s=n}^{+\infty} s^l (R_1(s) + R_2(s)) \right] \end{aligned}$$

From condition (10), where $0 < q_1 < 1$, so that $|Tx_1(n) - Tx_2(n)| \leq q_1 \|x_1 - x_2\|$.

Clearly, when $n_0 \leq n < n_1$, we have $|Tx_1(n) - Tx_2(n)| \leq q \|x_1 - x_2\|$. Thus T is the contraction mapping in A .

According to Banach contraction mapping, T has a fixed point on A such that $Tx = x$. And $x = \{x(n)\}$ we have

$$Tx(n) = \begin{cases} 1 - p - px(n - \tau) + \sum_{s=n}^{+\infty} C_{s+l-n}^l [R_1(s)x(s - \delta_1) - R_2(s)x(s - \delta_2)] & n \geq n_1 \\ Tx(n_1) & n_0 \leq n < n_1 \end{cases}$$

So this fixed point $x = \{x(n)\}$ is a positive sequence.

To get the $l + 1$ order difference equation from the above equation,

$$\Delta^{l+1}[x(n) + px(n - \tau)] + R_1(n)x(n - \delta_1) - R_2(n)x(n - \delta_2) = o$$

Thus, the fixed point $\{x(n)\}$ is a positive solution of equation (1). This completes the proof of Claim2.

Claim 3. $p > 1$

From condition (2), choose a large enough positive integer $n_2 > T_1 > n_0$, where $n_2 + \tau = n_0 + \max\{\delta_1, \delta_2\}$, so that

$$\sum_{n=n_2}^{+\infty} n^l R_1(n) \leq \frac{p(M_4 - 1) + 1}{M_4} \tag{12}$$

$$\sum_{n=n_2}^{+\infty} n^l R_2(n) \leq \frac{p(1 - M_3) - (1 + M_4)}{M_4} \tag{13}$$

$$\sum_{n=n_2}^{+\infty} n^l [R_1(n) + R_2(n)] < p - 1 \tag{14}$$

hold. Where M_3 and M_4 are positive constants, $(1 - M_3)p \geq 1 + M_4$ and $p(1 - M_4) < 1$

Let $A = \{x \in B_N : M_3 \leq x(n) \leq M_4, n \in N(n_0)\}$, then it is easy to see A is a bounded, closed, and convex subset of B_N .

Define a mapping $T: A \rightarrow B_N$ as follows

$$Tx(n) = \begin{cases} 1 - \frac{1}{p} - \frac{1}{p}x(n - \tau) + \frac{1}{p} \sum_{s=n+\tau}^{+\infty} C_{s+l-n-\tau}^l [R_1(s)x(s - \delta_1) - R_2(s)x(s - \delta_2)] & n \geq n_2 \\ Tx(n_2) & n_0 \leq n < n_2 \end{cases} \tag{15}$$

Claim 4. $-1 < p < 0$

From condition (2), choose a large enough positive integer $n_3 \geq \max\{T_1, n_0 + \delta\}$, where $\delta = \max\{\tau, \delta_1, \delta_2\}$, so that

$$\sum_{n=n_3}^{+\infty} n^l R_1(n) \leq \frac{M_6(1 + p) - (1 + p)}{M_6} \tag{16}$$

$$\sum_{n=n_3}^{+\infty} n^l R_2(n) \leq \frac{(1 + p) - M_5(1 + p)}{M_6} \tag{17}$$

$$\sum_{n=n_3}^{+\infty} n^l [R_1(n) + R_2(n)] < 1 + p \tag{18}$$

hold. Where M_5, M_6 are positive constants, and $0 < M_5 \leq 1 < M_6$.

Let $A = \{x \in B_N : M_5 \leq x(n) \leq M_6, n \in N(n_0)\}$, then it is easy to see A is a bounded, closed, and convex subset of B_N .

Define a mapping $T: A \rightarrow B_N$ as follows

$$Tx(n) = \begin{cases} 1 + p - px(n - \tau) + \sum_{s=n}^{+\infty} C_{s+l-n}^l [R_1(s)x(s - \delta_1) - R_2(s)x(s - \delta_2)] & n \geq n_3 \\ Tx(n_3) & n_0 \leq n < n_3 \end{cases} \tag{19}$$

Claim 5. $p < -1$

From condition (2), choose a large enough positive integer $n_4 > T_1 > n_0$, where $n_4 + \tau = n_0 + \max\{\delta_1, \delta_2\}$, so that

$$\sum_{n=n_4}^{+\infty} n^l R_1(n) \leq \frac{(M_7-1)(p+1)}{M_8} \tag{20}$$

$$\sum_{n=n_4}^{+\infty} n^l R_2(n) \leq \frac{(1-M_8)(1+p)}{M_8} \tag{21}$$

$$\sum_{n=n_4}^{+\infty} n^l [R_1(n) + R_2(n)] < -1 - p \tag{22}$$

hold. Where M_7, M_8 are positive constants, and $0 < M_7 < 1 < M_8$.

Let $A = \{x \in B_N : M_7 \leq x(n) \leq M_8, n \in N(n_0)\}$, then it is easy to see A is a bounded, closed, and convex subset of B_N .

Define a mapping $T : A \rightarrow B_N$ as follows

$$Tx(n) = \begin{cases} 1 + \frac{1}{p} - \frac{1}{p}x(n-\tau) + \frac{1}{p} \sum_{s=n+\tau}^{+\infty} C'_{s+l-n-\tau} [R_1(s)x(s-\delta_1) - R_2(s)x(s-\delta_2)] & n \geq n_4 \\ Tx(n_4) & n_0 \leq n < n_4 \end{cases} \tag{23}$$

Due to the proofs of Claim 3, 4, 5 are similar as Claim 2, these proofs are left out.

References

Cheng, Jinfu & Z. Annie. Existence of Nonoscillatory Solution to Second Order Linear Neutral Delay Equation. *System Science and Mathematics*, 2004, 24(3):389-397.

Liu, Yue-hua & Chen, Ya-bo. Existence of Nonoscillatory Solution of Second Order Linear Neutral Difference Equation. *Journal of Hunan Agricultural University (Natural Sciences)*, 2001, 27(1):76-79.

Lin, Wenxian. Neutral Partial Functional Differential Equation. *Journal of Anhui University (Natural Science Edition)*, 2006, 30(4):12-14.

Liang, Jingcui, Zhong, Xiaozhu, Wang, Donghua & Ge, Lixia. Existence of Nonoscillatory Solution of Third Order Linear Neutral Delay Difference Equation. *Journal of Yanshan University*, 2006, 30(2):101-104.

Sun, Shu-rong & Asymptotic. Behavior and Existence of Positive Solution for the Higher Order Neutral Difference Equations. *Journal of Engineering Mathematics*, 2002, 19(3):15-20.

Xing, Hailong & Zhong, Xiaozhu. Existence of Nonoscillatory Solution of High Order Linear Neutral Delay Difference Equation with Positive and Negative Coefficients. *Journal of Yanshan University*, 2007, 31(1):33-40.



Bandwidth Enhancement for Microstrip Antenna in Wireless Applications

RSA Raja Abdullah, D Yoharaaj & A Ismail

Department of Computer and Communication Engineering

Universiti Putra Malaysia (UPM)

43400 Serdang, Selangor, Malaysia

Tel: 60-3-8946-4347 E-mail: rsa@eng.upm.edu.my, alyani@eng.upm.edu.my

Abstract

Antenna is a vital component in wireless application systems. The microstrip antenna can be used for wireless applications as it has features such as light weight, easily mounted and it is easy to mass produce. Although there are many features that suits well for microstrip antenna to be deployed for wireless applications, there is a very serious limitation where it has a very narrow bandwidth. The typical bandwidth of the microstrip antennas is between 1 - 3%. If this limitation is eliminated, the microstrip antenna can be used to its full potential. An alternative bandwidth enhancement technique is studied and then proposed in order to broaden the bandwidth of the microstrip antenna. The wireless application that is selected to be studied is the Wireless Local Area Network (WLAN) based on the IEEE 802.11b standard. In Malaysia, this WLAN band spans from 2.4GHz to 2.48GHz. The bandwidth enhancement technique which is selected is the Identical Dual-Patch Microstrip Antenna with Air-Gap (IDMA). By using this technique, a bandwidth enhancement of about 11% has been achieved. This bandwidth very well covers the required WLAN band with an operating frequency of 2.45GHz.

Keywords: Wireless Local Area Network (WLAN), Identical Dual Patch Microstrip Antenna with Air-Gap (IDMA)

1. Introduction

In recent years, the popularity of wireless applications is ever increasing in the industry as well as in our very own society. There is a very large demand for wireless applications because of its mobility. This is evident as the usage of mobile telephones which is integrated with wireless data services is very common these days. Portable devices which support data and telephony are being used in a mobile computing environment. There is a large investment that has been put into wireless communication by the major companies in the telecommunication industry. This shows that wireless applications are gaining an increase in its usage in our society. One particular wireless application that has experienced this trend is the Wireless Local Area Network (WLAN). According to the guideline by Malaysian Communications and Multimedia Commission (MCMC) on the provision of WLAN service, the unlicensed spread spectrum band in Malaysia for WLAN technologies are from 2.4GHz to 2.48GHz, 5.250 GHz to 5.350GHz and from 5.725GHz to 5.875GHz [1]. In this design, the wireless application that is selected to be studied is the 2.4GHz to 2.48GHz frequency band which is based on the 802.11b WLAN standard. This frequency band is very popular due to its low cost.

The role of antenna for wireless applications has become more vital because the antenna will ensure the efficient connectivity in a WLAN system. WLAN antennas required being low profile, light weight and broad bandwidth. The microstrip antenna suits the features very well except for its narrow bandwidth [2]. The WLAN antenna should have a minimum bandwidth of 100 MHz to fully utilize the WLAN band based on the 802.11b standard. The conventional microstrip antenna could not fulfill this requirement as its bandwidth usually ranges between 1 – 3%. Although the required operating frequency range is from 2.4 GHz to 2.48 GHz, at least double the bandwidth is required to avoid expensive tuning operations and to cause uncritical manufacturing [3]. Therefore, there is a need to enhance the bandwidth of the microstrip antenna for WLAN applications.

This paper investigates a technique which can enhance the bandwidth of the microstrip antenna without increasing the lateral size and the complexity of the microstrip antenna too much. The Identical Dual Patch Microstrip Antenna with Air-Gap (IDMA) bandwidth enhancement technique takes the advantage of using the air gap to increase the total thickness of the microstrip antenna which is essential for bandwidth enhancement. This bandwidth enhanced microstrip antenna can be deployed for the WLAN application operating at a frequency of 2.45GHz.

2. Design of the single-layer microstrip antenna.

The dimensions of the basic single-layer microstrip antenna are calculated using the equations (1) to (7). The shape for the patch which is selected is rectangular for ease of analysis and it is commonly used [4]. The dielectric substrate of low permittivity is selected for the microstrip antenna which is RT/Duroid 5880. The type of copper cladding used for this substrate is the 35 μ m thick rolled copper. The feeding method for this antenna is coaxial probe method. The 50 Ohms-SMA connector is used as the feed. The simulation was carried out using the full wave analysis simulation tool by Ansoft. The effective permittivity, width, extension of the length and effective length of the patch, the bandwidth as well as the location of the coaxial probe are shown below [5 – 8]:

For $w/h > 1$

$$\epsilon_{\text{reff}} = \frac{\epsilon_r + 1}{2} + \frac{\epsilon_r - 1}{2} \left[1 + 12 \frac{h}{w} \right]^{-1/2} \quad (1)$$

$$W = \frac{c}{2f_r} \sqrt{\frac{2}{\epsilon_r + 1}} \quad (2)$$

$$\frac{\Delta L}{h} = 0.412 \frac{(\epsilon_{\text{reff}} + 0.3) \left(\frac{W}{h} + 0.264 \right)}{(\epsilon_{\text{reff}} - 0.258) \left(\frac{W}{h} + 0.8 \right)} \quad (3)$$

$$L_{\text{eff}} = L + 2\Delta L \quad (4)$$

$$L = \frac{c}{2f_r \sqrt{\epsilon_{\text{reff}}}} - 2\Delta L \quad (5)$$

$$Y_f \text{ (along the width)} = \frac{W}{2} \quad (6)$$

$$X_f \text{ (along the length)} = \frac{L}{2\sqrt{\xi_{re}(l)}} \quad (7)$$

where

$$\xi_{re}(l) = \frac{\epsilon_r + 1}{2} + \frac{\epsilon_r - 1}{2} \left(1 + 12 \frac{h}{L} \right)^{-1/2} \quad (8)$$

$$BW(\%) = \left(3.77 \left(\frac{\epsilon_r - 1}{\epsilon_r^2} \right) \frac{W}{L} \frac{h}{\lambda} \right) \times 100$$

These calculated dimensions are just approximations but they serve as the starting parameters for the simulation process. After numerous iterative processes to obtain the desired operating frequency and input impedance, the optimum dimensions are obtained and the relative bandwidth is recorded. Figure 1 and Table 1 show the simulated and measured results of the single-layer microstrip antenna.

3. Design of identical dual patch microstrip antenna with air-gap (IDMA).

Initially, the basic single-layer microstrip antenna is designed and fabricated to serve as a benchmark for the design of the bandwidth enhanced microstrip antenna. The rectangular probe-fed patch was selected for both the microstrip antennas

due to its ease of analysis and it is commonly used. These microstrip antennas are fed using the 50 Ohms-SMA connector. A low permittivity dielectric substrate was used, namely the 1.575mm thick RT/Duroid 5880. The copper cladding for this substrate is the 35µm thick rolled copper. A full-wave analysis simulation tool by Ansoft was used. The fabricated microstrip antennas were measured with the Agilent E8362B Network Analyzer.

The Identical Dual-Patch Microstrip Antenna with Air-Gap (IDMA) takes the advantage of the air gap which increases the total thickness of the microstrip antenna which is an essential factor for bandwidth enhancement. Another advantage of this design is that the operating frequency of the fabricated microstrip antenna can easily be tuned without the need of a new design by just varying the size of the air gap. Therefore, this makes the design very cost effective. The structure of this bandwidth enhanced microstrip antenna is shown in Figure 2. It uses the same substrate, feeding method and patch shape as the single-layer microstrip antenna.

The following are the Equations (9) and (10) that are used to calculate the bandwidth of the IDMA [4 – 8]:

$$\epsilon_{av} = \left(\frac{(\epsilon_r h_{d1} + \epsilon_r h_a + \epsilon_r h_{d2})}{\left(\frac{h_t}{3}\right)} \right) \tag{9}$$

Where $h_t = h_{d1} + h_a + h_{d2}$

$$BW = \frac{\sqrt{2}p}{45\pi} \left(1 - \frac{1}{\epsilon_{av}} + \frac{2}{5\epsilon_{av}^2} \right) \left(\frac{1}{\epsilon_{av}} \right) \left(\frac{h_t}{\lambda} \right) \left(\frac{W}{L} \right)$$

where

$$p = 1 + \frac{a_2}{20} (k_0 w)^2 + a_4 \left(\frac{3}{560} \right) (k_0 w)^4 + b_2 \left(\frac{1}{10} \right) (k_0 L)^2$$

where $a_2 = -0.16605$, $a_4 = 0.00761$, $b_2 = -0.09142$, $k_0 = 2\pi/\lambda$

The dimensions are calculated from [6-8]. These calculated results are approximated values. It is used to begin with the simulation work. Numerous iterative simulations were done to obtain the optimum configuration of the microstrip antenna. Once the desired operating frequency and input impedance are obtained, the bandwidth is taken at $VSWR \leq 2$.

The simulated bandwidth was plotted together with the calculated bandwidth to determine the size of the air gap. When the maximum simulated bandwidth is achieved, the size of the air gap is determined. Once the size of the air gap is determined, the calculated bandwidth can easily be obtained. The reason this is done is because the calculated bandwidth is a straight line equation. This means that the size of the air gap is directly proportional with the bandwidth. However, this is true only up to a certain threshold. Therefore, the calculated and simulated bandwidths are compared to determine this threshold. The calculated and the simulated results are compared in order to determine the exact size of the air gap. The results of these comparisons are shown in Figure 3.

Once the optimum bandwidth is obtained which is 250 MHz, the spacing between the probe-fed patch and the stacked patch can be determined. To further increase the accuracy of the simulated results, fine-tuning is done. After fine-tuning, the maximum achievable simulated bandwidth is 270 MHz. The final configuration of the microstrip antenna is shown in Table 2 and the simulated results are shown in Figure 4.

Using the optimized configuration of the microstrip antenna in the simulation results, this design is fabricated. The measured results of this bandwidth enhanced microstrip antenna are shown in Table 2, Figure 5.

4. Discussion

Based on the results from the simulations and measurements, it is found that the single-layer microstrip antenna has a very narrow bandwidth that is less than 2% which is not sufficient to fully cover the WLAN band based on the 802.11b standard. There is a need to use a bandwidth enhancement technique in this microstrip antenna and the IDMA is deployed. Using this technique, both the simulated and measured results give a bandwidth enhancement at more than 11%. Furthermore, there is a very good agreement between the simulated and measured results of this design. The comparison between the simulated and measured bandwidths of IDMA is shown in Figure 6.

The comparison between the simulated bandwidth of the single-layer microstrip antenna and the IDMA is shown in Figure 7. As for the comparison of the measured bandwidth between those microstrip antennas, this is shown in Figure 8. Figure 9 shows the simulated radiation pattern of IDMA. Figure 10 shows the fabricated microstrip antennas.

5. Conclusion

The summary of the results obtained are shown in Table 3. It is shown clearly that the simulated and measured results are very similar. This bandwidth enhanced microstrip antenna is suitable for the required WLAN application. As mentioned, this technique has its advantages such as it does not increase the lateral size of the microstrip antenna and disadvantages such as it increases the height of the microstrip antenna. Therefore, in microstrip antenna design, it is very important to determine which feature to be prioritized as trade-off issues will always be present.

References

Malaysian Communications and Multimedia Commission (MCMC). 2005. *Guideline on the Provision of Wireless LAN Service (MCMC/G/01/05/-WLAN)*. Malaysia.

Ramesh, G., B. Prakash, B Inder and I. Apisak. 2001. *Microstrip Antenna Design Handbook*. USA: Artech House, Inc.

Gardelli, R, G. La Cono, and M. Albani. 2004. A Low-Cost Suspended Patch Antenna for WLAN Access Points and Point-to-Point Links. *IEEE Antennas and Wireless Propagation Letters*, 3(1): 90.

Warren, L.S and A.T. Gary. 1997. *Antenna Theory and Design*. USA: John Wiley & Sons, Inc.

Nirun, K, N. Chalernpol and T. Taspong. 2001. Parametric Study of the Rectangular Microstrip Antenna with an Air Gap, *R&D Journal*. 24(2): 131-142.

David, R and A. Nicolaos. 1991. Simple Approximate Formulas for Input Resistance, Bandwidth and Efficiency of a Resonant Rectangular Patch. *IEEE Transactions on Antennas and Propagation*. 39(March): 409.

Balanis. Constantine A. 2005. *Antenna Theory: Analysis and Design*. USA: John Wiley & Sons, Inc.

Salman, H. 2003. *Project Report Part 4, Microstrip Patch Antennas for Broadband Indoor Wireless Systems*. Department of Electrical and Computer Engineering, University of Auckland.

Table 1. Simulated and Measured results of the Single-Layer MSA

Dimensions	Simulated	Measured results
Width	51mm	51mm
Length	41mm	41mm
Location of the Probe (from the edge)	3.5mm	3.5mm
Spacing (air-gap)	9mm	9mm
Operating frequency	2.45GHz	2.44GHz
Input Impedance	50.15 Ω	61.63 Ω
Bandwidth	270MHz (11.020%)	287.77MHz (11.794%)

Table 2. Simulated and Measured Results of IDMA

Parameters [±]	Single-Layer Microstrip Antenna [±]		IDMA [±]	
	Simulated [±]	Measured [±]	Simulated [±]	Measured [±]
Operating Frequency (GHz) [±]	2.45 [±]	2.4248 [±]	2.45 [±]	2.44 [±]
Impedance (Ω) [±]	50.69 [±]	50.15 [±]	51.238 [±]	61.63 [±]
Bandwidth (MHz) [±]	35 [±]	46.71 [±]	270 [±]	287.77 [±]
	(1.429%) [±]	(1.699%) [±]	(11.020%) [±]	(11.794%) [±]

Table 3. Comparison between the Simulated and Measured Results of the Single-Layer Microstrip Antenna and IDMA

Dimensions	Simulated	Measured
Width	50mm	same
Length	39.5mm	same
Location of the Probe	13.25mm	same
Operating frequency	2.45GHz	2.425GHz
Input Impedance	50.69 Ohms	54.64 Ohms
Bandwidth	36MHz (1.469%)	46.71MHz (1.699%)

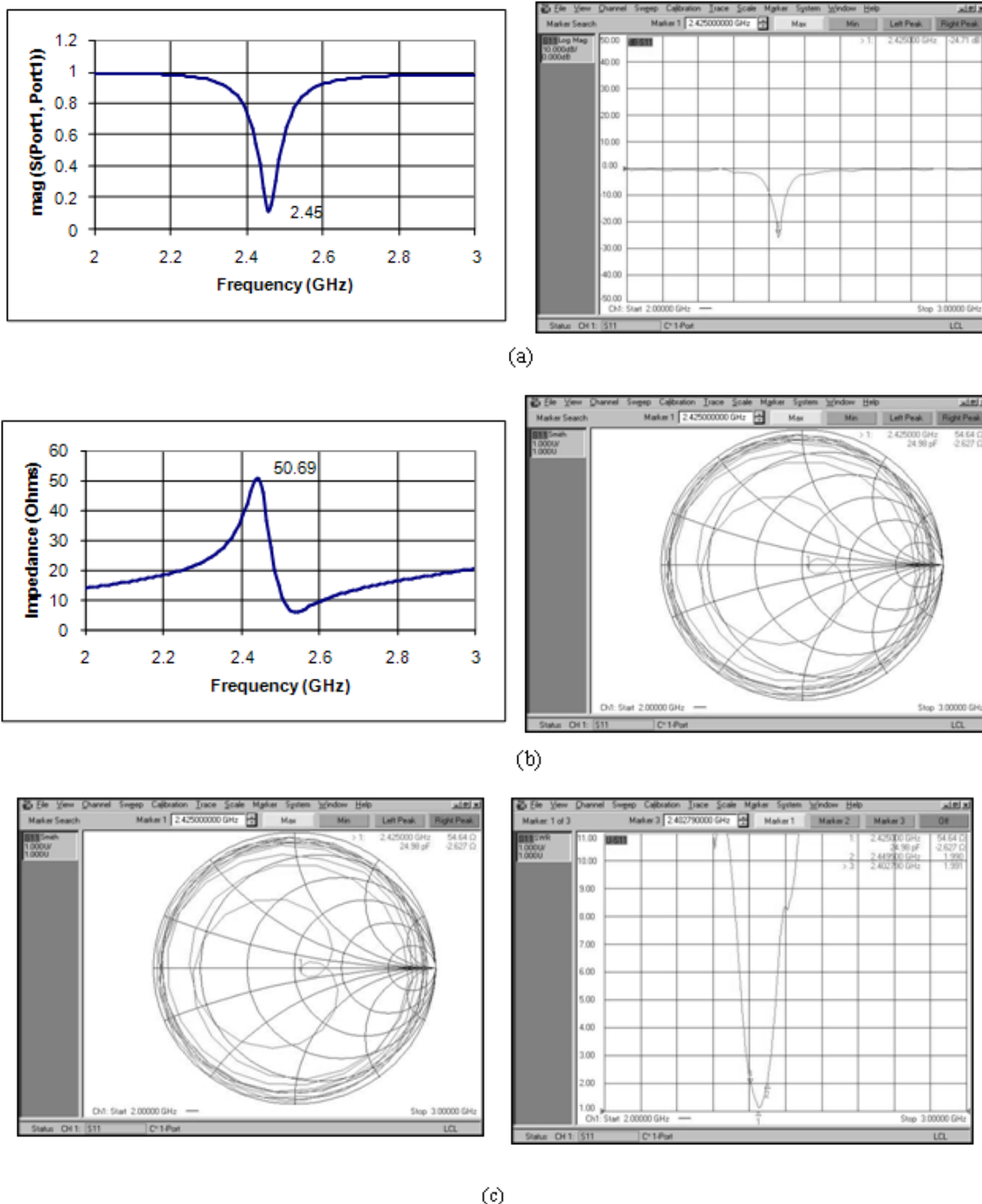


Figure 1. Simulated and Measured of the Single-Layer Microstrip Antenna for (a) Operating Frequency, (b) Input Impedance and (c) Bandwidth

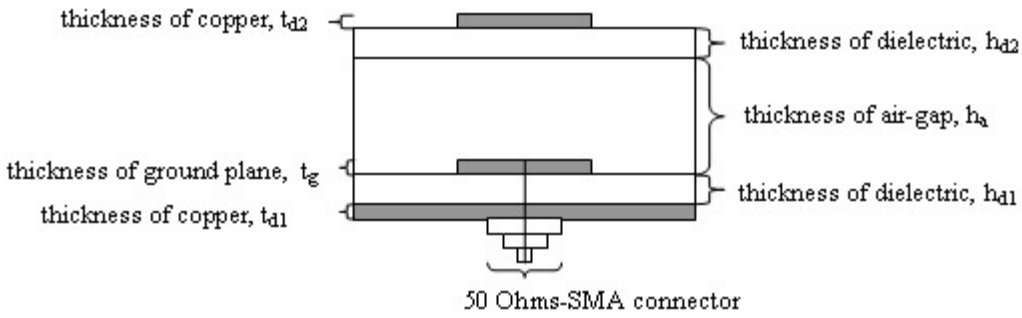


Figure 2. Structure of the IDMA Bandwidth Enhancement Technique

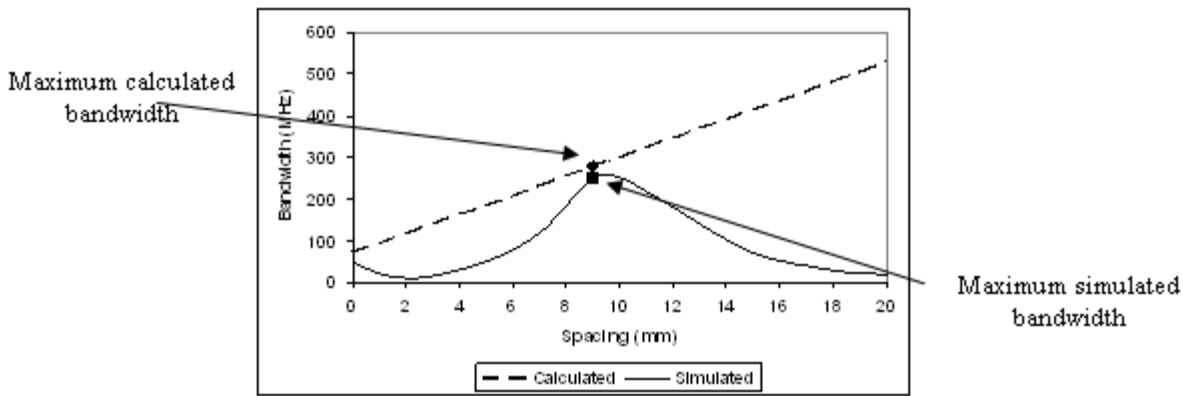
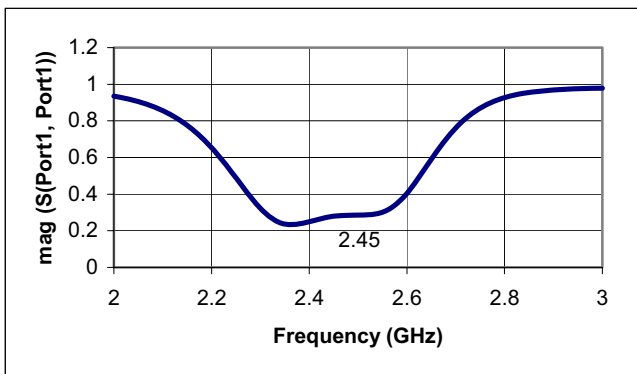
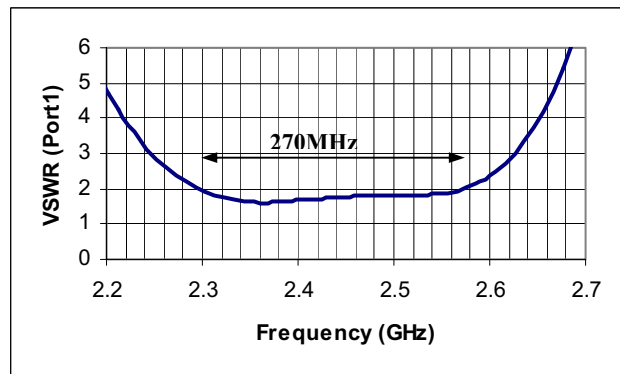


Figure 3. Comparison between the Calculated and Simulated Bandwidth of IDMA

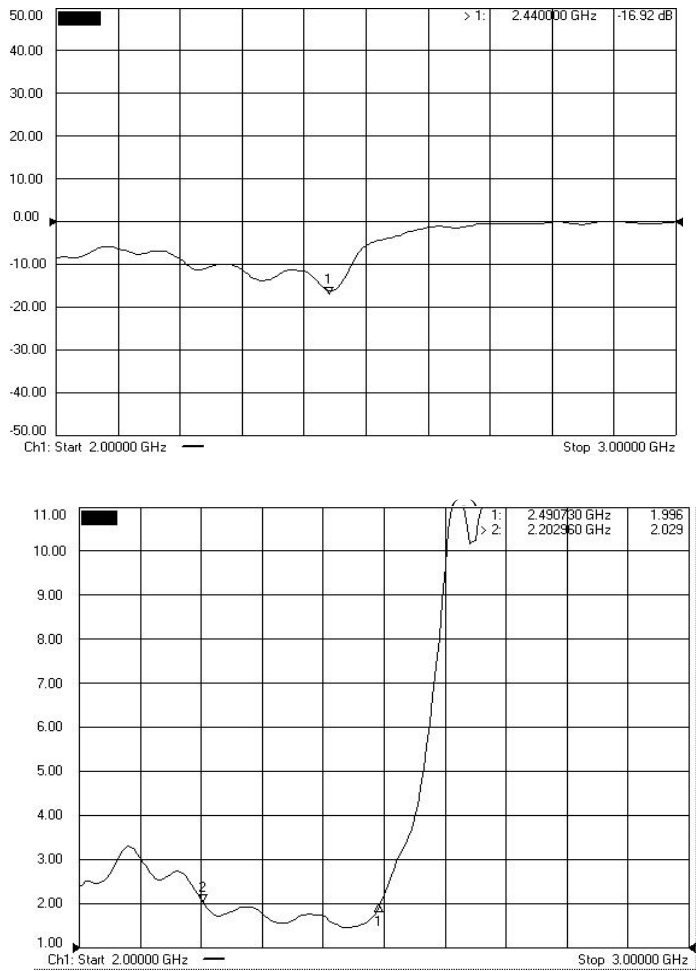


(a)



(b)

Figure 4. Simulated (a) Operating Frequency and (b) Bandwidth of IDMA



(b)

Figure 5. Measured (a) Operating Frequency and (b) Bandwidth of IDMA

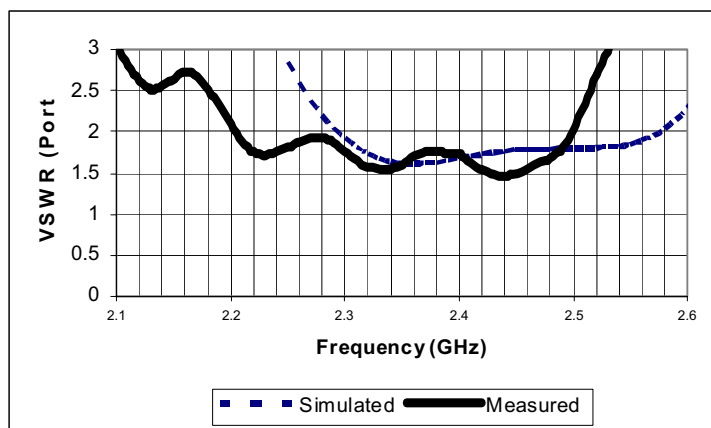


Figure 6. Comparison between the Simulated and Measured Bandwidth of IDMA

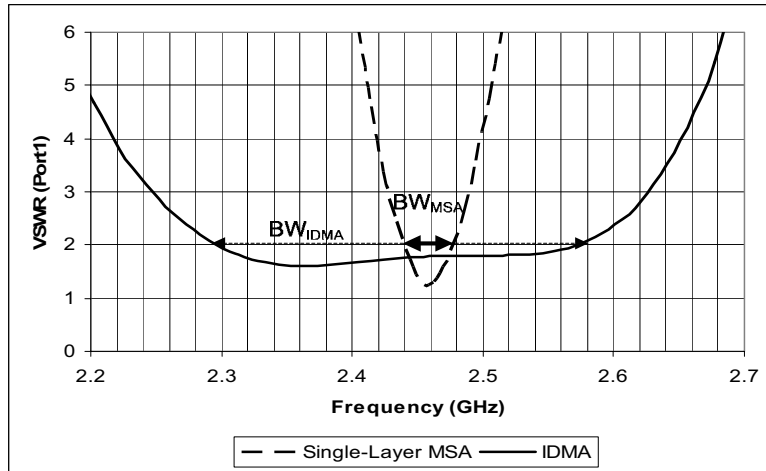


Figure 7. Comparison of the Simulated Bandwidth between the Single-Layer Microstrip Antenna and IDMA

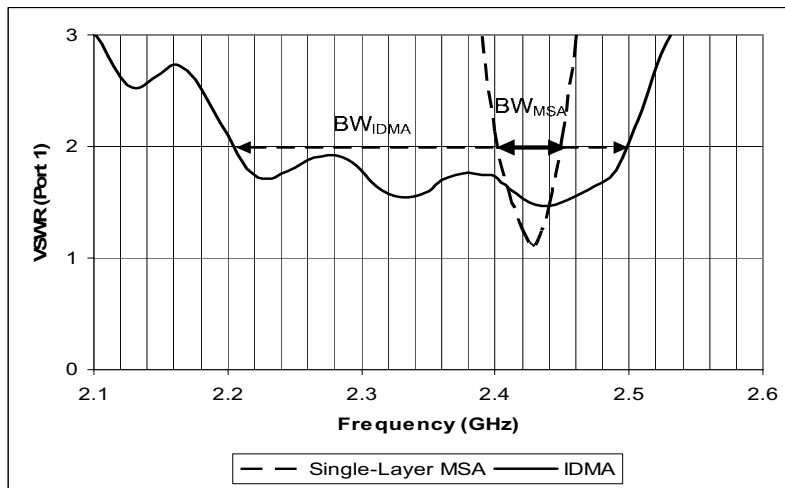


Figure 8. Comparison of the Measured Bandwidth between the Single-Layer Microstrip Antenna and IDMA

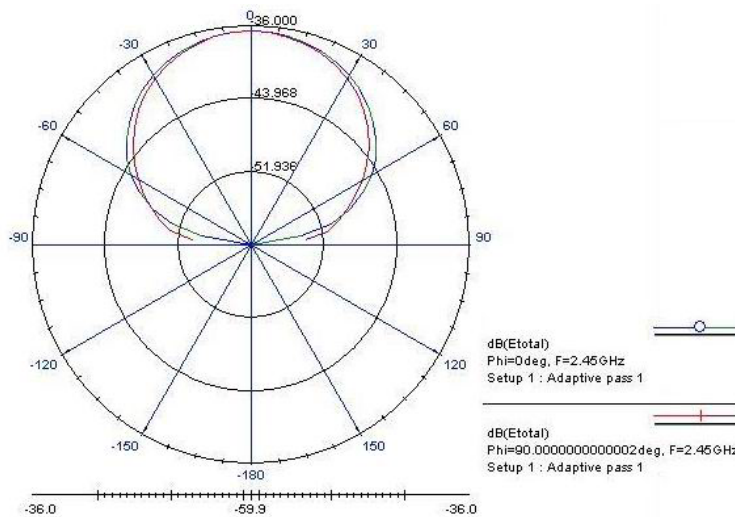


Figure 9. Simulated radiation pattern of IDMA

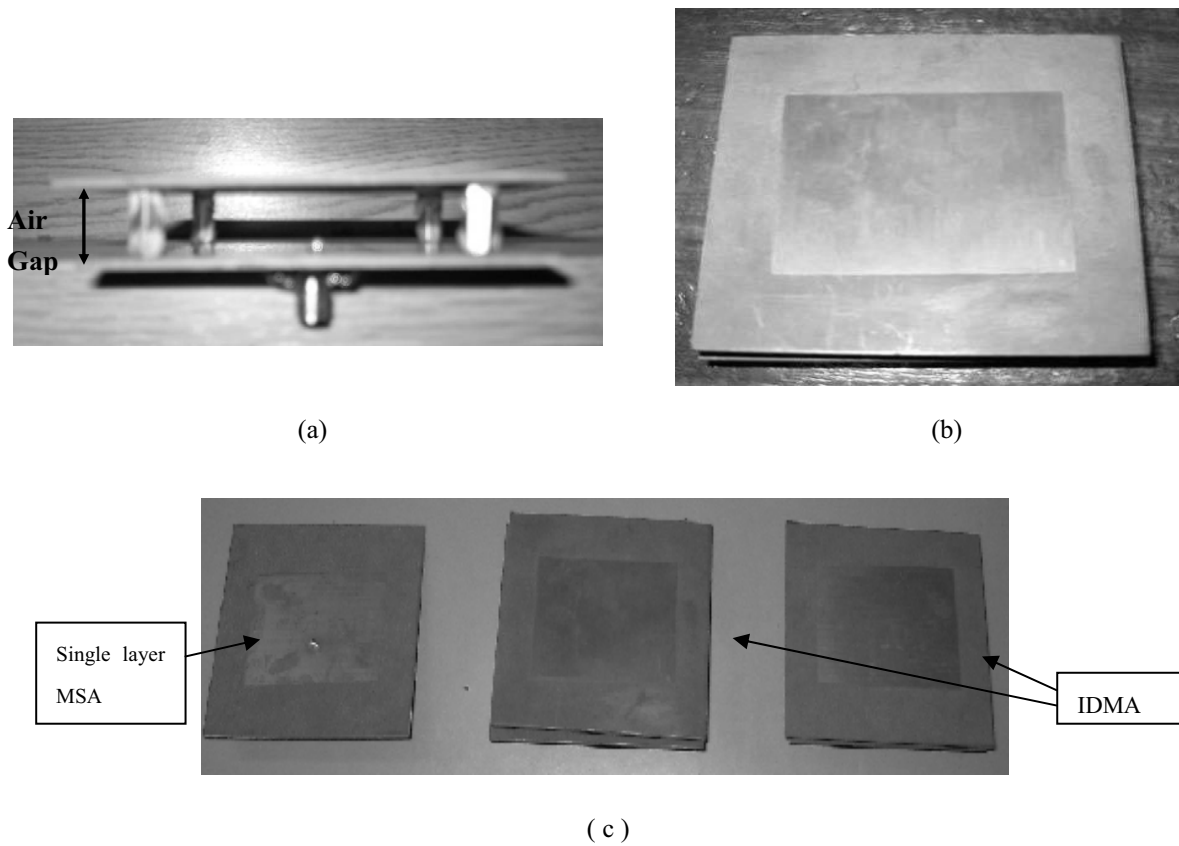


Figure 10. The fabricated microstrip antenna (a) Side View of IDMA, (b) Top view of IDMA and (c) Single-layer Microstrip Antenna and IDMA



Application of Nanometer Aluminum Magnesium Hydroxide in PVDF Membrane Modification

Hanhui Wei, Dong Liu

College of Material Science and Chemistry Engineering

Tianjin Polytechnic University

Tianjin 300160, China

Tel: 86-22-24584809 E-mail: dreamwing9520@163.com

Abstract

In this article, we adopted the phase inversion process to prepare nanometer aluminum magnesium hydroxide/PVDF hybrid membrane, studied the influences of nanometer materials on pure water flux, retention, pore diameter, porosity, microstructure, mechanical property and adsorption property for membranes, researched the influences of different AMH contents on membrane property, and analyzed element contents of membrane transect through x-radial energy dispersive analysis (EDS). Comparing with PVDF membrane without nanometer materials, the results indicated that the addition of nanometer materials obviously enhanced the pure water flux, retention, microstructure, mechanical property and adsorption property for membranes, and didn't largely influence the pore diameter and porosity for membranes. The analysis of SEM indicated that the addition of nanometer materials could obviously change the microstructure of membrane.

Keywords: Nanometer aluminum magnesium hydroxide, Polyvinylidene fluoride (PVDF), Property modification, Hybrid membrane

PVDF is a sort of macromolecule material with good property, and it possesses good chemical stability, heat stability and tenacity, so the research of PVDF membrane is extensively emphasized by domestic and foreign research institutions, and it is successfully applied in many domains such as chemical industry, electron, textile, food and biochemistry (O. Shina K H, 1996, p.137-145, Degen, 1998, Yang, 1997, p.75-86, Degen, 1995). With continual development of PVDF membrane application, different applied situations require different requirements for its property, so we need to modify its property in use process. In recent years, the modification method which introduces few hydrophilic inorganic nanometer particles into hydrophobic polymer system arouses human large interests, especially for the introduction of Organo-mineral technology since 1990s, and this technology introduces ceramic powders into polymer system, and adopts translation technology to prepare composite membrane, which could effectively combine the heat-resistant, chemical stability of ceramic with flexibility and low cost of polymer and fully enhance the pore diameter and pollution-resistant of membrane (Doyen, 1996, P.247-258 & Genne, 1996, P.343-350).

Because nanometer materials possess many properties such as small grain size, large surface area and high surface activity, so we introduce them into the polymer system to modify its property, which make obtained material possess special excellent properties than original materials (Doyen, 1996, P.247-258, Genne, 1996, P.343-350, Li, 2004, P.709-712 & Qu, 2006).

The nanometer materials in the experiment are homemade nanometer aluminum magnesium hydroxides which are hydrophilic materials, and they possesses the layered structure similar with brucite, and because part of Mg^{2+} is isomorphously replaced by Al^{3+} and brings permanent positive charges, and adsorbs Cl^- and OH^- to keep the electric neutrality, so they are a sort of charged materials. There are many researches about the adsorption property of nanometer aluminum magnesium hydroxide (E. Klumpp, 2004, P.111-116, Ramesh, 2005, P.45-51 & Wei, 2005, P.31-33).

In this article, we select nanometer aluminum magnesium hydroxide to modify the property of PVDF micro-porous filtered membrane, and utilize dry/wet phase translation method to prepare nanometer aluminum magnesium hydroxide/PVDF hybrid micro-porous filtered membrane. We studied the influence of the introduction of nanometer materials on flux of pure water, retention, pore diameter, porosity, mechanical property, adsorption, and micro structure for membrane, fully utilize the characters of nanometer materials to perfect the property of PVDF membrane, endows its charged property to enhance its function, and studied the influence of the introduction of different nanometer materials on the property of membrane.

1. Experiment

1.1 Reagents

PVDF: Shanghai 3F New Materials Co., Ltd, FR904.

N,N-Dimethylacetamide (DMAc): analytical reagent, Tianjin Hongyan Chemical Reagent Factory.

Polyvinyl pyrrolidone (PVP): analytical reagent, BASF import to load separately, K-30.

Nanometer aluminum magnesium hydroxide: homemade.

Bovine serum albumin (BSA): molecular weight 67000, Tianjin Lianxing Biological Technology Co., Ltd.

Titan Yellow: molecular weight 695, Purchase and Supply Center of Chemical Reagents of Shanghai.

1.2 Preparation of membrane

Add nanometer aluminum magnesium hydroxide into solvent DMAc, and after ultrasonic separation, add PVDF and additive PVP, control certain water bathing temperature, obtain the casting solution after mixing of beater, defoaming quietly, scrape membrane on clean glass board with homemade drawknife under certain liquid membrane thickness, pre-vaporize certain time, and immerse concretion bathing of pure water to form membrane, and the finished membrane piece is immersed in the pure water to defoam solvent and additive, waited to test. Note the made hybrid membrane as sample A, and adopt same membrane making method and technical condition to prepare the PVDF membrane without nanometer materials, and note it as sample B.

The additive of nanometer aluminum magnesium hydroxide selected in the experiment is PVDF which quality molecular weight is 2%, and the molecular formula is $Mg_{2.04}Al(OH)_{6.48}Cl_{0.60}$, and the average size of crystal grain is 15.1nm, and the ζ electric position is about 42mV, and it has strong positive electricity (Ma, 2007, P.193-195).

1.3 Analysis and testing

Test the pure eater flux of micro-pore filtered membrane by homemade equipment, and the testing conditions are room temperature, 0.1MPa and pure water, and measure the BSA retention of 400ppm and the 10 μ g/ml Titan Yellow removal rate by ultraviolet-visible spectrophotometer (UV-1700 series made by Shimadu Corp), and the adopt Coulter-porometer II to measure the pore diameter of membrane (Zheng, 1999, P.31-33). The porosity is computed by following formula.

$$\text{porosity} = \frac{(W_{\text{wet}} - W_{\text{dry}}) / \rho_{\text{water}}}{(W_{\text{wet}} - W_{\text{dry}}) / \rho_{\text{water}} + W_{\text{dry}} / \rho_{\text{PVDF}}} \quad (1)$$

In the formula (1), W_{wet} is the wet weight of membrane (the unit is g), W_{dry} is the dry weight of membrane (the unit is g), ρ_{water} is the density of water (the unit is g/cm³), ρ_{PVDF} is the density of PVDF material (the unit is g/cm³) which density is 1.77g/cm³ in the experiment.

Represent the micro-structure of membrane by scanning electron microscope (SHIMADZU SS-550), test the mechanical property of sample on the mechanical tester of Instron 5865 (Super Duper Multi National Conglomerates R Us. Corporation), adopt Nicolet308 infrared spectrum meter (Thermo Electron Corporation) to represent the infrared property of membrane, and analyze the transect element of membrane by SEM/EDS (JEOL, JSM-6700F).

2. Results and discussions

2.1 Infrared spectral analysis

Utilize infrared spectral analysis to judge the hybrid character, and judge whether pure physical mixing or chemical function exists though comparing infrared spectrums of hybrid membrane and PVDF membrane (seen in Figure 1). In the FT-IR spectrum of PVDF membrane, the position near 1404cm⁻¹ is the distortion libration apex of CF₂ in PVDF, and the position near 1180cm⁻¹ is the flexing libration apex of CF₂ in PVDF, the position near 1640cm⁻¹ is the adsorption apex of carbonyl group because PVP is not dissolved completely and few PVP leaving in the sample induces the occurrence of disturbance apex. PVDF membrane presents half crystalline phase state, and it is composed by non-crystal state, α phase and β phase, and the positions near 880cm⁻¹ and 840cm⁻¹ are character apexes without amorphous state, and the positions near 763cm⁻¹ and 613cm⁻¹ are weak α phase libration apex, and the position near 1280cm⁻¹ has weak β phase libration apex (Huang, 2003, P.45-48). Comparing with the spectrum of PVDF membrane, the infraed spectrums of nanometer aluminum magnesium hydroxide/PVDF hybrid membrane have not new adsorption apex, which indicates that there is no new chemical bond in the hybrid membrane, i.e. it is pure physical mixing.

2.2 Influence of nanometer materials on membrane microstructure

Figure 2 and Figure 3 respectively are SEM photos of nanometer aluminum magnesium hydroxide/PVDF hybrid membrane and PVDF membrane, and it is obvious that the transects of PVDF membrane and hybrid membrane are asymmetric structure, and above surface of PVDF membrane is the dense function layer, and the lower surface is

obvious figure pore structure, but the transect structure of hybrid membrane changes obviously, and its transect structure is the micro-network pore structure close to two layers, and this structure foams because the existence of nanometer particles enhance the mass transfer resistance of nonsolvent in solvent and gelatin bathing in the casting solution, and baffle the mass transfer speed to some extent, and in the process that the micro-pores form in the separation when casting solution enters into the gelatin bathing, the internal stress could be eliminated and the hybrid membrane could foam finally. This structure could enhance the mechanical property of membrane, and the above surface has obvious white points comparing with PVDF membrane, and we think they are atoms of nanometer aluminum magnesium hydroxide on the membrane surface which could perfect the property of membrane. Next, the introduction of nanometer materials reduces the cortex thickness little and changes the sub-cortex structure of membrane, which could enhance the pure water flux of membrane to some extents.

2.3 Influence of nanometer materials on membrane separation

Table 1 is the property index of nanometer aluminum magnesium hydroxide/PVDF hybrid membrane and PVDF membrane. From table 1, we can see that for the hybrid membrane obtained from the introduction of nanometer particles in casting solution, its separation property could be enhanced obviously. Comparing with common membrane, the pure water flux of hybrid membrane could be enhanced from $971.04 \text{ L}\cdot\text{m}^{-2}\cdot\text{h}^{-1}$ to $1344.40 \text{ L}\cdot\text{m}^{-2}\cdot\text{h}^{-1}$, and the porosity could be enhanced little, and the average pore diameter of hybrid membrane reduce, and the retention of BSA is enhanced from 57.79% to 78.01%. The property of hybrid membrane is excellent because the nanometer particles in the casting solution eliminate the stress produced when the pure waters in solution and solidification bathing exchange to foam micro-pore, which could effectively avoid the occurrence of big pores and limitation, and the nanometer aluminum magnesium hydroxide has good hydrophilicity, which could improve the hydrophilicity of membrane and enhance the dense pressure of membrane, so the hybrid membrane puts up large pure water flux, small average pore diameter and high retention.

2.4 Influence of nanometer materials on membrane mechanical property and adsorption property

From Table 2, we can see that the mechanical property of hybrid membrane could be enhanced obviously, and the breaking stress could be enhanced from 0.95MPa to 1.30MPa, and the breaking strain basically changes little. The reasons for the enhancement of mechanical property of hybrid membrane are that the accession of nanometer material eliminates the internal stress produced when the membrane pore foams and effectively avoid the productions of big pores and limitations and the accession of nanometer materials changes the pore structure of membrane. The adsorption property could be presented by the removal experiment of Titan Yellow with 2 negative charges in the molecule, and from the data in Table 2, the removal rate of hybrid membrane to Titan Yellow is two times than PVDF membrane. Because the molecular weight of Titan Yellow is 695, so the removal basically depends on the adsorption property of membrane. The nanometer aluminum magnesium hydroxide in the hybrid membrane has obvious positive electricity, big proportion surface area and pore capacity, and it has obvious adsorption property to Titan Yellow with negative electricity, so the removal rate of hybrid membrane to Titan Yellow could be obviously enhanced.

2.5 Influence of different AMH contents on membrane structure and properties

Implement property testing to the membrane formed by the casting solutions with different AMH contents and the obtained curves are seen in Figure 4 to Figure 7. The results show that with the increase of nanometer particle contents, the water flux of membrane increases, the increasing speed is quick, the porosity of membrane changes little, the pore diameter gradually declines, the retention and removal rate of membrane increase, and the breaking stress and breaking strain first reduce and then go to stable. Because of the increase of AMH accession, the viscosity of casting solution will increase, which will baffle the exchange speed of solution and non-solution, and AMH is rigid particle, and its accession will increase the pressured density, so the flux of membrane will increase and the mechanical property of membrane will be enhanced, but with the increase of accession, the membrane will become crisp, so the breaking elongation rate reduces. The increase of nanometer material accession could enhance the adsorption property of membrane and the removal rate of Titan Yellow.

2.6 EDS element analysis

EDS is a sort of measure to analyze the composing of surface election for material. In the experiment, we analyze the element composing of hybrid membrane transect through EDS. Because of the deficiency of analysis measure and the convenience of analysis, we adopt EDS to analyze the transect of hybrid membrane (the removal ratio is 68.2%) which content of nanometer aluminum magnesium hydroxide in PVDF is 8% to judge the composing content of transect element for hybrid membrane. The analysis results are seen in Figure 6 and Figure 7, and from Figures, we can see that nanometer aluminum magnesium hydroxide presents uneven distribution on the transect of membrane and the nanometer content near the surface of membrane are more. From the EDS element content analysis, we can see that the content of total nanometer material of membrane transect approaches the theoretical appending quantity, and it indirectly indicates the distribution of nanometer materials is basically even in the casting solution, but the re-uniting

phenomena occurs in the local areas of transect, which may be induced by that the increasing probability of collision in the membrane foaming process with the increase of nanometer material accession.

3. Conclusions

Comparing with general PVDF membrane, nanometer aluminum magnesium hydroxide/ PVDF hybrid micro-porous filter membrane prepared through phase translation method possesses following characters.

- (1) The pore structure changes obviously, and this sort of pore structure is more propitious to enhance the mechanical property of the membrane.
- (2) The flux of pure water and the retention to BSA are enhanced notably, and the pore diameter and porosity change little.
- (3) The mechanical property of membrane is enhanced obviously, and the removal rate to Titan Yellow is 2 times than PVDF membrane.
- (4) The increase of AMH content could obviously enhance the flux of pure water and removal rate for the membrane.
- (5) EDS analysis indicated that nanometer aluminum magnesium hydroxide distributed unevenly in the membrane, and was contained more in cortex and near cortex, but it distributed evenly in the total membrane.

Thus it can be seen that the introduction of nanometer particles could perfect membrane property, enhance the function of membrane, prepare the charged membrane with special separation function and develop the application of PVDF membrane in water treatment and other domains.

References

- Degen PeterJohn. (1998). Polyvinylidene Fluoride Membrane and Method for Removing Viruses from Solution. *USP:5736051*. 1998.04.07.
- Degen PeterJohn. (1995). Poly (vinylidene fluoride) Membranes. *DE:4445973*. 1995.06.29.
- Doyen W, Adriansens W, Molenberghs B, et al. (1996). A Comparison between Polysulfone, Zirconia and Organo-mineral Membranes for Use in Ultrafiltration. *Journal of Membrane Science*. No.113(2). P.247-258.
- E. Klumpp, C.Contreras-Ortega & P.Klahre, et al. (2004). Sorption of 2,4-dichlorophenol on Modified Hydr-otalcites. *Colloids and Surfaces A: Physicochem. Eng. No.230*. P.111-116.
- Genne I, Kuypers S & Leysen R. (1996). Effect of the Addition of ZrO₂ to Polysulfone based UF Membranes. *Journal of Membrane Science*. No.113(3). P.343-350.
- Huangning. (2003). Infrared Spectrogram Explanation and Composition Analysis on PVDF Fluorocarbon Coatings. *Paint & Coatings Industry*. No.33(12). P.45-48.
- Majun, Liu, Hongbin & Gong, Chengyuan. (2007). Preparation of Nanometer Sized Aluminum-magnesium Hydroxide Charge-modified Material. *Modern Chemical Industry*. No.27(s). P.193-195.
- O. Shina K H. (1996). The Use of a Microporous Polyvinylidene fluoride (PVDF) Membrane Filter to Separate Contaminating Viral Particles from Biologically Important Proteins. *Biologicals*. No. 24(2). p.137-145.
- Qu, Yun. (2006). Study on Pollution-resistant Nanometer TiO₂/PVDF Composite Membrane. *Doctor Thesis of Tianjin University*.
- Ramesh Chitrakar, Satoko Tezuka & Akinari Sonoda, et al. (2005). Adsorption of Phosphate from Seawater on Calcined MgMn-layered Double Hydroxides. *Journal of Colloid and Interface Science*. No.290. P.45-51.
- Wei, Yunhe, Zhu, Chenfu & Gaofeng. (2005). Study of the Adsorption of Cr(VI) on Aluminum-magnesium Hydroxide Positive Nanomaterial. *Industrial Water Treatment*. No.22(11). P.31-33.
- Yang Z Y. (1997). Use of Membrane in Wastewater Treatment in China. Experiments with Hollow Fiber Membranes in a Bioreactor. *Stuttg Ber Siedlungs Wasser Wirtsch*. No.145. p.75-86.
- Zheng, Cuiping & Xiao, Siqing. (1999). Testing the Performance of the Microporous Membrane by the COULTER POROMETER II. *Membrane Science and Technology*. No.19(1). P.31-33.

Table 1. Separation property comparison of nanometer aluminum magnesium hydroxide hybrid membrane and PVDF membrane

Sample	Flux of pure water (L·m ⁻² ·h ⁻¹)	Retention (%)	Maximum Pore Diameter (μm)	Average Pore Diameter (μm)	Porosity (%)
A	1344.40	78.01	0.230	0.197	88.45
B	971.04	57.79	0.244	0.213	87.03

Table 2. Mechanical property and adsorption property comparison of nanometer aluminum magnesium hydroxide hybrid membrane and PVDF membrane

Sample	Breaking stress (MPa)	Breaking strain (%)	Yang's simulation (MPa)	Removal rate (%)
A	1.30	65.18	22.96736	41.67
B	0.95	64.45	18.91604	20.18

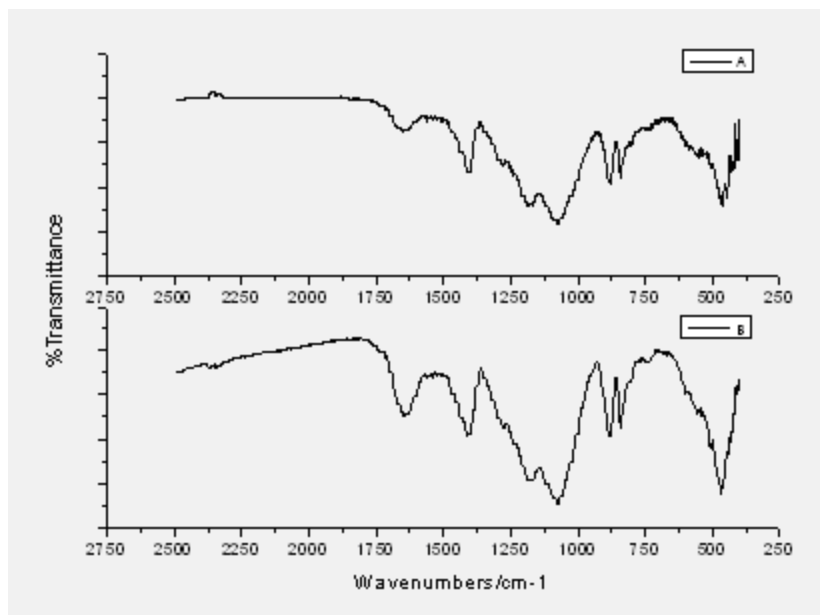


Figure 1. Infrared Spectrogram of Nanometer Aluminum Magnesium Hydroxide Hybrid Membrane and PVDF Membrane

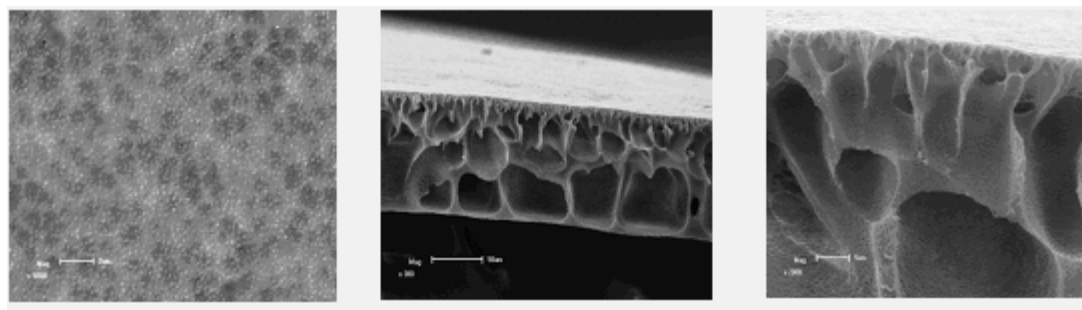


Figure 2. Surface and Transect SEM Photos of Nanometer Aluminum Magnesium Hydroxide Hybrid Membrane

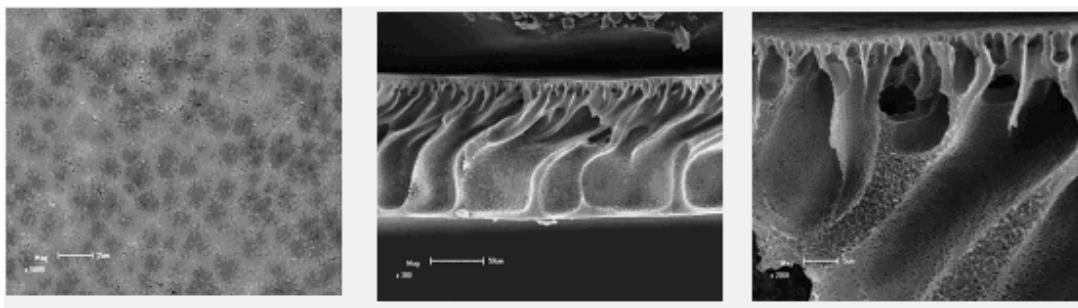


Figure 3. Surface and Transect SEM Photos of PVDF Membrane

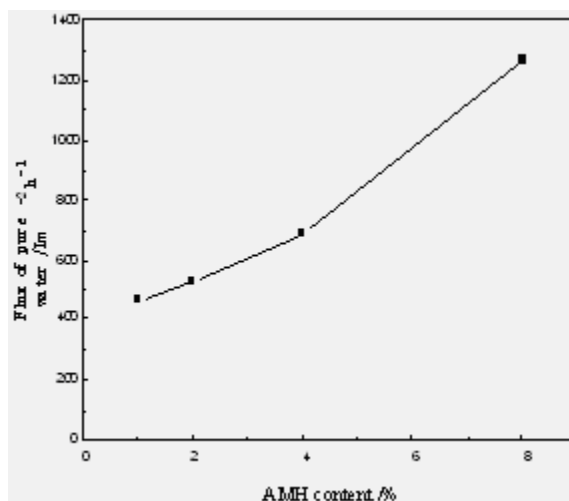


Figure 4. Influence of Different AMH Contents on Membrane Flux

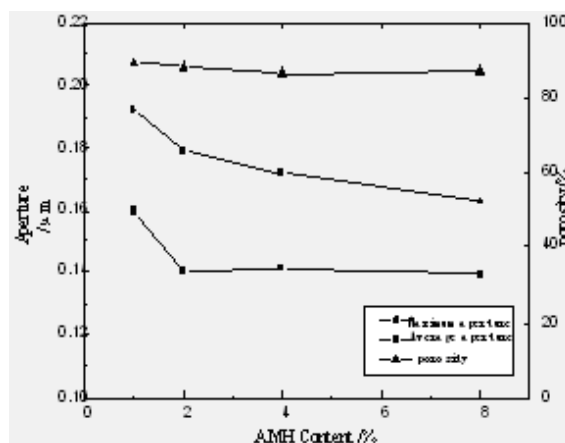


Figure 5. Influence of Different AMH Contents on Membrane Pore Diameter and Porosity

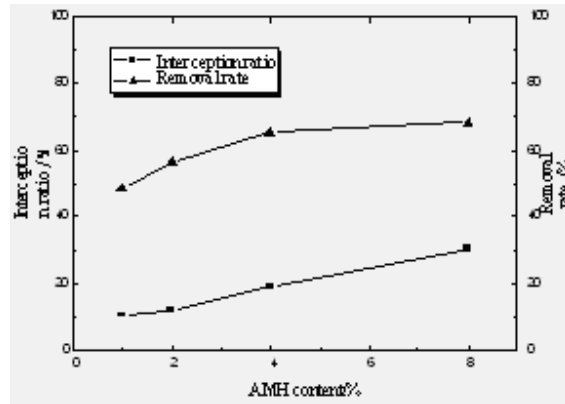


Figure 6. Influence of Different AMH Contents on Membrane Retention and Removal Rate

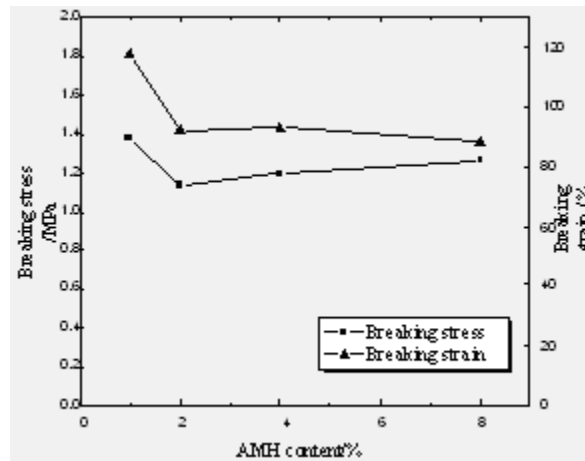


Figure 7. Influence of Different AMH Contents on Membrane Extension Property

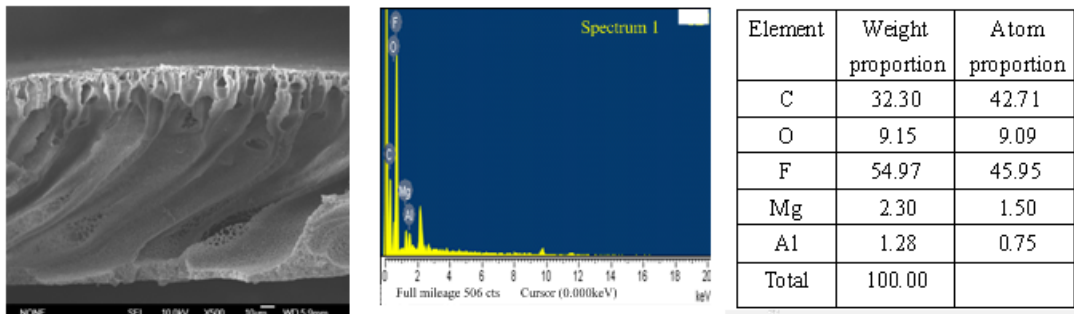


Figure 8. Transect SEM/EDS Analysis of Nanometer Aluminum Magnesium Hydroxide/ PVDF Hybrid Membrane

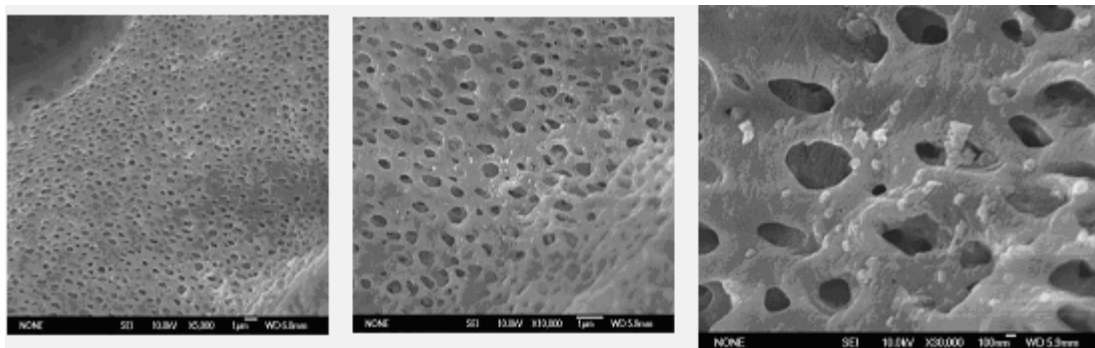


Figure 9. Local Transect SEM Magnified Image of Nanometer Aluminum Magnesium Hydroxide/ PVDF Hybrid Membrane

Editorial Board

Ahmad Mujahid Ahmad Zaidi Universiti Tun Hussein Onn Malaysia, Malaysia

J S Prakash Sri Bhagawan Mahaveer Jain College of Engineering, India

Sundus H Ahmed Ministry of Science and Technology, Iraq

Susan Sun Canadian Center of Science and Education, Canada

Sutopo Hadi University of Lampung, Indonesia

Wenwu Zhao Macrothink Institute, USA

A journal archived in Library and Archives Canada
A journal indexed in CANADIANA (The National Bibliography)
A journal indexed in AMICUS
A leading journal in applied science research
A journal indexed in Zentralblatt MATH

Modern Applied Science

Bimonthly

Publisher Canadian Center of Science and Education

Address 4915 Bathurst St. Unit # 209-309, Toronto, ON. M2R 1X9

Telephone 1-416-208-4027

Fax 1-416-208-4028

E-mail mas@ccsenet.org

Website www.ccsenet.org

Printer William Printing Inc.

Price CAD.\$ 20.00

